241
Topics in Current Chemistry

Topics in Current Chemistry

Recently Published and Forthcoming Volumes

Functional Molecular Nanostructures
Volume Editor: Schlüter, A.D.
Vol. 245, 2004

Natural Product Synthesis II
Volume Editor: Mulzer, J.H.
Vol. 244, 2004

Natural Product Synthesis I
Volume Editor: Mulzer, J.H.
Vol. 243, 2004

Immobilized Catalysts
Volume Editor: Kirschning, A.
Vol. 242, 2004

Transition Metal and Rare Earth Compounds III
Volume Editor: Yersin, H.
Vol. 241, 2004

The Chemistry of Pheromones and Other Semiochemicals II
Volume Editor: Schulz, S.
Vol. 240, 2004

The Chemistry of Pheromones and Other Semiochemicals I
Volume Editor: Schulz, S.
Vol. 239, 2004

Orotidine Monophosphate Decarboxylase
Volume Editors: Lee, J.K., Tantillo, D.J.
Vol. 238, 2004

Long-Range Charge Transfer in DNA II
Volume Editor: Schuster, G.B.
Vol. 237, 2004

Long-Range Charge Transfer in DNA I
Volume Editor: Schuster, G.B.
Vol. 236, 2004

Spin Crossover in Transition Metal Compounds III
Volume Editors: Gütlich, P., Goodwin, H.A.
Vol. 235, 2004

Spin Crossover in Transition Metal Compounds II
Volume Editors: Gütlich, P., Goodwin, H.A.
Vol. 234, 2004

Spin Crossover in Transition Metal Compounds I
Volume Editors: Gütlich, P., Goodwin, H.A.
Vol. 233, 2004

New Aspects in Phosphorus Chemistry IV
Volume Editor: Majoral, J.-P.
Vol. 232, 2004

Elemental Sulfur and Sulfur-Rich Compounds II
Volume Editor: Steudel, R.
Vol. 231, 2003

Elemental Sulfur and Sulfur-Rich Compounds I
Volume Editor: Steudel, R.
Vol. 230, 2003

New Aspects in Phosphorus Chemistry III
Volume Editor: Majoral, J.-P.
Vol. 229, 2003

Dendrimers V
Volume Editors: Schalley, C.A., Vögtle, F.
Vol. 228, 2003

Colloid Chemistry II
Volume Editor: Antonietti, M.
Vol. 227, 2003

Colloid Chemistry I
Volume Editor: Antonietti, M.
Vol. 226, 2003

Modern Mass Spectrometry
Volume Editor: Schalley, C.A.
Vol. 225, 2003

Transition Metal and Rare Earth Compounds III

Excited States, Transitions, Interactions

Volume Editor: Hartmut Yersin

With contributions by
R. Beaulac · H. Bélisle · G. Bussière, C.-M. Che · C. Daniel
A. Hauser · S. Kairouani · S.-W. Lai · V.S. Langford · C. Lescop
D. Luneau · U. Oetliker · A. Pillonnet · C. Reber · P. Rey
P.A. Tanner · M.E. von Arx · H. Yersin

Springer

The series *Topics in Current Chemistry* presents critical reviews of the present and future trends in modern chemical research. The scope of coverage includes all areas of chemical science including the interfaces with related disciplines such as biology, medicine and materials science. The goal of each thematic volume is to give the non specialist reader, whether at the university or in industry, a comprehensive overview of an area where new insights are emerging that are of interest to a larger scientific audience.

As a rule, contributions are specially commissioned. The editors and publishers will, however, always be pleased to receive suggestions and supplementary information. Papers are accepted for *Topics in Current Chemistry* in English.

In references *Topics in Current Chemistry* is abbreviated Top Curr Chem and is cited as a journal.

Visit the TCC content at http://www.springerlink.com/

Library of Congress Control Number: 2004112159

ISSN 0340-1022
ISBN 3-540-20948-4 **Springer-Verlag Berlin Heidelberg New York**
DOI 10.1007/b83770

Springer-Verlag is a part of Springer Science+Business Media
springeronline.com

Printed in Germany

Cover design: KünkelLopka, Heidelberg/design & production GmbH, Heidelberg
Typesetting: Stürtz AG, Würzburg

Printed on acid-free paper 02/3020 ra – 5 4 3 2 1 0

Volume Editor

Prof. Dr. Hartmut Yersin

Insitut für Physikalische
und Theoretische Chemie
Universität Regensburg
Universitätsstraße 31
93053 Regensburg
Germany
hartmut.yersin@chemie.uni-regensburg.de

Editorial Board

Topics in Current Chemistry
Also Available Electronically

For all customers who have a standing order to Topics in Current Chemistry, we offer the electronic version via SpringerLink free of charge. Please contact your librarian who can receive a password for free access to the full articles by registering at:

http://www.springerlink.com

If you do not have a subscription, you can still view the tables of contents of the volumes and the abstract of each article by going to the SpringerLink Homepage, clicking on "Browse by Online Libraries", then "Chemical Sciences", and finally choose Topics in Current Chemistry.

You will find information about the

– Editorial Board
– Aims and Scope
– Instructions for Authors
– Sample Contribution

at http://www.springeronline.com using the search function.

Preface

For a long time, the properties of transition metal and rare earth compounds have fascinated chemists and physicists from a scientific point of view. Recently, also the enormous potential of these compounds as new materials has become evident. Applications in different fields are now established, such as new laser materials, IR to visible upconversion materials, systems involving photoredox processes for solar energy conversion, new photovoltaic devices, phosphorescent sensors, and in particular electroluminescent devices (OLEDs). The applications mentioned are directly related to the properties of the electronic ground state and the lower-lying excited states. Metal complexes with organic ligands or organometallic compounds exhibit outstanding features as compared to purely organic molecules. For instance, metal compounds can often be prepared and applied in different oxidation states. Furthermore, various types of low-lying electronic excitations can be induced by a suitable choice of the metal center and/or the ligands, such as metal-centered (MC, e.g. d-d^* or f-f^* transitions), ligand-centered (LC, e.g. π-π^*), metal-to-ligand-charge transfer (MLCT, e.g. d-π^*), intra-ligand-charge-transfer (ILCT) transitions, etc. In particular, the orbitals involved in the resulting lowest excited states determine the photophysical and photochemical properties and thus the specific use of the compound. It is also high interesting that the lowest excited electronic states can be shifted over the large energy range from the U.V. to the I.R. by chemical variation of the ligands and/or the central metal ion. Moreover, these excited states have mostly spin-multiplicities different from those of the electronic ground states. Thus, in contrast to organic molecules, spin-orbit coupling induced by the metal center is of crucial importance, for example, for the splitting and the population and decay dynamics of these multiplets as well as for transition probabilities and emission quantum yields. In summary, transition metal and rare earth compounds can be prepared with photophysical properties that are over a wide range user-definable. In view of the fascinating potential of these compounds, it is of substantial interest to develop a deeper understanding of their photophysical properties. In this volume[1],

[1] See also the preceding volumes, Electronic and Vibronic Spectra of Transition Metal Complexes I and II, edited by H. Yersin, Topics in Current Chemistry 171 (1994) and 191 (1997) and two companion volumes, Transition Metal and Rare Earth Compounds – Excited States, Transitions, Interactions I and II, edited by H. Yersin, Topics in Current Chemistry 213 (2001) and 214 (2001)

leading scientists present modern research trends in comprehensive reviews which not only provide a deep insight into the specific subjects, but are also written in a style that enables researchers from related fields and graduate students to follow the interesting presentations.I am convinced that the contributions in the present and in the companion volumes demonstrate the attractiveness and the great potential for applications of metal compounds and that a more detailed understanding of the photophysical properties will open pathways for new developments.

Regensburg, Germany
April 2004 Hartmut Yersin

Contents

Contents of Volume 213

Transition Metal and Rare Earth Compounds

Excited States, Transitions, Interactions I

Volume Editor: Hartmut Yersin

ISBN 3-540-67986-3

Contents of Volume 214

Transition Metal and Rare Earth Compounds

Excited States, Transitions, Interactions II

Volume Editor: Hartmut Yersin

ISBN 3-540-67976-6

Top Curr Chem (2004) 241:1–26
DOI 10.1007/b96858

Triplet Emitters for OLED Applications. Mechanisms of Exciton Trapping and Control of Emission Properties

Hartmut Yersin

Institut für Physikalische Chemie, Universität Regensburg, 93040 Regensburg, Germany
hartmut.yersin@chemie.uni-regensburg.de

Abstract Triplet emitter materials present attractive possibilities for optimizations of organic/organometallic light emitting diodes (OLEDs). This is due to the significantly higher efficiencies obtainable with these compounds as compared to organic emitters. In this contribution, first a schematic introduction is given, how an OLED device is built-up and why multi-layer structures are preferred. Then a basic model is presented, how electron-hole recombination, i.e. the exciton formation process, can be visualized and how the singlet and triplet states of the (doped) emitter compounds are populated. This takes place by specific singlet and triplet paths. The occurrence of such paths is explained by taking into account that the dynamical process of exciton trapping involves dopant-to-matrix charge transfer states (^{1,3}**DMCT** states). It is also explained, why the excitation energy is harvested in the lowest triplet state of organo-transition-metal complexes. Due to spin statistics, one can in principle obtain an efficiency of a factor of four higher than using organic singlet emitter molecules. Simple comparisons suggest that electron-hole recombination should preferentially occur on the triplet emitter itself, rather than on ma-

trix molecules with subsequent energy transfer to the emitter. Further, it is pointed out that essential photophysical properties of organometallic triplet emitters depend systematically on the metal participation in the triplet state and on the effective spin-orbit coupling. These factors control the amount of zero-field splitting (ZFS) of the triplet state into substates. Increase of ZFS corresponds to higher metal character in the triplet state. Higher metal character reduces the energy difference between excited singlet and triplet states, enhances the singlet-triplet intersystem crossing rate, lowers the emission decay time, changes the vibrational satellite structure, decreases the excited state reorganization energy, etc. These effects are discussed by referring to well characterized compounds. Based on a new ordering scheme presented for triplet emitter materials, a controlled development of compounds with pre-defined photophysical properties becomes possible.

Keywords Triplet emitters · OLED · Organic/organometallic light emitting diode · Exciton trapping · Emission properties · Electroluminescence · Electrophosphorescence · Ordering scheme for triplet emitters

1 Introduction

Transition metal compounds with organic ligands or organometallic compounds[1] find an increasing interest due to their large potential for new photophysical and photochemical applications. This is particularly valid for compounds which exhibit high emission quantum yields from the lowest triplet states to the singlet ground states. Such compounds are frequently found. Their emission colors may lie in the whole visible range from the blue to the red and also in the IR. The emission decay times are usually orders of magnitude longer than those of purely organic singlet emitters. The compounds are often photo-redox active involving the triplet states and can be stable over the whole redox cycle. These photo-redox properties are important, for example, in systems that convert solar energy into electrical or chemical energy [1–3]. Moreover, emission spectra or decay times of the organometallic compounds are often sensitive to environmental factors, such as oxygen, water, rigidity of the environment, pH value, specific organic vapors, concentration of glucose, or simply vary with temperature, etc. Thus, these compounds are also in the focus of the strongly developing field of luminescence sensors [4–10].

In the scope of this chapter, organometallic triplet emitters are of particular interest due to their promising use in electro-luminescent devices such as OLEDs (organic/organometallic light emitting diodes). (See for example [11–16].) In Sect. 2, the construction and working principle of an OLED is

[1] In the chemical nomenclature *organometallic compounds* contain direct metal-carbon bonds, while this is not necessarily the case for *metal compounds with organic ligands*. In the scope of this review, however, this distinction is not always important. Therefore, mostly the shorter term organometallic compounds is used in a more general meaning.

presented on an introductive basis. Specifically, by use of organometallic compounds, it is possible to obtain, at least in principle, a four times higher electro-luminescence efficiency than with typical singlet emitters. This property is related to the specific mechanisms of exciton formation in the electron-hole recombination zone and to fast and efficient intersystem crossing (ISC) from the excited singlet to the light emitting triplet state. This process of accumulating the excitation energy in the lowest excited triplet state is often called *triplet harvesting*. These mechanisms are addressed in detail in Sect. 3.

The triplet states of the emitter materials play an essential role in OLEDs. Therefore, it is highly desirable to control the properties of these states and to synthesize compounds with pre-defined behavior. However, this is only achievable if a good understanding of the electronic structures of the states involved in the emission process is available. In particular, it is very useful to know how these electronic states react on chemical variations, changes of the environment or temperature. Obviously, there are already important approaches to these objectives available. For example, variations of emission energies and redox-potentials with ligand replacements or substitutions have been studied especially for complexes of Ru(II) and Os(II) [17–22], but also of Re(I) [23, 24], Ir(III) [13, 25] and others (e.g., see [12, 22, 26–29])[2]. Modifications of emission properties with solvent or matrix variation have been described for many organometallic compounds [22, 23, 30–34]. Of particular interest are those factors that determine emission decay times and photoluminescence quantum yields. In this respect, one has to consider symmetry effects, spin-orbit coupling (SOC) of the emitting state to higher lying states, self-quenching (for example, by triplet-triplet annihilation resulting from interactions between adjacent excited emitter compounds), radiationless energy transfer to impurity centers, vibronic coupling, vibrational energies, coupling to the environment, etc. Specifically, vibronic coupling is responsible for radiationless deactivation. This coupling leads to the well-known energy gap law. It relates the increase of radiationless deactivation and thus a decrease of photo-luminescence quantum yield and emission decay time to a decrease of the energy separation between the emitting state and the ground state (see for example [20, 23, 30, 32, 35]; for background information see also [35–39]).

In the present investigation, a different strategy leading to a control of photophysical properties is discussed. In this approach, a new ordering scheme is presented which is based on the extent of metal participation, such as 4d or 5d orbital character, in the emitting triplet state. The metal participation in the corresponding wavefunction is also responsible for the importance of spin-orbit coupling. Interestingly, the corresponding extent of these influences is displayed in the size of the splitting of the triplet state

[2] References are only given as examples.

into substates, the total zero-field splitting (ZFS). This parameter can be varied over more than three orders of magnitude by appropriate combination of the transition metal ion and the organic ligands. This ordering scheme is presented in Sect. 4. The essential photophysical effects that are induced by the increasing metal character in the triplet state are discussed in Sect. 5. The paper is concluded with Sect. 6.

2 OLED Structure and Device Architecture

Figure 1 shows the basic and simplified structure of an OLED which is largely built up of organic materials. Under action of a driving voltage of 5 to 10 V or even lower, electrons are injected from a metal cathode with a low work function into the electronic state corresponding to the LUMO (lowest unoccupied molecular orbital) of the adjacent layer material (electron transporting layer). In this layer, the electrons hop via the LUMOs of neighboring molecules towards the anode. The hopping process under action of an exter-

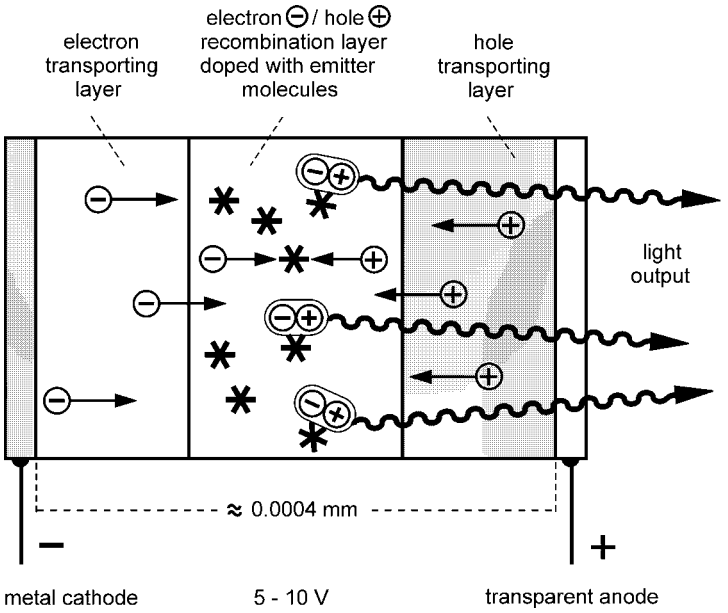

Fig. 1 Basic set-up of a layered OLED structure. Electrons and holes are injected from the respective electrodes (metal cathode, semiconducting and transparent anode). The charge carriers move from different sides into the recombination/emitter layer, where electrons and holes recombine and excite the doped emitter molecules (asterisks, e.g., organometallic triplet emitters). For more details see Fig. 2. For clarity, light emission is only shown for one direction although the photons are emitted in all directions

nal driving potential is related to a specific electron mobility. It is remarked that the electron mobility in organic materials is orders of magnitude smaller than in crystalline inorganic semiconductors. This is due to the quasi-localized nature of the electronic states in disordered (amorphous) organic materials, the relatively small overlap of electronic wavefunctions of neighboring molecules, and other irregularities of molecular packing within the layers. The charge carrier transport occurs in these disordered materials mainly by thermally activated hopping processes.

The anode of the device is a transparent semiconducting layer which usually consists of a nonstoichiometric composite of SnO_2 (10–20%) and In_2O_3 (90–80%), usually called indium tin oxide (ITO). This material is coated, for example, on a glass support. The ITO layer exhibits a low work function for hole[3] injection into the highest occupied molecular orbital (HOMO) of the organic material which acts as hole conducting layer. Again, the hole mobility in the amorphous organic layer material is much smaller than the mobility via the valence band of an inorganic semiconductor.

Both particles, electron and hole—coming from the different electrodes—move from opposite directions towards the recombination layer. There they can combine and form excitons. This may happen near to the layer interface, on matrix molecules within the layer, and/or at doped emitter molecules. In suitable cases, as required for OLEDs, this leads to a population of excited states of the emitter material which subsequently emits light. Obviously, this process should occur with high efficiency. Details of the mechanism of exciton formation and population processes of excited emitter states are discussed in the next section.

The simple set-up of an OLED as presented in Fig. 1 is in most cases not well suited to exploit the potential of efficiency of light emission that is in principle obtainable. Independent from the quantum efficiency of the emitter molecules, losses can occur for several reasons, such as poor adjustments of workfunctions of the electrodes relative to the HOMO/LUMO of the adjacent organic layers, bad alignments of HOMOs and LUMOs of the different organic layers relative to each other which can cause charge carrier trapping and unfavorable space charges, unbalanced electron and hole transports, low electron or hole mobility which can lead to ohmic losses, low cross sections for electron-hole recombination, low light outcoupling efficiency, etc.

[3] The HOMO of a neutral organic molecule us usually populated with two electrons. If one electron is taken off, for example by transferring it to the anode, the remaining situation is characterized by a positively charged molecule. Subsequently, the free electron position in the HOMO can be populated by an electron from the HOMO of a neighboring molecule. Thus, the positive charge has moved to the neighbor. An equivalent process occurs involving the next nearest neighbor, and so on. Thus, the positive charge—called a hole—moves from molecule to molecule into direction of the cathode. Such a hole has properties of a particle, it carries a positive charge, a spin (the one of the residual electron) and can move with a specific hole mobility by use of the HOMOs.

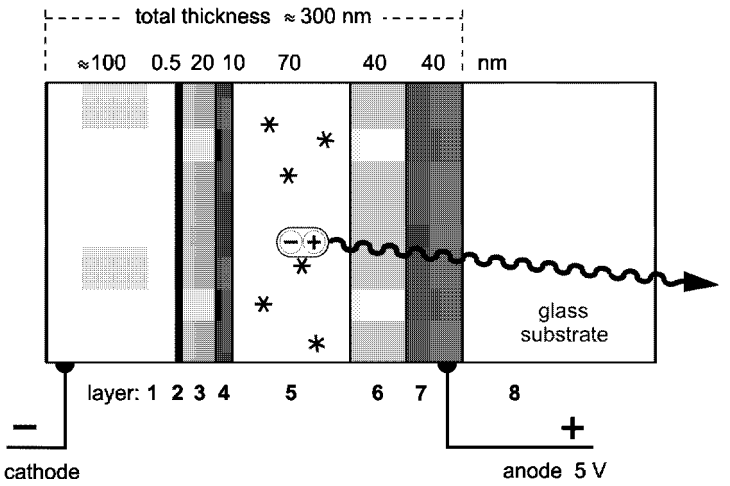

Fig. 2 Example of an optimized OLED structure. (**1**) (**2**): cathode, Ag and LiF. (**3**): electron transporting layer; Alq_3 (=$Alqol_3$). (**4**): hole blocking layer, BCP. (**5**): electron-hole recombination zone/emitter layer, PVK doped, for example, with $Ir(ppy)_3$. (**6**) and (**7**): anode, PEDOT doped with PSS (**6**) for improvement of hole injection and substrate smoothness and ITO (**7**) (=indium tin oxide). (**8**): glass support. For further details and explanations see text

The OLED technology is far from being completely developed, although substantial progress has been made during the last years.

An improved OLED device structure is displayed in Fig. 2 and will subsequently be discussed on an introductory basis. By careful adjustment of the different layers a much more efficient OLED can be constructed (device architecture). The device shown consists of eight layers including the electrodes and the glass support. (**1**) and (**2**): The cathode is mostly built-up by a bi-layered material to reduce the work function of electron injection. For example, Al/LiF [40, 41] or Ag/MgAg [42, 43] are frequently applied. (**3**): In most devices, Alq_3 (q^-=qol^-=8-quinolinolato-O,N) is used as electron transporting layer [40–45]. (**4**): Holes, coming from the anode, have to be present with high density in the recombination layer, but they should be blocked from further transport to the cathode. Therefore, hole blocking increases the efficiency of light emission. This is achieved by a material with a sufficiently low lying HOMO (e.g., see [44]). On the other hand, it is important that this layer does not block electron transport. In many cases, BCP (bathocuproine=4,7-diphenyl-2,9-dimethyl-1,10-phenanthroline) has been employed as hole blocking layer [16, 40, 42–44]. (**5**): In the recombination or emitter layer, holes and electrons have to be accumulated at high, but balanced densities and should recombine to induce light emission. The device efficiency depends essentially on the emitter compound as well as on the

matrix material of layer (**5**). Particularly efficient emitter compounds are organo-transition-metal complexes, which are in the focus of this contribution. They are doped into a suitably selected layer (matrix) material. It seems to be advantageous, when the electron-hole recombination occurs directly at the doped emitter molecules (see Sects. 3.1 and 3.4). Obviously, the HOMO and LUMO positions of the emitter layer matrix material have to fit to those of the adjacent layers as well as to the oxidation potential of the electronic ground state and to the reduction potential of the (active) excited state of the doped emitter. Moreover, the triplets of the matrix molecules have to lie at higher energies than the triplets of the doped emitter molecules. Otherwise, the emission of the dopants would be quenched. A successful emitter layer is, for example [43], PVK (polyvinylcarbazole) doped with about 5 wt% $Ir(ppy)_3$ (fac-tris(2-phenylpyridine)Ir(III)). PVK represents a good hole transporting polymer. It is remarked that also several other matrix materials have successfully been tested with $Ir(ppy)_3$ as emitter compound (e.g., see [40, 44]). However, in this latter case other materials of the adjacent layers might be required to obtain a fit of the potentials. (**6**) and (**7**) are the anode layers. (7) is the transparent ITO anode, while (6) is a material used to improve hole injection and substrate smoothness. For this material PEDOT (poly(ethylenedioxythiophene) doped with polystyrenesulfonic acid (PSS) has, for example, been applied [43, 46]. It is remarked that good contact between the ITO and the PEDOT:PSS layers is crucial. Thus, specific cleaning of the ITO substrate, for example, by oxygen plasma or UV ozone treatment is required, e.g. see [47, 48]. (**8**): Finally, the layers discussed so far have to be positioned on a support, since the total thickness of the layers (1) to (7) is only about 300 nm (Fig. 2). Mostly, a glass support is employed.

Obviously, the state of art of research and development of highly efficient devices cannot be summarized in this introductory discussion of device architecture. This would be outside the scope of the present review. Here it is only possible to point to several recent further developments in various fields, such as (i) improvement of light outcoupling by controlling interference effects [49, 50], (ii) increase of charge carrier mobilities by doping of donors into electron conducting materials or acceptors into hole-transporting layers [51], (iii) improvement of adaption of workfunctions for hole and electron injection and optimization of redox potentials of the different layers (compare review [45]), (iv) development of materials with sufficiently high glass-transition temperature to avoid crystallization [45], (v) use of organosiloles as electron transporting materials [52–55], (vi) high-efficiency white light OLEDs [56], (vii) techniques for increase of device lifetime by device encapsulation to prevent water or oxygen penetration [57, 58], and (viii) materials and/or methods for better or less expensive OLED fabrication [59–61], etc.

3
Exciton Formation and Energy Harvesting in the Triplet State

3.1
Model of Exciton Formation

It is instructive to discuss how the process of electron-hole recombination and the formation of a neutral exciton and finally the population of an excited state of the emitter molecule can be visualized. Here, we focus on processes that occur within the emitter layer (layer (**5**) in Fig. 2). This layer of a thickness of about 70 nm consists of an organic matrix which is doped with emitter molecules (dopants). In the subsequent model it is assumed that the recombination of electrons and holes occurs at the dopants. The importance of this process has been deduced by comparison of photoluminescence and electroluminescence properties [62, 63]. If the matrix is excited optically, one observes an emission of both matrix and dopant. The intensity of the latter one increases gradually with the concentration of the dopant. Its emission can be ascribed to result from a radiationless energy transfer from the initially photo-excited matrix to the dopant. Thus, relatively high dopant concentrations are required to achieve quenching of matrix emission. On the other hand by electro-luminescent excitation, the concentration of the dopant can be reduced by more than two orders of magnitude to achieve complete quenching of matrix emission. Only dopant emission is observable. These results [62, 63] show that one of the charge carriers, either hole or electron, is trapped first at the dopant. For completeness, it is remarked that the effective recombination zone can be significantly thinner than the whole emitter layer, since the recombination may occur near to a layer interface within a range of only 5–10 nm due to a high density of charge carriers in this region [16, 64]. In Sect. 3.4 the processes of exciton formation and trapping are addressed again to focus on an aspect of OLED material design.

Figure 3 displays a simplified and schematic model to describe the process of exciton formation. The first step is characterized by trapping of a charge carrier. In our model it is assumed that the hole is trapped first at the emitter molecule as proposed, for example, for Ir(F-ppy)$_3$[4] in PVK [65]. This process induces (for a short time interval) the formation of an oxidized Ir(F-ppy)$_3$ complex. However, trapping of an electron as first step would result in an equivalent model and might be of relevance for other emitter molecules. For example, a corresponding process might be demanded for emitter layers doped with compounds which exhibit irreversible oxidation, as found for several Pt(II) complexes [12]. The process of charge carrier trapping can induce a reorganization at the emitter molecule which means that intramolecular distances, electronic energies, interactions with the environ-

[4] fac-tris[2-(4′,5′-difluorophenyl)pyridine]Ir(III)

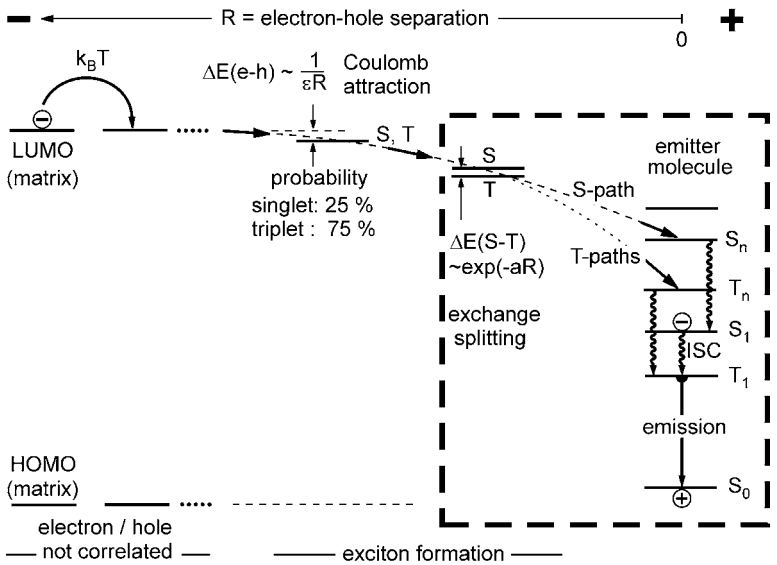

Fig. 3 Dynamics of exciton formation. It is assumed that the hole (+) is trapped first on the doped emitter molecule. The exciton formation starts due to Coulomb interaction between the trapped hole and the electron (−) on a matrix molecule. At the beginning of the exciton formation the spins of hole and electron are already correlated to one singlet and three triplet substates. This corresponds in a statistical limit to a ratio of 25% to 75%. The S-path and T-path populate the excited states of the emitter molecule (exciton trapping process). These paths can also be interpreted as relaxation processes from dopant-to-matrix charge transfer states. The DMCT states are deduced from the situation displayed in the framed part shown at the right hand side of the figure. The corresponding energy level diagram is depicted in Fig. 4. For clarity, the diagram does not show shifts of matrix orbitals due to the external potential, also reorganization energies are not depicted in the figure. ISC: intersystem crossing, ΔE (e-h): electron (e)-hole (h) binding energy; ΔE (S-T): singlet-triplet splitting

ment, etc. can be altered. The corresponding effects depend strongly on the individual emitter molecule and its specific matrix environment. They are not depicted in the model of Fig. 3. Under an applied external potential, the electron will migrate along the matrix material towards the anode. Usually, this process of electron hopping (more exactly: polaron hopping[5]) requires a thermal activation energy due to inhomogeneities from spatial and energy disorder and due to matrix reorganization effects. The related energy shifts should be less or of the order of the thermal energy k_BT with k_B being the Boltzmann constant and T the absolute temperature. For clearness, the dia-

[5] Electron (or hole) hopping is normally connected with a polarization of the matrix. Therefore, the corresponding negatively (positively) charged particle represents a polaron (for background information see, for example, [66]).

gram is simplified and does not show the inhomogeneous distribution of the energy levels of the matrix molecules and their energy shifts induced by the external potential.

When the electron is still far from the trapped hole, it will migrate independently from this hole towards the anode. Thus, hole and electron are not bound or correlated. This situation corresponds to the exciton continuum in solid-state semiconductors (see left hand side of the diagram, Fig. 3). However, when the electron migrates into a region given by a specific electron-hole separation R, the positively charged hole will attract the electron. This separation is reached when the energy of the Coulomb attraction is of similar size as the larger one of the two values, the mean inhomogeneous distribution of the energy levels of the matrix material or the thermal energy k_BT. Due to the Coulomb attraction, an electron (e)-hole (h) binding results. The binding energy ΔE(e-h) depends on the separation R and on the electric permittivity (dielectric constant ϵ) of the matrix material. Induced by this attraction, the exciton is formed. The Coulomb attraction represents a long-range interaction as compared to nearest neighbor separations.

For the further processes, it is required to take also the spins of both electron and hole into account. The spin of the hole is given by the spin of the residual electron at the emitter molecule. In a quantum mechanical treatment, these spins can be coupled to *four* new combined states. One obtains *one* singlet state and one triplet state. The triplet consists of *three* triplet substates. These substates differ from each other mainly by their relative spin orientations. An energy splitting between the resulting singlet and triplet states may be disregarded at large electron-hole separations. Therefore, the corresponding exciton state is shown in Fig. 3 (middle) just by one energy level. In a statistical limit, all *four* substates of this exciton state will be formed (populated) with an equal probability. Consequently, one obtains a *population ratio of one to three* for singlet and triplet substates, respectively.

Driven by electron-hole attraction, the electron will further move on matrix molecules towards the trapped hole. At least, when the electron reaches nearest neighbor matrix molecules of the emitter, an overlap of electron and hole wavefunctions has also to be taken into account. The resulting (short-range) exchange interaction leads to an energy splitting of singlet (**S**) and triplet (**T**) states by ΔE(S-T). As depicted in Fig. 3, this energy depends approximately exponentially on the electron-hole separation (a is a constant which depends on the respective matrix and the emitter material).

In a final step, the electron jumps in a very fast process directly to the emitter molecule and it results an excited emitter. This process may occur as singlet or triplet path (S-path, T-path) depending on the initial spin orientation of the electron-hole pair. The corresponding time constants are of the order of one picosecond (see next section). The population of $\mathbf{S_n}$ and $\mathbf{T_n}$ states, as shown in Fig. 3, is only depicted as an example. Subsequently, the system will exhibit the usual behavior of an optically excited emitter mole-

cule with typical relaxation processes to the lowest excited states and typical emission properties (right hand side of Fig. 3).

3.2 Charge Transfer States and Relaxation Paths

The final steps of the mechanisms described above can also be discussed in a slightly different way, to illustrate the occurrence of specific singlet and triplet paths. The situation of a lacking electron in the ground state of the doped emitter molecule (dopant D) and of additional electron charge density on nearest neighbor matrix molecules M can be characterized by dopant-

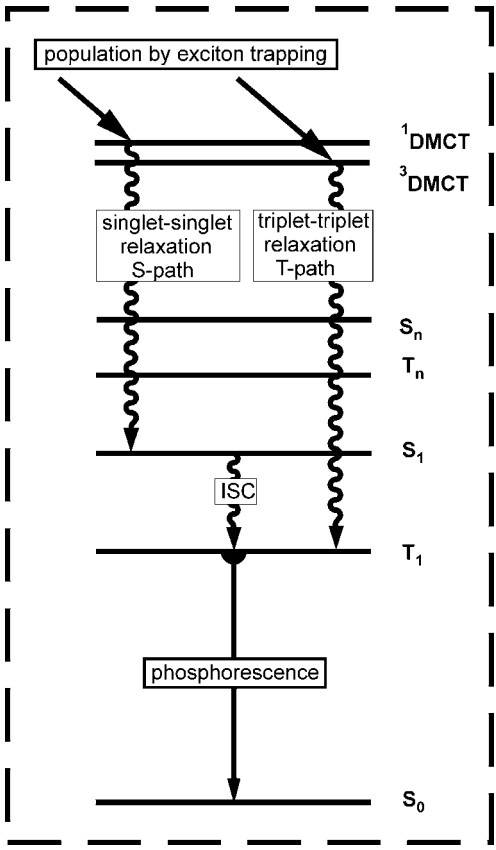

Fig. 4 Energy level diagram of an emitter compound with its first coordination sphere of matrix molecules. The states ^{1}**DMCT** and ^{3}**DMCT** represent dopant-to-matrix charge transfer states. The lower lying states are largely those of the isolated emitter molecule itself. The relaxations from the ^{1}**DMCT** and ^{3}**DMCT** states, respectively, represent the S-path and T-path of exciton formation as depicted in Fig. 3

to-matrix charge transfer (DMCT) states, specifically by singlet (^{1}**DMCT**) and triplet (^{3}**DMCT**) states.

It may be visualized that these states belong to a large molecular complex that consists of the doped emitter itself and of the first nearest neighbor sphere of matrix molecules. The energy level diagram of this emitter-matrix-cage unit is schematically displayed in Fig. 4. It corresponds to the framed part of Fig. 3. In particular, the states **S** and **T** shown in the frame represent the ^{1}**DMCT** and ^{3}**DMCT** states of the large molecular unit. The lower excited states $\mathbf{S_0}$, $\mathbf{T_1}$, $\mathbf{S_1}$ to $\mathbf{S_n}$ are largely confined to the doped molecule itself, while the higher lying charge transfer states are spatially more extended to the first matrix coordination sphere. For these latter states, the exchange interaction between the two electrons involved is relatively small. Thus, the energy separation between the ^{1}**DMCT** state and the ^{3}**DMCT** state is expected to be much smaller than singlet-triplet separations of the spatially more confined states of the original dopant itself.

On the basis of the energy level diagram of Fig. 4, one also obtains information about the relaxation paths from the excited charge transfer states. In particular, the relaxation from the ^{1}**DMCT** to lower states will be faster within the system of singlet states than making a spin-flip first. This is due to the fact that spin-orbit coupling in the organic matrix material will be relatively small and, thus, intersystem crossing (ISC) is not favored. Consequently, one obtains the fast singlet path that finally populates the $\mathbf{S_1}$ state. (Figs. 3 and 4). Subsequently, the population of the $\mathbf{S_1}$ state will be followed by an ISC to the $\mathbf{T_1}$ state, though usually with a smaller rate (see also next subsection). An initial population of the ^{3}**DMCT** state is similarly followed by a very fast relaxation within the system of triplet states down to the lowest triplet state $\mathbf{T_1}$ (Fig. 4). The beginning of this relaxation process corresponds to the triplet path in the exciton trapping model shown in Fig. 3. The relaxation times within the singlet and triplet system, respectively, are of the order of one picosecond or faster, while the ISC processes can be significantly slower (see next section).

In conclusion, it is remarked that the exciton trapping process and thus the efficiency of light emission in an OLED will usually depend on both the emitter molecule and the matrix environment.

3.3 Triplet Harvesting

Spin-orbit coupling will not strongly alter the mechanism of exciton formation in an organic matrix material, but it will have drastic effects on the efficiency of electro-luminescence in an OLED device. To illustrate this property, we will compare the efficiency which is obtainable with a purely organic molecule to the efficiency achievable with a transition metal complex, if both molecules exhibit equal photo-luminescence quantum yields. If one as-

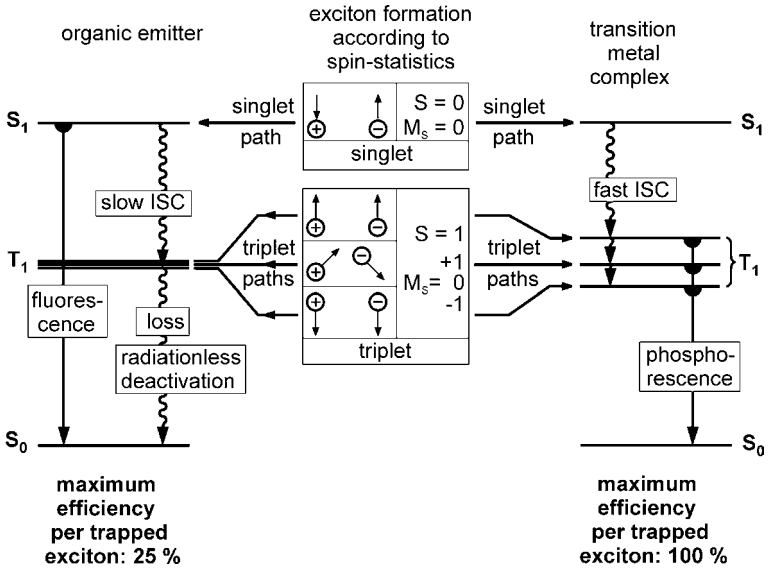

Fig. 5 The diagram explains the effect of triplet harvesting. Due to spin-statistics, electron-hole recombination leads to 25% singlet and 75% triplet state population. In organic molecules, only the singlets emit light (fluorescence), while the triplet excitation energy is transferred into heat (left hand side). On the other hand, organometallic compounds with transition metal centers do not exhibit a fluorescence, but show a fast intersystem crossing (ISC) to the lowest triplet state. Thus, the triplet *harvests* singlet and triplet excitation energy and can efficiently emit. In principle, a triplet emitter can—in the limit of vanishing radiationless deactivations—exhibit a four times higher electroluminescence efficiency than a singlet emitter

sumes that the initial process of exciton formation occurs statistically with respect to the spin orientations, one obtains 25% of excitons with singlet character and 75% with triplet character. At least for small molecules, this view is largely accepted[6].

After exciton formation and relaxations according to the specific singlet and triplet paths, as discussed in the preceding section, the lowest excited singlet and triplet states are populated. This is valid for organic as well as for organo-transition-metal emitter materials. The corresponding processes are schematically displayed in the middle of Fig. 5. The organic molecule can exhibit an efficient emission as $S_1 \rightarrow S_0$ fluorescence, since usually the $S_1 \rightarrow T_1$ intersystem crossing rate is small. On the other hand, since the radiative $T_1 \rightarrow S_0$ rate is also small, the deactivation of the T_1 state occurs normally non-radiatively at ambient temperature. Therefore, 75% of the excitons, the

[6] Currently it is discussed in the literature that for large conjugated polymers spin-statistics might not be applicable; however, this discussion is irrelevant for triplet emitters with high ISC rates (compare [67–74]).

triplet excitons, are lost. Their energy is transferred into heat (Fig. 5, left hand side). The conditions are more favorable for transition metal complexes, in which the central metal ion carries significant spin-orbit coupling (Fig. 5, right hand side). This is particularly valid for metal ions of the second and third row of transition metals. For these complexes, ISC to the lowest $\mathbf{T_1}$ state is usually very efficient and thus a singlet $\mathbf{S_1}$ emission is not observable. Moreover, the radiative $\mathbf{T_1 \rightarrow S_0}$ rate can become sufficiently high so that efficient phosphorescence can occur, even at ambient temperature (for a more detailed discussion see below). Consequently, all four possible spin orientations of the excitons can be harvested to populate the lowest $\mathbf{T_1}$ state. In conclusion, by this process of *triplet harvesting* one can in principle obtain a four times larger electro-luminescence efficiency for triplet emitters than for singlet emitters. This factor of four can be attained if the radiationless deactivation is equal for both emitter types.

3.4 Exciton Trapping at a Matrix Site and Energy Transfer

Exciton formation and trapping can also occur at matrix sites. Both the lowest singlet and triplet states of matrix molecules will be populated. From there, triplet and singlet exciton diffusion as Frenkel excitons can occur, although with different transport probabilities. This will alter the spatial distribution of matrix molecules that are excited in singlet and triplet states, respectively, as compared to the situation immediately after excitation. For an efficient OLED, it is mostly required to harvest the excitation energy completely in an efficiently phosphorescent triplet state of an organometallic dopant. This requires the realization of two distinctly different, but effective processes of energy transfer (Fig. 6). For example, the singlet excitation energy is transferred by a long-range Förster transfer mechanism from a matrix molecule to the acceptor (dopant). Independently, the triplet excitation energy is transferred by a second process of energy transfer from the matrix molecule, for example, by a short-range Dexter transfer mechanism. Both transfer mechanisms should be highly efficient and therefore they should fulfill the resonance conditions. This can be expressed by non-vanishing spectral overlap integrals of donor emissions and acceptor absorptions (for background information see, for example [38]). The fulfillment of these two independent conditions for singlet and triplet energy transfer seems to make this concept of material design—apart from specific and selected combinations—less favorable, as compared to systems with charge carrier trapping directly on the triplet emitters, as discussed in Sect. 3.1 (compare also [73, 74]).

Independent from the discussion presented above, Fig. 6 also shows that the lowest triplet state of the emitter compound always has to lie at lower energy than the triplet of the matrix material. Otherwise the matrix would

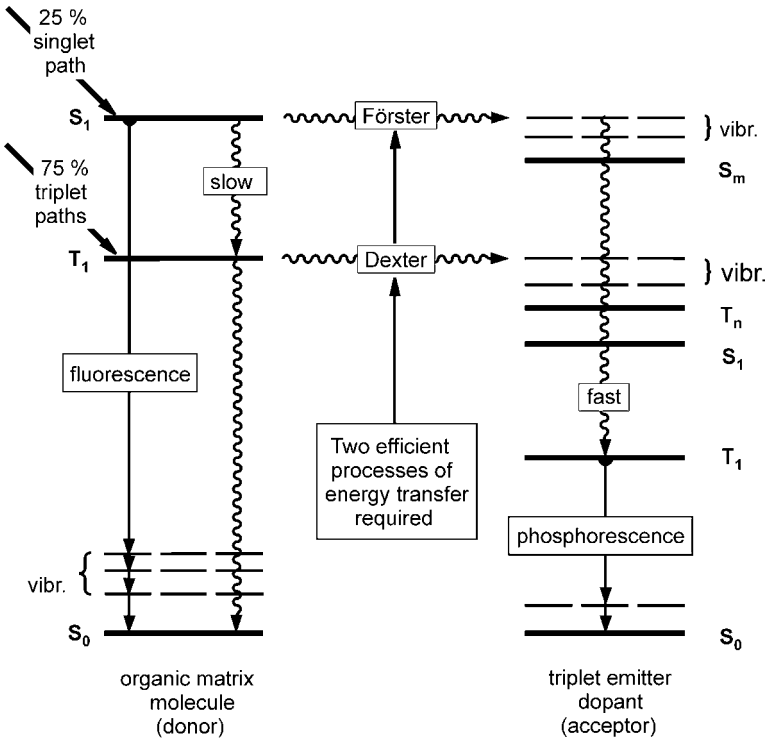

Fig. 6 Exciton trapping on organic matrix molecules with subsequent energy transfer. Exploitation of matrix singlet and triplet excitation energy requires the effectiveness of two independent processes of energy transfer. Such a matching of molecular energies might be difficult to achieve, when OLED emitter layers are developed. vibr.: vibrational states

quench the excited emitter. In a slightly different approach, one can also express the following requirement. The states corresponding to HOMO and LUMO of the dopant have to be within the gap of the states that stem from the matrix material. Thus, hole or electron trapping as the initial process is possible and quenching of emitter triplets by matrix triplets is prevented.

4 Ordering Scheme for Organometallic Triplet Emitters

Many photophysical properties of the lowest excited triplet states and the corresponding transitions of organometallic compounds are essentially determined by the extent of metal participation in the wavefunctions. This metal participation not only alters the spatial extension of the wavefunc-

tions, but also induces significant mixtures of singlet and triplet states by spin-orbit coupling (SOC) which is mainly carried by the metal orbitals. It is of interest to develop an understanding how these effects influence the photophysical properties of emitter materials. Indeed, this is possible. Moreover, it can be shown that a simple ordering scheme can be helpful in this respect [75–79]. Specifically, the energy splitting of the triplet state into substates, the zero-field splitting (ZFS) measured in cm^{-1}, can be utilized, since this parameter displays the importance of metal character and SOC for the respective triplet state.

The amount of ZFS is usually determined spectroscopically. Nevertheless, it is instructive to visualize that it is dominantly controlled by specific interactions. For example, the splitting of a pure $^3\pi\pi^*$ state which is not metal-perturbed is only given by spin-spin interactions (e.g., see [38, 80–82]). In this situation, the ZFS is of the order of 0.1 cm^{-1}. However, if **^{3}MLCT** and **^{1}MLCT** states are in proximity, the substates of these latter states will interact due to SOC with the substates of the $^3\pi\pi^*$ term. This can lead to a significant triplet splitting in particular, when 5d orbitals are involved in the **^{1,3}MLCT** states. As a consequence, the ZFS can increase by more than three orders of magnitude, up to more than 200 cm^{-1} [75–79]. The amount of ZFS can be determined, at least formally, by second order perturbation theory, whereby the perturbation is given by the spin-orbit Hamiltonian. The resulting matrix elements that induce the coupling are essentially controlled by d-orbital participation in the admixing wavefunction (compare also [81–86]).

Figure 7 shows a sequence of a series of compounds which are arranged according to an increasing ZFS of the emissive triplet state. The ZFS values of most of the compounds have been determined from highly resolved optical spectra [34, 75–79] (references for the individual compounds are given in [79]). Only for $Ir(ppy)_3$ [87] and $Ir(ppy)_2(CO)(Cl)$ [25] were such resolved spectra not yet obtainable, and therefore the information was determined indirectly from the temperature dependence of the emission decay time.

The low-lying electronic states of the compounds shown in Fig. 7 have to be assigned to different types of frontier orbital transitions. Thus, the lowest triplets of $[Rh(bpy)_3]^{3+}$ and $[Pt(bpy)_2]^{2+}$ are characterized as ligand centered **^{3}LC**($^3\pi\pi^*$) states with very small metal admixtures and those of $[Ru(bpy)_3]^{2+}$, $Ir(ppy)_3$, $[Os(bpy)_3]^{2+}$, and $[Os(phen)_3]^{2+}$ represent **^{3}MLCT** (metal-to-ligand charge transfer) states. The cyclometalated Pt(II)-compounds and $[Pt(mnt)_2]^{2-}$ have to be assigned to intermediate situations with significant **^{3}LC/^{3}MLCT** mixtures, whereas the lowest states of the oxinate complexes, such as $Pd(qol)_2$, $Pt(qol)_2$, and $Pt(qtl)_2$, are characterized as **^{3}ILCT** states (intra-ligand charge transfer from the phenolic moiety to the pyridine part of the ligand) with relatively small metal-d or MLCT admixtures. Nevertheless, the ordering expressed by the sequence shown in

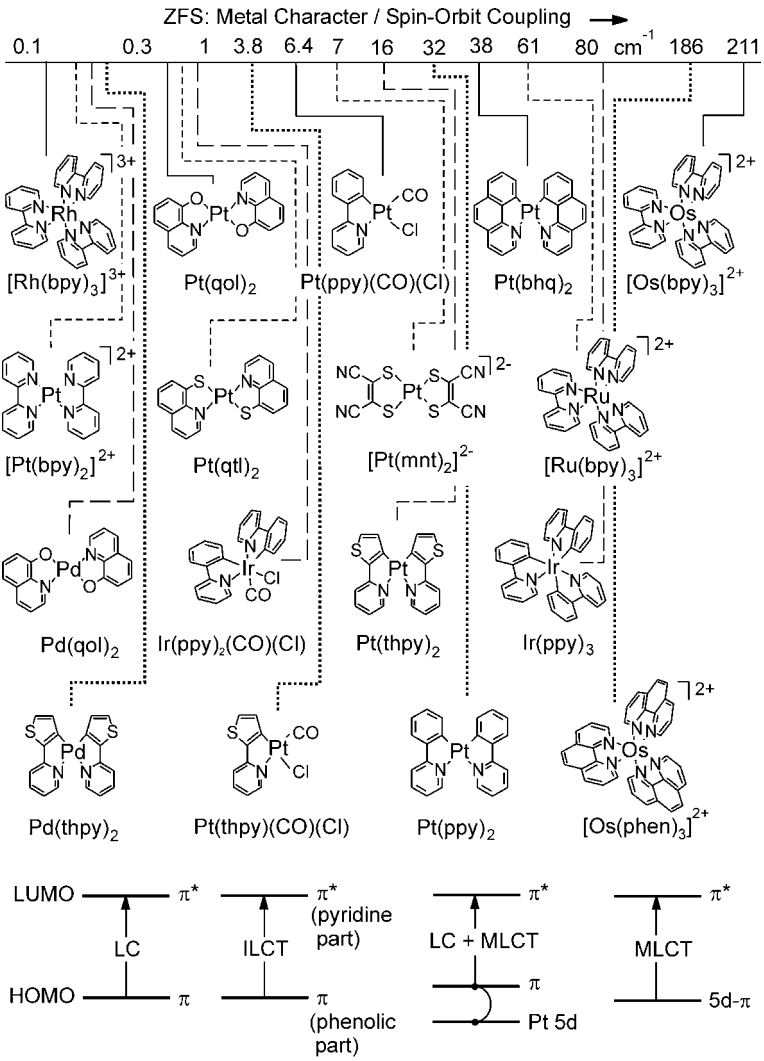

Fig. 7 Ordering scheme for organometallic triplet emitters according to the amount of zero-field splitting (ZFS) of the emissive triplet state. This splitting reflects the size of metal participation (MLCT and/or d-orbital character) and spin-orbit coupling in the corresponding wavefunctions. The diagrams *at the bottom* show energy levels of the relevant frontier molecular orbitals for the different compounds. For details see text. (Compare [79] and for the Ir(III) compounds [25, 87, 88])

Fig. 7 can in fact be employed in the sense of a controlled variation of metal participation/spin-orbit coupling. In the next section, it will be discussed how photophysical properties vary with the increase of the zero-field splitting parameter.

5
Photophysical Properties of Triplet Emitters Controlled by Metal Participation

The energy splitting (ZFS) of a triplet state into substates displays the importance of metal character and spin-orbit coupling for this state. The ZFS value varies by more than a factor of 2000 (Fig. 7). Thus, essential changes of photophysical properties are expected to occur. Several important trends will be discussed in the following subsections. This is carried out on a qualitative and introductory basis (Fig. 8). For comparison, properties of typical organic molecules ($\pi\pi^*$ emitters) are also referred to.

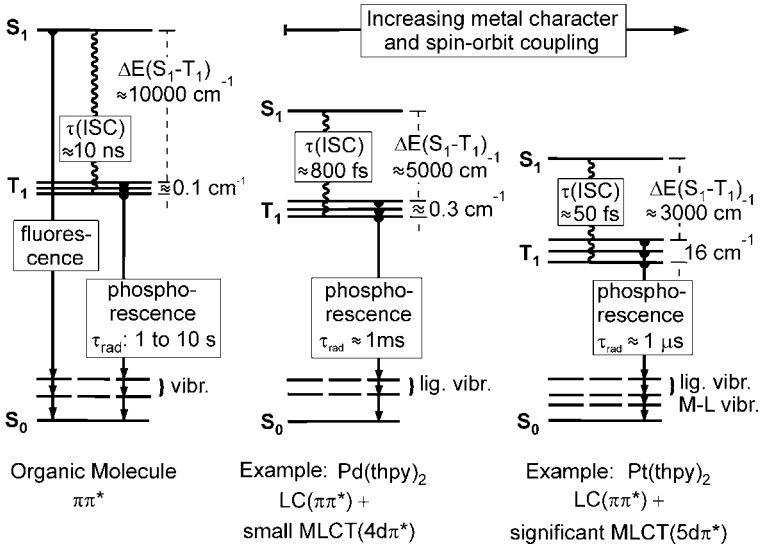

Fig. 8 Photophysical properties of a representative organic molecule compared to two organo-transition-metal emitters. The emissive triplets of $Pd(thpy)_2$ and $Pt(thpy)_2$ exhibit small and significant **MLCT** admixtures to the **LC**($\pi\pi^*$) states, respectively. The positions of the compounds in the ordering scheme and the molecular structures are found in Fig. 7. Photophysical properties of $Pd(thpy)_2$ and $Pt(thpy)_2$ are discussed in detail in [79]. lig. vibr.=ligand vibrations, M-L vibr.=metal-ligand vibration

5.1
Singlet-Triplet Splitting

Organic molecules exhibit $\mathbf{S_1}$-$\mathbf{T_1}$ splittings being typically of the order of 10^4 cm^{-1} (Fig. 8) for states which stem from a $\pi\pi^*$ configuration and for molecules of similar sizes like those shown as ligands in Fig. 7. The $\Delta E(S_1\text{-}T_1)$ splitting is essentially given by the exchange interaction and is a

consequence of electron-electron interaction. For an organo-metallic compound, such as $Pd(thpy)_2$, one finds a value of 5418 cm^{-1} [79]. The emissive triplet of this compound has been classified experimentally [79, 89–91] and later also by CASPT2 ab initio calculations [92] as being mainly of **LC**($\pi\pi^*$) character with a small **MLCT**(**4d**π^*) admixture. Therefore, the compound is found at the left hand side of the ordering scheme of Fig. 7 [79]. On the other hand, for $Pt(thpy)_2$ with a significant **MLCT**(**5d**π^*) admixture to the **LC**($\pi\pi^*$) state [34, 78, 79], the amount of $\Delta E(S_1\text{-}T_1)$ is reduced to 3278 cm^{-1} [79] (Fig. 8). Obviously, enhancing of metal character in the corresponding wavefunctions increasingly reduces the $\Delta E(S_1\text{-}T_1)$ value. Due to the higher metal character, the electronic wavefunctions extend over a larger spatial region of the complex. This is connected to an on average larger spatial separation between the interacting electrons. Thus, electron-electron interaction and also exchange interaction are reduced. This explains both the lowering of the $\mathbf{S_1}$ state and the reduction of $\Delta E(S_1\text{-}T_1)$ for compounds with higher metal character.

5.2 Inter-System Crossing

After excitation of the singlet state $\mathbf{S_1}$ either optically or by electron-hole recombination, the organic molecule can exhibit an efficient fluorescence ($\mathbf{S_1}\rightarrow\mathbf{S_0}$ emission) with a time constant of the order of 1 ns. In competition to this process, ISC can at least principally depopulate the $\mathbf{S_1}$ state. However, the time constant of τ(ISC) is often much larger (order of 10 ns) than the radiative decay constant of the $\mathbf{S_1}$ state and thus ISC does not effectively quench the fluorescence (Fig. 8). On the other hand, in transition metal complexes, the ISC time is drastically reduced due to singlet-triplet mixing induced by SOC and due to the reduction of the energy separation $\Delta E(S_1\text{-}T_1)$. Further, due to this latter effect, the number of vibrational quanta which are responsible for the deactivation is reduced and thus the ISC process becomes even more probable. For example, already for a compound, such as $Pd(thpy)_2$, with a relatively small metal participation in the wavefunction of the $\mathbf{T_1}$ state and a halved $\Delta E(S_1\text{-}T_1)$ value, ISC is by four to five orders of magnitude faster (800 ps [79]) than in usual organic compounds with $^1\pi\pi^*$ and $^3\pi\pi^*$ states. For $Pt(thpy)_2$ with a higher metal participation, the process is again much faster (τ(ISC)$\approx$50 fs [79]) (Fig. 8).

In conclusion, the process of inter-system crossing in organometallic compounds with transition metal ions is fast and efficient for all compounds shown in Fig. 7. The quantum efficiency for this process is often nearly one (e.g., see [4]). Therefore, an emission from the $\mathbf{S_1}$ state is not observable. This property is the basis of the triplet harvesting effect discussed above.

5.3 Phosphorescence Decay Time

In pure organic molecules, the $\mathbf{S_0}(\pi^2) \leftrightarrow \mathbf{T_1}(\pi\pi^*)$ transition is usually strongly forbidden. The radiative decay time can be of the order of 10 s. [38] On the other hand, non-radiative processes are mostly much faster. Thus, phosphorescence from the $\mathbf{T_1}$ state is normally totally quenched at ambient temperature. With increasing SOC, the radiative decay time of the $\mathbf{T_1} \rightarrow \mathbf{S_0}$ transition is reduced and thus the radiative path can compete with the non-radiative one. Interestingly, already a relatively small ^{3}**MLCT**/^{1}**MLCT** admixture to the $^3\mathbf{LC}(\pi\pi^*)$ state increases the $\mathbf{S_0} \leftrightarrow \mathbf{T_1}$ transition probability drastically. For example, for $Pd(thpy)_2$ the radiative decay time is reduced to be of the order of 1 ms. For $Pt(thpy)_2$ with a significant **MLCT** admixture to the lowest ^{3}**LC** state, it is even reduced by six to seven orders of magnitude as compared to the organic emitters, and one finds a radiative decay time of the order of 1 μs (Fig. 8). For completeness, it is remarked that the values given refer to an average radiative decay of the triplet, since the different triplet substates exhibit distinctly different decay properties (e.g., see the following sub-section and [79]).

In summary, for organometallic compounds the transition probability between the $\mathbf{T_1}$ and the $\mathbf{S_0}$ states can be tuned by several orders of magnitude as compared to organic emitters. This is mainly induced by an increase of spin-orbit coupling. Thus, the radiative processes can well compete with the non-radiative ones. Consequently, organo-transition-metal compounds can exhibit efficient emissions (phosphorescence) and therefore are well suited as emitter materials for OLEDs.

5.4 Zero-Field Splitting

Triplet states split generally into substates. This is also valid for purely organic molecules. However, for these one finds only small values of ZFS of the order of 0.1 cm^{-1} which result from spin-spin coupling between the electrons in the π and π^* orbitals, respectively (e.g., see [80–82]). On the other hand, in organo-transition-metal compounds SOC will modify the triplet states' properties by mixing in higher lying states of singlet and triplet character. Already small admixtures have drastic consequences. For example, one finds an increase of the ISC rate (see above) and of the phosphorescence decay rate (see previous subsection) by orders of magnitude, although the ZFS is not yet distinctly altered [79]. Well studied examples with this behavior are $[Rh(bpy)_3]^{3+}$ and $Pd(qol)_2$ (=Pdq_2) [81, 93, 94].

Higher metal participation and larger SOC lead to distinct ZFSs as has already been discussed and depicted in Fig. 7. Importantly, the individual triplet substates can have very different photophysical properties with regard to

radiative decay rates, vibronic coupling, coupling to the environment, emission quantum yields, population and relaxation dynamics due to spin-lattice relaxation, sensitivity with respect to symmetry changes, etc. [25, 34, 75–79, 81, 87, 89–91, 93–97]. At ambient temperature, the individual properties are largely smeared out and one finds mostly only an averaged behavior. Nevertheless, the individual triplet substates still determine the overall emission properties.

5.5 Emission Band Structure and Vibrational Satellites

At ambient temperature, the phosphorescence of organometallic compounds consists usually of superimposed spectra, which stem from the different triplet substates (see previous subsection, Fig. 8). An individual spectrum which results from one specific substate is composed of a transition at the electronic origin (0–0 transition), a large number of vibrational satellites, and of in part overlapping low-energy satellites which involve librations of the complex in its environment. Moreover, all of these individual transitions are smeared out by inhomogeneity effects. Thus, at ambient temperature normally only a broad-band emission results. Sometimes residual, moderately resolved structures occur, which often stem from overlapping vibrational satellites (not necessarily from progressions). Interestingly, at low temperature and under suitable conditions, these structures can be well resolved and characterized [34, 75–79, 89–91, 93–103]. From this kind of investigations it follows that the vibrational satellite structure is also influenced by metal participation in the electronic states [100]. Specifically, the spectra of compounds with electronic transitions of mainly LC($\pi\pi^*$) character (small metal participation) are largely determined by satellites corresponding to ligand vibrations (fundamentals, combinations, progressions). However, with increasing metal participation, low-energy vibrational satellites of metal-ligand character grow in additionally (up to about 600 cm^{-1} from the electronic origin) [100] (Fig. 8). Thus, the maximum of the unresolved emission spectrum shifts towards the electronic 0–0 transition.

To summarize, metal participation in the emitting state leads to a slight blue shift of the unresolved emission maximum as compared to an LC spectrum with the same 0–0 transition energy. Moreover, the occurrence of additional low-energy metal-ligand vibrational satellites causes a further smearing out of the spectrum. The slight spectral shift might be of interest for fine-tuning of the emission color.

5.6
Electronic Charge Distribution and Excited State Reorganization

The singlet-triplet transitions of compounds with small metal character, situated on the left hand side of Fig. 7, are localized to one of the ligands, even if the formal symmetry of the complex would allow a delocalization over all of the ligands. This has been proven for $[Rh(bpy)_3]^{3+}$ [93] and $[Pt(bpy)_2]^{2+}$ [101] by use of the method of deuteration labeling [76, 78]. On the other hand, for compounds with emissive ^{3}**MLCT** states such as $[Ru(bpy)_3]^{2+}$ [102] and $[Os(bpy)_3]^{2+}$ [103] it has been shown that the excited state is delocalized over the three ligands and the metal [76, 78, 102, 103]. This is even valid for $Pt(thpy)_2$, in which the triplet state is largely of LC($\pi\pi^*$) character, but for which the metal orbital admixture induces sufficient coupling between the ligands (Fig. 7, middle). Thus, one obtains a delocalization in the lowest excited state [78, 79]. It is remarked that these results were determined for compounds doped into rigid matrices.

Moreover, since the metal character or MLCT contribution in the triplet state, if sufficiently large, can induce a ligand-ligand coupling that delocalizes the excited state wavefunction, the metal contribution will also affect the geometry change that follows an excitation. For the localized situation in the compounds mentioned above, one finds a maximum Huang-Rhys parameter [79] of S=0.3, while for the compounds with delocalized triplets, this characteristic parameter is by a factor of three to four smaller [76, 79]. Geometry changes or reorganization effects which occur upon excitation of the emissive triplet states are small for nearly all of the complexes investigated (in rigid matrices). However, it can be concluded that the reorganization effects are further minimized for those organometallic compounds with high metal participation in the triplet states (complexes at the right hand side of Fig. 7). The emissive states of these compounds exhibit a weaker coupling to the environment and therefore represent good candidates for OLED emitter materials with high emission quantum yields.

6
Summary and Conclusion

Organo-transition-metal triplet emitters have a great potential to be applied in OLEDs. Thus, an understanding of the processes, which lead to electron-hole recombination (exciton formation) and to the population of the emissive triplet states is presented. In particular, it is shown that the dynamical process of exciton formation and trapping on an emitter molecule involves charge transfer states which result from excitations of the dopant to its nearest neighbor matrix environment (^{1,3}**DMCT** states). Individual singlet and triplet trapping and relaxation paths lead to the population of the lowest ex-

cited singlet and triplet states of the dopant. In typical organic molecules with weak spin-orbit coupling and highly forbidden triplet-singlet transitions, triplet state population is transferred into heat (at ambient temperature). Only the singlet can emit radiatively (fluorescence). On the other hand, in organo-transition-metal compounds, fast intersystem crossing induced by spin-orbit coupling effectively depopulates the excited singlet into the lowest triplet. Again, due to SOC, the triplet can decay radiatively as phosphorescence even with high emission quantum yield at ambient temperature. In case of validity of spin statistics only 25% of the excitons can be exploited by organic emitters, while for triplet emitters additional 75% of the excitons are harvested in the triplet states. Thus due to triplet harvesting, the efficiency of light emission in an electro-luminescent device with triplet emitters can be—in the limit of vanishing radiationless deactivation—higher by a factor of four compared with singlet emitters. Moreover, on the basis of a detailed knowledge about the photophysical properties of organo-transition-metal emitters, clear trends are elucidated for triplet emitters. This leads to the possibility to control important factors, such as metal participation and spin-orbit coupling in the triplet states, by chemical variation. Thus, the controlled development of compounds with predefined photophysical properties will be achievable. Specifically, increase of metal participation and SOC is displayed in a growing zero-field splitting of the triplet into substates. This parameter can be determined experimentally. The corresponding ZFS values of the compounds discussed in this investigation vary by more than a factor of 2000. In particular, increasing metal character lowers the energy of the excited singlet, reduces the energy separation between the excited singlet and triplet states, enhances the intersystem crossing rate from the lowest excited singlet to the lowest triplet, lowers the emission decay time by increasing the radiative rate between the triplet and the singlet ground state, changes the vibrational satellite structure and thus the spectral distribution of the emission band, decreases the excited state reorganization energy, etc. This promising new concept is not only applicable to small molecules, it can also usefully be applied if combined with other strategies, which are based, for example, on the use of functionalized ligands [104], dendrimeric shielding effects [14, 105], and attachments of organo-metallic compounds to polymers [106].

Acknowledgement Financial support of the Bundesministerium für Bildung and Forschung (BMBF) is acknowledged.

References

1. Hagfeldt A, Grätzel M (2000) Acc Chem Res 33:269
2. Kuciauskas D, Freund MS, Gray HB, Winkler JR, Lewis NS (2001) J Phys Chem B 105:392

3. Tai WP, Inoue K, Oh JH (2002) Sol Energy Mater 71:553
4. Demas JN, DeGraff BA (2001) Coord Chem Rev 211:317
5. Liebsch G, Klimant I, Frank B, Holst G, Wolfbeis OS (2000) Appl Spectrosc 54:548
6. Buss CE, Mann KR (2002) J Am Chem Soc 124:1031
7. Guo X-Q, Castellano FN, Li L, Szmacinski H, Lakowicz JR, Sipior J (1997) Anal Chem 63:337
8. Cary DR, Zaitseva NP, Gray K, O'Day KE, Darrow CB, Lane SM, Peyser TA, Satcher JH Jr, VanAntwerp WP, Nelson AJ, Reynolds JG (2002) Inorg Chem 41:1662
9. Drew SM, Janzen DE, Buss CE, MacEwan DI, Dublin KM, Mann KR (2001) J Am Chem Soc 123:8414
10. Wei L, Chan MCW, Cheung K-K, Che C-M (2001) Organometallics 20:2477
11. Lamansky S, Djurovich PI, Murphy D, Abdel-Razzaq F, Kwong R, Tsyba I, Bortz M, Mui B, Bau R, Thompson ME (2001) Inorg Chem 40:1704
12. Brooks J, Babayan Y, Lamansky S, Djurovich PI, Tsyba I, Bau R, Thompson ME (2002) Inorg Chem 41:3055
13. Grushin VV, Herron N, LeCloux DD, Marshall WJ, Petrov VA, Wang Y (2001) Chem Commun 1494
14. Lo S-C, Male NAH, Markham JPJ, Magennis SW, Burn PL, Salata OV, Samuel IDW (2002) Adv Mater 14:975
15. Tsuzuki T, Shirasawa N, Suzuki T, Tokito S (2003) Adv Mater 15:1455
16. Nazeeruddin MK, Humphry-Baker R, Berner D, Rivier S, Zuppiroli L, Graetzel M (2003) J Am Chem Soc 125:8790
17. Juris A, Balzani V, Barigelletti F, Campagna S, Belser P, von Zelewsky A (1988) Coord Chem Rev 84:85
18. Caspar JV, Meyer TJ (1983) Inorg Chem 22:2444
19. Kober EM, Marshall JL, Dressick WJ, Sullivan BP, Caspar JV, Meyer TJ (1985) Inorg Chem 24:2755
20. Kober EM, Caspar JV, Lumpkin RS, Meyer TJ (1986) J Phys Chem 90:3722
21. Kinnunen T-JJ, Haukka M, Nousiainen M, Patrikka A, Pakkanen TA (2001) J Chem Soc Dalton Trans 2649
22. Kalyanasundaram K (1992) Photochemistry of polypyridine and porphyrin complexes. Academic Press, London
23. Caspar JV, Meyer TJ (1983) J Phys Chem 87:952
24. Striplin DR, Crosby GA (1994) Chem Phys Lett 221:426
25. Finkenzeller W, Stößel P, Kulikova M, Yersin H (2004) Proc SPIE 5214:356
26. Roundhill DM (1994) Photochemistry and photophysics of metal complexes. Plenum Press, New York
27. Vogler A, Kunkely H (2001) Top Curr Chem 213:143
28. Lai S-W, Che C-M (2004) Top Curr Chem 241:37
29. Maestri M, Balzani V, Deuschel-Cornioley C, von Zelewsky A (1992) Adv Photochem 17:1
30. Caspar JV, Sullivan BP, Kober EM, Meyer TJ (1982) Chem Phys Lett 91:91
31. Timpson CJ, Bignozzi CA, Sullivan BP, Kober EM, Meyer TJ (1996) J Phys Chem 100:2915
32. Chen P, Meyer TJ (1998) Chem Rev 98:1439
33. Sullivan BP (1989) J Phys Chem 93:24
34. Wiedenhofer H, Schützenmeier S, von Zelewsky A, Yersin H (1995) J Phys Chem 99:13385
35. Auzel F (1980) In: DiBartolo B (ed) Radiationless processes. Plenum Press, New York

36. Mataga N, Kubota T (1970) Molecular interactions and electronic spectra. Marcel Dekker, New York
37. DiBartolo B (ed) (1980) Radiationless processes. Plenum Press, New York
38. Turro NJ (1978) Modern molecular photochemistry. Benjamin/Cummings Publ, Menlo Park, California, USA
39. Flint CD (ed) (1989) Vibronic processes in inorganic chemistry. Kluwer Academic Publishers, Dordrecht, Series C, Mathematical and Physical Sciences, vol 288
40. Fukase A, Dao KLT, Kido J (2002) Polym Adv Technol 13:601
41. Zhou X, Qin DS, Pfeiffer M, Blochwitz-Nimoth J, Werner A, Drechsel J, Maenning B, Leo K, Bold M, Erk P, Hartmann H (2002) Appl Phys Lett 81:4070
42. Adachi C, Baldo MA, Forrest SR, Lamansky S, Thompson ME, Kwong RC (2001) Appl Phys Lett 78:1622
43. Kawamura Y, Yanagida S, Forrest SR (2002) J Appl Phys 92:87
44. Baldo MA, Lamansky S, Burrows PE, Thompson ME, Forrest SR (1999) Appl Phys Lett 75:4
45. Fuhrmann T, Salbeck J (2002) Adv Photochem 27:83
46. Lee C-L, Lee KB, Kim J-J (2000) Appl Phys Lett 77:2280
47. Nguyen TP, LeRendu P, Dinh NN, Fourmigue M, Mézière C (2003) Synth Met 138:229
48. Wang X, Rundl P, Bale M, Mosley A (2003) Synth Met 137:1051
49. Riel H, Karg S, Beierlein T, Ruhstaller B, Rieß W (2003) Appl Phys Lett 82:466
50. Lee Y-J, Kim S-H, Huh J, Kim G-H, Lee Y-H, Cho S-H, Kim Y-C, Do YR (2003) Appl Phys Lett 82:3779
51. Pfeiffer M, Forrest SR, Leo K, Thompson ME (2002) Adv Mater 14:1633
52. Murata H, Kafafi ZH, Uchida M (2002) Appl Phys Lett 80:189
53. Liu MS, Luo J, Jen AK-Y (2003) Chem Mater 15:3496
54. Chen HY, Lam WY, Luo JD, Ho YL, Tang BZ, Zhu DB, Wong M, Kwok HS (2002) Appl Phys Lett 81:574
55. Watkins NJ, Mäkinen AJ, Gao Y, Ushida M, Kafafi ZH (2004) Proc SPIE 5214:368
56. Tung Y-J, Lu MM-H, Weaver MS, Hack M, Brown JJ (2004) Proc SPIE 5214:114
57. Chwang AB et al. (2003) Appl Phys Lett 83:413
58. Huang W, Wang X, Sheng M, Xu L, Stubhan F, Luo L, Feng T, Wang X, Zhang F, Zou S (2003) Mater Sci Eng B 98:248
59. Müller CD, Falcon A, Reckefuss N, Rojahn M, Wiederhirn V, Rudati P, Frohne H, Nuyken O, Becker H, Meerholz K (2003) Nature 421:829
60. Kim C, Forrest SR (2003) Adv Mater 15:541
61. Auch MDJ, Soo OK, Ewald G, Soo-Jin C (2002) Thin Solid Film 417:47
62. Gong X, Robinson MR, Ostrowski JC, Moses D, Bazan GC, Heeger AJ (2002) Adv Mater 14:581
63. O'Brien DF, Giebeler C, Fletcher RB, Cadby AJ, Palilis LC, Lidzey DG, Lane PA, Bradley DDC, Blau W (2001) Synth Met 116:379
64. Tutiš E, Berner D, Zuppiroli L (2003) J Appl Phys 93:4596
65. Lamansky S, Kwong RC, Nugent M, Djurovich PI, Thompson ME (2001) Org Electron 2:53
66. Hellwege K-H (1976) Einführung in die Festkörperphysik. Springer, Berlin Heidelberg New York, p 509
67. Garten F, Hilberer A, Cacially C, Esselink E, vanDam Y, Schlachtmann B, Friend RH, Klapwijk TM, Hadziianoanou (1997) Adv Mater 9:127
68. Burin AL, Ratner MA (1998) J Chem Phys 109:6092
69. Shuai Z, Beljonne D, Silbey RJ, Brédas JL (2000) Phys Rev Lett 84:131
70. Hong T-M, Meng H-F (2001) Phys Rev B 63:075206

71. Wohlgenannt M, Tandon K, Mazumdar S, Ramasesha S, Vardeny ZV (2001) Nature 409:494
72. Virgili T, Cerullo G, Lüer L, Lanzani G, Gadermaier C, Bradley DDC (2003) Phys Rev Lett 90:247402
73. Baldo MA, O'Brien DF, You Y, Shoustikov A, Silbley S, Thompson ME, Forrest SR (1998) Nature 395:151
74. Cleave V, Yahioglu G, LeBarny P, Friend RH, Tessler N (1999) Adv Mater 11:285
75. Yersin H, Humbs W, Strasser J (1997) Coord Chem Rev 159:325
76. Yersin H, Humbs W, Strasser J (1997) Top Curr Chem 191:153
77. Yersin H, Strasser J (1997) J Lumin 72/74:462
78. Yersin H, Humbs W (1999) Inorg Chem 38:5820
79. Yersin H, Donges D (2001) Top Curr Chem 214:81
80. Lumb MD (ed) (1978) Luminescence spectroscopy. Academic Press, London
81. Glasbeeek M (2001) Top Curr Chem 213:95
82. Azumi T, Miki H (1997) Top Curr Chem 191:1
83. Komada Y, Yamauchi S, Hirota N (1986) J Phys Chem 90:6425
84. Ikeda S, Yamamoto S, Nozaki K, Ikeyama T, Azumi T, Burt JA, Crosby GA (1991) J Phys Chem 95:8538
85. Colombo MG, Hauser A, Güdel HU (1994) Top Curr Chem 171:143
86. Funayama T, Kato M, Kosugi H, Yagi M, Higuchi J, Yamauchi S (2000) Bull Chem Soc Jpn 73:1541
87. Finkenzeller WJ, Yersin H (2003) Chem Phys Lett 377:299
88. Hay PJ (2002) J Phys Chem A 106:1634
89. Yersin H, Schützenmeier S, Wiedenhofer H, von Zelewsky A (1993) J Phys Chem 97:13496
90. Schmidt J, Wiedenhofer H, von Zelewsky A, Yersin H (1995) J Phys Chem 99:226
91. Glasbeek M, Sitters R, van Veldhofen E, von Zelewsky A, Humbs W, Yersin H (1998) Inorg Chem 37:5159
92. Pierloot K, Ceulemans A, Merchán M, Serrano-Andrés L (2000) J Phys Chem A 104:4374
93. Humbs W, Yersin H (1996) Inorg Chem 35:2220
94. Yersin H, Donges D, Nagle JK, Sitters R, Glasbeek M (2000) Inorg Chem 39:770
95. Yersin H, Strasser J (2000) Coord Chem Rev 208:331
96. Strasser J, Homeier HHH, Yersin H (2000) Chem Phys 255:301
97. Yersin H, Donges D, Humbs W, Strasser J, Sitters R, Glasbeek M (2002) Inorg Chem 41:4915
98. Yersin H, Kratzer C (2002) Coord Chem Rev 229:75
99. Yersin H, Kratzer C (2002) Chem Phys Lett 362:365
100. Yersin H, Huber P, Wiedenhofer H (1994) Coord Chem Rev 132:35
101. Humbs W, Yersin H (1997) Inorg Chim Acta 265:139
102. Braun D, Huber P, Wudy J, Schmidt J, Yersin H (1994) J Phys Chem 98:8044
103. Huber P, Yersin H (1993) J Phys Chem 97:12705
104. Chan WK, Ng PK, Gong X, Hou S (1999) Appl Phys Lett 75:3920
105. Furata P, Brooks J, Thompson ME, Fréchet JMJ (2003) J Am Chem Soc 125:13165
106. Chen X, Liao J-L, Liang Y, Ahmed MO, Tseng H-E, Chen S-A (2003) J Am Chem Soc 125:636

Top Curr Chem (2004) 241:27–63
DOI 10.1007/b96859

Luminescent Cyclometalated Diimine Platinum(II) Complexes: Photophysical Studies and Applications

Siu-Wai Lai · Chi-Ming Che (✉)

Department of Chemistry and HKU-CAS Joint Laboratory on New Materials, The University of Hong Kong, Pokfulam Road, Hong Kong
cmche@hku.hk

Abstract The photoluminescent properties of mono- and polynuclear cyclometalated platinum(II) complexes are discussed. Spectroscopic studies have revealed weak intra- or intermolecular metal-metal and ligand-ligand interactions that are affected by the molecular structure and microenvironment. The structure-emission relationships observed in these platinum(II) complexes are described and comparisons with palladium(II) analogues regarding the structural and photoluminescent properties are highlighted. With judicious modification of cyclometalated and/or ancillary ligands, robust platinum luminophores with tunable emission energies and lifetimes have been synthesized. These complexes can be employed as luminescent sensors and electrophosphorescent materials in organic light-emitting devices (OLED).

Keywords Cyclometalation · Luminescence · OLED · Platinum · Sensors

1 Introduction

The unusual color of square planar d^8 metal complexes in the solid state has been reported for several decades. In the early 1970s, interest in the electrical conductivity of molecular materials sparked a renewed research effort into this class of compounds [1, 2]. Many of these solids exhibit interesting electrical, magnetic and optical properties that are anisotropic in nature, and some of their structures, determined by X-ray crystallography, show stacked or slipped stacked structures in which the distance between metal ions along the chain is less than 4 Å. Their solid-state emissions were attributed to metal-metal interactions arising from stacking of the square planar units which are usually observed in the visible region for platinum(II) compounds containing π-acid ligands. Gliemann and Yersin [3] had studied the spectroscopic behavior of $M_2[Pt(CN)_4]\cdot nH_2O$ compounds which crystallize in columnar structures and the energies of the optical transitions sensitively depend on the Pt-Pt distance in the columns which can be altered under high pressure and temperature variation. Adamson and coworkers had investigated the emissions of $K_2Pt(CN)_4$ and $BaPt(CN)_4$ solids and the red shift for $[Pt(CN)_4]^{2-}$ oligomers in solution is attributed to Pt-Pt interactions [4].

The intriguing solid-state polymorphism and spectroscopic properties displayed by the Pt(II) α-diimine complexes $[Pt^{II}(\alpha\text{-diimine})X_2]$ (X=halide or cyanide) and $[Pt^{II}(\alpha\text{-diimine})_2]X_2$ have attracted considerable attention. This class of luminescent compounds revealed a remarkable variety of low-energy excited states [5], including (i) α-diimine intraligand (IL) states of monomer type (π–π^*), (ii) α-diimine intraligand (IL) states of 'excimer' type $[\sigma^*(\pi)\rightarrow\sigma(\pi^*)]$, (iii) oligomeric metal-metal-to-ligand charge transfer $[d\sigma^*(dz^2)\rightarrow\sigma(\pi^*)]$ (MMLCT), and (iv) monomer ligand-field (LF) states. Gliemann [5c, 6] reported that when two platinum(II) α-diimine units are in close proximity so as to allow metal-metal contacts, a low energy photoluminescence that is red-shifted from the ^{3}MLCT or ^{3}IL emission of mononuclear species becomes observable. In other words, such intermolecular stacking interactions can impose notable perturbation upon the emission properties [7]. The electronic excited state associated with this emission is denoted as $^3[d\sigma^*, \pi^*]$ by Miskowski [5e, 5f], although the metal–metal-to-ligand charge transfer (MMLCT) notation has also been used in the literature. Yip and Che reported the discrete binuclear $[Pt_2(trpy)_2(\mu\text{-guanidine anion})](ClO_4)_3$ (trpy=2,2′:6′,2″-terpyridine) compound [8], which was structurally and spectroscopically characterized. This complex was used to model intermolecular metal-metal and/or excimeric interactions in Pt(II) polypyridine species and to probe the spectroscopic properties of low-energy MMLCT: $[d\sigma^*(dz^2(Pt))\rightarrow\pi^*(diimine)]$ and excimeric ligand-to-ligand excited states.

The electronic excited states of many square planar d^8 complexes are known to be unstable with respect to D_{2d} distortion. Metal-centered (MC) d-d excited states in these species lie close in energy to the triplet metal-to-ligand charge transfer (^{3}MLCT) and triplet ligand-centered (^{3}LC) excited states and provide an efficient radiationless decay pathway for excited Pt(II) complexes. Variation of auxiliary ligands could induce a high-energy MC excited state, which hinders the radiationless deactivation [9], while some researchers have diverted their attention to the trpy ligand, which favors a planar geometry upon coordination and discourages D_{2d} distortion. The extended π system within trpy also increases the energy difference between the ligand field (d-d) and MLCT states [10, 11]. Several discrete binuclear d^8–d^8 complexes of the type $[Pt_2(trpy)_2(\mu\text{-}L)]^{n+}$ (L=bidentate ligand) have been synthesized to model intermolecular interactions in Pt(II) polypyridine species that lead to MMLCT and excimeric emissions [8, 12]. A schematic molecular orbital diagram illustrating d^8-d^8 and π-π interactions in binuclear platinum(II) polypyridine complexes is given in Fig. 1 [5e].

The square planar geometry of platinum(II) complexes confers photophysical and photochemical properties that are different from octahedral $[Ru^{II}(bpy)_3]^{2+}$ derivatives; for example, the former can undergo substrate-binding reactions at the metal center in both the ground and excited states. In view of the triplet ($d\sigma^*$, $p\sigma$) excited state of the binuclear derivative $[Pt_2(\mu\text{-}P_2O_5H_2)_4]^{4-}$, which originates from substantial Pt(II)-Pt(II) interaction and which can mediate intriguing photochemical reactions [13] such as carbon-hydrogen and carbon-halogen bond cleavage, the $^3[d\sigma^*, \pi^*]$ excited states (Fig. 1) of platinum(II) diimines are envisioned to have useful applications in photochemical organic transformations.

The spectroscopic properties of platinum complexes containing bidentate C-deprotonated 2-phenylpyridine or 2-(2′-thienyl)pyridine ligands was previously studied by von Zelewsky [14] and others [15]. These complexes typical-

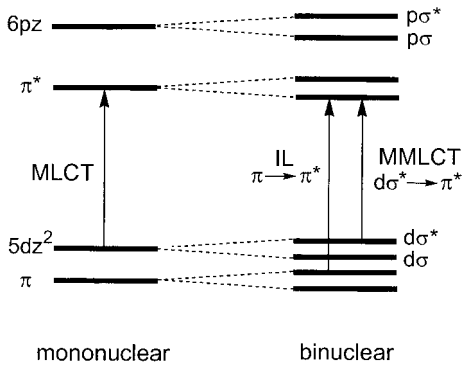

Fig. 1 Schematic molecular orbital diagram illustrating d^8-d^8 and π-π interactions in binuclear platinum(II) polypyridine complexes [5e]

ly exhibit strong luminescence with emission quantum yields in the order of 10^{-1} from low-lying MLCT excited states in the 500–600 nm range. A tridentate cyclometalated diimine ligands, which favor planar geometry upon coordination, would discourage D_{2d} distortion, while the extended π ligand system and the strongly σ-donating carbanionic moiety would increase the energy difference between the ligand field (d-d) and MLCT states. Che and coworkers have investigated the photoluminescent properties of Pt(II) complexes bearing tridentate C-deprotonated 6-phenyl-2,2′-bipyridine $[C^1\text{^}N\text{^}N]^-$ and related ligands [16, 17]. Significantly, these luminophores display low-lying MLCT excited states, which are emissive in solution at room temperature with improved photophysical parameters compared to trpy [8, 12] and $[C\text{^}N\text{^}C]^{2-}$ (HC^N^CH=2,6-diphenylpyridine) [18] analogues.

To examine the relationship between the low-energy luminescence and intramolecular metal-metal distances, a series of $[Pt_2(C\text{^}N\text{^}N)_2(\mu\text{-}L)]^{n+}$ (HC^N^N=4-(aryl)-6-phenyl-2,2′-bipyridine) derivatives supported by different bridging ligands (L) have been prepared by Che and coworkers [17]. Subsequent spectroscopic assignments of cyclometalated platinum(II) or palladium(II) derivatives were made by comparing their emission energies with those of the $[Pt_2(C\text{^}N\text{^}N)_2(\mu\text{-}L)]^{n+}$ complexes.

2 Syntheses and Characterization

Constable [19] first reported complexation of 6-phenyl-2,2′-bipyridine ($HC^1\text{^}N\text{^}N$) with Pt(II) and Pd(II) to form the cyclometalated $[M(C^1\text{^}N\text{^}N)Cl]$ (M=Pt, Pd) complexes, in which the $C^1\text{^}N\text{^}N$ ligand behaves as an anionic analogue of the 2,2′:6′,2″-terpyridine (trpy) ligand. Solvolysis of $[M(C^1\text{^}N\text{^}N)Cl]$ in acetonitrile gave $[M(C^1\text{^}N\text{^}N)(MeCN)]^+$, which is a useful precursor for reactions with a variety of substrates including I^-, PPh_3, CO, and 3,5-dimethylpyridine, and allows versatile functionalization of this class of cyclometalated complexes.

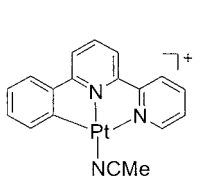

1

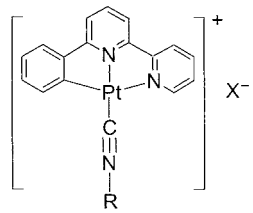

R = ^{t}Bu **2** ; $X^- = ClO_4^-$
= Ar (2,6-$Me_2C_6H_3$, **3**); $X^- = PF_6^-$

2.1 Crystal Structures

In the molecular structure of $[Pt(C^1\text{^}N\text{^}N)(MeCN)]^+$ **1**, the geometry of the $C^1\text{^}N\text{^}N$ ligand is similar to that of 2,2′:6′,2″-terpyridine in $[Pt(trpy)L]^{n+}$ (L=neutral, n=2; L=anionic, n=1). The cations of **1** form discrete dimeric units linked through short Pt-Pt contacts of 3.28(1) Å, and the intermolecular Pt-Pt contacts between the dimeric units are notably longer (shortest=4.59(1) Å). The observation of a zig-zag chain of alternating long/short metal-metal contacts is common in these cyclometalated platinum(II) complexes. In addition, the crystal packing shows π-stacking interactions between aromatic rings.

The crystal lattices of $[Pt(C^1\text{^}N\text{^}N)(C{\equiv}N\textit{t}\text{-Bu})](ClO_4)$ **2** and $[Pt(C^1\text{^}N\text{^}N)(C{\equiv}NAr)](PF_6)$ (Ar=2,6-$Me_2C_6H_3$) **3** show interplanar separations of ca. 3.4–3.6 Å between $C^1\text{^}N\text{^}N$ ligands [20], which are sufficiently close for π-π interactions [21]. The extent of stacking interactions between complex cations is affected by the substituent on the isocyanide ligand. In the crystal packing diagram of **2**, the cations are orientated in a head-to-tail fashion and form a continuous stack with no metal-metal interaction (mean Pt-Pt distance=4.74 Å). However, the cations of **3** are arranged in pairs in a head-

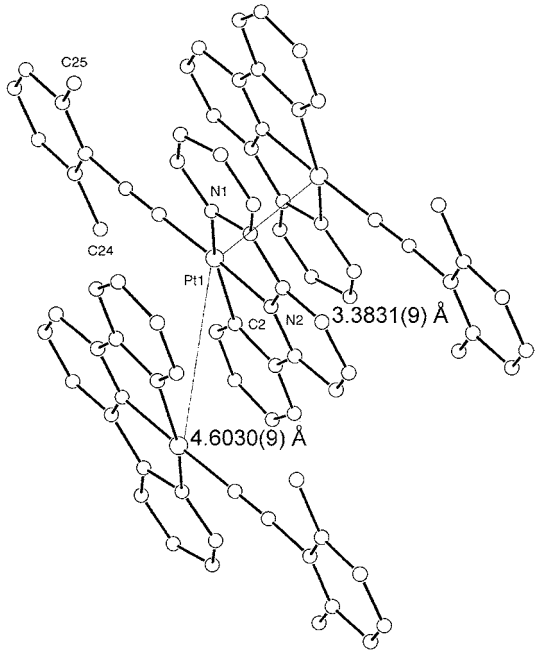

Fig. 2 Crystal packing in the crystal lattice of **3**, showing metal-metal and π-π interactions

to-tail fashion with alternating short/long Pt-Pt distances (3.3831(9) and 4.6030(9) Å respectively, Fig. 2). The former distance is comparable to that in $[Pt_2(trpy)_2(\mu\text{-pyrazolyl})](ClO_4)_3$ (3.432(3) Å) [22] and the intermolecular Pt-Pt contacts of 3.48 Å in *cis*-$[PtCl_2(CNPh)_2]$ [23]. These types of contacts are responsible for notable perturbation effects in the emission properties (see later sections).

Rourke [24, 25] reported the synthesis of the di-metalated platinum carbonyl complexes [Pt(C^N^C)(CO)] (HC^N^CH=2,6-bis(4′-hexyloxyphenyl)pyridine **4**, 4-(4′-octyloxyphenyl)-2,6-diphenylpyridine **5**, and 2,6-diphenylpyridine **6**) through double cycloplatination of the HC^N^CH ligands. In the crystal structures of **4** and **6**, there are no significant intermolecular interactions arising from stacking arrangements. In contrast, the solid-state structure of **5** reveals [Pt(C^N^C)(CO)] dimers held together by a weak platinum-platinum contact (3.243(1) Å), which is similar to that of 3.345(2) Å in [Pt(C^1^N^N)Cl] [16e]. The platinum atoms of adjacent dimers are separated by 6.17 Å, and this vector of the long Pt-Pt contact occurs at an angle of 53.5 ° to that of the short Pt-Pt contact, giving rise to a zigzag extended platinum chain. However, Yersin and coworkers [26] have observed strong intermolecular interactions from stacking of **6**.

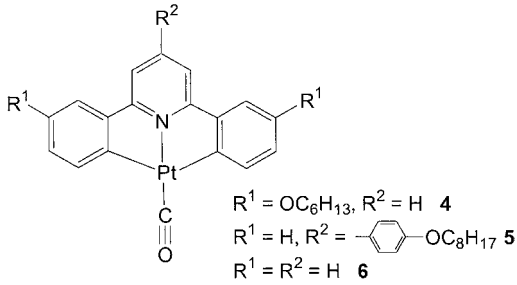

A series of binuclear cyclometalated platinum(II) complexes, namely $[Pt_2(C^N^N)_2(\mu\text{-dppm})]^{2+}$ (**7b–12b**, dppm=bis(diphenylphosphino)methane), $[Pt_2(C^1^N^N)_2(\mu\text{-pz})]^{+}$ (**13**, Hpz=pyrazole), and $[Pt_2(C^1^N^N)_2(\mu\text{-dppC}_n)]^{2+}$ (bis(diphenylphosphino)propane (**14**, *n*=3) and -pentane (**15**, *n*=5)), were synthesized to examine the oligomeric d^8-d^8 and ligand-ligand interactions [17]. In the crystal structures of **7b**, **9b**, and **10b**, the two $[Pt(C^N^N)]^{+}$ units are linked in a parallel fashion by a dppm bridge with intramolecular Pt-Pt contacts of 3.270(1), 3.150(1), and 3.245(2) Å respectively. The structure of **13** reveals the platinum atoms in a distorted square planar geometry, and the $[Pt(C^1^N^N)]^{+}$ moieties are not parallel due to the rigid coordination mode of the pyrazolate linker. The Pt-Pt distance of 3.612(2) Å in **13** is significantly longer than those in **7b**, **9b**, and **10b** (Fig. 3), suggesting negligible metal-metal communication, although weak π-π interaction is possible. Although the crystal structures of **14** and **15** have not been

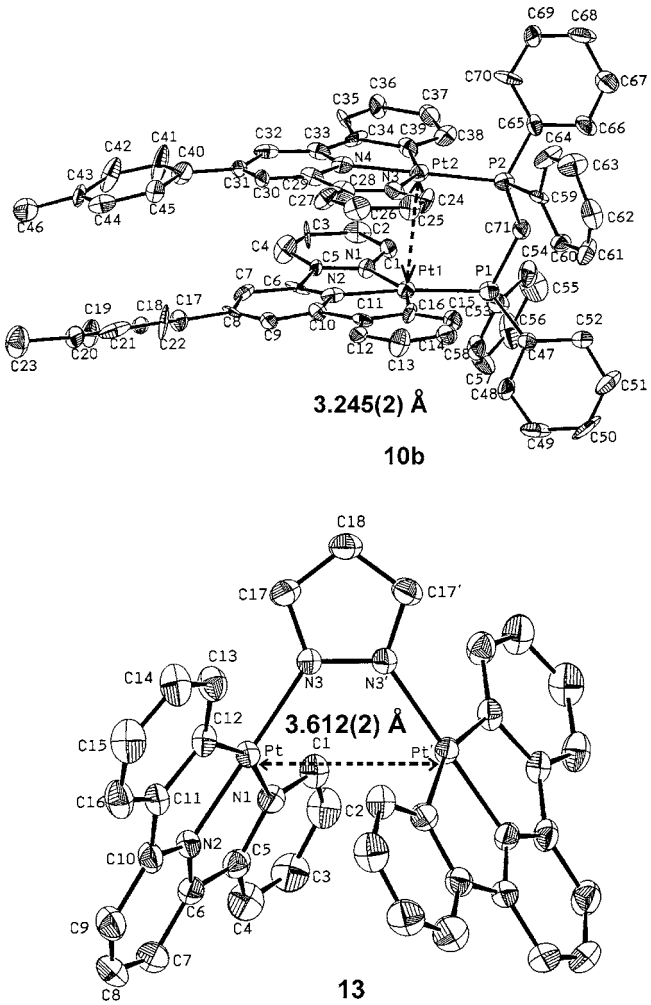

Fig. 3 Perspective views of **10b** and **13**

obtained, their photoluminescent properties (in later sections) suggest that the two separate $[Pt(C^1\text{^}N\text{^}N)]^+$ units are linked by the longer $dppC_3$ and $dppC_5$ bridging ligands without the presence of metal-metal or ligand-ligand (π-π) interactions.

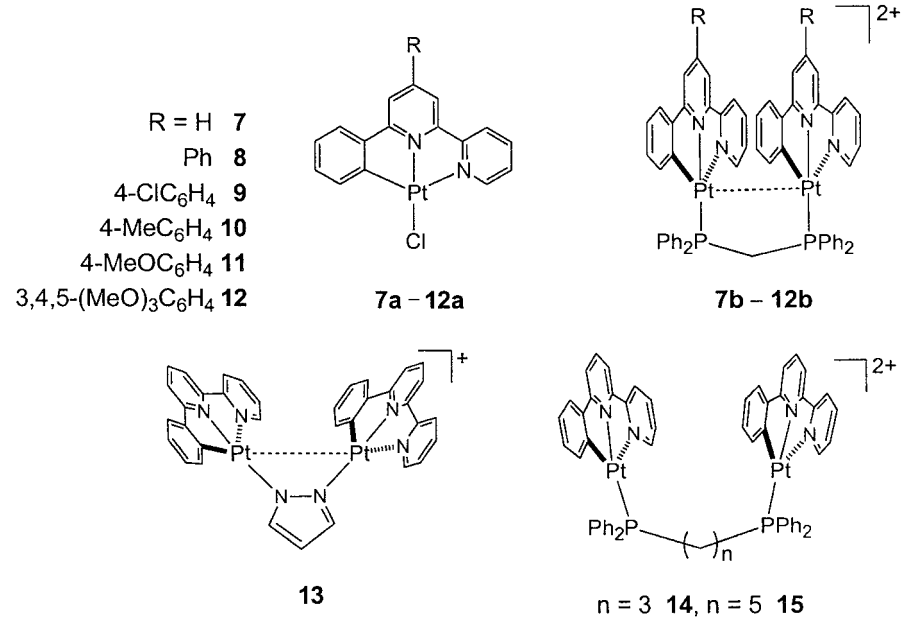

The crystallization conditions and media and the employment of different anions afforded crystals of Pt(II) luminophores in various colors and with different crystal packing lattices. We reported the synthesis of trinuclear cyclometalated platinum(II) complexes, $[Pt_3(C^n\text{^}N\text{^}N)_3(\mu_3\text{-dpmp})](ClO_4)_3$ (dpmp=bis(diphenylphosphinomethyl)phenylphosphine, $HC^1\text{^}N\text{^}N$=6-phenyl-2,2′-bipyridine) **16**$(ClO_4)_3$, ($HC^2\text{^}N\text{^}N$=4-methoxyphenyl-6-phenyl- 2,2′-bipyridine) **17**$(ClO_4)_3$, and ($HC^3\text{^}N\text{^}N$=6-(2′-thienyl)-2,2′-bipyridine)**18**$(ClO_4)_3$ [27]. The *red* form of **16**$(ClO_4)_3$ was obtained from slow diffusion of benzene into acetonitrile solution and the crystal structure revealed three $[Pt(C^1\text{^}N\text{^}N)]^+$ units that are tethered in parallel with Pt-Pt distances of 3.19 and 3.40 Å. Weak metal-metal interactions are evident among the three Pt cores. After standing in air, the *red* form slowly turned *brown-red* presumably as a result of lattice contraction induced by loss of solvated molecules. However, recrystallization of **16**$(ClO_4)_3$ by diffusion of diethyl ether into acetonitrile afforded *yellow* and *orange* crystals. The crystal structure of the *orange* form shows intramolecular metal-metal separations of 3.36 and 3.62 Å. The former Pt-Pt distance indicates weak metal-metal interaction, whereas the later separation of 3.62 Å is beyond the expected range of intermetal bonding. The complex cations of **16**$(ClO_4)_3$ in both the *red* and *orange* forms are packed into slightly off-center head-to-tail pairs by π-π stacking interactions, with separation of ~3.5 Å. Changing the counter anion to BF_4^- gave the *orange* form, whereas only the *red* form was obtained for the PF_6^- salt. No polymorphism was observed for **17**$(ClO_4)_3$ and **18**$(ClO_4)_3$ crystals which are *brown-red* in color. The crystal structure of

18$(ClO_4)_3$ reveals weak intramolecular metal-metal contacts of 3.25 and 3.39 Å.

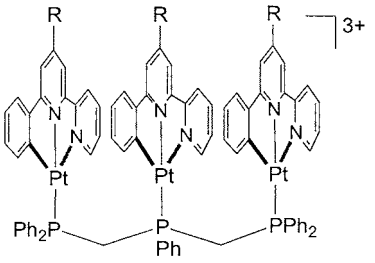

R = H **16**
4-MeOC_6H_4 **17**

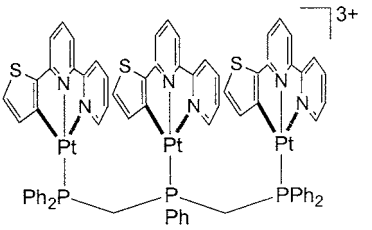

18

2.2
Structural Comparison with Pd(II) Analogues

A number of palladium(II) complexes have been crystallographically characterized [28] and comparisons between their structures with that of the platinum(II) congeners provides useful information for probing the metal-metal and ligand-ligand interactions in these systems. In the crystal lattice of $[Pd(C^1\text{^}N\text{^}N)PPh_3]^+$ **19**, no distinct π-π stacking interactions are apparent. This is in contrast to the structure of $[Pt(C^1\text{^}N\text{^}N)PPh_3]ClO_4$ [16e], which displays head-to-tail π-stacking interactions with intermolecular planar separations of 3.35 Å. In addition, Jeffery, Ward and coworkers [29] reported the crystal structure of the Pd(II) complex [Pd(L′)Cl] (HL′=6-(2-hydroxyphenyl)-2,2′-bipyridine), which reveals an average stacking distance of 3.44 Å between the L′ planes.

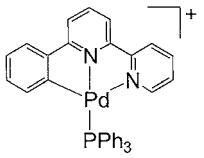

19

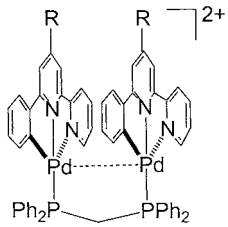

R = H **20**
Ph **21**

The molecular structures of the $[Pd_2(C^1\text{^}N\text{^}N)_2(\mu\text{-dppm})]^{2+}$ **20** and $[Pd_2(C^4\text{^}N\text{^}N)_2(\mu\text{-dppm})]^{2+}$ ($HC^4\text{^}N\text{^}N$=4,6-diphenyl-2,2′-bipyridine) **21** cations depict two $[Pd(C^n\text{^}N\text{^}N)]^+$ moieties tethered by a dppm linker. The intramolecular Pd-Pd separations of 3.230(1) Å in **20** and 3.320(2) Å in **21** are significantly greater than that expected for Pd-Pd bonding interaction

(typically 2.6–2.8 Å) [30]. The intermolecular Pd-Pd contact of 3.354(4) Å in $[Pd(bpy)(CN)_2]$ [31] and the Pt-Pt distance of 3.270(1) Å in $[Pt_2(C^1\text{^}N\text{^}N)_2(\mu\text{-dppm})](ClO_4)_2$ **7b** [17] should also be noted. Since the latter is indicative of weak intermetal communication, and the ionic radius of Pt(II) is larger than for Pd(II), the comparable intramolecular metal-metal separations observed for **20**, **21**, and **7b** imply that the degree of ground-state metal-metal interaction is even smaller in the Pd_2 system. The small dihedral angles between the two $[Pd(C^n\text{^}N\text{^}N)]^+$ mean planes (5.7° in **20** and 4.8° in **21**) and the close interplanar separations between the $C^n\text{^}N\text{^}N$ ligands (3.34 Å in **20** and 3.35 Å in **21**) signify π-stacking interactions within the binuclear complexes (even though there is minimal Pd-Pd communication in the ground state). The torsion angles of 25.8° and 5.4° between the two $[Pd(C^n\text{^}N\text{^}N)]^+$ moieties in **20** and **21** respectively are smaller than the corresponding angle of 44.6° in $[Pt_2(C^1\text{^}N\text{^}N)_2(\mu\text{-dppm})](ClO_4)_2$ **7b** [16e]. The magnitude of this torsion angle for the Pt(II) congener was attributed to optimized π-π interactions between the aromatic $C^1\text{^}N\text{^}N$ ligands, in order to avoid repulsive forces arising from eclipsed overlapping of π orbitals (i.e., torsion angle ca. 0°) [21]. Hence like the metal-metal interaction, the π-π orbital overlap in **20** is presumably inferior compared to the platinum analogue. There are no close intermolecular contacts between the aromatic ligands in the crystal lattices of **20** and **21** (distance>4 Å).

3
Photophysical Properties

The photoluminescent properties of cyclometalated platinum(II) complexes can be systematically tuned by modification of the cyclometalated ligand [32] with respect to its symmetry, degree of aromaticity and nature of substituents. For oligomeric cyclometalated complexes, their absorption and emission energies can be concomitantly varied to a large extent by altering the intramolecular metal-metal and/or ligand-ligand distances with different bridging ligands [17, 27].

3.1
UV-Vis Absorption Spectroscopy

In the absorption spectra of the monomeric platinum(II) complexes [Pt(C^N^N)Cl] **7a–12a** [17], the high-energy absorption bands at λ<370 nm are dominated by intraligand: ^{1}IL ($\pi\rightarrow\pi^*$) transitions, while the moderately intense low-energy bands with λ_{max} in the range 430–438 nm ($\epsilon\approx$1.6–5.2×10^3 dm^3 mol^{-1} cm^{-1}) are assigned to singlet metal-to-ligand charge transfer: ^{1}MLCT (5d)Pt$\rightarrow\pi^*$ (C^N^N) transitions. The weak absorption at 510–525 nm (ϵ<600 dm^3 mol^{-1} cm^{-1}) are attributed to ^{3}MLCT transitions.

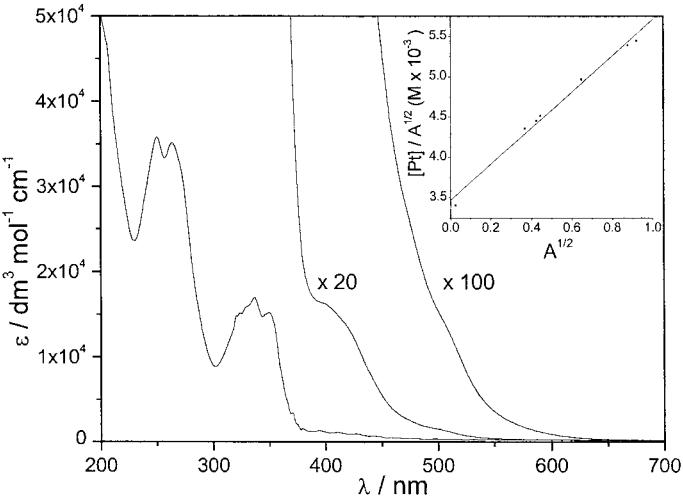

Fig. 4 UV-vis absorption spectrum of **22** in acetonitrile at 298 K (*inset*: dimerization plot of $[Pt]/A^{1/2}$ vs $A^{1/2}$ for **22** at 511 nm in acetonitrile) (Reproduced with permission from [20]. Copyright 2002 American Chemical Society)

The binuclear complexes **7b–12b** exhibit an intense absorption band at 420–485 nm ($\epsilon \approx 2.6\text{–}4.5\times10^3$ dm^3 mol^{-1} cm^{-1}) in acetonitrile which is ascribed to singlet [d$\sigma^* \rightarrow \pi^*$] transitions [17] (see Fig. 1).

In the series of mononuclear isocyanide complexes $[Pt(C^1\text{^}N\text{^}N)(C{\equiv}NR)]^+$ (R=*t*-Bu **2**, Ar **3**, *n*-Bu **22**, *i*-Pr **23**, Cy **24**) [20], the vibronically structured absorption at λ_{max} 340 nm ($\epsilon \approx 10^4$ dm^3 mol^{-1} cm^{-1}) is similarly assigned to the ^{1}IL ($\pi \rightarrow \pi^*$) transition of the $C^1\text{^}N\text{^}N$ group whereas the moderately intense low-energy bands at λ_{max} 390–430 nm are assigned to ^{1}MLCT (5d)Pt$\rightarrow\pi^*$ ($C^1\text{^}N\text{^}N$) transitions. At concentrations higher than 10^{-3} mol dm^{-3}, a shoulder at λ_{max} 511 nm ($\epsilon \sim 120$ dm^3 mol^{-1} cm^{-1}) for **22** is observed at room temperature (Fig. 4). A nonlinear plot of absorbance at 511 nm against the concentration of **22**(ClO_4) in acetonitrile demonstrates that this absorption band does not obey the Beer-Lambert Law. From studies of the concentration dependence upon the UV absorbance, an equation of $[Pt]/A^{1/2} = 1/(\epsilon K)^{1/2} + (2/\epsilon)(A^{1/2})$ where [Pt] is the total Pt concentration, A is the absorbance, ϵ is the extinction coefficient, and K is the dimerization constant, is derived. A straight line was obtained in the dimerization plot of $[Pt]/A^{1/2}$ vs $A^{1/2}$ for **22**(ClO_4) (inset of Fig. 4) in the 8.4×10^{-5} to 5.0×10^{-3} mol dm^{-3} concentration range at λ_{max} 511 nm in acetonitrile, thus confirming $[Pt(C^1\text{^}N\text{^}N)(C{\equiv}N$*n*-Bu$)]_2^{2+}$ species to be responsible for the low-energy ^{1}(d$\sigma^* \rightarrow \pi^*$) absorption at 511 nm.

To correlate the intermetallic/interplanar interaction between $[Pt(C^1\text{^}N\text{^}N)]^+$ moieties with the excited state properties, comparisons between the absorption spectra of **7b** and **13–15** were made. Because of longer carbon

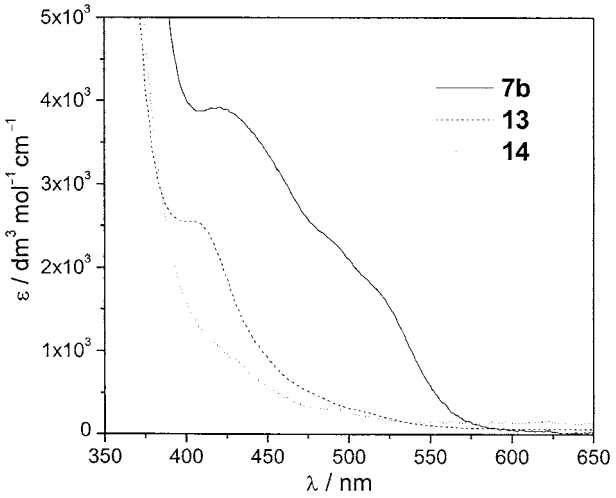

Fig. 5 Lowest energy UV-vis absorption bands of **7b**, **13**, and **14** in acetonitrile at 298 K (Reproduced with permission from [17]. Copyright 1999 American Chemical Society)

chains between the phosphorus atoms, the intramolecular separations between the two $[Pt(C^1\text{^}N\text{^}N)]^+$ units in **14** and **15** are expected to be greater than that in **7b**. This is reflected in the absorption spectra of **14** and **15**, which closely resemble that of the mononuclear phosphine congener $[Pt(C^1\text{^}N\text{^}N)PPh_3]^+$. No moderately intense absorption for **14** and **15** is evident at λ above 400 nm reminiscent of the $^1(d\sigma^*\rightarrow\pi^*)$ absorption band in **7b**, hence the $[Pt(C^1\text{^}N\text{^}N)]^+$ fragments in **14** and **15** behave as discrete non-interacting moieties from a spectroscopic viewpoint (see emission spectra below). In contrast, the absorption spectrum of **13** in acetonitrile at room temperature displays a moderately intense band at 409 nm (ϵ=2500 dm^3 mol^{-1} cm^{-1}), which is absent in **14** and the mononuclear pyridine derivative $[Pt(C^1\text{^}N\text{^}N)py]^+$. Nevertheless, the absorption band of **13** at λ>400 nm is with noticeably smaller intensity than that of **7b** in the same spectral region (Fig. 5). For assignment purposes, this absorption band for **13** exhibits intermediate characteristics between ^{1}MLCT and $^1(d\sigma^*\rightarrow\pi^*)$ transitions (Fig. 1). This is in accordance with the relatively long Pt-Pt distance in **13** (3.612(2) Å) compared to that in **7b** (3.270(1) Å), which implies **13** has virtually no metal-metal interaction, although the presence of intramolecular π-π contacts is feasible.

The UV-visible absorption spectra of the trinuclear complexes, $[Pt_3(C^n\text{^}N\text{^}N)_3(\mu_3\text{-dpmp})](ClO_4)_3$ **16**$(ClO_4)_3$–**18**$(ClO_4)_3$ feature intense low energy broad absorptions at λ~400–600 nm ($\epsilon\approx$4.0–8.5×10^3 dm^3 mol^{-1} cm^{-1}). The allowed transitions at 517 and 522 nm for **16**$(ClO_4)_3$ and **17**$(ClO_4)_3$ respectively are assigned as ^{1}MMLCT in nature (Fig. 6).

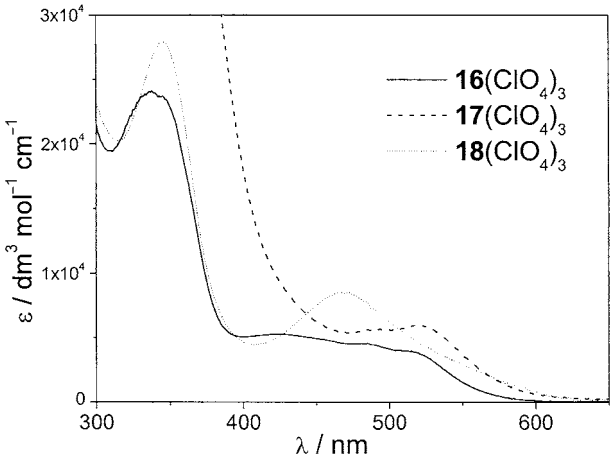

Fig. 6 UV-vis absorption spectra of **16**$(ClO_4)_3$, **17**$(ClO_4)_3$, and **18**$(ClO_4)_3$ in acetonitrile at 298 K

3.2 Emission Spectroscopy

3.2.1 Solid-State Emission Spectroscopy

For mononuclear cyclometalated Pt(II) complexes, less bulky π-acceptor ligands such as isocyanide and CO were found to favor intermolecular stacking interactions that result in the observation of low-energy ^{1}MMLCT transitions (Fig. 1). We recorded the solid-state emissions of the intensely *red*-colored [Pt(C^1^N^N)(C≡NR)](ClO_4) (R=Ar **3**, *n*-Bu **22**, *i*-Pr **23**) and [Pt(C^1^N^N)(CO)](CF_3SO_3) **25**(CF_3SO_3) complexes [20]; their emissions are in the range λ_{max} 701–748 nm at room temperature which red-shift to 775–813 nm upon cooling to 77 K and ^{3}MMLCT excited states are assigned (Fig. 7 for **22**). The *orange* solid **24** (R=Cy) exhibits an emission at λ_{max} 625 nm at room temperature, but red-shifts to 640 nm with reduced bandwidth at 77 K. This is reminiscent of an excimeric ^{3}IL transition at λ_{max} 600 nm resulting from π-stacking of C^1^N^N ligands in the [Pt(C^1^N^N)PPh_3]ClO_4 solid [16e].

At room temperature, solid [Pt(bph)$(CO)_2$] **26** (H_2bph=biphenyl) displays an intense and broad emission at 726 nm [33]. As described in earlier report [34], [Pt(bph)$(CO)_2$] packs in a columnar structure with Pt-Pt distances of 3.24 Å. Such close interatomic contacts in the chain packing of square planar platinum(II) complexes always impart red-shifts in their emission spectra. The emission maximum is red-shifted to 791 nm upon decreasing the temperature from 296 to 77 K, which is consistent with a decrease in the Pt-Pt separation observed by Connick [35] and Yersin [3a].

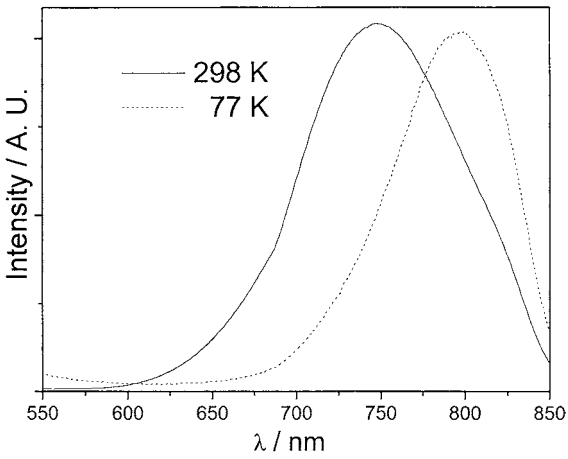

Fig. 7 Solid-state emission spectra of **22**(ClO_4) at 298 and 77 K (λ_{ex} 350 nm, normalized intensities) (Reproduced with permission from [20]. Copyright 2002 American Chemical Society)

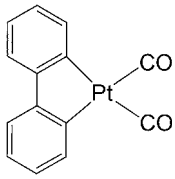

26

The binuclear Pt(II) terpyridine complexes $[Pt_2(trpy)_2(\mu\text{-L})]^{n+}$ show emissions ranging from 650 to 750 nm [12a] which are distinctly red-shifted from the ^{3}MLCT states of monomeric congeners. For oligomeric cyclometalated Pt(II) complexes, the absorption and emission energies are affected by the magnitude of the metal-metal and/or ligand-ligand contacts and by electronic modification of the cyclometalating ligands. The 298 K solid-state emission maxima for the binuclear $[Pt_2(C^1\text{^}N\text{^}N)_2(\mu\text{-dppm})](ClO_4)_2$ (**7b**$(ClO_4)_2$, Pt-Pt=3.270(1) Å) and $[Pt_2(C^1\text{^}N\text{^}N)_2(\mu\text{-pz})]ClO_4$ (**13**(ClO_4), Pt-Pt=3.612(2) Å) complexes appear at 630 and 596 nm respectively. As the intermetal separation increases by lengthening bridging ligand in **13**, the origin of the excited state changes from $^3[d\sigma^*, \pi^*]$ to ^{3}MLCT (Fig. 1) and the solid-state emission is displayed at higher energies (<600 nm). The 298 K solid-state emission of $[Pt_2(C^1\text{^}N\text{^}N)_2(\mu\text{-dppC}_3)](ClO_4)_2$ **14**$(ClO_4)_2$ and $[Pt_2(C^1\text{^}N\text{^}N)_2(\mu\text{-dppC}_5)](ClO_4)_2$ **15**$(ClO_4)_2$ at λ_{max} 577 and 579 nm respectively show significant blue-shifts from those observed for **7b–12b**$(ClO_4)_2$ and **13**(ClO_4), suggesting that the two $[Pt(C^1\text{^}N\text{^}N)]^+$ units are non-interacting.

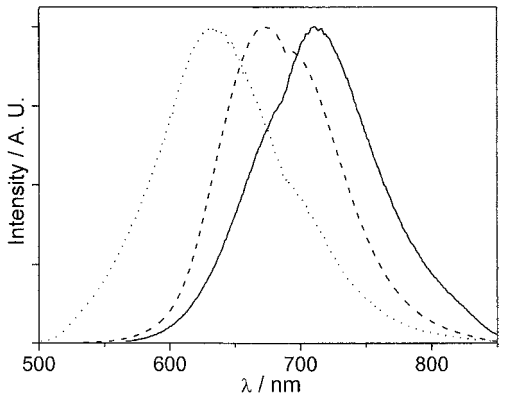

Fig. 8 Normalized solid-state emission spectra of (*dotted line*) orange **16**$(BF_4)_3$, (*dashed line*) red, and (*continuous line*) brown-red forms of **16**$(ClO_4)_3$ at 298 K

For the trinuclear complex $[Pt_3(C^1\text{^}N\text{^}N)_3(\mu_3\text{-dpmp})]^{3+}$ **16** [27], the *orange* **16**$(BF_4)_3$ exhibits solid-state emission at λ_{max} 630 nm which is reminiscent of $^3(\pi\pi^*)$ excimeric emission. The luminescence of the *red* and *brown-red* forms of **16**$(ClO_4)_3$ appear at λ_{max} 674 and 709 nm respectively, suggesting an increase in ^{3}MMLCT character (Fig. 8).

3.2.2 Solution Luminescence Spectroscopy

The monomeric cyclometalated platinum(II) complexes [Pt(C^N^N)Cl] **7a–12a** display structureless emission in CH_2Cl_2 at room temperature at λ_{max}~565 nm which are assigned as ^{3}MLCT in nature [17]. For $[Pt(C^2\text{^}N\text{^}N)py]^+$ (HC^2^N^N=4′-methoxyphenyl-6-phenyl-2,2′-bipyridine) **27**, the emission maximum blue-shifts to 541 nm, which is consistent with the cationic charge on the platinum(II) complex leading to an increase in the ^{3}MLCT energy (Fig. 9). The binuclear complexes **7b–12b** exhibit structureless emissions with λ_{max} at 652–662 nm in acetonitrile at room temperature (Fig. 9 for **11b**), while at 77 K, these emissions are blue-shifted to λ_{max} 633–644 nm and are ascribed to $^3[d\sigma^*, \pi^*]$ excited states [17].

For complexes with longer bridging ligands (**13–15**), the emission spectra in acetonitrile at room temperature show a structureless band centered at ca. 545 nm which are assigned as ^{3}MLCT in nature. A comparison of the 77 K frozen acetonitrile emissions of **7b**, **13**, and **14** reveals the effect of intramolecular metal-metal and/or ligand-ligand interactions on emission energies (Fig. 10). The lowering in emission energies from 530 (**14**) to 555 (**13**), and 638 (**7b**) nm indicated that the degree of $^3[d\sigma^*, \pi^*]$ (^{3}MMLCT) character in these excited states is increasing [17]. Similar discussion has been made from their absorption spectra above.

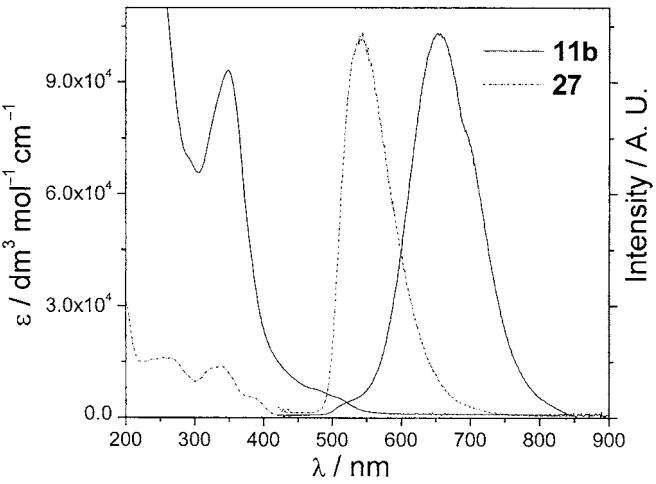

Fig. 9 Absorption and normalized emission spectra of mononuclear $[Pt(C^2\text{^}N\text{^}N)py]^+$ **27** and binuclear **11b** in acetonitrile at 298 K

The emission spectrum of $[Pt(C^1\text{^}N\text{^}N)(C{\equiv}NCy)](ClO_4)$ **24**(ClO_4) at concentrations $\geq 7\times10^{-3}$ mol dm^{-3} in acetonitrile (λ_{ex} 500 nm) displays a broad band at 710 nm (dotted line in Fig. 11) [20]. When monitoring the emission wavelength at 710 nm, the excitation spectrum exhibits a well-resolved band at 500 nm (solid line in Fig. 11) that is absent from the absorption spectra of 'conventional' monomeric derivatives. This 500-nm excitation band is comparable in energy to the singlet MMLCT ($d\sigma^*\rightarrow\pi^*$) absorption band discussed above. Therefore, the 710-nm emission band presumably originates

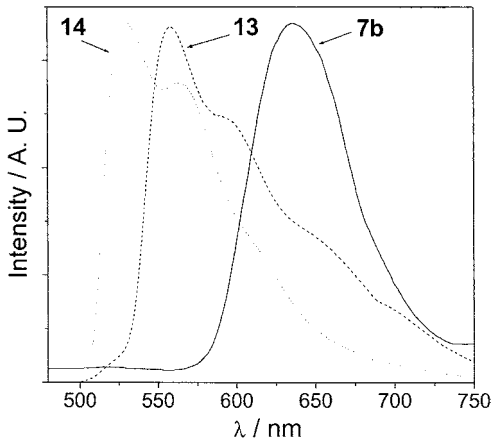

Fig. 10 Normalized emission spectra of **7b**, **13** and **14** in acetonitrile at 77 K (λ_{ex} 350 nm) (Reproduced with permission from [17]. Copyright 1999 American Chemical Society)

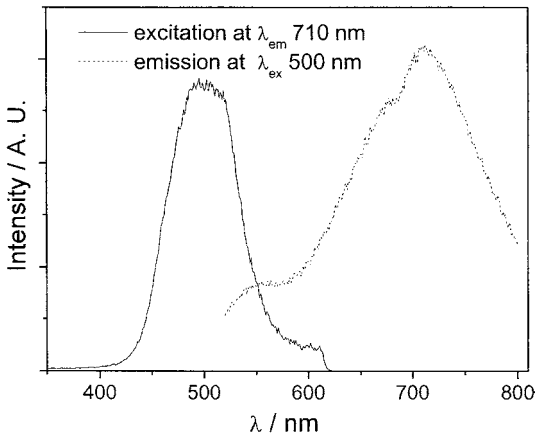

Fig. 11 Normalized excitation and emission spectra (λ_{em} 710 nm and λ_{ex} 500 nm, respectively) of **24** in acetonitrile at 298 K (concentration $\geq 7\times10^{-3}$ mol dm^{-3}) (Reproduced with permission from [20]. Copyright 2002 American Chemical Society)

from the metal-metal interaction of dimeric $[Pt(C^1\text{^}N\text{^}N)(C{\equiv}NCy)]_2^{2+}$ species and is tentatively assigned to triplet MMLCT: ($\pi^*\rightarrow d\sigma^*$) emission. At a concentration of 4×10^{-3} mol dm^{-3}, in addition to the 710-nm band, an emission at λ_{max} 550 nm that is similar in energy to the ^{3}MLCT emission of monomeric $[Pt(C^1\text{^}N\text{^}N)L]^{n+}$ derivatives is also recorded.

The emissive behaviors of **2**, **3**, and **22–25** at 77 K in glassy solutions are sensitive to the complex concentration in the range 10^{-3} to 10^{-5} mol dm^{-3}. At complex concentration below 10^{-5} mol dm^{-3}, the emission spectrum is

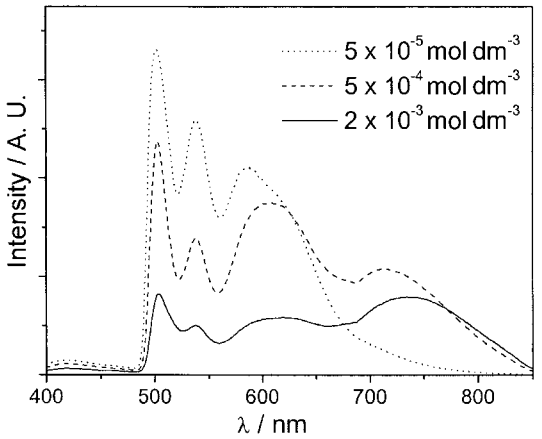

Fig. 12 Emission spectra of **22** in the 5×10^{-5} to 2×10^{-3} mol dm^{-3} concentration range in glassy butyronitrile solution at 77 K (λ_{ex} 350 nm) (Reproduced with permission from [20]. Copyright 2002 American Chemical Society)

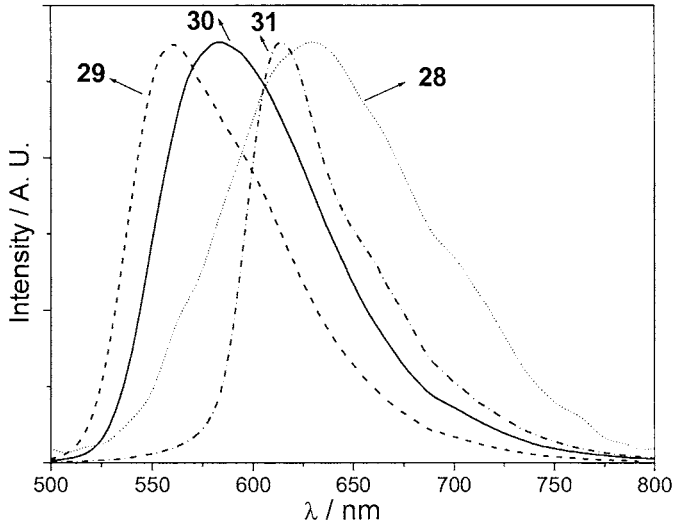

Fig. 13 Normalized photoluminescence spectra of complexes **28–31** in CH_2Cl_2 at 298 K, illustrating tunability of emission energies

vibronically structured with peak maxima at λ_{max}~502 nm (Fig. 12 for **22**). At higher concentrations ($\geq 10^{-4}$ mol dm^{-3}), a new red emission band centered at 600–625 nm develops which is tentatively ascribed to excimeric intraligand excited state arising from weak π-stacking interactions of C^1^N^N ligands. Low-energy emission bands at λ_{max} 711, 739, 710, and 714 nm also appear for **3**, **22**, **24**, and **25** respectively and these can be attributed to MMLCT excited states (Fig. 1) resulting from aggregation of Pt(II) centers in glassy solutions.

The emission maximum of the neutral alkynyl [Pt(C^1^N^N)(C≡CR)] (R=C_6H_4OMe-4 **28** and $C_6H_4NO_2$-4 **29**) complexes in dichloromethane at 298 K ranges from 560 nm (**29**) to 630 nm (**28**) [36]. This implies tunability of the emission energy by varying the 4-substituent in the arylacetylide moiety (Fig. 13). The photoluminescent properties are also affected by the cyclometalating ligand. Replacing the [C^1^N^N] ligand in **30** with [C^3^N^N] (HC^3^N^N=6-(2′-thienyl)-2,2′-bipyridine) in **31** red-shifts the emission maximum from 582 to 614 nm in CH_2Cl_2 at 298 K (Fig. 13). Similar findings have previously reported for [Pt(C^N)$_2$] (HC^N=2-phenylpyridine, 2-(2′-thienyl)pyridine) [14a, 14b].

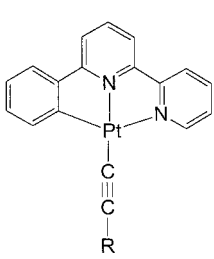

R = C_6H_4OMe-4 **28**
$C_6H_4NO_2$-4 **29**
C_6H_5 **30**

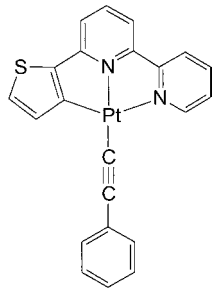

31

Yip reported [37] that the absorption and emission energies of [Pt(C^1^N^N)L]ClO_4 complexes (L=pyridine **32**, 4-aminopyridine **33**, 2-aminopyridine **34**, 2,6-diaminopyridine **35**) are sensitive to the ancillary ligand L. The glassy emission spectra of **32** and **33** exhibit highly structured bands at λ_{max} 502 nm which are attributed to ligand-centered $^3\pi\pi^*$ excited states, thus indicating that this state is not affected by the ancillary ligand. The emission of **34** is red-shifted to λ_{max} 540 nm and its shape and energy is typical for ^{3}MLCT emissions. The intramolecular N···Pt interactions between the lone-pair orbitals of the NH_2 groups and the Pt $5d_{xz}$ orbitals are expected to destabilize the Pt orbitals, leading to a decrease in the energy gap between the metal and π^* orbitals. Compound **35** is not emissive, even at 77 K; however, its absorption spectrum shows that the MLCT transitions are red-shifted from those of **32–34.**

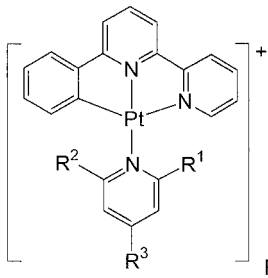

ClO_4^-

$R^1 = R^2 = R^3 = H$ **32**
$R^1 = R^2 = H$; $R^3 = NH_2$ **33**
$R^1 = NH_2$; $R^2 = R^3 = H$ **34**
$R^1 = R^2 = NH_2$; $R^3 = H$ **35**

3.3
Solvatochromic Effects

The effect of solvents upon the emission of [Pt(C^1^N^N)Cl] **7a** has been examined and the solution emission data measured at room temperature and 77 K are listed in Table 1. At room temperature, both the band shape and emission energy of **7a** show no significant change from CH_2Cl_2 to CH_3CN, but the emission lifetime and quantum yield decrease as the solvent polarity increases. In the frozen state at 77 K, the emission of **7a** shows more pro-

Table 1 Solvent dependence of the MLCT emission of **7a** (1×10^{-5} mol dm^{-3})

Solvent	77 K λ_{max}/nm	298 K λ_{max}/nm; τ_o/μs; ϕ_o
Dichloromethane	535, 567 (max), 610	565; 0.5; 0.025
Acetone	527 (max), 536	564; 0.2; 0.018
Chloroform	567 (max), 610	563; 0.3; 0.012
Acetonitrile	512 (max), 544	550; 0.2; 0.002
Dimethylformamide[a]	528, 560, 600	–

[a] **7a** is non-emissive in dimethylformamide solution at room temperature

nounced solvatochromic shift. The emission maximum changes from 512 nm in CH_3CN to 567 nm in CH_2Cl_2 and $CHCl_3$. The remarkable solvatochromism of the emission is consistent with the assignment of the excited state as MLCT in nature.

The solvatochromic behavior of the ^{3}[dσ*, π*] (^{3}MMLCT) emissions of **7b**$(ClO_4)_2$ and **11b**$(ClO_4)_2$ has also been studied (Table 2). The emission ener-

Table 2 Solvent dependence of the ^{3}[dσ*, π*] emission of **7b**$(ClO_4)_2$ and **11b**$(ClO_4)_2$

Solvent	λ_{max}/nm; τ_o/μs; ϕ_o $[Pt_2(C^1\text{^}N\text{^}N)_2(\mu\text{-dppm})]^{2+}$, **7b**	 $[Pt_2(C^2\text{^}N\text{^}N)_2(\mu\text{-dppm})]^{2+}$, **11b**
Dichloromethane	640; 2.6; 0.18	645; 2.5; 0.20
Chloroform	643; 2.5; 0.17	647; 2.1; 0.19
Acetone	657; 0.5; 0.026	657; 0.9; 0.051
Acetonitrile	652; 0.2; 0.015	655; 0.4; 0.025
Methanol	654; 0.2; <0.01	653; 0.3; <0.01
Dimethylformamide	non-emissive	675; 0.3; <0.01

gy, lifetime and quantum yield are sensitive to the solvent polarity, but insensitive to the complex concentration. For **11b**$(ClO_4)_2$, the emission maximum shifts by 689 cm^{-1} from dichloromethane to dimethylformamide (DMF) while the luminescence lifetimes (τ_o) and quantum yields (ϕ_o) change from 2.5 to 0.3 μs and 0.20 to less than 0.01 respectively. This is ascribed to greater rates of non-radiative decay in highly polar solvents such as DMF.

3.4 Spectroscopic Comparison with Pd(II) Counterparts

3.4.1 Absorption Spectroscopy

The absorption spectrum of $[Pd_2(C^1\text{^}N\text{^}N)_2(\mu\text{-dppm})]^{2+}$ **20** shows intense intraligand transitions at λ_{max} 309 and 331 nm ($\epsilon\sim10^4$ dm^3 mol^{-1} cm^{-1}) and

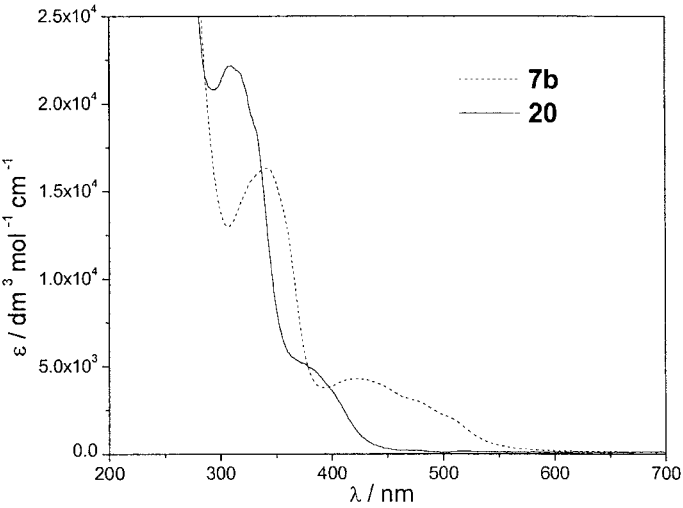

Fig. 14 UV-vis absorption spectra of $[M_2(C^1\text{^}N\text{^}N)_2(\mu\text{-dppm})]^{2+}$ (M=Pt **7b**, Pd **20**) in CH_3CN at 298 K (Reproduced with permission from [28]. Copyright 2000 American Chemical Society)

moderately intense and broad absorptions at λ_{max} 378–401 nm (ϵ=4900–3400 $dm^3\ mol^{-1}\ cm^{-1}$) (Fig. 14) [28]. Upon comparing with the mononuclear counterpart $[Pd(C^1\text{^}N\text{^}N)(PPh_3)]^+$ **19**, both spectra are similar except that the ϵ values are greater for **20**. This may be explained by an increase in the number of $[Pd(C^1\text{^}N\text{^}N)]^+$ chromophores per molecule. The virtual match between the low energy absorptions at λ>360 nm for **19** and **20**, together with the structural data (see above), imply very weak or minimal Pd-Pd interaction in **20**. Presumably, the absorptions at λ_{max} 378–401 nm for **19** and **20** have similar electronic origin, which could be MLCT and/or intraligand in nature. The lowest energy $^1[d\sigma^*\rightarrow\pi^*]$: metal-metal-to-ligand charge transfer (MMLCT) absorption band of $[Pt_2(C^1\text{^}N\text{^}N)_2(\mu\text{-dppm})]^{2+}$ **7b** is located at λ_{max}~420 nm in acetonitrile, which is red-shifted from the MLCT transition of the mononuclear species and is absent from the absorption spectrum of **20** (Fig. 14). This is also consistent with the assignment of very weak/negligible Pd-Pd interaction in **20**.

3.4.2 Emission Spectroscopy

The 77 K emission of $[M_2(C^1\text{^}N\text{^}N)_2(\mu\text{-dppm})]^{2+}$ in frozen CH_3CN occurs at λ_{max} 598 and 638 nm for M=Pd **20** and Pt **7b** respectively (Fig. 15). Since a π-π excimeric ^{3}IL excited state is invoked for the Pd_2 species, the red shift for the Pt_2 analogue is indicative of an excited state arising from π-π (excimeric ^{3}IL) *and* metal-metal (previously assigned as $d\sigma^*\rightarrow\pi^*$) interactions. The 77 K solid-state emission spectra for $[M_2(C^1\text{^}N\text{^}N)_2(\mu\text{-dppm})](ClO_4)_2$

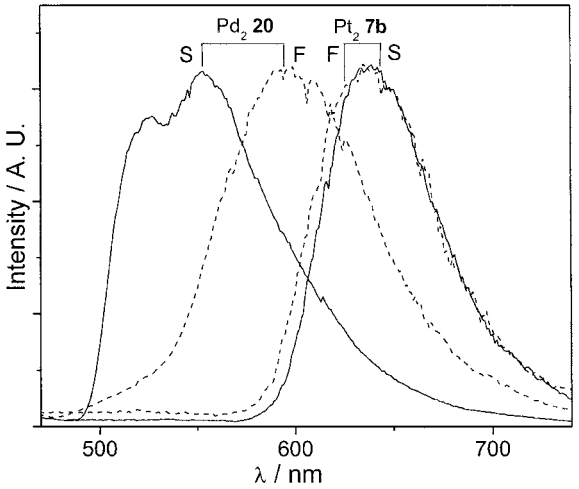

Fig. 15 Normalized 77 K emission spectra (λ_{ex} 350 nm) of $[M_2(C^1\text{^}N\text{^}N)_2(\mu\text{-dppm})](ClO_4)_2$ (M=Pt **7b**, Pd **20**) in frozen CH_3CN (**F**) and solid state (**S**) (Reproduced with permission from [28]. Copyright 2000 American Chemical Society)

reveal a similar trend (Fig. 15). A structureless band appears at λ_{max} 640 nm for Pt_2 **7b**, while a structured emission is observed at 526 and 553 nm for Pd_2 **20**. The nature of the former is again ascribed to mixed $d\sigma^*\rightarrow\pi^*$/excimeric $\pi\rightarrow\pi^*$, while the excited state of the Pd_2 **20** species is assigned as ^{3}IL accompanied by weak π-π excimeric character.

At this juncture, in order to facilitate comparisons of the families of luminophores described in this account, a table illustrating the correlation between the metal-metal distances and photophysical properties of relevant cyclometalated diimine Pt(II)/Pd(II) complexes is provided (Table 3).

4
Applications on the Design of New Materials

4.1
Luminescent Molecular Sensors

The low quantum yield of the ^{3}MLCT emission for $[Pt(C^1\text{^}N\text{^}N)L]ClO_4$ **36** ($L=Ph_2PCH_2NHPh$) is attributable to photoinduced electron transfer (PET) quenching by the amine component [38]. However, the emission intensity varies over a wide pH range in aqueous and micellar solutions presumably due to the extent of PET suppression through protonation at the amine moiety. As the amine receptor becomes protonated at low pH, quenching of the excited state is precluded. Hence the emission intensity is noticeably en-

Table 3 Comparison of structural and photophysical data for cyclometalated diimine Pt(II)/Pd(II) complexes

Compound		M···M distance	UV-vis absorption[a]	Solid-state emission: λ_{max}/nm		Fluid emission[c]: λ_{max}/nm	
		/Å	λ_{max}/nm	298 K	77 K	298 K[a]	77 K[d]
$[Pt(C^1\text{^}N\text{^}N)(C{\equiv}N\textit{t}\text{-}Bu)]^+$	**2**	4.74	^{1}MLCT: 398	579	568	533	505 (625)[e]
$[Pt(C^1\text{^}N\text{^}N)(C{\equiv}NAr)]^+$	**3**	3.3831(9) 4.6030(9)	^{1}MLCT: 402, 419	701	776	528	502 (711)[e]
$[Pt(C^1\text{^}N\text{^}N)(C{\equiv}N\textit{n}\text{-}Bu)]^+$	**22**	-	^{1}MLCT: 406 $^1(d\sigma^*{\rightarrow}\pi^*)$: 511	748	798	529	502 (615, 739)[e]
$[Pt(C^1\text{^}N\text{^}N)(C{\equiv}N\textit{i}\text{-}Pr)]^+$	**23**	-	^{1}MLCT: 411	722	775	529	502 (600)[e]
$[Pt(C^1\text{^}N\text{^}N)(C{\equiv}NCy)]^+$	**24**	-	^{1}MLCT: 400, 418	625	640	530 710 ($\geq 7{\times}10^{-3}$ mol dm^{-3})	501 (625, 710)[e]
$[Pt(C^1\text{^}N\text{^}N)(CO)]^+$	**25**	-	^{1}MLCT: 425 $^1(d\sigma^*{\rightarrow}\pi^*)$: 505	726	813	526	580[f] (714[f])[e]
$[Pt(bph)(CO)_2]$	**26**	3.24	^{1}MLCT: 304[b], 330[b]	726	791	506[g]	500[g], (660[h], 750[i])[e,g]
[Pt(C^N^C)(CO)]	**6**	-	^{1}MLCT: 440[b]	583	576	528[b], 563[b]	529[g], 561[g]
[Pt(C^N^N)Cl]	**7a–12a**	3.345(2) **7a**	^{1}MLCT: 430–438[b] ^{3}MLCT: 510–525[b]	600–687	591–722	^{3}MLCT: 562–568[b]	552–578[b]
$[Pt_2(C^N^N)_2(\mu\text{-dppm})]^{2+}$	**7b**	3.270(1)	$^1(d\sigma^*{\rightarrow}\pi^*)$: 420–485	630	640	652	638[a]
	9b	3.150(1)	**7b–12b**	643	665	661	644[a]
	10b	3.245(2)		665	668	654	633[a]
$[Pt_2(C^1\text{^}N\text{^}N)_2(\mu\text{-pz})]^+$	**13**	3.612(2)	lowest λ_{abs}: 409	596	580	548	555[a]
$[Pt_2(C^1\text{^}N\text{^}N)_2(\mu\text{-dppC}_3)]^{2+}$	**14**	-	^{1}MLCT: ~400	577	543, 573	547	530[a]
$[Pt_2(C^1\text{^}N\text{^}N)_2(\mu\text{-dppC}_5)]^{2+}$	**15**	-	^{1}MLCT: ~400	579	541, 572	544	532[a]
$[Pt_3(C^1\text{^}N\text{^}N)_3(\mu_3\text{-dpmp})]^{3+}$	**16**	*Orange*: 3.36, 3.62 *Red*: 3.19, 3.40	$^1(d\sigma^*{\rightarrow}\pi^*)$: 517	*Orange*: 630 *Red*: 674 *Brown-red*: 709	*Red*: 680 *Brown-red*: 730	710	516[g], 552[g]; 677[g]
$[Pt_3(C^2\text{^}N\text{^}N)_3(\mu_3\text{-dpmp})]^{3+}$	**17**	-	$^1(d\sigma^*{\rightarrow}\pi^*)$: 522	710	677	710	697[g]
$[Pt_3(C^3\text{^}N\text{^}N)_3(\mu_3\text{-dpmp})]^{3+}$	**18**	3.25, 3.39	468	658	649	657	627[g]
$[Pd_2(C^1\text{^}N\text{^}N)_2(\mu\text{-dppm})]^{2+}$	**20**	3.230(1)	^{1}MLCT: 378	Non-emissive	526, 553	Non-emissive	480[g], 510[g] (626[g])[e] 598[a]
$[Pd_2(C^4\text{^}N\text{^}N)_2(\mu\text{-dppm})]^{2+}$	**21**	3.320(2)	^{1}MLCT: 386	Non-emissive	516	Non-emissive	480[g], 523[g] (633[g])[e]

[a] In acetonitrile unless otherwise stated [b] In dichloromethane [c] Complex concentration $5{\times}10^{-5}$ mol dm^{-3}, λ_{ex} 350 nm
[d] In butyronitrile unless otherwise stated [e] Additional emission band(s) observed in $\geq 10^{-3}$ mol dm^{-3} glasses [f] In 1:4:5 DMF/MeOH/EtOH
[g] In MeOH/EtOH mixture [h] λ_{ex} 436 nm [i] λ_{ex} 501 nm See [16e, 17, 20, 27, 28, 33] for details of measurements

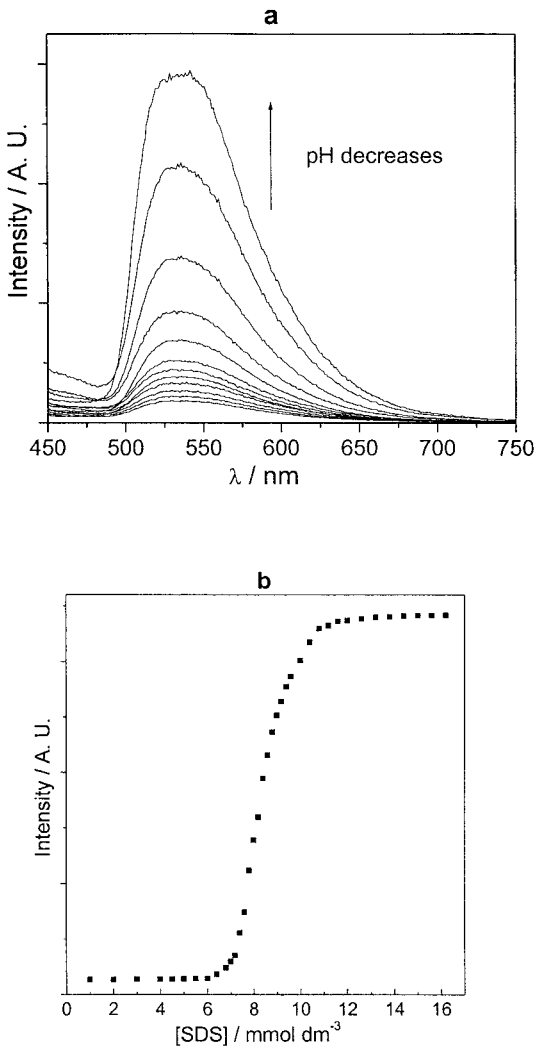

Fig. 16 **a** Emission spectral traces of **36** at different pH in 0.01 mol dm^{-3} SDS solution at 298 K (pH: 12, 11, 10, 9, 8, 7, 6, 5, 4, 3, 2, 1; λ_{ex}=350 nm). **b** Variation of luminescence intensity vs [SDS] for **36** (monitored at 534 nm, λ_{ex}=350 nm, 298 K, [**36**]=1.3×10^{-5} mol dm^{-3}) (Reproduced with permission from [38]. Copyright 1999 Wiley-VCH)

hanced in acidic media due to proton-induced suppression of PET (Fig. 16a). The luminescence of **36** can be employed to estimate the critical micelle concentration (CMC). At high sodium dodecyl sulfate (SDS) concentrations (>10 mmol dm^{-3}), micelle assemblies are formed around the hydrophobic C^1^N^N head of the complex so that solvent-induced quenching is suppressed and the photoluminescence is enhanced (Fig. 16b). This demon-

strates a bifunctional platinum(II) spectroscopic probe that exhibits luminescence enhancement at low pH and in the presence of SDS micelles.

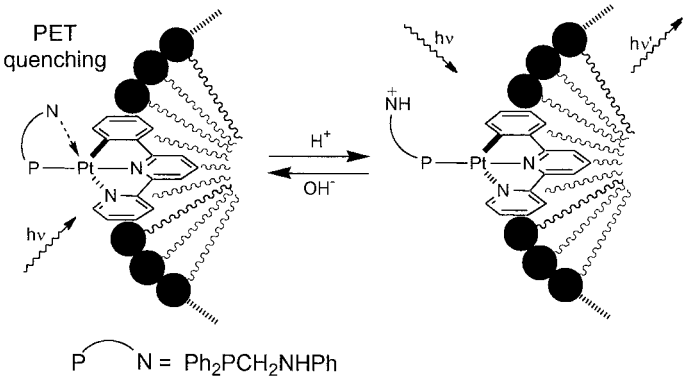

The conformationally nonrigid dinuclear cyclometalated $[Pt_2(C^5\text{^}N\text{^}N)_2(\mu\text{-dppm})]^{2+}$ **37** (HC^5^N^N=4-(*p*-diethylphosphonophenyl)-6-phenyl-2,2′-bipyridine) complex can function as a spectroscopic probe for SDS micelles [16f]. The flexible conformation of the molecule affords intramolecular metal-metal and/or ligand-ligand interactions, and hence MMLCT emissions that are sensitive to the microheterogeneous environments of SDS micelles. Addition of SDS micelles to an aqueous solution of **37** leads to a MLCT emission at λ_{max} 530 nm suggesting negligible intra-/inter-molecular metal-metal and ligand-ligand interactions. Increasing the ionic strength causes micelles to undergo substantial transformations in size and shape, so that cylinder micelles with larger aggregation numbers are

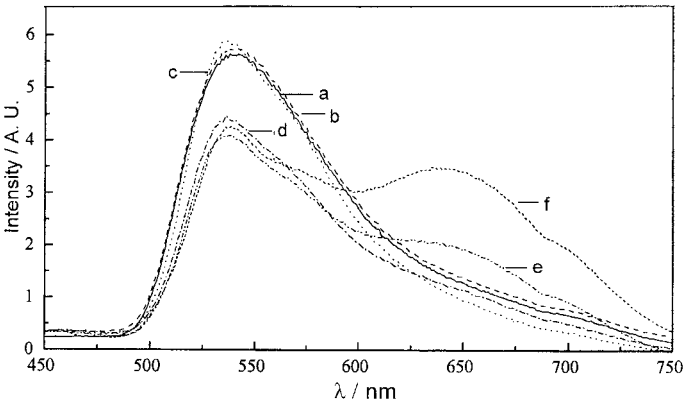

Fig. 17 Emission spectra of **37** at various [NaCl] in SDS micellar solution ([SDS]=1.52×10^{-2} mol dm^{-3}, [**37**]=3.46×10^{-6} mol dm^{-3}, [NaCl]/mol dm^{-3}=0 **a**, 0.06 **b**, 0.2 **c**, 0.3 **d**, 0.4 **e**, 0.5 **f**) (Reproduced with permission from [16f]. Copyright 1998 Royal Society of Chemistry)

formed and the SDS head groups become closer in proximity. Thus, an additional ^{3}MMLCT emission at λ_{max} 650 nm gradually develops as [NaCl] increases (Fig. 17). The alignment of the SDS head groups with Na^+ cations enables two cyclometalated $[Pt(C^5\text{^}N\text{^}N)]^+$ units to approach sufficiently close for intramolecular metal-metal and/or ligand-ligand interactions to occur.

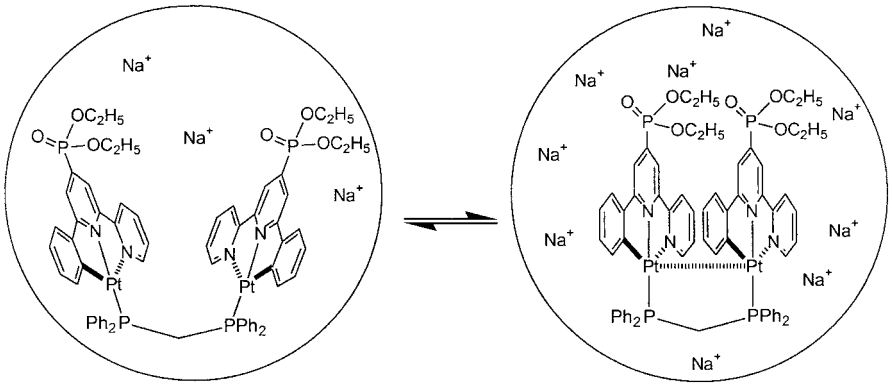

The $[Pt(C^2\text{^}N\text{^}N)NH_2(CH_2)_3Si(OEt)_3]^+$ **38** complex was incorporated into a sol-gel glass by co-condensation with $Si(OEt)_4$, which shows a rapid and sensitive response to oxygen gas [39]. The luminescence intensity decreases by 58% in ca. 10 s when switching from N_2 to O_2 (Fig. 18). This Pt-based material displays several advantages over the sensing ability of $[Ru(bpy)_3]^{2+}$ derivatives in polymer [40], and these include: (i) the platinum(II) complex exhibits longer lifetime, especially in sol-gel matrix, which provides a larger quenching response, (ii) the pore-like microstructure of sol-gel films allows effective permeation by oxygen molecules, resulting in a faster response, (iii) immobilization of Pt(II) complex into sol-gel films via coordinative bonding offers stability for the sensor and minimizes leaching of luminophores from the sol-gel matrix.

The luminescent cyclometalated complex $[Pt(C^4\text{^}N\text{^}N)py]^+$ **39** immobilized in Nafion film has been observed to exhibit a solvatochromic shift in emission maximum from 530 to 650 nm upon immersion in ethanol but no effect was detected with aprotic organic solvents (Fig. 19) [41]. On the contrary, the emission of the $[Pt(C^4\text{^}N\text{^}N)]^+$ luminophore anchored on silica materials (MCM-41/-48 and silica gel) showed a blue shift from λ_{max}~665 to 550 nm upon exposure to pentane vapor but no shift was observed for ethanol vapor (Fig. 20).

The distinctive shift in emission energy arising from reversible switching between ^{3}MMLCT and ^{3}MLCT excited states, which can be induced by intru-

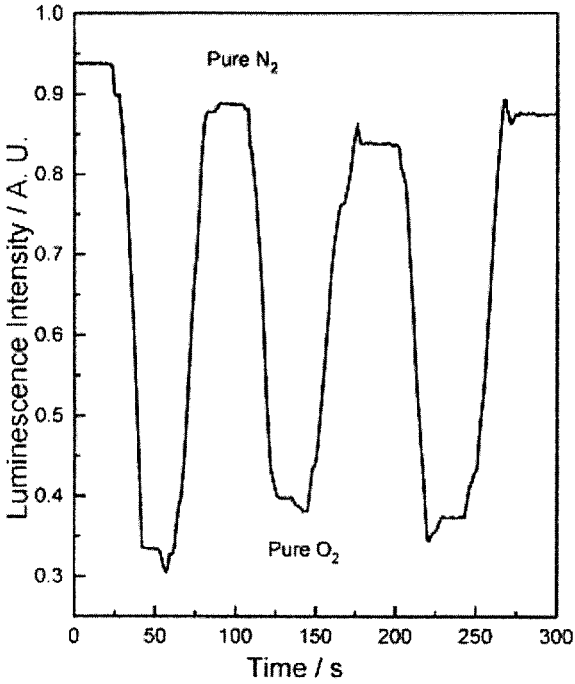

Fig. 18 Change of luminescence intensity towards alternate environments of pure oxygen and nitrogen for a Pt sol-gel film ([Pt]=1.0 wt%) (Reproduced with permission from [39]. Copyright 1998 Elsevier)

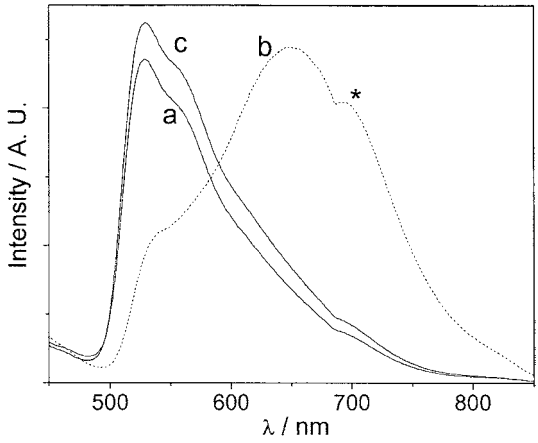

Fig. 19 Emission spectra (λ_{ex} 350 nm) of Nafion film incorporated with **39** (for 90 min) before **a**, and after **b** immersion in ethanol for 20 min, and after drying in air **c** for 24 h (* denotes instrumental artifact) (Reproduced with permission from [41]. Copyright 2003 Royal Society of Chemistry)

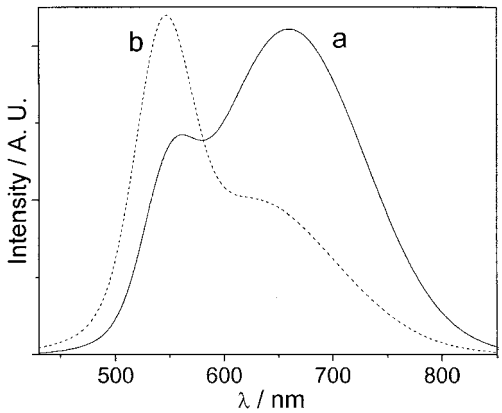

Fig. 20 Emission spectra (λ_{ex} 380 nm) of [Pt(C^4^N^N)-MCM-41] ([Pt]=2.8 wt%) before **a**, and after **b** exposure to pentane vapor for 10 min at 298 K (Reproduced with permission from [41]. Copyright 2003 Royal Society of Chemistry)

sion of guest molecules or other changes in the microenvironment of these luminophores, constitutes an optical signaling response. The incorporation of the luminescent platinum(II) component into different solid matrices therefore not only provides supporting anchorage but also offers a discriminating effect with respect to the nature of the molecules to be sorbed and detected.

4.2 Organic Light-Emitting Materials and Electrophosphorescent Devices

The intense tunable phosphorescence of the [Pt(C^n^N^N)(C≡CR)] (e.g., **28–31**) complexes, plus their neutrality and stability under vacuum deposition conditions, render them good candidates as emitters for high-efficiency OLEDs [36]. The electroluminescence (EL) energies are tunable by the nature of (i) the 4-arylacetylide substituent and (ii) the tridentate ligand (Fig. 21). This is similarly observed in their photoluminescence properties (Fig. 13). A maximum luminance of 3100 cd m^{-2} at 12 V and a maximum efficiency of 1.0 cd A^{-1} at 30 mA cm^{-2} were observed for the device using [Pt(C^3^N^N)(C≡CC_6H_4Me-4)] (HC^3^N^N=6-(2′-thienyl)-2,2′-bipyridine) **40**. These values are comparable with the best red-light OLEDs in the literature [42] and demonstrate the potential usefulness of these platinum(II)-alkynyl complexes as electrophosphorescent emitters.

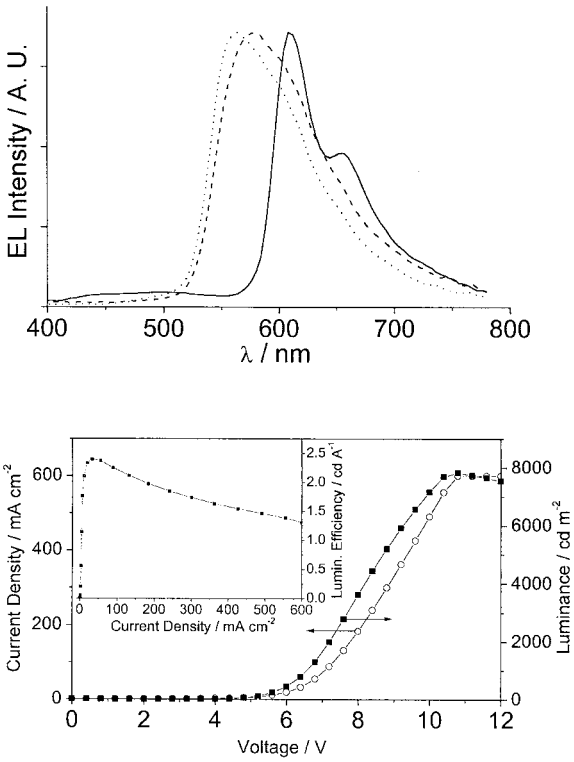

Fig. 21 *Top*: normalized electroluminescence spectra for (*dotted line*) **30**, (*dashed line*) [Pt(C^1^N^N)(C≡CC_6H_4Me-4)], and (*continuous line*) **40** at 4% doping level and multilayer configuration of device. *Bottom*: current density, voltage and luminance characteristics (*inset*: luminescent efficiency vs current density) for OLED using **30** as emitter as 4% doping level (Reproduced with permission from [36a]. Copyright 2002 Royal Society of Chemistry)

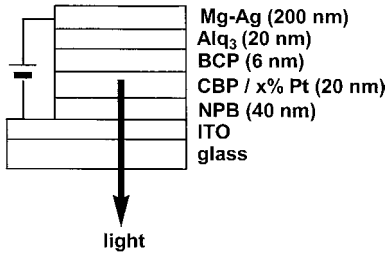

Forrest and Thompson have demonstrated high-efficiency, high-brightness red phosphorescent OLEDs employing cyclometalated benzothienylpyridine (btp) iridium and platinum complexes [43], such as in (2-(2′-benzo[4,5-α]thienyl)pyridinato-N,$C^{3'}$)platinum(acetylacetonate), [Pt(btp)(acac)] **41**.

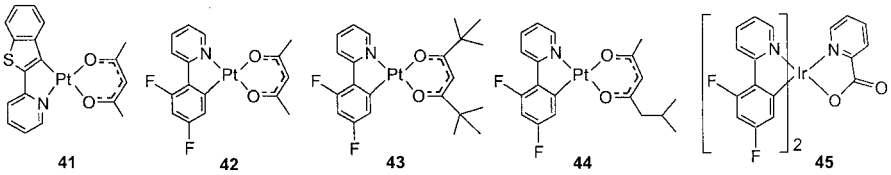

Thompson had reported the synthesis and photophysical properties of a series of phosphorescent cyclometalated platinum complexes, [(C^N)Pt(O^O)] (HC^N=2-phenylpyridyl, 2-(2′-thienyl)pyridyl, 2-(4′,6′-difluorophenyl)pyridyl; O^O=acetyl acetonate **42**, 2,2,6,6-tetramethyl-3,5-heptanedionato-O,O **43** [44], 6-methyl-2,4-heptanedionato-O,O **44**). Their emission characteristics are governed by the nature of the cyclometalating ligand through modifying the 2-phenylpyridyl group with electron-donating or -withdrawing substituents. Incorporating electronegative atoms such as fluorine onto the phenyl ring blue-shifts the emission while substituting with electron-donating methoxy group gives a pronounced red shift. This allows the emission to be tuned in energy with λ_{max} in the range 456–600 nm [44]. These complexes are stable in air and sublimable. Forrest reported the use of the phosphorescent excimer arising from the phosphor **42**, coupled with blue monomer emission from either **44** or iridium-*bis*(4,6-difluorophenylpyridinato-N,C^2)-picolinate **45**, to achieve efficient electrophosphorescent white light OLEDs [45].

4.3 Metallointercalators for DNA and Polymeric Molecular Switch for Protein Binding Reactions

Since square planar platinum(II) complexes have vacant coordination site at the platinum atom, upon intercalation with DNA base pairs, the local environment around the Pt core changes and the mobility of the complexes decreases. Subsequently, a profound impact upon the photoluminescent properties can be envisioned.

Intercalation of the luminescent cyclometalated $[Pt(C^6\text{^}N\text{^}N)(MeCN)]^+$ **46** (HC^6^N^N=2,9-diphenyl-1,10-phenanthroline) and $[Pt_2(C^1\text{^}N\text{^}N)_2(\mu\text{-dppm})]^{2+}$ **7b** complexes into calf-thymus DNA leads to a dramatic enhancement of their photoluminescence [16d]. The intercalation is likely to prohibit the solvent-induced quenching process, which typically occurs at the coordinative unsaturated platinum site for the MLCT excited state. The DNA-intercalating platinum(II) complex, $[Pt(dppz)(t\text{N^C})]CF_3SO_3$ (dppz=dipyrido[3,2-a:2′,3′-c]phenazine, *t*N^CH=4-*tert*-butyl-2-phenylpyridine) **47** similarly exhibits an increase in emission intensity at λ_{max} 650 nm on addition of calf thymus DNA (Fig. 22) [46].

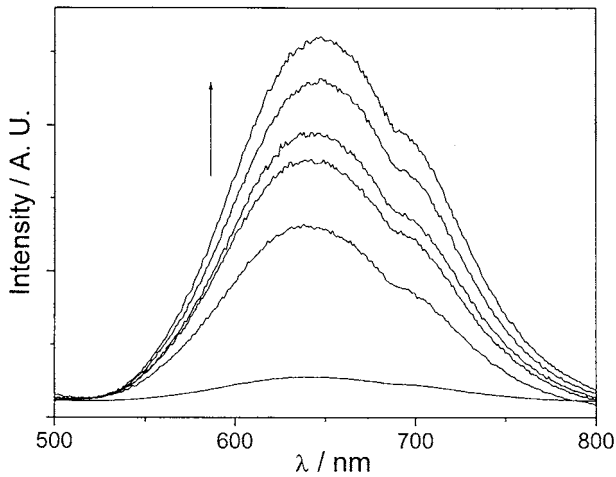

Fig. 22 Emission spectral traces of **47**(CF_3SO_3) (20 μmol dm^{-3}) in aqueous tris buffer (5 mmol dm^{-3} tris, 50 mmol dm^{-3} NaCl, pH=7.2) with increasing calf-thymus DNA concentrations: 0, 21, 42, 63, 84, 105 μmol dm^{-3}

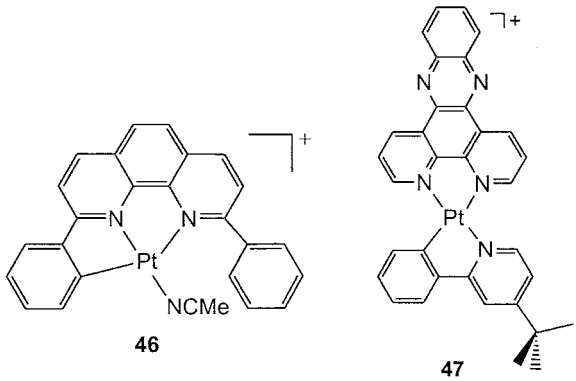

Attachment of the water-soluble polymer, poly(ethylene)glycol (PEG) to [Pt(4-HOC_6H_4C^N^N)Cl] gave **48** which can be utilized as a luminescent probe [47] for binding reactions with bovine serum albumin (BSA), human blood γ-globulin, and human and chicken egg albumin. The emission intensity is significantly enhanced upon addition of these proteins (Fig. 23 for BSA), presumably due to the interaction of **48** with hydrophobic region(s) of proteins. The Scatchard plots of V/[L] vs V for these proteins afforded straight lines (inset of Fig. 23) with binding constants (K) of (1.3–4.2)$\times 10^4$ mol^{-1} dm^3, according to the equation: V/[L]=KN−KV, where V is the number of **48** molecules bound in one protein molecule, [L] is the concentration of free **48**, K is the binding constant, and N is the total number of **48** molecules bound in one protein molecule. Therefore, incorporating lumi-

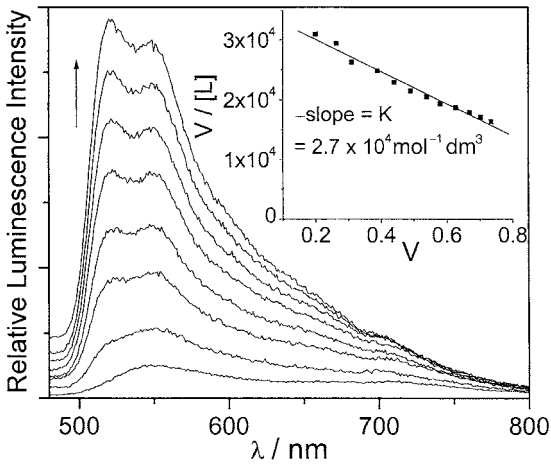

Fig. 23 Emission spectral traces of **48** (20 μmol dm^{-3}) at different concentration of bovine serum albumin (BSA) in aqueous solution (pH=7.40, 100 mmol dm^{-3} Na_2HPO_4-NaH_2PO_4 with 0.9% NaCl; [BSA]=0 to 3.15 μmol dm^{-3}, increases by 0.45 μmol dm^{-3} per plot). *Inset*: Scatchard plot for obtaining the binding constant (K) (Reproduced with permission from [47]. Copyright 2002 Royal Society of Chemistry)

nescent platinum(II) complexes into a water-soluble polymer could pave the way to luminescent biosensors for protein binding reactions under aqueous conditions.

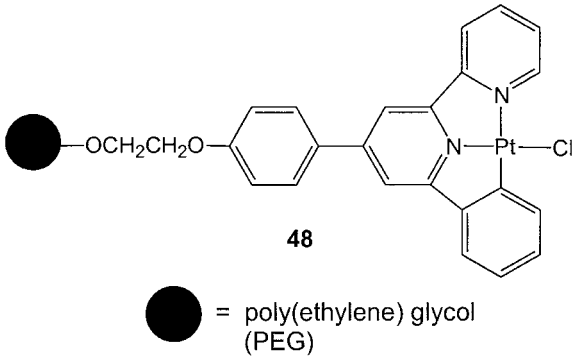

4.4 Other Examples

The employment of diphenylphosphinopropanoic acid as a building block in the supramolecular assembly of a cyclometalated platinum(II) polymer **49** directed by π-stacking and hydrogen-bonding interactions has been described [16g].

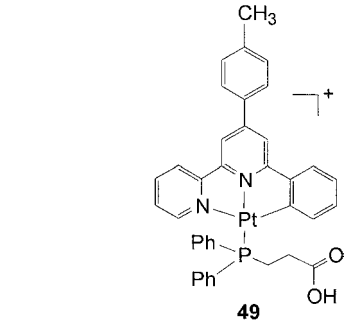

49

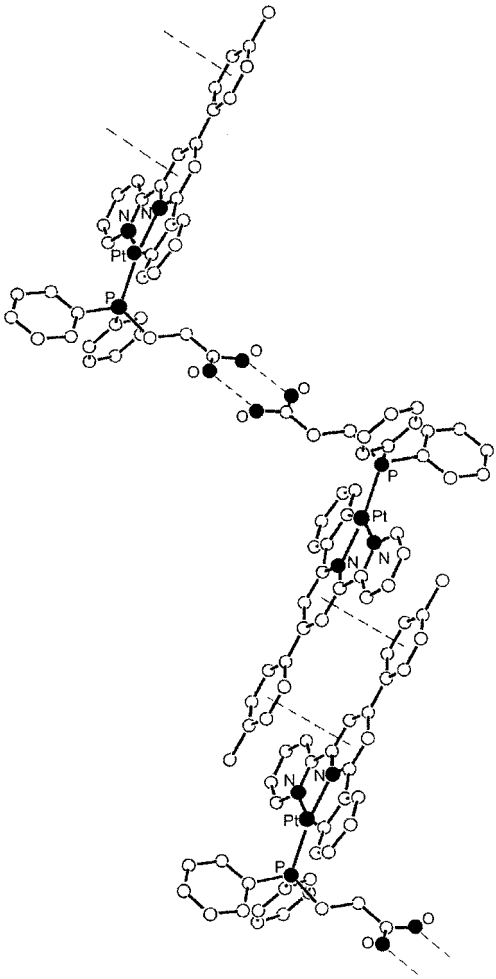

The orthometalated Pt(II) complexes $[Pt(phpy)_2]$ and $[Pt(thpy)_2]$ (Hphpy=2-phenylpyridine, Hthpy=2-(2′-thienyl)pyridine) are photosensitive in several organic solvents, giving rise to oxidative addition reactions

that lead to the formation of new luminescent Pt(IV) products [14c], for example [Pt(thpy)$_2$(CH_2Cl)Cl].

Cyclopalladation of 4′-(functionalized)-6′-phenyl-2,2′-bipyridine ligands (HL) afforded several new [PdLCl] complexes; liquid crystalline complex **50** exhibits thermotropic nematic mesomorphism, which represents the first example of an organometallic mesogen with a terdentate o-C deprotonated ligand. Complex **50** is photoluminescent at 77 K [48]. Other researchers have reported the applications of *ortho*-platinated or -palladated complexes bearing azobenzene or imine ligands as liquid crystalline materials [49].

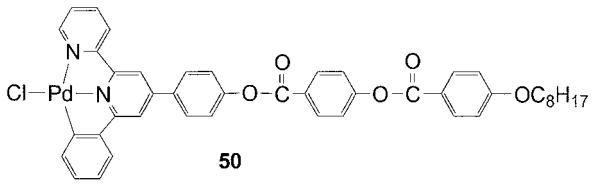

50

5
High-Resolution Spectroscopic Studies at Ultra-low Temperatures

Yersin and coworkers [50] have pioneered spectroscopic investigation on the excited states of metal-organic luminescent compounds, especially Pt complexes, in inert *n*-octane (Shpol'skii) matrices at temperatures around 1–5 K. Spectroscopic studies on [Pt(thpy)$_2$] under high pressure revealed that the emitting state is $^3\pi\pi^*$ in nature with significant MLCT character [50a]. The spectra are highly resolved and show electronic origin (0–0 transition) of the most intense emitting triplet sublevel. For [Pt(thpy)(CO)Cl], the emitting triplet state was investigated by complementary use of high-resolution optical and optically detected magnetic resonance spectroscopy, which allowed determination of several photophysical parameters including the zero-field splittings (ZFS) of the triplet state. Upon comparing the spectra of a series of organometallic Pt(II) complexes, Yersin concluded that higher ZFS values correspond to significantly increased MLCT participation in the lowest triplet $\pi\pi^*$ state of these compounds [15b, 50c, 51].

6
Concluding Remarks

In recent years, square planar platinum(II) systems bearing cyclometalating tridentate ligands based on 6-phenyl-2,2′-bipyridine have been demonstrated to offer favorable photophysical characteristics compared to 2,2′:6′,2″-terpyridine analogues, and interest in these luminescent cyclometalated complexes has proliferated [16, 17, 38]. Like tris(2,2′-bipyridine)rutheni-

um(II) and its derivatives, these platinum(II) compounds have found applications in photochemical devices [14c] and as chemical sensors [16, 38]. Their square planar geometry facilitates substrate-binding reactions in both the ground and MLCT excited states. Their photoluminescent properties can be systematically tuned through modification of the cyclometalated and/or ancillary ligands. The employment of less bulky π-acceptor ligands such as isocyanide or CO favors intermolecular metal-metal interactions and hence aggregation in mononuclear species, which accounts for the observation of low-energy ^{1}MMLCT transitions (Fig. 1). The bi- and trinuclear counterparts have been designed to model intermolecular metal-metal and/or excimeric interactions in the Pt(II) polypyridine systems and to probe the spectroscopic properties of low-energy MMLCT: $[d\sigma^*(dz^2(Pt)) \rightarrow \pi^*(diimine)]$ and excimeric ligand-to-ligand excited states. Their photoluminescent properties have been shown to be sensitive to their microenvironment, which could be employed for molecular sensing and signaling purposes. By taking advantage of their ability to undergo outer- and *inner*-sphere interactions with substrates, it is envisaged that future applications in photochemical transformation and photocatalysis, plus chemosensing and molecular probe technologies, could be developed with luminescent platinum(II) complexes.

Acknowledgements We are grateful for financial support from the University Development Fund of The University of Hong Kong, the Hong Kong University Foundation, and the Research Grants Council of the Hong Kong SAR, China [HKU 7039/03P].

References

1. Keller HJ (1977) Chemistry and physics of one-dimensional metals. Plenum Press, New York
2. Miller JS (1982) Extended linear chain compounds. Plenum Press, New York
3. (a) Yersin H, Gliemann G (1978) Ann NY Acad Sci 313:539; (b) Gliemann G, Yersin H (1985) Struct Bond 62:87; (c) Yersin H, Riedl U (1995) Inorg Chem 34:1642
4. Schindler JW, Fukuda RC, Adamson AW (1982) J Am Chem Soc 104:3596
5. (a) Miskowski VM, Houlding VH (1989) Inorg Chem 28:1529; (b) Che CM, He LY, Poon CK, Mak TCW (1989) Inorg Chem 28:3081; (c) Biedermann J, Gliemann G, Klement U, Range KJ, Zabel M (1990) Inorg Chem 29:1884; (d) Kunkely H, Vogler A (1990) J Am Chem Soc 112:5625; (e) Miskowski VM, Houlding VH (1991) Inorg Chem 30:4446; (f) Houlding VH, Miskowski VM (1991) Coord Chem Rev 111:145; (g) Wan KT, Che CM, Cho KC (1991) J Chem Soc Dalton Trans 1077; (h) Connick WB, Henling LM, Marsh RE, Gray HB (1996) Inorg Chem 35:6261; (i) Humbs W, Yersin H (1997) Inorg Chim Acta 265:139
6. (a) Biedermann J, Wallfahrer M, Gliemann G (1987) J Lumin 37:323; (b) Weiser-Wallfahrer M, Gliemann G (1990) Z Naturforsch 45b:652
7. Kato M, Kosuge C, Morii K, Ahn JS, Kitagawa H, Mitani T, Matsushita M, Kato T, Yano S, Kimura M (1999) Inorg Chem 38:1638

8. Yip HK, Che CM, Zhou ZY, Mak TCW (1992) J Chem Soc Chem Commun 1369
9. (a) Barigelletti F, Sandrini D, Maestri M, Balzani V, von Zelewsky A, Chassot L, Jolliet P, Maeder U (1988) Inorg Chem 27:3644; (b) Zuleta JA, Burberry MS, Eisenberg R (1990) Coord Chem Rev 97:47; (c) Blanton CB, Rillema DP (1990) Inorg Chim Acta 168:145; (d) Scolaro LM, Alibrandi G, Romeo R, Ricevuto V, Campagna S (1992) Inorg Chem 31:2074; (e) Cummings SD, Eisenberg R (1996) J Am Chem Soc 118:1949; (f) Paw W, Cummings SD, Mansour MA, Connick WB, Geiger DK, Eisenberg R (1998) Coord Chem Rev 171:125
10. (a) Jennette KW, Gill JT, Sadownick JA, Lippard SJ (1976) J Am Chem Soc 98:6159; (b) Yip HK, Cheng LK, Cheung KK, Che CM (1993) J Chem Soc Dalton Trans 2933; (c) Bailey JA, Hill MG, Marsh RE, Miskowski VM, Schaefer WP, Gray HB (1995) Inorg Chem 34:4591; (d) Arena G, Calogero G, Campagna S, Scolaro LM, Ricevuto V, Romeo R (1998) Inorg Chem 37:2763
11. (a) Aldridge TK, Stacy EM, McMillin DR (1994) Inorg Chem 33:722; (b) Büchner R, Field JS, Haines RJ, Cunningham CT, McMillin DR (1997) Inorg Chem 36:3952; (c) Büchner R, Cunningham CT, Field JS, Haines RJ, McMillin DR, Summerton GC (1999) J Chem Soc Dalton Trans 711; (d) Michalec JF, Bejune SA, Cuttell DG, Summerton GC, Gertenbach JA, Field JS, Haines RJ, McMillin DR (2001) Inorg Chem 40:2193; (e) Hobert SE, Carney JT, Cummings SD (2001) Inorg Chim Acta 318:89; (f) McMillin DR, Moore JJ (2002) Coord Chem Rev 229:113
12. (a) Bailey JA, Miskowski VM, Gray HB (1993) Inorg Chem 32:369; (b) Ratilla EMA, Scott BK, Moxness MS, Kostić NM (1990) Inorg Chem 29:918
13. Roundhill DM, Gray HB, Che CM (1989) Acc Chem Res 22:55
14. (a) Chassot L, Müller E, von Zelewsky A (1984) Inorg Chem 23:4249; (b) Maestri M, Sandrini D, Balzani V, Chassot L, Jolliet P, von Zelewsky A (1985) Chem Phys Lett 122:375; (c) Sandrini D, Maestri M, Balzani V, Chassot L, von Zelewsky A (1987) J Am Chem Soc 109:7720; (d) Maestri M, Sandrini D, von Zelewsky A, Deuschel-Cornioley C (1991) Inorg Chem 30:2476; (e) Maestri M, Deuschel-Cornioley C, von Zelewsky A (1991) Coord Chem Rev 111:117; (f) Wiedenhofer H, Schützenmeier S, von Zelewsky A, Yersin H (1995) J Phys Chem 99:13385
15. (a) Craig CA, Garces FO, Watts RJ, Palmans R, Frank AJ (1990) Coord Chem Rev 97:193; (b) Yersin H, Donges D (2001) Top Curr Chem 214:81
16. (a) Chan CW, Lai TF, Che CM, Peng SM (1993) J Am Chem Soc 115:11245; (b) Chan CW, Cheng LK, Che CM (1994) Coord Chem Rev 132:87; (c) Liu HQ, Peng SM, Che CM (1995) J Chem Soc Chem Commun 509; (d) Liu HQ, Cheung TC, Che CM (1996) Chem Commun 1039; (e) Cheung TC, Cheung KK, Peng SM, Che CM (1996) J Chem Soc Dalton Trans 1645; (f) Wu LZ, Cheung TC, Che CM, Cheung KK, Lam MHW (1998) Chem Commun 1127; (g) Tse MC, Cheung KK, Chan MCW, Che CM (1998) Chem Commun 2295
17. Lai SW, Chan MCW, Cheung TC, Peng SM, Che CM (1999) Inorg Chem 38:4046
18. Lu W, Chan MCW, Cheung KK, Che CM (2001) Organometallics 20:2477
19. Constable EC, Henney RPG, Leese TA, Tocher DA (1990) J Chem Soc Chem Commun 513
20. Lai SW, Lam HW, Lu W, Cheung KK, Che CM (2002) Organometallics 21:226
21. Hunter CA, Sanders JKM (1990) J Am Chem Soc 112:5525
22. Bailey JA, Gray HB (1992) Acta Crystallogr C48:1420
23. Jovanović B, Manojlović-Muir L, Muir KW (1972) J Chem Soc Dalton Trans 1178
24. Cave GWV, Fanizzi FP, Deeth RJ, Errington W, Rourke JP (2000) Organometallics 19:1355

25. Newman CP, Cave GWV, Wong M, Errington W, Alcock NW, Rourke JP (2001) J Chem Soc Dalton Trans 2678
26. Yersin H (unpublished results)
27. (a) Lu W, Zhu N, Che CM (2002) Chem Commun 900; (b) Lu W, Chan MCW, Zhu N, Che CM, Li C, Hui Z (2004) J Am Chem soc 126:7639
28. Lai SW, Cheung TC, Chan MCW, Cheung KK, Peng SM, Che CM (2000) Inorg Chem 39:255
29. Bardwell DA, Crossley JG, Jeffery JC, Orpen AG, Psillakis E, Tilley EEM, Ward MD (1994) Polyhedron 13:2291
30. (a) Cotton FA, Matusz M, Poli R, Feng X (1988) J Am Chem Soc 110:1144; (b) Ogoshi S, Tsutsumi K, Ooi M, Kurosawa H (1995) J Am Chem Soc 117:10415; (c) Tanase T, Ukaji H, Yamamoto Y (1996) J Chem Soc Dalton Trans 3059
31. Che CM, He LY, Poon CK, Mak TCW (1989) Inorg Chem 28:3081
32. DePriest J, Zheng GY, Goswami N, Eichhorn DM, Woods C, Rillema DP (2000) Inorg Chem 39:1955
33. Zheng GY, Rillema DP (1998) Inorg Chem 37:1392
34. Chen YH, Merkert JW, Murtaza Z, Woods C, Rillema DP (1995) Inorg Chim Acta 240:41
35. Connick WB, Marsh RE, Schaefer WP, Gray HB (1997) Inorg Chem 36:913
36. (a) Lu W, Mi BX, Chan MCW, Hui Z, Zhu N, Lee ST, Che CM (2002) Chem Commun 206; (b) Lu W, Mi BX, Chan MCW, Hui Z, Che CM, Zhu N, Lee ST (2004) J Am Chem Soc 126:4958
37. Yip JHK, Suwarno, Vittal JJ (2000) Inorg Chem 39:3537
38. Wong KH, Chan MCW, Che CM (1999) Chem Eur J 5:2845
39. Ma YG, Cheung TC, Che CM, Shen JC (1998) Thin Solid Films 333:224
40. DiMarco G, Lanza M, Campagna S (1995) Adv Mater 7:468
41. Che CM, Fu WF, Lai SW, Hou YJ, Liu YL (2003) Chem Commun 118
42. Baldo MA, O'Brien DF, You Y, Shoustikov A, Sibley S, Thompson ME, Forrest SR (1998) Nature 395:151
43. Adachi C, Baldo MA, Forrest SR, Lamansky S, Thompson ME, Kwong RC (2001) Appl Phys Lett 78:1622
44. Brooks J, Babayan Y, Lamansky S, Djurovich PI, Tsyba I, Bau R, Thompson ME (2002) Inorg Chem 41:3055
45. D'Andrade BW, Brooks J, Adamovich V, Thompson ME, Forrest SR (2002) Adv Mater 14:1032
46. Che CM, Yang M, Wong KH, Chan HL, Lam W (1999) Chem Eur J 5:3350
47. Che CM, Zhang JL, Lin LR (2002) Chem Commun 2556
48. Neve F, Ghedini M, Crispini A (1996) Chem Commun 2463
49. (a) Buey J, Espinet P (1996) J Organomet Chem 507:137; (b) Ghedini M, Pucci D, Crispini A, Barberio G (1999) Organometallics 18:2116
50. (a) Yersin H, Trümbach D, Wiedenhofer H (1999) Inorg Chem 38:1411; (b) Yersin H, Humbs W (1999) Inorg Chem 38:5820; (c) Yersin H, Donges D, Humbs W, Strasser J, Sitters R, Glasbeek M (2002) Inorg Chem 41:4915
51. (a) Yersin H (2003) In: Proceedings of SPIE International Symposium on Optical Science and Technology, San Diego (USA), vol 5214; (b) Yersin H (2004) Top Curr Chem (this volume)

Top Curr Chem (2004) 241:65–96
DOI 10.1007/b96860

Photophysical Properties of Three-Dimensional Transition Metal Tris-Oxalate Network Structures

Andreas Hauser (✉) · Marianne E. von Arx · Vaughan S. Langford · Ueli Oetliker · Selim Kairouani · Anne Pillonnet

Département de Chimie Physique, Université de Genève, Bâtiment de Science II, 30 quai Ernest Ansermet, 1211 Genève 4, Switzerland
andreas.hauser@chiphy.unige.ch

Abstract Excitation energy transfer processes play an important role in many areas of physics, chemistry and biology. The three-dimensional oxalate networks of composition $[M^{III}(bpy)_3][M^{I}M'^{III}(ox)_3]ClO_4$ (bpy=2,2′-bipyridine, ox=oxalate, M^{I}=alkali ion) allow for a variety of combinations of different transition metal ions. The combination with chromium(III) on both the tris-bipyridine as well as the tris-oxalate site constitutes a model system in which it is possible to differentiate unambiguously between energy transfer from $[Cr(ox)_3]^{3-}$ to $[Cr(bpy)_3]^{3+}$ due to dipole-dipole interaction on the one hand and exchange interaction on the other hand. Furthermore it is possible to just as unambiguously differentiate between the common temperature dependent phonon-assisted energy migration within the ^2E state of $[Cr(ox)_3]^{3-}$, and a unique resonant process.

Keywords Oxalate networks · $[Cr(ox)_3]^{3-}$ · $[Cr(bpy)_3]^{3+}$ · ^2E state · Resonant energy transfer · Phonon-assisted energy transfer · Förster transfer · Exchange interaction

1 Introduction

Excitation energy transfer processes, whereby the excitation energy from an initially excited chromophore, usually referred to as donor, is transferred in a non-radiative process to a nearby chromophore, usually referred to as ac-

ceptor, play an important role in a number of technological applications as well as in life science and in nature. Technological applications include solid state lasers [1], fluorescent lamps and displays [2], solar energy conversion cells [3] and information technology. In life science so-called fluorescence resonance energy transfer (FRET) is used for the conformational analysis of proteins and for investigations on the folding dynamics of DNA [4]. In nature antenna pigments of the chloroplasts harvest the light energy from the sun and transfer it to the photosynthetic reaction centre [5]. Research in this area therefore was [6] and still is [7] of paramount interest.

As far back as 1948, Förster [8] laid the theoretical foundations for our understanding of energy transfer processes in a seminal paper, postulating a dipole-dipole mechanism which involves the transition dipole moments of the respective electronic transitions of the donor and the acceptor. Whereas for organic energy donor-acceptor pairs with singlet-singlet energy transfer, this so-called Förster transfer is the dominant mechanism, this is not always the case for donor-acceptor pairs involving transition metal complexes with an open shell electronic structure. For such cases, Dexter [9] extended the work of Förster to include higher order multipole interactions, magnetic dipole interactions as well as exchange interactions. All mechanisms consider the excitation energy transfer to be a resonant process, for which, according to Fermi's Golden Rule, the probability for an energy transfer process from the initially excited donor D* to the acceptor A is given by [10]

$$w_{DA} = \frac{2\pi}{\hbar} |\langle DA^* | H' | D^* A \rangle|^2 \Omega_{DA} \tag{1}$$

where $\langle DA^* | H' | D^* A \rangle$ is the electronic coupling matrix element between the donor and the acceptor, with H' being the perturbation operator for electrostatic, magnetic or exchange interaction. In Eq. (1) the spectral overlap integral of the absorption of the acceptor and the emission of the donor, Ω_{DA}, takes care of energy conservation.

Whereas higher order multipole and magnetic dipole interactions are important for energy transfer processes in crystalline systems of high symmetry, in particular involving rare earth ions [11], dipole-dipole interactions and to a lesser extent exchange interactions usually dominate energy transfer processes between low-symmetry transition metal complexes. In the following, the discussion is therefore restricted to the latter two mechanisms. The key difference between them is that the dipole-dipole interaction falls off as the inverse power of three of the donor-acceptor distance R_{DA}, whereas the exchange interaction depends upon direct overlap of the electronic wavefunctions of the donor and the acceptor, and thus falls off exponentially with increasing values of R_{DA}. As indicated schematically in Fig. 1, the exchange mechanism can therefore be dominant for small values of R_{DA}, but the dipole-dipole interaction is expected to take over at larger values of R_{DA}. A large number of papers addressing the nature of the interaction responsi-

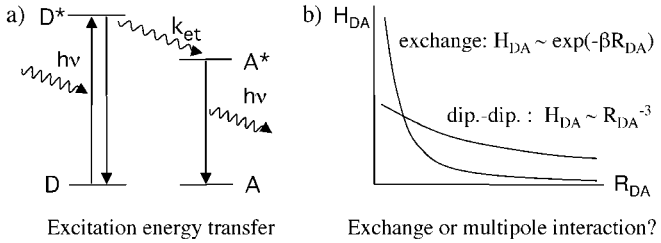

Fig. 1 **a** In the presence of an acceptor A, the luminescence of the originally excited donor D is quenched by a non-radiative energy transfer process. **b** In order for the energy transfer to be efficient, the acceptor must be in the vicinity of the donor. The ensuing interaction can be either multipole-multipole interaction or exchange interaction. Whereas for dipole-dipole interaction $H_{DA}=\langle DA^*|H'|D^*A\rangle$ falls off with the third power of the distance R_{DA}, the exchange interaction falls of exponentially with R_{DA}

ble for the energy transfer between a given donor-acceptor pair involving transition metal complexes have appeared over the years [12], and quite often the conclusions with regard to the basic question regarding the nature of the interaction are nothing but unambiguous.

Likewise, a large number of studies treat so-called energy migration [13], that is the energy transfer between chemically identical chromophores in concentrated solids. Such energy migration, schematically shown in Fig. 2, is most efficient if a substantial fraction of the intensity of the relevant electronic transition is in the zero-phonon line. Even then, due to the inhomogeneous broadening, nearest neighbour pairs as a rule are not truly resonant with each other. Truly resonant chromophores are normally spatially separated by a comparatively large distance. As a result, energy migration is usually a phonon-assisted process, that is, it occurs between nearest neighbours, which are not necessarily resonant with each other and lattice phonons

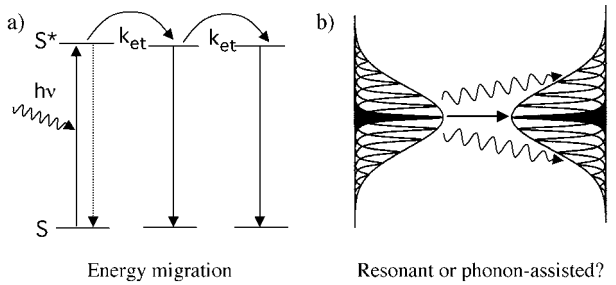

Fig. 2 **a** Energy migration, that is multi-step energy transfer between chemically identical chromophores. **b** Within the inhomogeneous distribution it can proceed via an resonant process (*straight arrow*) or via a phonon-assisted process whereby the energy mismatch between the donor and the acceptor is made up by lattice phonons (*curly arrows*)

serve as thermal bath making up for the energy mismatch [14]. Nevertheless, the elusive resonant process, for instance in ruby (Al_2O_3:Cr^{3+}), has aroused the continued interest of many researchers over the years [15].

In our contribution to this issue of Topics in Current Chemistry we present a model system in the form of a three-dimensional network structure, in which, by judicious combination of well known chromophores in transition metal coordination chemistry, we can unambiguously distinguish between exchange interaction and dipole-dipole interaction for the energy transfer between a specific donor-acceptor pair, and in which, at higher donor concentrations, we can just as unambiguously distinguish between resonant and phonon-assisted energy migration.

2 The Model System

2.1 The Three-Dimensional Oxalate Network Structure

The two transition metal complexes, $[Cr(ox)_3]^{3-}$ and $[Cr(bpy)_3]^{3+}$ (ox=oxalate, bpy=2,2′-bipyridine) depicted in Fig. 3a are well known chromophores in transition metal photochemistry and photophysics. In the three-dimensional oxalate network structure of composition $[Cr(bpy)_3][NaCr(ox)_3]ClO_4$, the two can be combined in an unique manner [16]. The sodium ions, in fact, serve as glue in such a way that each oxalate ligand serves as bridging

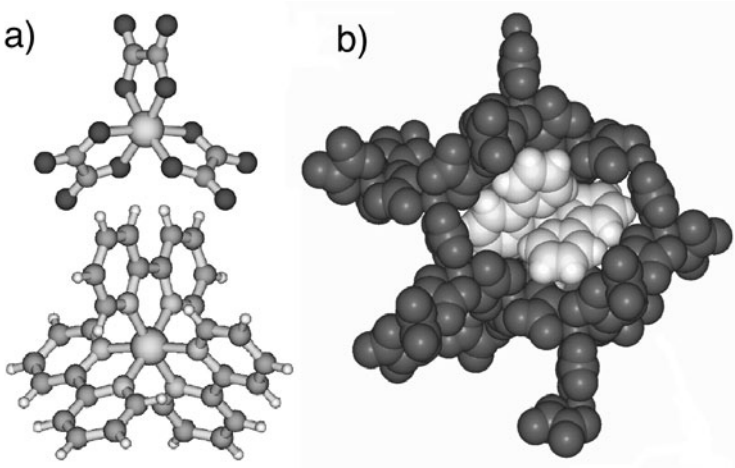

Fig. 3 **a** The building blocks $[Cr(ox)_3]^{3-}$ and $[Cr(bpy)_3]^{3+}$. **b** Space-filling model of the three-dimensional oxalate network (*dark*) encapsulating the tris-bipyridine cation (*light*) as in $[NaCr(ox)_3][Cr(bpy)_3]ClO_4$

ligand between a chromium ion and a sodium ion. The resulting three-dimensional metal-tris-oxalate network is stabilised by the metal-tris-bipyridine cations which fit neatly into the cavities provided by the negatively charged oxalate backbone. This is shown in the space-filling model of Fig. 3b. The crystals belong to the chiral cubic space group $P2_13$, the site symmetry of both chromophores is C_3, that is, the molecular trigonal axis is retained in the solid state. The chromium and the sodium ions on the oxalate backbone are perfectly ordered in an alternating fashion. Thus the chromium ions are never directly bridged by an oxalate ligand. Exchange interactions between chromium ions on the oxalate backbone are thus virtually non-existent. Weak exchange interactions between $[Cr(ox)_3]^{3-}$ and $[Cr(bpy)_3]^{3+}$ as a result of π-π stacking, however, cannot be excluded for $[Cr(bpy)_3][NaCr(ox)_3]ClO_4$.

2.2 The Absorption Spectrum of $[Cr(bpy)_3][NaCr(ox)_3]ClO_4$

The low-temperature single crystal absorption spectrum of $[Cr(bpy)_3][NaCr(ox)_3]ClO_4$ shown in Fig. 4 is basically a superposition of the spectra of the individual chromophores, as reported in [17] for $[Cr(ox)_3]^{3-}$ and in [18] for $[Cr(bpy)_3]^{3+}$. According to the Tanabe-Sugano diagram for a system with three d electrons in an octahedral environment [19] and by comparison with the known absorption spectrum of $[Cr(ox)_3]^{3-}$, the broad band centred at 18300 cm^{-1} can be assigned to the spin-allowed ligand-field transition $^4A_2(t_{2g}^3) \rightarrow {}^4T_2(t_{2g}^2 e_g^1)$. The sharp doublet at 14400 cm^{-1} (694.3 nm) corresponds to the spin-flip transition $^4A_2(t_{2g}^3) \rightarrow {}^2E(t_{2g}^3)$. It is exactly at the same energy as the famous R lines of ruby, that is Al_2O_3 doped with Cr^{3+} [20]. With an oscillator strength of $\sim 10^{-6}$ the intensity is basically of electric dipole origin, as expected for a non-centrosymmetric complex. As schematically shown in Fig. 5, the splitting is due to the combined effect of spin-orbit coupling and the trigonal ligand field inherent to tris-chelate complexes. For $[Cr(ox)_3]^{3-}$ this so-called zero-field splitting of the ^2E state is 16 cm^{-1}, which is somewhat smaller than the 29 cm^{-1} of ruby. Similarly, the sharp doublet at 13720 cm^{-1} (723 nm) can be assigned to the $^4A_2 \rightarrow {}^2E$ spin-flip transition of the $[Cr(bpy)_3]^{3+}$ chromophore. This is slightly lower in energy than the one for $[Cr(ox)_3]^{3-}$ due to the fact that the nephelauxetic effect and thus the reduction of the electron-electron repulsion as compared to the free ion is stronger for bipyridine than for oxalate. With a value of 13 cm^{-1}, the zero-field splitting of the ^2E state of $[Cr(bpy)_3]^{3+}$ is within the range observed for this chromophore in different environments [18, 21]. The spin-allowed $^4A_2 \rightarrow {}^4T_2$ transition of $[Cr(bpy)_3]^{3+}$ on the other hand is at higher energy than the one for $[Cr(ox)_3]^{3-}$ because, according to the spectrochemical series, the ligand-field strength of bipyridine is substantially larger than the one of oxalate. As a result, the total oscillator strength of $\sim 1.4 \times 10^{-7}$ of the

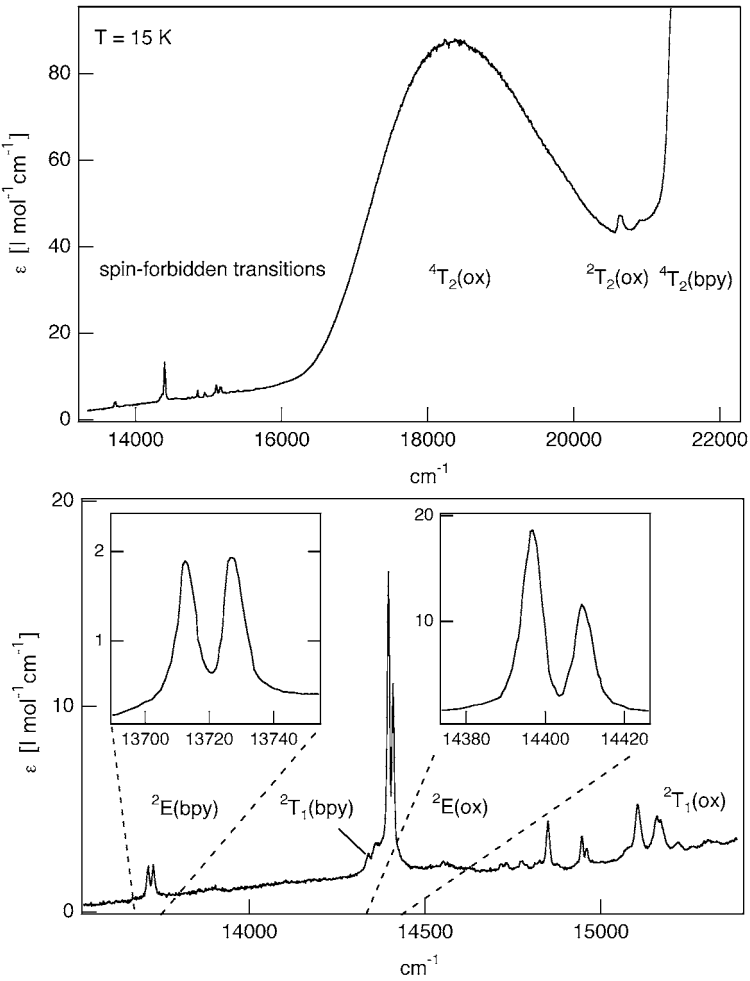

Fig. 4 Single crystal absorption spectra of $[NaCr(ox)_3][Cr(bpy)_3]ClO_4$ at 15 K (adapted from [16])

spin-flip transition for $[Cr(bpy)_3]^{3+}$ is smaller than the one for $[Cr(ox)_3]^{3-}$, because the energy difference to the $^4A_2 \rightarrow {}^4T_2$ transition from which the intensity of the spin-forbidden transition is borrowed is substantially larger for the latter. Nevertheless, it is still predominantly electric dipole intensity [18]. For both $^4A_2 \rightarrow {}^2E$ transitions, more than 90% of the total intensity is concentrated in the electronic origins, as expected for a spectral transition between states involving minimal differences in equilibrium nuclear geometry.

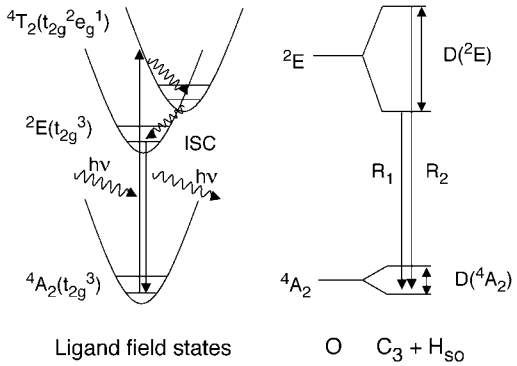

Fig. 5 Configurational coordinate diagram for a d^3 system in octahedral symmetry including the ground state and the first two excited ligand-field states (*left*), and zero-field splittings of the $^2A_2$ ground state and the ^2E state under the combined influence of spin-orbit coupling and the C_3 symmetry (*right*). ISC: intersystem crossing

2.3
Emission Spectra of $[Cr(bpy)_3]^{3+}$ and $[Cr(ox)_3]^{3-}$ in $[Rh(bpy)_3][NaAl(ox)_3]ClO_4$

As the starting point for the discussion of energy transfer processes, the luminescence properties of the unperturbed chromophores have to be determined. This has to be done by doping them at low concentration into an isostructual host-lattice using cations which are photophysically inert in the spectral region of interest, as for instance $[Rh(bpy)_3][NaAl(ox)_3]ClO_4$. Accordingly, Fig. 6 shows the low-temperature luminescence spectra of the two chromophores doped into the above host lattice. The two emission spectra

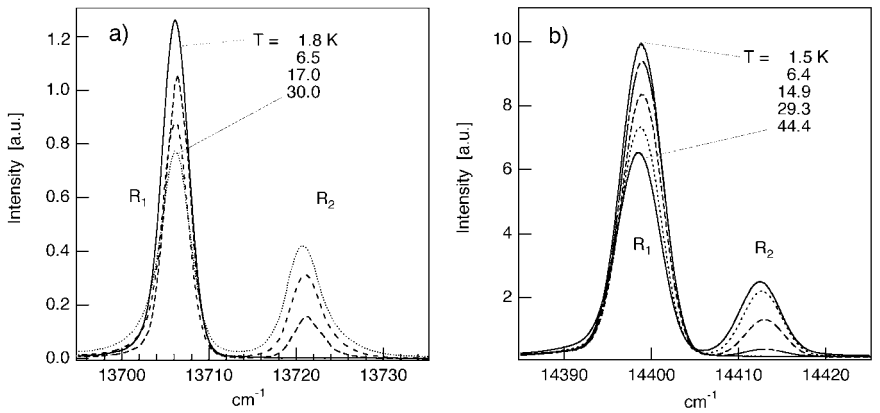

Fig. 6a, b Luminescence spectra of diluted systems: **a** $[NaAl(ox)_3][Rh_{1-y}Cr_y(bpy)_3]ClO_4$ (y=0.5%, excitation at 457.5 nm); **b** $[NaAl_{1-x}Cr_x(ox)_3][Rh(bpy)_3]ClO_4$ (x=1%, excitation at 514.5 nm)

are superimposable with the respective absorption spectra in the region of the $^4A_2 \rightarrow {}^2E$ transitions. The temperature dependence clearly shows the expected behaviour with almost all the intensity in the electronic origins following the prediction of a Boltzmann distribution between the two ^2E components. The luminescence decay times at 1.5 K of 1.3 ms for $[Cr(ox)_3]^{3-}$ and 5.2 ms for $[Cr(bpy)_3]^{3+}$ are in accordance with the observed oscillator strengths and may thus be considered the natural lifetimes of the ^2E states of the two chromophores, the quantum efficiency of the luminescence of the isolated chromophores below ~50 K being close to unity.

Below 10 K, the bandwidths of the R lines are approximately 4 cm^{-1}, corresponding to the so-called inhomogeneous linewidth Γ_{inh}, which is orders of magnitude larger than the homogeneous linewidth Γ_{inh} at cryogenic temperatures. The inhomogeneous broadening is due to imperfections in the crystal lattice, as a result of which the transition energies of the chromophores are distributed around an average value. It is also responsible for the fact that the zero-field splittings of the $^4A_2$ ground states into the $M_S=\pm1/2$ and $\pm3/2$ components are not resolved spectroscopically in the above absorption and emission spectra. In principle, ground-state zero-field splittings are accessible by EPR spectroscopy. However, so-called Fluorescence Line Narrowing (FLN) [22] by laser selective excitation provides an all optical technique to determine the ground-state zero-field splitting. The

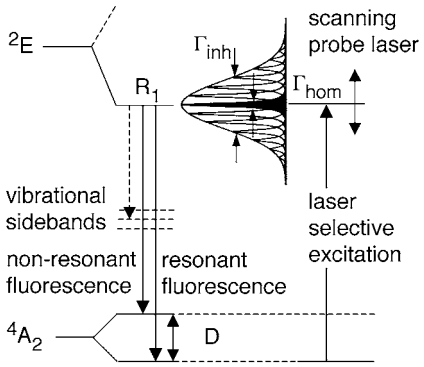

Fig. 7 The principle of fluorescence line narrowing using laser selective excitation exciting a subset of complexes within the inhomogeneously broadened electronic origin. In order to prevent laser light from the excitation source from entering the detection system, the excitation source is chopped at a comparatively high frequency and the luminescence light is only collected during the dark time of the excitation source. For transient spectral hole burning, a single frequency pump laser is kept at a fixed frequency keeping up a steady state population in the excited state. This spectral hole is probed by a second single frequency laser which is scanned across the corresponding spectral range. Detection can be either done by direct transmission or in an excitation type configuration using the vibrational side bands of the emission [10]

technique is well known in laser physics and its application to the photophysics of transition metal complexes has been extensively pioneered by Riesen et al. [23]. Figure 7 shows a schematic representation of how the technique is best applied to the chromium(III) complexes in question. As mentioned above, at cryogenic temperatures, the homogeneous linewidth Γ_{hom} of an electronic origin is usually much narrower than the inhomogeneous linewidth Γ_{inh}. A narrow band laser tuned to the electronic origin of interest thus selectively excites only a subset of chromophores within the inhomogeneously broadened band. In the absence of energy transfer processes, only these selectively excited chromophores emit light. They do so at the exact wavelength of the laser (resonant line) and shifted to lower energy by the zero-field splitting of the ground state (non-resonant line). In addition, there is a hot band symmetric to the central line, resulting in the typical three-line spectra recorded for the two chromophores at 1.5 K and shown in Fig. 8. The ground state zero-field splitting of $[Cr(ox)_3]^{3-}$ is 1.3 cm^{-1}, the one of $[Cr(bpy)_3]^{3+}$ is 0.8 cm^{-1}. These values are in agreement with previously reported values for the two complexes in a variety of different environments [17, 18, 21]. Previous experiments in magnetic fields have also shown that for both $[Cr(bpy)_3]^{3+}$ [18] as well as for $[Cr(ox)_3]^{3-}$ [24] the $M_S=\pm3/2$ is below the $M_S=\pm1/2$ component.

In the above FLN spectra the observed linewidth is limited by the spectral resolution of 0.3 cm^{-1} of the monochromator used for recording the spectra. However, at 1.5 K, the homogeneous linewidth, Γ_{hom}, is generally much smaller than this. It can in principle be resolved using a scanning Fabry-Perrot interferometer. Provided the linewidth of the laser is sufficiently small

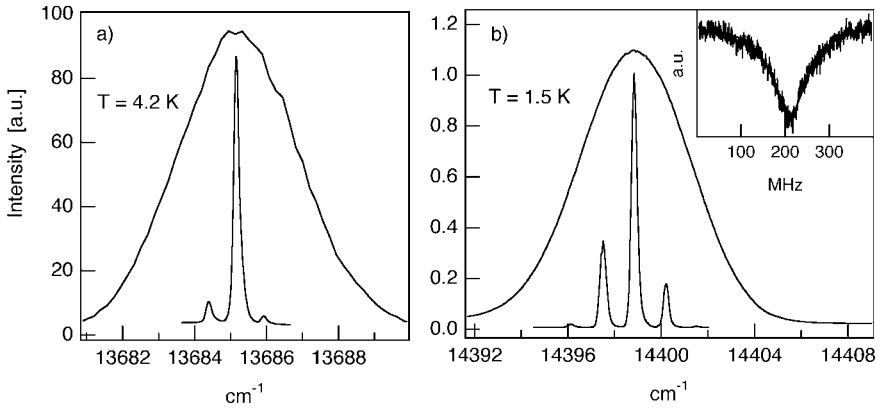

Fig. 8 **a** FLN spectrum of $[Rh_{1-y}Cr_y(bpy)_3][NaAl(ox)_3]ClO_4$, y=0.5%, at 4.2 K. **b** FLN spectrum of $[Rh(bpy)_3][NaAl_{1-x}Cr_x(ox)_3]ClO_4$, x=0.5%, at 1.8 K. *Insert*: transient hole burning spectrum at 1.5 K

and the finesse of the interferometer sufficiently high, the actually observed linewidth in the FLN experiment is given by [22]

$$\Gamma_{obs} = 2\Gamma_{hom} \tag{2}$$

Alternatively, the homogeneous linewidth can be determined by transient hole burning techniques. For such an experiment, a single frequency laser is tuned to the maximum of the broad band emission of $[Cr(ox)_3]^{3-}$. Already at low power, this laser keeps up a substantial steady state population of the low-energy component of the ^2E state. A scanning single frequency diode laser can then be used to probe this hole in an excitation spectrum detected in the vibrational side bands of the emission spectrum. As the laser scans across the hole, the emission intensity induced by the probing laser is reduced with respect to the intensity on either side of the hole. The inset of Fig. 8b shows a representative hole burning spectrum of $[Rh(bpy)_3][NaAl:Cr(0.5\%)(ox)_3]ClO_4$ recorded at 1.5 K. The line shape is well described by a pure Lorentzian with an observed linewidth Γ_{obs} of 41 MHz. This suggests a value for Γ_{hom} of ~20 MHz. This is a factor of 15 smaller than the previously reported upper limit as extracted from an FLN experiment on the same system at 1.8 K [25]. It is, however, of the same order as the value reported at 2.5 K for the same chromophore doped into a different crystalline host lattice [26]. The homogenous linewidth is given by [22]

$$\Gamma_{hom} = \frac{1}{2\pi T_1} + \frac{1}{\pi T_2^*} \tag{3}$$

where T_1 corresponds to the lifetime of the states involved in the transition, and T_2^* is the pure dephasing time given by quasielastic scattering of phonons and other types of interactions of the dopant with the environment. According to Riesen et al. [26], at 1.5 K the contribution of the lifetime of the excited state as well as thermalization between the zero-field split components of the $^4A_2$ ground state to the homogeneous linewidth of the R_1 line of $[Cr(ox)_3]^{3-}$ are negligible. The residual linewidth at this temperature is thought to be due to dephasing as a result of electron spin-spin interactions, and hyperfine and superhyperfine interactions with the ligand atoms and the host. Indeed at higher chromium concentrations the spin-spin interactions are expected to become dominant (see below).

In addition to the increase in homogeneous linewidth, at higher concentrations of chromophores, excitation energy transfer processes, for instance from $[Cr(ox)_3]^{3-}$ as donor to $[Cr(bpy)_3]^{3+}$ as acceptor, as well as energy migration within the ^2E state of $[Cr(ox)_3]^{3-}$ become important. These two processes are to be discussed in some detail in the following two sections of this review.

3
Energy Transfer: Dipole-Dipole vs Exchange Interaction

Figure 9a shows the emission spectra of co-doped $[Rh_{1-y}Cr_y(bpy)_3][NaAl_{1-x}Cr_x(ox)_3]ClO_4$ at 1.5 K for x=1% and y between 0 and 2.5%. Despite the fact that at the excitation wavelength of 568 nm only the $[Cr(ox)_3]^{3-}$ chromophores are excited, quite strong luminescence from the ^2E state of $[Cr(bpy)_3]^{3+}$ is observed [27]. As schematically shown in Fig. 10, this luminescence is the result of excitation energy transfer from the ^2E state of

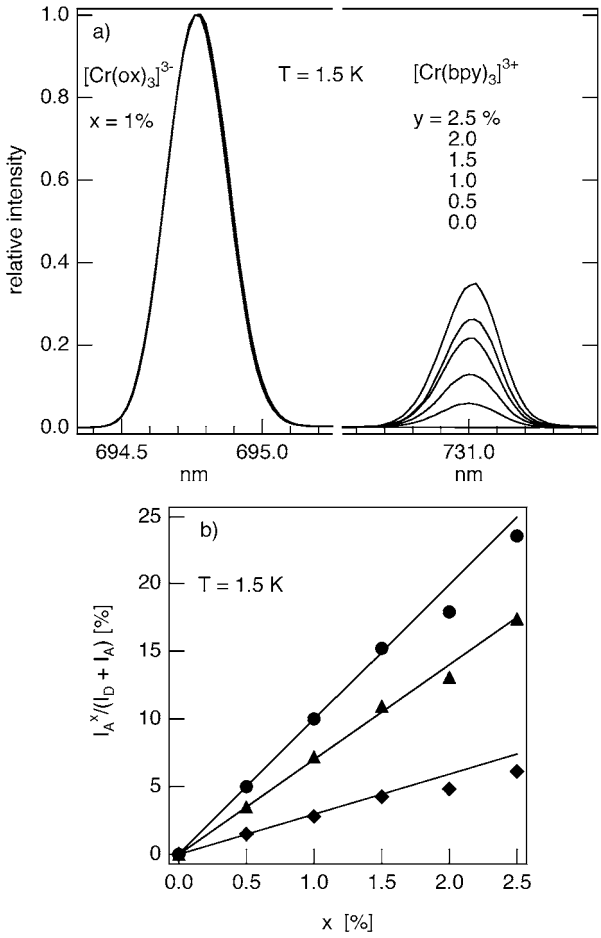

Fig. 9 **a** Luminescence spectra of $[Rh_{1-y}Cr_y(bpy)_3][NaAl_{1-x}Cr_x(ox)_3]ClO_4$ at 1.5 K, λ_{ex}=568 nm, x=1%, y=0–2.5%. **b** Quantum efficiency of the energy transfer as a function of acceptor concentration, (*filled circles*) total, (*filled triangles*) fast process, and (*filled diamonds*) slow process (adapted from [27])

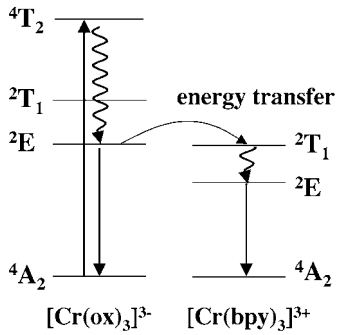

Fig. 10 Mechanism for the excitation energy transfer from $[Cr(ox)_3]^{3-}$ as donor to $[Cr(bpy)_3]^{3+}$ as acceptor in co-doped $[Rh_{1-y}Cr_y(bpy)_3][NaAl_{1-x}Cr_x(ox)_3]ClO_4$

$[Cr(ox)_3]^{3-}$ as donor to the $^2T_1$ state of $[Cr(bpy)_3]^{3+}$ as acceptor. For the case of intrinsic luminescence quantum efficiencies of close to unity for both donor and acceptor chromophores, the quantum efficiency of the energy transfer process can be calculated from the experimental spectra according to

$$\eta_{et}^{tot} = \frac{I_A}{I_A + I_D} \tag{4}$$

where I_D and I_A are the integrated luminescence intensities of the donor and the acceptor, respectively. Figure 9b shows the quantum efficiency of this energy transfer process as a function of acceptor concentration y. For y between 0 and 2.5%, it follows basically a straight line. This information alone is not sufficient to answer the question with regard to the type of interaction being responsible for the energy transfer process. The time evolution of the $[Cr(bpy)_3]^{3+}$ luminescence following pulsed excitation of $[Cr(ox)_3]^{3-}$ at 532 nm, given in Fig. 11a and b for the system with x=1% and y=0.5%, shows that in fact the energy transfer occurs with two very different rate constants. A fast process is responsible for the rise of the $[Cr(bpy)_3]^{3+}$ luminescence within less than 1 μs following the excitation pulse, a much slower process results in a risetime corresponding approximately to the intrinsic lifetime of the ^2E state of $[Cr(ox)_3]^{3-}$. Thus, as shown in Fig. 9b, the overall quantum efficiency of the energy transfer as function of acceptor concentration can be decomposed into a fast and a slow process:

$$\eta_{et}^{tot} = \eta_{et}^{fast} + \eta_{et}^{slow} \tag{5}$$

As schematised in Fig. 12, in the dilute co-doped systems, the distribution of donor and acceptor complexes is random. The actual rate constant of energy transfer for a given donor depends upon the distribution of accessible acceptors according to

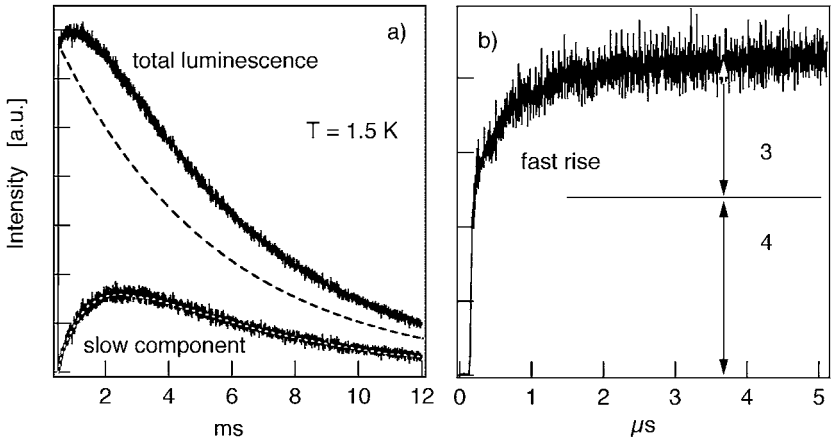

Fig. 11a, b Time-resolved luminescence intensity of $[Cr(bpy)_3]^{3+}$ following pulsed excitation of $[Cr(ox)_3]^{3-}$ in $[Rh_{1-y}Cr_y(bpy)_3][NaAl_{1-x}Cr_x(ox)_3]ClO_4$ at 1.5 K: **a** the decomposition of the total luminescence into the fast and the slow component of the energy transfer process, (*continuous line*) experimental, (*dashed line*) calc using the shell model; **b** rise of the fast component of the energy transfer (adapted from [27])

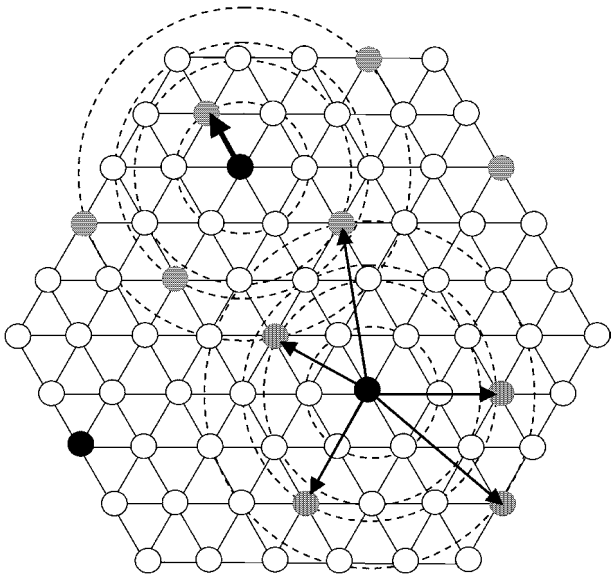

Fig. 12 Schematic representation of the fast and the slow component of energy transfer in the co-doped system. The *fat arrow* indicates a transfer process between a donor (*in black*) with an acceptor (*in grey*) in its nearest neighbour shell attributed to the fast component, the *thin arrows* indicate that for donors which do not happen to have an acceptor in the nearest neighbour shell, the energy transfer is less efficient

$$k_D^{et} = \sum_A w_{DA} \tag{6}$$

where w_{DA} is the energy transfer probability for a given donor-acceptor pair according to Eq. (1).

In a mixed-crystal system, k^{et} differs from donor to donor according to each donor's specific acceptor environment. The total quantum efficiency for energy transfer from the ensemble of donors is given by

$$\eta_{et}^{tot} = \frac{1}{N_D} \sum_D \frac{k_D^{et}}{k_D^{et} + k_D} \tag{7}$$

where the sum goes over all donors D. N_D is the total number of donors, and $k_D = 1/\tau_D$, that is, the intrinsic decay rate constant of the donor in the absence of acceptor complexes.

The fast rise in the $[Cr(bpy)_3]^{3+}$ luminescence can be attributed to energy transfer from those $[Cr(ox)_3]^{3-}$ chromophores which happen to have an acceptor complex within the shell of nearest neighbour sites, in which case the probability of an energy transfer process is close to unity. The slow component can be attributed to energy transfer from $[Cr(ox)_3]^{3-}$ chromophores which do not have an acceptor in the nearest neighbour shell, in which case the probability for an energy transfer process to occur within the natural lifetime of the ^2E state of $[Cr(ox)_3]^{3-}$ is less than unity. The fact that there is a more than three orders of magnitude difference between the rate constants of the two processes indicates that the nature of the interaction must be different, irrespective of the actual nature of the interaction!

For the dilute systems under consideration, that is for acceptor concentrations $y \leq 2.5\%$, the probability of finding one acceptor chromophore within the nearest neighbour shell is given by

$$p_1 \approx n_1 \cdot y \tag{8}$$

where n_1 is the number of potential acceptor sites in the shell. For $y \leq 2.5\%$, the probability of simultaneously finding two or more acceptors in the nearest neighbour shell is negligible. Theoretically the slope of the quantum efficiency for the fast component as a function of acceptor concentration is thus given by

$$\eta_{fast} \approx n_1 \cdot y \tag{9}$$

The corresponding curve in Fig. 9b yields an experimental value for n_1 of 7. This also makes sense from a structural point of view. The nearest neighbour shell around a given donor chromophore in the three-dimensional oxalate network does indeed contain seven sites. However, as shown in Fig. 13, they are not all crystallographically equivalent. One of the seven, with a metal-metal distance R_{DA} of only 6.1 Å, sits on the same trigonal axis as the do-

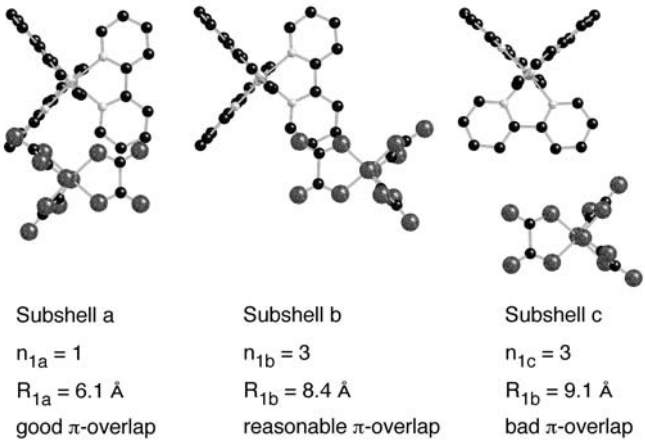

Fig. 13 Structural relationships between a given tris-oxalate complex and the tris-bipyridine complexes in its nearest neighbour shell (adapted from [27])

nor complex. In this case there are three direct contacts via π-π interactions between oxalate and bipyridine ligands due to pair wise parallel ligands with a ligand-ligand plane separation of ~3.45 Å. The next three neighbours with a metal-metal distance R_{DA} of 8.4 Å have one such direct contact with good π-π interaction. For the last three, the ligand planes of closest approach are orthogonal to each other and thus the interaction is expected to be smaller, despite the only slightly larger metal-metal distance R_{DA} of 9.1 Å. This is in line with the initial fast build-up of the $[Cr(bpy)_3]^{3+}$ luminescence, which can be separated into a very fast component with a risetime of less than 30 ns (limited by the time resolution of the set-up) and into a slightly slower, single exponential component with a risetime of 1 μs. The relative amplitudes of the two processes of 4:3 can be understood on the basis of the above discussion: the four nearest-neighbour sites with good π-π interaction are responsible for the very fast rise, the three nearest-neighbour sites with not so good π-π interaction are responsible for the second component.

As stated above, the nature of the interaction for the fast and the slow process must be different. The π-π interactions, although weak, provides the necessary overlap between donor and acceptor wavefunctions required for superexchange between nearest neighbour pairs. The order of magnitude of this interaction can be inferred from the FLN spectrum shown in Fig. 14 as recorded at 1.5 K with $[Rh_{1-y}Cr_y(bpy)_3][NaCr(ox)_3]ClO_4$ (y=0.5%) in the region of the $[Cr(bpy)_3]^{3+}$ luminescence. Although the $[Cr(bpy)_3]^{3+}$ chromophore is present at low concentrations, the spectrum shows far more than the typical three lines separated by the zero-field splitting of the $^4A_2$ ground state shown in Fig. 8a. This must be due to the interaction between the $[Cr(bpy)_3]^{3+}$ chromophore and its shell of $[Cr(ox)_3]^{3-}$ neighbours. It is be-

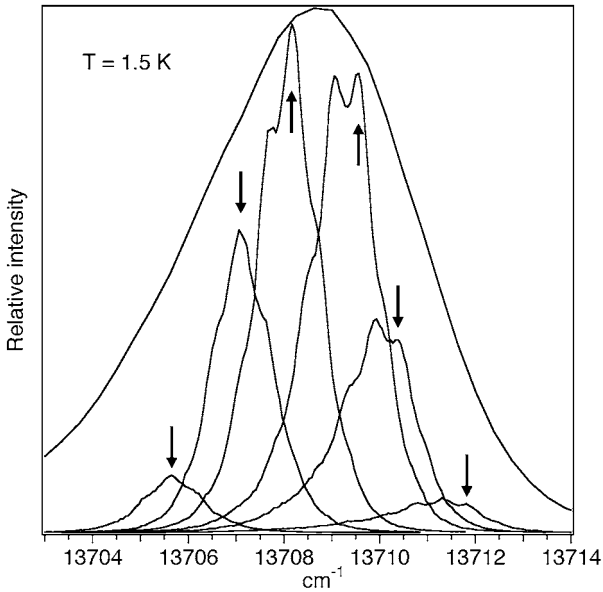

Fig. 14 FLN spectra of $[Rh_{1-y}Cr_y(bpy)_3][NaCr(ox)_3]ClO_4$ (y=0.5%) at 1.5 K in the region of $[Cr(bpy)_3]^{3+}$ R_1 line. The observed splitting does not correspond to the 0.8 cm^{-1} zero-field splitting of the ground state of $[Cr(bpy)_3]^{3+}$ (*arrows* indicate irradiation wavelengths)

yond the scope of this review to present a full analysis of this spectrum, but the splitting between adjacent peaks of ~0.5 cm^{-1} gives an indication of the magnitude of the strongest interaction, that is the one between $[Cr(bpy)_3]^{3+}$ and $[Cr(ox)_3]^{3-}$ sitting on the same trigonal axis. Weaker interactions with the other $[Cr(ox)_3]^{3-}$ complexes in the nearest neighbour shell and spin-spin relaxation processes are responsible for the asymmetry and the substantial broadening of the lines as compared to the fully dilute system. Exchange interaction energies of around 0.5 cm^{-1} or less are sufficiently large to explain the observed fast initial rise of less than 30 ns in the acceptor luminescence. From the above data it is not possible to actually extract a value for the exponential factor β usually associated with the distance dependence of the exchange interaction as indicated in Fig. 1b. In fact, the simple exponential dependence is only valid if otherwise the relative orientation between donor and acceptor does not change as a function of R_{DA}. In addition to the exponential factor, an important geometric factor has to be taken into consideration. In the present system, for instance, the interaction for the donor-acceptor pairs at R_{DA}=8.4 Å is at least a factor of ten larger than the one for pairs with only the slightly larger value of R_{DA}=9.1 Å. This is due to the much more favourable geometric factor for the overlap of donor and acceptor wavefunctions for the former.

As mentioned above, the slow component of the excitation energy transfer to $[Cr(bpy)_3]^{3+}$ is due to $[Cr(ox)_3]^{3-}$ complexes, which do not have an acceptor in the nearest neighbour shell, but do have acceptors in further shells. In this case superexchange can be ruled out as interaction mechanism because there is no reasonable pathway for an overlap of the relevant electronic wave functions. The most probable interaction is electric dipole-dipole interaction, for which the energy transfer probability according to Eq. (1) in SI units takes the form [10]

$$w_{DA} = \left(\frac{1}{4\pi\varepsilon_0}\right)^2 \left(\frac{3\hbar e^4}{4\pi n^4 m^2}\right) \times \frac{f_D f_A \Omega_{DA}}{R_{DA}^6 \nu_{DA}^2} \tag{10}$$

where f_D and f_A are the dimensionless oscillator strengths of the respective donor and acceptor transitions according to [28]

$$f = 4.32 \times 10^{-9} \int \varepsilon(\tilde{\nu}) d\tilde{\nu} \tag{11}$$

As before, R_{DA} is the metal-metal distance between the donor and acceptor pair in question, ν_{DA} is the frequency and $\tilde{\nu}_{DA}$ is the energy in wavenumbers at which the transfer takes place, and n is the refractive index of the material. As mentioned in the introduction, the spectral overlap integral, Ω_{DA}, of the normalised line shape functions, g_D and g_A, of the donor and the acceptor transitions, respectively takes care of energy conservation [10]

$$\Omega_{DA} = \int g_A(\tilde{\nu}) g_D(\tilde{\nu}) d\tilde{\nu} \tag{12}$$

The oscillator strength, f_D, and the radiative lifetime, τ_D^r, of the donor transition are related by [10]

$$f_D = \frac{1.5 g_e}{[(n^2+2)/3]^2 g_g n \tilde{\nu}_D^2 \tau_D^r} \tag{13}$$

where g_g and g_e are the electronic degeneracies of the ground state and the excited state of the donor, respectively.

With all this, Eq. (7) can be cast into the well-known form

$$w_{DA} = \frac{1}{\tau_D} \left(\frac{R_c}{R_{DA}}\right)^6 \tag{14}$$

with the definition of the critical radius [29]

$$R_c = \left(const \times \frac{f_A \Omega_{DA} \eta_D^r}{\tilde{\nu}_{DA}^4}\right)^{1/6} \tag{15}$$

The intrinsic lifetime of the donor state, τ_D, and the luminescence quantum efficiency, η_D^r, of the donor in the absence of any acceptors are related by

$$\eta_D^r = \frac{\tau_D}{\tau_D^r} \tag{16}$$

Expressing Ω_{DA} in [cm], τ_D in [s], $\tilde{\nu}$ in [cm^{-1}], and using the appropriate value of $n \approx 1.7$, to be considered typical for the organometallic systems under consideration [30], and setting the total ground state degeneracy $g_a=4$, and the excited state degeneracy for the R_1 line $g_b=2$, *const* takes on a value of $\sim 10^{31}$ for R_c expressed in [Å]. The significance of the critical radius is that for R_{DA} equal to R_c, the probability for an energy transfer process to occur is equal to the probability for intrinsic decay of the donor.

In principle, R_c can be estimated from spectroscopic data, provided the relevant parameters can be determined with sufficient accuracy. For the postulated resonant energy transfer from the ^2E state of $[Cr(ox)_3]^{3-}$ to the $^2T_1$ state of $[Cr(bpy)_3]^{3+}$, the luminescence quantum efficiency of the donor transition at 1.5 K is close to unity and therefore τ_D is equal to the corresponding radiative lifetime of 1.3 ms. From the absorption spectrum of Fig. 4, it can be deduced that it is not actually the electronic origin of the $^4A_2 \rightarrow {}^2T_1$ transition of $[Cr(bpy)_3]^{3+}$ which is resonant with the $[Cr(ox)_3]^{3-}$ emission but rather it is a vibrational side band, for which it is not quite as straightforward to estimate the corresponding oscillator strength. However, by comparison with the absorption spectrum of the compound $[Cr(bpy)_3](PF_6)_2$ [18], the vibrational side band with maximum overlap has an extinction coefficient $\varepsilon < \sim 0.5$ l mol^{-1} cm^{-1} and a halfwidth $\Delta\tilde{\nu}_{1/2}$ of the order of 10 cm^{-1}, and therefore $f \approx 2 \times 10^{-8}$. With a homogeneous linewidth of the purely electronic donor transition of 20 MHz (0.0001 cm^{-1}) and considering the above mentioned halfwidth of 10 cm^{-1} to be typical for the homogeneous width of a vibronic transition, the spectral overlap integral Ω_{DA} takes on a value of the order of 10^{-1} cm [10]. With these values, R_c can be estimated to be approximately 10 Å.

Alternatively, R_c can be determined from experiment. By using Eqs. (7) and (14) and by summing over all but the nearest neighbour shell $i \geq 2$, the quantum efficiency for the slow component can be expressed as

$$\eta_{et}^{slow} = y \cdot \sum_{i \geqslant 2} n_i \frac{\left(R_{DA}^i / R_c\right)^6}{1 + \left(R_{DA}^i / R_c\right)^6} \tag{17}$$

where y is the acceptor concentration, n_i the number of acceptor sites in shell i around a given donor and R^i_{DA} is the donor-acceptor separation for shell i. As before, for low acceptor concentrations multiple occupancies have been neglected in Eq. (17). At low acceptor concentrations, Eq. (17) predicts

Table 1 Structural parameters and corresponding contributions to the dipole-dipole energy transfer rate constants k_{et}^{D} for the slow rise to the $[Cr(bpy)_3]^{3+}$ luminescence calculated by using Eq. (6) with R_c=10.6 Å for the three next-nearest shells of acceptor sites

Shell	Range of R_{DA} in group (Å)	Number of sites	Average R_{DA} (Å)	k_{et}^{D} (s^{-1})
1	6.1–9.1	7	8.4	not appl.
2	12.84–13.8	9	13.3	197
3	17.15–18.1	15	17.5	38
4	19.6–20.95	22	20.5	15

a linear increase of η_{et}^{slow} with increasing acceptor concentration, in agreement with experiment. Small deviation of the experimental points from the linear behaviour towards y=2.5% can be attributed to multiple occupancies. From the known structural data shown in Table 1, the sum can be evaluated explicitly for any given value of R_c. Or conversely, from the slope of η_{et}^{slow} vs y, R_c can be obtained by solving Eq. (17) implicitly. This gives a value of R_c of 10.6 Å, which is in perfect agreement with the above estimate. This value, in turn, can be used to actually calculate the build-up and decay of the slow component according to the simple shell model [31]. As shown in Fig. 11a, the calculated curve for the slow process agrees well with the experimental one.

In conclusion, on the basis of the good agreement between the experimental and theoretical results, the slow rise of the $[Cr(bpy)_3]^{3+}$ luminescence can thus be unambiguously attributed to a dipole-dipole mechanism involving acceptors at distances between 12.5 and 21 Å, having no reasonable pathway for superexchange. The fast rise, which is three orders of magnitude faster, is attributed to energy transfer from $[Cr(ox)_3]^{3-}$ having a $[Cr(bpy)_3]^{3+}$ acceptor in the nearest neighbour shell and the small but non-negligible exchange coupling between the two.

4 Energy Migration: Resonant and Phonon-Assisted Processes

Energy migration is a common enough phenomenon for systems with high concentrations of the photosensitizer. Usually this results in a quenching of the sensitizer luminescence due to the presence of so-called killer traps in the form of unavoidable impurity centres. That energy migration within the ^2E state of $[Cr(ox)_3]^{3-}$ actually occurs in the three-dimensional networks of composition $[Rh_{1-y}Cr_y(bpy)_3][NaAl_{1-x}Cr_x(ox)_3]ClO_4$ is demonstrated by the effective quantum efficiency of energy transfer to $[Cr(bpy)_3]^{3+}$ as function of the donor concentration x at constant acceptor concentration y=0.5% shown in Fig. 15.

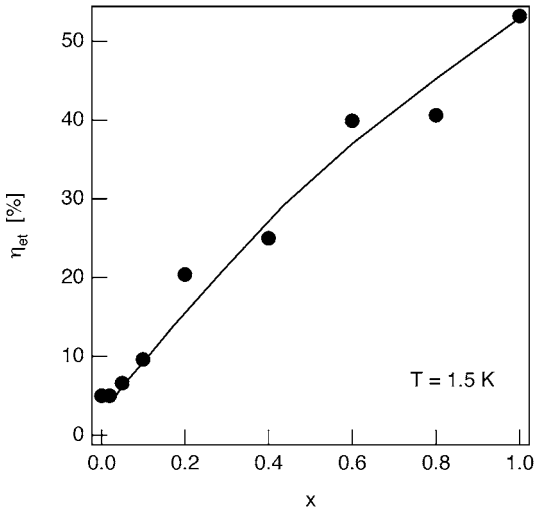

Fig. 15 Quantum efficiency of energy transfer in the mixed crystal series $[Rh_{1-y}Cr_y(bpy)_3][NaAl_{1-x}Cr_x(ox)_3]ClO_4$ (y=0.5%) at 1.5 K as a function of donor concentration x (adapted from [27])

Without energy migration between the donor chromophores, this quantum efficiency would not depend on x and just stay at the value of 5% as found for low donor concentrations. Instead, the quantum efficiency of the energy transfer increases rapidly with increasing donor concentration. With regard to Fig. 2b discussed in the introduction, the question as to the mechanism arises, that is, is this process resonant or phonon-assisted. More specifically, does an excited complex transfer its energy to the nearest neighbour, with which it is not necessarily resonant due to the inhomogeneous distribution of excitation energies, or does it prefer to look around in the lattice for a chromophore with which it happens to be resonant within its homogeneous linewidth? This question had best be answered by the FLN technique. If the process is resonant, an FLN spectrum should show narrowed features, if it is phonon-assisted the narrowing is lost due to the spectral diffusion into the inhomogeneously broadened line. Figure 16 shows the corresponding FLN spectra of the R_1 line of the ^2E state of $[Cr(ox)_3]^{3-}$ in neat $[Rh(bpy)_3][NaCr(ox)_3]ClO_4$, with the excitation wavelength tuned slightly to the high-energy side of the inhomogeneous distribution [25].

At 4.2 K the spectrum does not show any narrowed features, that is at 4.2 K, energy migration is dominated by the phonon-assisted process in accordance with previous observations on chromium(III) containing systems [14]. As the temperature is lowered to 1.8 K, sharp features appear in the FLN spectrum. Such sharp features are indicative of energy selective and thus of resonant processes. However, the spectrum observed at 1.8 K with its

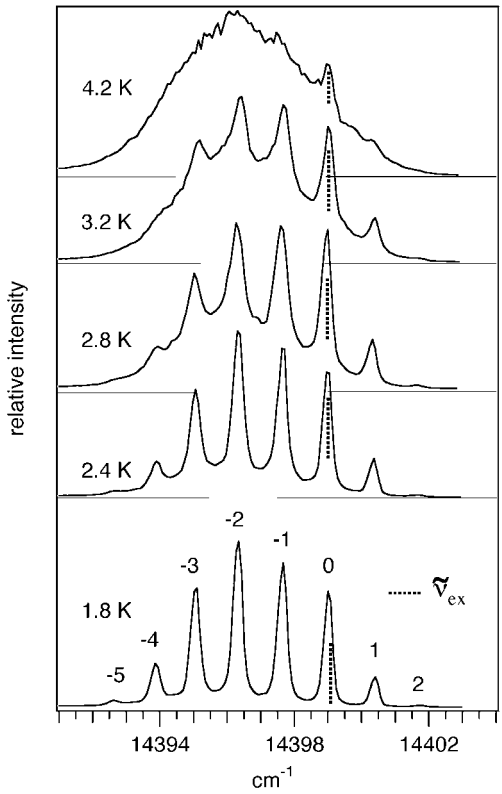

Fig. 16 Steady state fluorescence line narrowing in neat $[Rh(bpy)_3][NaCr(ox)_3]ClO_4$ as a function of temperature between 1.8 and 4.2 K (adapted from [25])

eight sharp lines is very different from the characteristic three-line spectrum of isolated $[Cr(ox)_3]^{3-}$ chromophores. Figure 17 schematically shows how in a series of resonant processes the multiline spectrum comes about. The initially excited complex can transfer its energy resonantly either at exactly the excitation energy, that is by going back to the $M_S=\pm 3/2$ component of the ground state, or at an energy which is smaller by the zero-field splitting of the ground state, D=1.3 cm^{-1}, by going to the $M_S=\pm 1/2$ component. In the latter case, a complex within the inhomogeneous distribution for which the transition from the $M_S=\pm 3/2$ component is resonant may act as acceptor. This complex will then emit light either at the same energy or at an energy which is now 2D from the excitation wavelength. Conversely, it may in turn act as donor for a further resonant energy transfer step to an acceptor for which the $M_S=\pm 3/2$ component of the R_1 transition is resonant with its $M_S=\pm 1/2$ component. As a result of these sequential steps, there is an energy selective ladder of excited complexes within the inhomogeneous distribu-

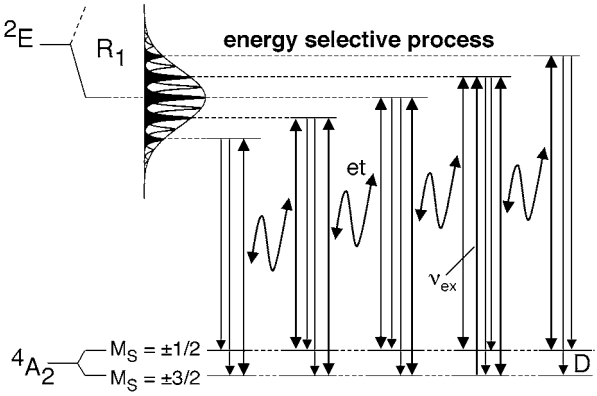

Fig. 17 Scheme for the resonant energy migration within the R_1 line of $[Cr(ox)_3]^{3-}$ in $[Rh(bpy)_3][NaCr(ox)_3]ClO_4$

tion, spaced by the zero-field splitting of the ground state. In addition, the fact that at 1.8 K there is a non-negligible thermal population of the $M_S=\pm1/2$ component of the ground state multiplet, results in hot bands at higher energy with respect to the excitation wavelength.

That the resonant energy transfer is indeed sequential is borne out by the time-resolved FLN spectra at 1.8 K shown in Fig. 18. Following a laser pulse of 4 μs, the spectrum initially consists of just the three lines expected for isolated $[Cr(ox)_3]^{3-}$ chromophores. As the delay between the pulse and the recording of the spectrum increases, more and more satellite peaks appear. The actual time-evolution of the individual peaks is shown in Fig. 19. The peak at the excitation wavelength decays within 0.5 ms, that is, substantially faster than the radiative lifetime of 1.3 ms observed for the isolated chromophores. The build-up of the satellite peaks is delayed, the maximum moving to longer and longer times for an increasing number of steps.

An important question to be addressed regards the nature of the interaction responsible for this resonant process. In $[Rh(bpy)_3][NaCr(ox)_3]ClO_4$ the chromium chromophores are separated by a sodium ion coordinated to the respective oxalate ligands. Thus there is no reasonable pathway for superexchange between them. The critical radius for dipole-dipole interaction on the other hand is quite large. It can be calculated using Eq. (15), with the $[Cr(ox)_3]^{3-}$ chromophore both as donor and as acceptor. The oscillator strength of the R_1 line of the $[Cr(ox)_3]^{3-}$ chromophore is straightforward to estimate from the absorption spectrum given in Fig. 4. It takes on a value of $\sim 6\times10^{-7}$. The spectral overlap integral for fully resonant species is given by

$$\Omega_{DA} = \int [g(\tilde{\nu})]^2 d\tilde{\nu} = \frac{1}{\pi\Gamma_{hom}} \tag{18}$$

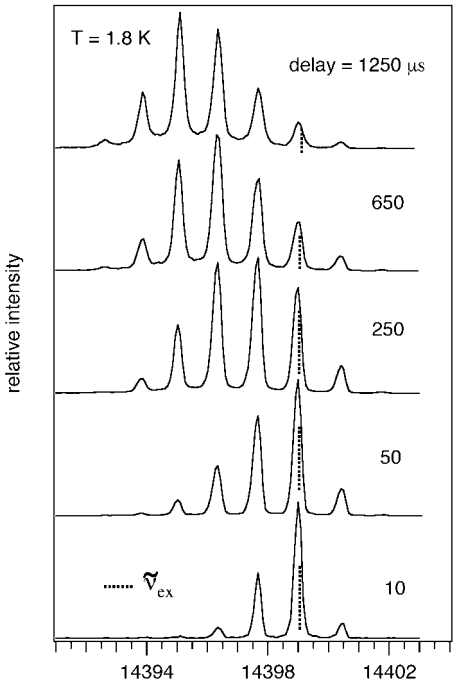

Fig. 18 Time-resolved FLN in $[Rh(bpy)_3][NaCr(ox)_3]ClO_4$ at T=1.8 K following pulsed excitation with a pulse width of 10 μs (adapted from [25])

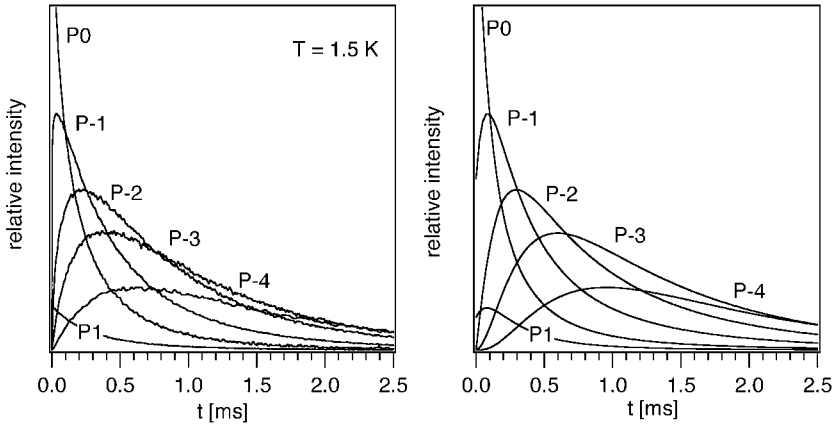

Fig. 19 **a** Temporal evolution of the FLN peaks in $[Rh(bpy)_3][NaCr(ox)_3]ClO_4$ shown in Fig. 18 at T=1.5 K. **b** Calculated curves using Eqs. (21) (adapted from [32]). The Pi number the peaks according to Fig. 16

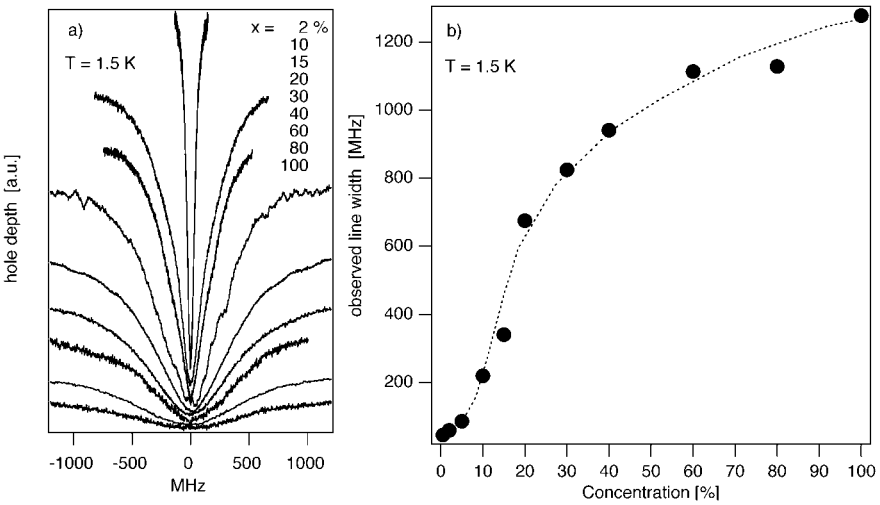

Fig. 20 **a** Transient hole burning spectra of $[Rh(bpy)_3][NaAl_{1-x}Cr_x(ox)_3]ClO_4$ at 1.5 K for different values of x. **b** The observed linewidth as a function of x

where $g(\tilde{\nu})$ is the Lorentzian line shape function with the corresponding homogeneous linewidth Γ_{hom}. As described above, the homogeneous linewidth for the dilute system with 0.5% $[Cr(ox)_3]^{3-}$ was found to be ~20 MHz (7×10^{-4} cm^{-1}). This value of Γ_{hom} would result in values for Ω_{DA} and R_c of ~500 cm and ~60 Å, respectively, as upper limits. However, as mentioned above, in the concentrated system the homogeneous linewidth is expected to be substantially larger than in the diluted system due to spin-spin relaxation. That this is indeed the case is borne out by the transient hole burning spectra shown in Fig. 20a, recorded at 1.5 K for different values of x between 0.5 and 100% in the mixed crystal series $[Rh(bpy)_3][NaAl_{1-x}Cr_x(ox)_3]ClO_4$. In Fig. 20b, the corresponding observed linewidths, Γ_{obs}, are plotted as a function of x. From the initial 40 Mz at x=0.5%, Γ_{obs} increases in a sigmoidal fashion to the limiting value of 1.25 GHz (0.04 cm^{-1}) at x=100%. As these spectra were recorded in a steady state type configuration, the 1.25 GHz do not necessarily correspond to twice the actual homogeneous linewidth, as resonant energy migration within one subset may result in additional broadening of the resonant line. It is however a good measure for the upper limit of $2\Gamma_{hom}$, and thus for high concentrations of $[Cr(ox)_3]^{3-}$, $\Gamma_{hom} \leq 0.02$ cm^{-1}. The corresponding values for Ω_{DA} and R_c of ~16 cm and ~34 Å, respectively, may thus be considered lower limits.

The theoretical value of R_c has to be compared to the mean minimal distance between resonant chromophores in the compound. In fact, it is not very probable that the condition of resonance within the homogeneous width of a given $[Cr(ox)_3]^{3-}$ chromophore is fulfilled by any of the nearest

neighbour chromophores. Rather, the concentration of resonant species, N_{res}, is quite small. At the maximum of the inhomogeneous distribution it is approximately given by

$$N_{res} = 2\frac{\Gamma_{hom}}{\Gamma_{inh}} N_{tot} \tag{19}$$

where N_{tot} is the total concentration of $[Cr(ox)_3]^{3-}$ sites. From crystallographic data N_{tot} takes on a value of 10^{21} cm^{-3}, and the experimental inhomogeneous linewidth for the system in question is ~4 cm^{-1}. The mean number of resonant chromophores within a volume of a sphere with radius R_c is given by

$$n_m = N_{res} \cdot \frac{4\pi}{3} R_c^3 \tag{20}$$

As N_{res} as well as R_c are functions of the homogeneous linewidth, n_m, too, can be expressed as a function of Γ_{hom}. This is shown in Fig. 21. Using the above value for Γ_{hom} of 0.02 cm^{-1} for the fully concentrated compound, the concentration of resonant species at the centre of the distribution $N_{res} \approx 10^{19}$ cm^{-3}. Together with the corresponding value of R_c of 34 Å, n_m takes on a value of ~1.7. This is sufficient to result in the observed quantum efficiency of the first transfer step for irradiation near the centre of the distribution of close to 90% as derived from the ratio of the resonant peak to the total luminescence intensity.

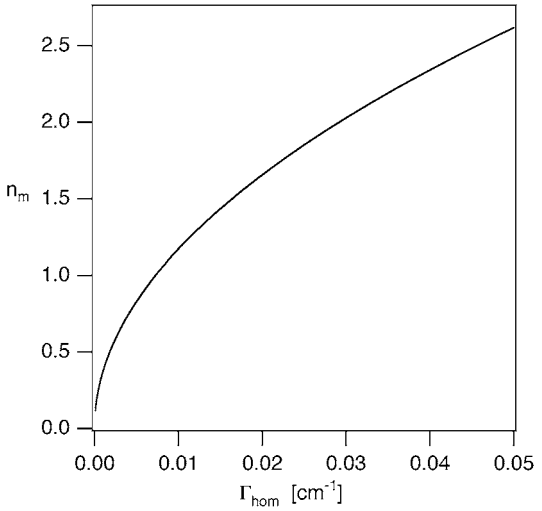

Fig. 21 The average number of resonant chromophores within a volume corresponding to a sphere with the Förster radius R_c as a function of the homogeneous linewidth

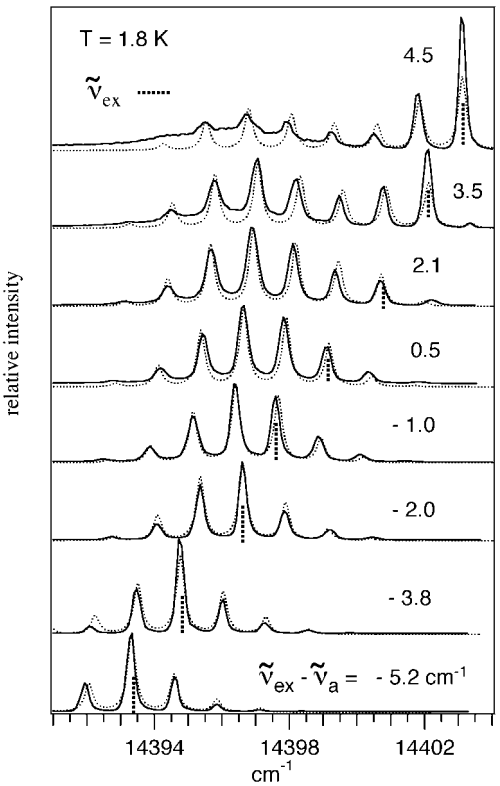

Fig. 22 FLN spectra of $[Rh(bpy)_3][NaCr(ox)_3]ClO_4$ at 1.8 K recorded for different excitation wavelengths across the inhomogeneous distribution: (*continuous lines*) experimental, (*dashed lines*) calculated. $\tilde{\nu}_a = 14400\,cm^{-1}$ indicates the central frequency of the absorption of the high-energy component of the R_1 line (adapted from [25])

The resonant process is most efficient at the centre of the inhomogeneous distribution because naturally the concentration of resonant species is higher than in the wings. Figure 22 shows the FLN spectra of $[Rh(bpy)_3][NaCr(ox)_3]ClO_4$ at 1.5 K for different irradiation wavelengths across the inhomogeneous distribution. Obviously, for irradiation on the low-energy side, the FLN spectrum resembles the three-line spectrum of the dilute system, basically because the concentration of resonant species in the low-energy wing is too low. In principle the situation for irradiation on the high-energy wing is similar. There is however a difference. For the transfer down the energy ladder more and more acceptors become available. Thus for irradiation into the high-energy wing there is an initial bottle neck, but as soon as this bottle neck has been bridged, the resonant migration becomes efficient again. This is very well exemplified by the FLN spectrum for irradiation at the highest energy shown in Fig. 22.

The FLN profiles of Fig. 22 can be modelled using a simple set of coupled rate equations of the form

$$\frac{dN_{ei}}{dt} = -N_{ei}[k_r + k_{et}(N_{ai-1} + N_{bi-1})] + k_{et}(N_{ei+1}N_{ai} + N_{ei-1}N_{bi}) + \delta_{0i}k_a^{ex}N_{ai} + \delta_{1i}k_b^{ex}N_{bi} \quad (21)$$

In Eq. (21), $k_r=k_a+k_b=1/\tau_r=770\ s^{-1}$ is the sum of the individual radiative rate constants for the two components of the R_1 line, k_a^{ex} and k_b^{ex} are the respective excitation rate constants, and N_e, N_a and N_b are the populations of the excited state and the two components of the ground state, respectively. k_{et} is the average bimolecular rate constant for energy transfer. "i" numbers the sets in the resonant ladder, i=0 being the one at which the excitation occurs from the lower component of the ground state. The δ function takes care of the fact that excitation occurs from the lower component of the ground state for i=0 and from i=1 for the hot bands originating from the thermal population of the higher energy component of the ground state. The set of coupled differential equations can be solved numerically, using the conditions that the laser power is low and assuming fast thermalization between the split components of the ground state. The concentration of resonant species at the centre of the inhomogeneous distribution is given by Eq. (19), and is scaled according to the measured absorption spectrum for the sets across the band. Figure 22 includes the corresponding simulated FLN spectra. Although the above procedure does not take care of the distribution of rate constants for the energy transfer steps, it reproduces the luminescence profiles to perfection using a value for the pseudo first order rate constant $k_{et}'=k_{et}N_{res}=10^4\ s^{-1}$. Likewise, the temporal evolution of the steps in the ladder is well described by the set of coupled rate equations (see Fig. 19). Only at short times after the pulse is there a systematic deviation of the calculated curves from the experimental ones. This is due to the fact that in the actual system the rate constants are distributed around some mean value, and thus there are always sites for which the energy transfer is much more rapid than the average value. This can, in principle, be taken care of by Monte Carlo methods, which allow for such a distribution in a perfectly straightforward way [31].

Figure 23 shows the FLN spectra of $[Rh(bpy)_3][NaAl_{1-x}Cr_x(ox)_3]ClO_4$ for different values of x and for irradiation just above the maximum of the inhomogeneous distribution. With decreasing values of x the concentration of resonant species decreases not only because of the obvious decrease in the total concentration of active chromophores but also due to the decrease in homogeneous linewidth. Nevertheless, the resonant energy transfer process is still observable at the comparatively low concentration of x=5%. That is, the decrease in concentration of resonant chromophores is at least partially compensated by a corresponding increase in R_c.

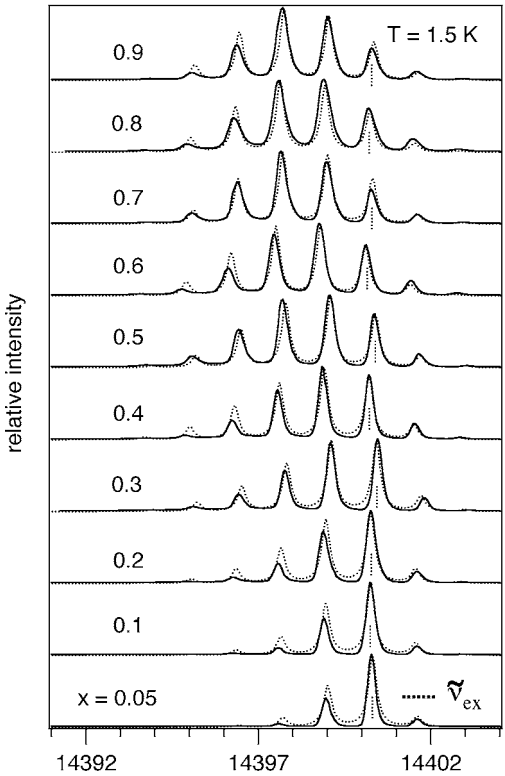

Fig. 23 FLN spectra of $[Rh(bpy)_3][NaAl_{1-x}Cr_x(ox)_3]ClO_4$ at 1.5 K for concentrations of x between 5 and 90%, (*continuous lines*) experimental, (*dotted lines*) calculated (adapted from [32])

What then are the requirements for the observation of the hitherto elusive resonant energy migration? Well, early work in the field was mostly performed on doped oxides, such as ruby. In these systems, energy migration was invariably found to be dominated by phonon-assisted processes with at most a very small resonant contribution [15]. The key difference between these doped systems and our stoichiometric compound is the fact that in our systems the concentration of chromophores can reach much higher levels without the interference of exchange coupling. The template synthesis results in the specific structure with a rigorous alternation of Na and Cr ions on the oxalate back-bone. In the doped oxide systems, the statistical distribution of Cr in the lattice results in exchange coupled pairs and clusters which serve as shallow traps for the excitation energy as soon as the doping level reaches sufficient levels for energy migration. Furthermore, in the three-dimensional oxalate network the relation between the inhomogeneous linewidth, the zero-field splitting of the ground state and the homogeneous

linewidth are optimal for the observation of the phenomenon, that is $\Gamma_{inh}>D>\Gamma_{hom}$.

Naturally there are a number of open questions with regard to the resonant energy migration within the R_1 line of the ^2E state of $[Cr(ox)_3]^{3-}$. a) What is the temperature dependence of the resonant process? As the homogeneous linewidth is temperature dependent, R_c as well as the concentration of resonant species are temperature dependent. This should accelerate the resonant process with increasing temperature. b) The FLN spectra only show the resonant process from one subset to another having a difference in their absorption energies corresponding to the zero-field splitting of the ground state. They do not give any information on the energy migration within the same subset of chromophores. This question could be addressed by following the time-evolution of the transient hole using pulsed excitation. c) What is the actual linewidth of the side bands? In principle it should become larger and larger with each transfer step. However, it can also become larger due to an inhomogeneous distribution of the zero-field splitting of the ground state.

5 Conclusions and Outlook

This chapter is not so much meant to be a general review of the important topic of excitation energy transfer in coordination compounds, it is much more meant to show how unambiguous answers to basic questions can be obtained from experimental results by choosing a well-defined model system and state-of-the-art spectroscopy. The three-dimensional oxalate networks thus well and truly constitute a model system with sufficient chemical flexibility to investigate a given process with the required variation of the relevant parameters.

In the mixed crystal system, $[Rh_{1-y}Cr_y(bpy)_3][NaAl_{1-x}Cr_x(ox)_3]ClO_4$, with $[Cr(ox)_3]^{3-}$ as donor and $[Cr(bpy)_3]^{3+}$ as acceptor for excitation energy transfer, it has been possible to quantitatively differentiate between an exchange mechanism for acceptors sitting in the nearest neighbour shell, and a dipole-dipole mechanism for acceptors at longer distances. In the stoichiometric compound $[Rh(bpy)_3][NaCr(ox)_3]ClO_4$, on the other hand, it has just as unambiguously been possible to distinguish between resonant and phonon-assisted energy migration within the R_1 line of the $[Cr(ox)_3]^{3-}$ luminescence. The key to understanding the mechanisms of these processes lies in the very special crystal structure of the three-dimensional oxalate networks.

The unique resonant energy migration in $[Cr(ox)_3]^{3-}$ is the result of the strictly alternating order of the sodium and the chromium ions on the oxalate backbone. This cuts off all exchange interactions between the chromium ions on the backbone even in the neat compound. Thus at temperatures

below 2 K, the long-range dipole-dipole interaction becomes important enough to result in the observed resonant process with a critical radius of the order of 34 Å, whereas at higher temperatures, the more common phonon-assisted process between nearest neighbours dominates.

The tris-bipyridine complexes on the other hand are encapsulated by the oxalate network. Thus in the co-doped systems a $[Cr(bpy)_3]^{3+}$ complex happening to sit in the first acceptor shell of a given donor is much closer to this donor than a $[Cr(bpy)_3]^{3+}$ complex sitting in the second shell. π-π overlap between ligand orbitals of the donor and an acceptor in the first shell ensure efficient energy transfer on the sub-microsecond timescale mediated by exchange interaction. Additionally, the relative orientation of donor and acceptor plays an important role for the π-π overlap. For acceptors further away, for which there is no exchange pathway, dipole-dipole interaction takes over. With a critical radius of the order of 11 Å, this is much less efficient and the overall quantum efficiency is thus less than unity.

Of course, the three-dimensional network structures can and have been used to look at other chromophores, and other donor-acceptor pairs. For instance, the well known chromophore $[Ru(bpy)_3]^{2+}$ has been used as photosensitizer to study energy transfer to $[Os(bpy)_3]^{2+}$ and $[Cr(ox)_3]^{3-}$ acting as acceptors [33], as well as light-induced electron transfer quenching by $[Fe(ox)_3]^{3-}$ and $[Co(ox)_3]^{3-}$ [34]. The compounds also have a certain interest for the field of molecular magnetism, where for various combinations of transition metal ions antiferromagnetic and ferrimagnetic phases have been reported [35]. And last but not least, the tight fit of the tris-bipyridine cation turned $[Co(bpy)_3]^{2+}$, which under normal circumstances is a so called high-spin complex, into a spin-crossover complex [36]. A hitherto unsolved challenge lies in the incorporation of photophysically active lanthanide ions into the oxalate networks.

Acknowledgements We thank N. Amstutz for the synthesis of the samples used in this study, and S. Decurtins and his co-workers for their help with the determination of the concentrations of donors and acceptors in the mixed crystals. We thank H. Riesen for helpful discussion in particular on the topic of FLN spectroscopy and spectral hole burning. Figure 3b is by courtesy of S. Decurtins. This work was financially supported by the Swiss National Science Foundation and NFP47.

References

1. Fejer MM, Injeyan H, Keller U (eds) (1999) Advanced solid state lasers. In: OSA trends in optics and photonics, vol 26. Optical Society of America, Washington
2. Jüstel T, Nikol H, Ronda C (1998) Angew Chem Int Ed 37:3084
3. Grätzel M (2001) Nature 414:338

4. a) Clegg RM (ed) (2002) Fluorescence resonance energy transfer in biology. In: Rev Mol Biotechnol 82:123, Elsevier, Oxford; b) Andrews DL, Demidov AA (eds) (1999) Resonance energy transfer. Wiley-VCH, New York
5. a) Searle GFW, Tredwell CJ, Barber J, Porter G (1979) Biochim Biophys Acta 545:496; b) Owens TG (1996) Adv Photosynth 5:1
6. DiBartolo B (ed) (1984) Energy transfer processes in condensed matter. In: Nato Advanced Studies Institutes Series B, vol 114. Plenum Press, New York
7. DiBartolo B, Chen X (eds) (2001) Advances in energy transfer processes. World Scientific Publishing, Singapore
8. Förster T (1948) Ann Phys 2:55
9. Dexter DL (1953) J Chem Phys 21:836
10. Henderson B, Imbusch GF (1989) Optical spectroscopy of inorganic solids. Clarendon Press, Oxford
11. a) Tanner PA (2004) Top Curr Chem 241 Yersin H (ed) Springer, Berlin Heidelberg New York, and references therein; b) Cavalli E, Bovero E, Belletti A (2002) J Phy Condens Matter 14:5221; c) Basiev TT, Orlovski MV, Papashvili AG, Doroshenko ME, Pelle F, Heber J (2001) J Lumin 94:123; d) Chua M, Tanner PA, Reid MF (1994) Solid State Commun 90:581; e) Basiev TT, Orlowski YV, Privis YS (1996) J Lumin 69:187
12. a) Tsushima M, Ikeda N, Yoshimura A, Nozaki K, Ohno T (2000) Coord Chem Rev 208:299; b) Furue M, Yoshidzumi T, Kinoshita S, Kushida T, Nozakura S, Kamachi M (1991) Bull Chem Soc Jpn 64:1632; c) Vögtle F, Frank M, Nieger M, Belser P, von Zelewski A, Balzani V, Barigelletti F, DeCola L, Flamigni L (1993) Angew Chem 105:1706; d) DeCola L, Balzani V, Barigelletti F, Flamigni L, Belser P, von Zelewski A, Frank M, Vögtle F (1993) Inorg Chem 32:5228; e) Belser P, von Zelewski A, Frank M, Seel C, Vögtle F, DeCola L, Barigelletti F, Balzani V (1993) J Am Chem Soc 115:4076; f) Juris A, Balzani V, Campagna S, Denti G, Serroni S, Frei G, Güdel HU (1994) Inorg Chem 33:1491; g) Barigelletti F, Flamigni L, Balzani V, Collin JP, Sauvage JP, Sour A, Constable EC, Cargill Thompson AMW (1994) Coord Chem Rev 132:209; h) Schlicke B, Belser P, DeCola L, Sabbioni E, Balzani V (1999) J Am Chem Soc 121:4207; i) Scandola F, Bignozzi CA, Chiorbelli C, Indelli MT, Rampi MA (1990) Coord Chem Rev 97:299; k) Bignozzi CA, Bortolini O, Chiorbelli C, Indelli MT, Rampi MA, Scandola F (1992) Inorg Chem 31:172; l) Otsuka T, Kaizu Y (1997) Chem Lett 79; m) Yersin H, Kratzer C (2002) Coord Chem Rev 229:75
13. a) Yatskou M, Meyer M, Huber S, Pfenniger M, Calzaferri G (2003) Chem Phys Chem 4:567; b) Blasse G (1987) In: NATO ASI Series, Series C 214: Mathematical and Physical Sciences, pp 355–370; c) Fleming CN, Maxwell KA, DeSimone JM, Meyer TJ, Papanikolas, John M (2001) J Am Chem Soc 123:10336; d) Chua M, Tanner PA (1999) Chem Phys 250:267
14. a) Holstein T, Lyo SK, Orbach R (1976) Phys Rev Lett 36:891; b) Selzer PM, Hamilton DS, Yen WM (1977) Phys Rev Lett 38:858; c) Selzer PM, Huber DL, Barnett BB, Yen WM (1978) Phys Rev B 17:4979
15. a) Chu S, Gibbs HM, McCall SL, Passner A (1980) Phys Rev Lett 45:1715; b) Jessop PE, Szabo A (1980) Phys Rev Lett 45:1712; c) Imbusch GF (1992) J Lumin 53:465; d) Imbusch GF (1985) In: DiBartolo B (ed) Energy transfer in condensed matter, NATO ASI Serie B 114, p 471. Plenum Publishing Corporation
16. Decurtins S, Schmalle HW, Pellaux R, Schneuwly P, Hauser A (1996) Inorg Chem 35:1451
17. Schönherr T, Spanier J, Schmidtke HH (1989) J Phys Chem 93:5969
18. Hauser A, Mäder M, Robinson WT, Murugesan R, Ferguson J (1987) Inorg Chem 26:1331

19. Sugano S, Tanabe Y, Kamimura H (1970) Pure and applied physics 33. Academic Press, New York London
20. Imbusch GF, Yen WM (1987) In: Yen WM, Levenson MD (eds) Lasers, spectroscopy and new ideas. Springer Series in Optical Sciences 54. Springer, Berlin Heidelberg New York, p 248
21. a) Riesen H (1992) J Lumin 54:71; b) Riesen H, Krausz E (1992) J Chem Phys 97:7902
22. a) Yen WM, Selzer PM (eds) (1981) Laser spectroscopy of solids. Applied Physics 49, Springer, Berlin Heidelberg New York; b) Moerner WE (ed) (1988) Persistent spectral hole burning. Top Curr Phys 44, Springer, Berlin Heidelberg New York
23. a) Riesen H, Krausz E (1993) Comm Inorg Chem 14:323; b) Krausz E, Riesen H (1999) In: Solomon EI, Lever ABP (eds) Inorganic electronic structure and spectroscopy I. Wiley, New York, p 307
24. Lahiry S, Kakkar R (1982) Chem Phys Lett 88:499
25. von Arx ME, Hauser A, Riesen H, Pelaux R, Decurtins S (1996) Phys Rev B 54:15800
26. Lewis ML, Riesen H (2002) J Phys Chem A 106:8039
27. Langford VS, von Arx ME, Hauser A (1999) J Phys Chem A 103:7161
28. Ballhausen CJ (1962) Introduction to ligand field theory. McGraw-Hill, New York
29. Blasse G (1984) In: DiBartolo B (ed) Nato Advanced Studies Institutes Series B, vol 114. Plenum Press, New York
30. Determined on a single crystal by measuring the real thickness using a micrometer and the effective thickness through the crystal by focussing on the top and bottom surfaces using a microscope
31. a) Dornauf H, Heber J (1980) J Lumin 22:1; b) Heber J, Dornauf H, Siebold H (1981) J Lumin 24:735; c) Vasquez SO, Flint CD (1995) Chem Phys Lett 238:378
32. von Arx ME, Langford VS, Oetliker U, Hauser A (2002) J Phys Chem A 106:7099
33. von Arx ME, Burattini E, van Pieterson L, Pellaux R, Decurtins S, Hauser A (2000) J Phys Chem A 104:883
34. Hauser A, von Arx ME, Pellaux R, Decurtins S (1996) J Mol Cryst Liq Cryst 286:225
35. Coronado E, Galan-Mascaros JR, Gomez-Garcia CJ, Martinez-Agudo JM (2001) Inorg Chem 40:113
36. Sieber R, Decurtins S, Stoeckli Evans H, Wilson C, Yufit D, Howard JAK, Capelli SC, Hauser A (2000) Chem Eur J 6:361

Top Curr Chem (2004) 241:97–118
DOI 10.1007/b96861

Excited States and Optical Spectroscopy of Nitronyl Nitroxides and their Lanthanide and Transition Metal Complexes

Guillaume Bussière[1] · Rémi Beaulac[1] · Hugo Bélisle[1] · Christophe Lescop[2] · Dominique Luneau[3] (✉) · Paul Rey[2] · Christian Reber[1] (✉)

[1] Département de Chimie, Université de Montréal, Montréal, QC, H3C 3J7, Canada
christian.reber@umontreal.ca
[2] Laboratoire de Chimie Inorganique et Biologique (UMR 5046), DRFMC, CEA-Grenoble, 17 rue des Martyrs, 38054 Grenoble Cedex 09, France
[3] Cristallographie et Ingénierie Moléculaire (Bât. J. Raulin), Laboratoire des Multimatériaux et Interfaces (UMR 5615), Université Claude Bernard Lyon 1, 43 Avenue du 11 Novembre 1918, 69622 Villeurbanne Cedex, France
dominique.luneau@univ-lyon1.fr

Abstract Nitronyl nitroxides are stable free radicals that have been used to prepare new molecular solids with intriguing magnetic properties. These properties have been probed for the electronic ground state using a large number of different physical techniques and theoretical methods. In contrast, the excited states and optical spectroscopy of these compounds and their metal complexes have received little attention until recently. In this overview, we present their absorption and luminescence spectra. Luminescence is observed between 700 nm and 1100 nm, and the lowest-energy absorption bands occur between 500 nm and 700 nm. Several excited electronic states are in the red to near-infrared wavelength range, leading to a wide variety of interesting spectroscopic features.

Keywords Nitroxide radicals · Lanthanide complexes · Low-temperature absorption spectroscopy · Low-temperature luminescence spectroscopy · Molecular magnetism

1 Introduction

An important current research direction in the area of molecular magnets is the development of multifunctional materials with a combination of magnetic and other physical properties [1–4]. Stable nitronyl nitroxide free radicals receive considerable attention as spin carriers in the field of molecular based magnets, either as tectons of pure organic materials[5–9] or in combination with metal ions in the engineering of organic-inorganic materials [10–15]. Molecular solids based on radicals are also highly promising systems from the perspective of novel magneto-optical properties [16]. In addition, nitronyl nitroxides show interesting nonlinear optical properties due to their large negative second hyperpolarizability [17].

Quantitative information on the optical spectroscopy and the properties of excited electronic states is essential in the search for such new materials. A recent review [3] on molecular solids incorporating free radicals indicates that their electronic spectroscopy has not been investigated in detail, in marked contrast to transition metal compounds with diamagnetic ligands, for which the effects of magnetic exchange interactions on absorption and luminescence spectra have been studied extensively over the past decades [18–20]. Even more recently, the room-temperature solution UV-VIS absorption and NMR spectroscopy of several d-block ions with nitroxide radical ligands has been summarized in a review [4]. Absorption spectra of nitroxides and their complexes in solution have been reported as short descriptions given when the compounds were first synthesized [21–23]. Over the past five years, several nitronyl nitroxide and related radicals and their transition metal and lanthanide complexes have been characterized with optical spectroscopic techniques [4, 9, 24–31]. We illustrate in the following the low-temperature optical spectra of uncoordinated nitroxide radicals and of their complexes with lanthanide ions and conclude with a short outlook on the optical spectra of complexes with metals of the d series. This comparison reveals the spectroscopic features common to all compounds and provides a general description of their low-energy electronic transitions.

2 Summary of Experimental Information

The synthesis and characterization of the nitronyl and imino nitroxide ligands discussed in the following, namely 2-(2-pyridyl)-4,4,5,5-tetramethylimidazoline-1-oxyl-3-oxide (abbreviated as NITPy), 2-(2-pyridyl)-4,4,5,5-tetramethylimidazoline-1-oxide (abbreviated as IMPy), 2-(2-benzimidazolyl)-4,4,5,5-tetramethylimidazoline-1-oxyl-3-oxide (abbreviated as NITBzImH), 2-(2-benzimidazolyl)-4,4,5,5-tetramethylimidazoline-1-oxide (abbre-

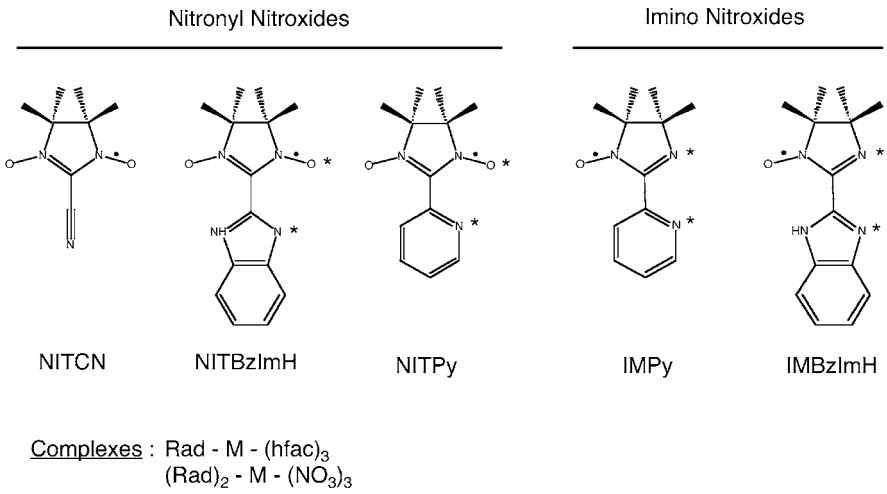

Fig. 1 Schematic representations of the nitronyl nitroxide (NIT) and imino nitroxide (IM) radicals studied by optical spectroscopy. Ligator atoms for lanthanide complexes are denoted by *asterisks*. The stoichiometry of the metal complexes is given, with Rad and hfac denoting radical and hexafluoroacetylacetonato ligands, respectively

viated as IMBzImH), and 2-cyano-4,4,5,5-tetramethylimidazoline-1-oxyl-3-oxide (abbreviated as NITCN) have been described earlier [9, 14, 21]. The syntheses and crystal structures of the lanthanide complexes have also been described in detail [32, 33]. The molecular structures of all fiveradicals and of the two predominant categories of lanthanide complexes studied in the following are shown schematically in Fig. 1. The ligator atoms of the radicals are marked by asterisks, based on the crystallographic structures of the complexes [26, 27, 33].

Absorption spectra were measured on a Varian Cary 5E spectrometer using the photomultiplier tube detector for the visible range. The sample crystals were cooled in a He gas flow cryostat (Oxford Instruments CF-1204) and the temperature was monitored with a RhFe resistor connected to an electronic controller (Oxford Instruments ITC4) to stabilize the temperature to better than ±1 K by adjusting both a heater for the He gas cooling the sample and the gas flow valve from the He storage dewar to the cryostat. All spectra presented in the following are unpolarized, as no strong dichroic effects were observed in preliminary spectra polarized along the optical extinction directions of sample crystals.

Luminescence was excited with the 488.0 nm and 514.5 nm lines of an Ar^+ ion laser. The sample crystals were again placed in the He gas flow cryostat. The emitted light was dispersed with a Spex 500 M monochromator and detected with a Ge diode (Applied Detector Corporation ADC403L). This detector is sensitive in the 600 nm to 1800 nm wavelength range and its

sensitivity varies very little over the range examined for the title compounds. The signal was averaged and stored with a lock-in amplifier, as described previously [34]. Raman spectra were measured using a commercial micro-Raman spectrometer (Renishaw System 3000) again with the 488.0 nm and 514.5 nm Ar^+ excitation lines. This sensitive instrument was also used to measure luminescence spectra at wavelengths shorter than 1000 nm [35]. Samples were cooled in a liquid helium flow cryostat designed for this microscope (Janis Research Supertran ST-500) [26].

3 Spectroscopic Characterization of the Lowest-Energy Excited States of Nitronyl Nitroxide Radicals

Nitroxide radicals show intense colors, indicating the presence of excited electronic states in the visible wavelength range. The lowest-energy electronic transitions are characterized by the combination of luminescence and absorption spectra. Figure 2 compares spectra for two uncoordinated nitronyl nitroxide radicals, NITPy in Fig. 2a and NITBzImH in Fig. 2b, to those of a lanthanide complex with a single radical ligand, [Gd(hfac)$_3$NITBzImH], in Fig. 2c. The luminescence spectra of uncoordinated NITBzImH and NITPy radicals have their onsets at very similar energies of approximately 14820 cm^{-1} and 15290 cm^{-1} and overall band widths at half height of approximately 1100 cm^{-1} and 2100 cm^{-1}, respectively. The luminescence intensities are low, indicating low quantum yields, and luminescence lifetimes are shorter than the lower limit of approximately 500 μs imposed by the near-infrared detector used. No luminescence was observed for the NITCN radical, likely due to efficient nonradiative relaxation processes involving the high-frequency C≡N vibrational mode [28]. The luminescence spectrum of NITBzImH is well resolved and shows a short vibronic progression with an average interval of 1450 cm^{-1}, as illustrated in Fig. 2b. Each member of this progression has a shoulder lower in energy by 590 cm^{-1}, corresponding to a different vibrational mode. The luminescence spectrum of NITPy also shows resolved maxima, but the resolution is not sufficient to clearly identify vibronic progressions. Nevertheless, two sets of maxima separated by 520 cm^{-1} are observed, an energy difference comparable to the interval of 590 cm^{-1} measured in the more highly resolved luminescence spectrum of NITBzImH. The energy separation between the two sets is on the order of 2300 cm^{-1}. Figure 2c shows the luminescence and absorption spectra of the lanthanide complex [Gd(hfac)$_3$NITBzImH]. Its spectra are very similar to those of the uncoordinated radical, but a detailed comparison shows that differences exist. All band maxima in Tables 1 and 2 are lower in energy by 200 cm^{-1} to 500 cm^{-1} for [Gd(hfac)$_3$NITBzImH] than for the uncoordinated NITBzImH radical. This small shift is a possible indication of metal-to-li-

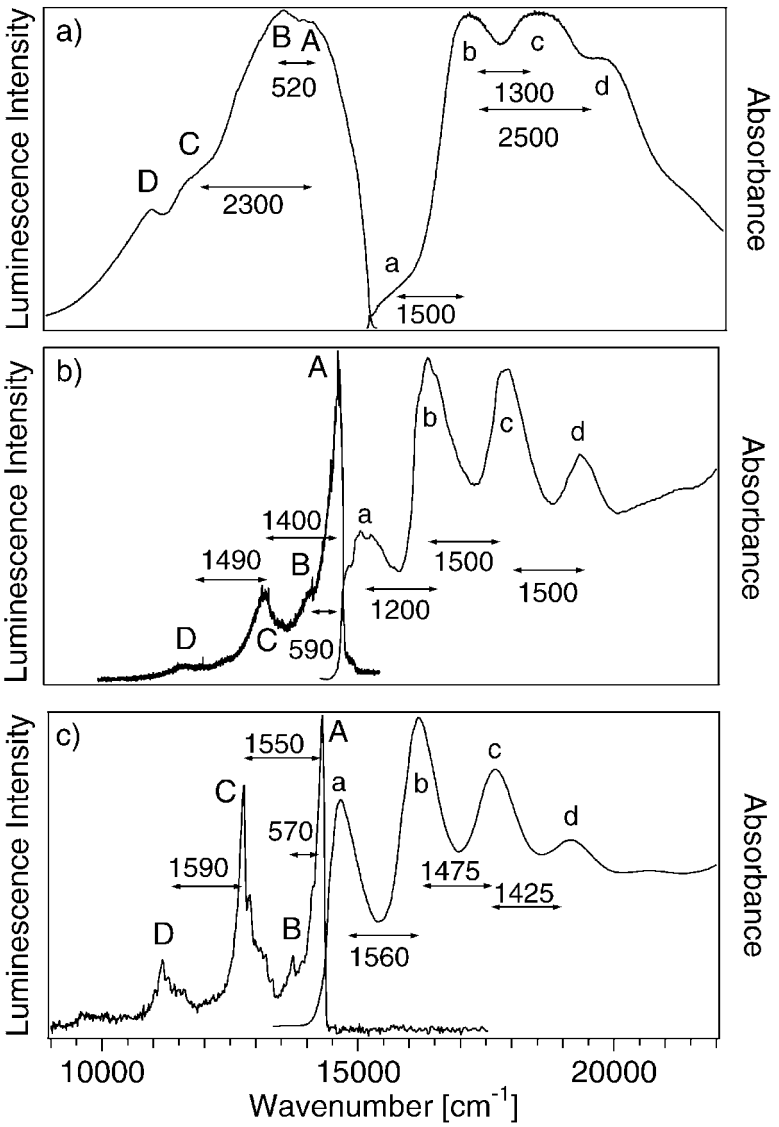

Fig. 2a–c Solid-state absorption and luminescence spectra of: **a** NITPy; **b** NITBzImH; **c** [Gd(hfac)$_3$]NITBzImH at 5 K. *Alphabetical labels* denote maxima summarized in Tables 1 and 2. Energy intervals in wavenumber units are indicated by *horizontal double arrows*

gand charge transfer character of the band system in metal complexes, an assignment proposed in a recent review [4]. In view of the similarities of both energies and band shapes, we nevertheless propose an assignment as a ligand-centered transition. The excited states of the radical ligand are only

Table 1 Luminescence band positions in wavenumber units (cm^{-1}) from the luminescence spectra with alphabetical labels in Fig. 2

Transition	NITPy	NITBzImH	[Gd(hfac)$_3$NITBzImH]
A	14090	14630	14320
B	13570	14040	13750
C	11750	13230	12770
D	11010	11740	11180

Table 2 Band positions in wavenumber units (cm^{-1}) from absorption spectra of uncoordinated radicals and selected metal complexes with radical ligands. The alphabetical labels refer to Figs. 2, 3, 4, 7, and 10

Uncoordinated radicals				
Transition	NITPy	NITCN	NITBzImH	IMBzImH
a	15550	13500	15180	19120
b	17190	14900	16390	20580
c	18450	16410	17920	22030
d	19570	17890	19340	23470
Metal complexes				
Transition	[Gd(hfac)$_3$NITBzImH]	[Gd(hfac)$_3$IMBzImH]	[Gd(hfac)$_3$IMPy]	[$PtCl_2$(NITPy)$_2$]
a	14770	18110	19680	14470
b	16240	19580	21050	15870
c	17700	20880	22430	17250
d	19120	22270	23710	

very weakly affected by the gadolinium(III) center, as illustrated by the very similar vibronic structure for the spectra in Fig. 2b,c. The main progression interval in the luminescence spectrum of the lanthanide complex is 1570 cm^{-1}, significantly larger than the value of 1450 cm^{-1} for the uncoordinated radical, another spectroscopic manifestation of the coordination to a metal center. All energies of luminescence transitions are summarized in Table 1 using the uppercase alphabetical labels given in Fig. 2 to identify each band.

It is obvious that the luminescence spectra in Fig. 2 are not mirror images of the lowest-energy absorption bands. All absorption spectra in Fig. 2, Fig. 3, Fig. 4, and Fig. 7 have widths at half height on the order of 4000 cm^{-1}, significantly larger than those of the luminescence bands in Fig. 2. Absorption band positions are summarized in Table 2 and identified by the lowercase alphabetical labels in Figs. 2, 3, 4, and 7. Most nitronyl nitroxides and their metal complexes show absorption spectra with resolved patterns as illustrated in Figs. 2, 3, and 7, consisting of a sequence of four to six peaks [26, 27, 30]. The energy differences between these maxima are constant within experimental precision, with the exception of the interval between the two lowest-energy peaks labeled a and b in the absorption spectra. This is well illustrated for NITBzImH in Fig. 2b, where the first interval is approx-

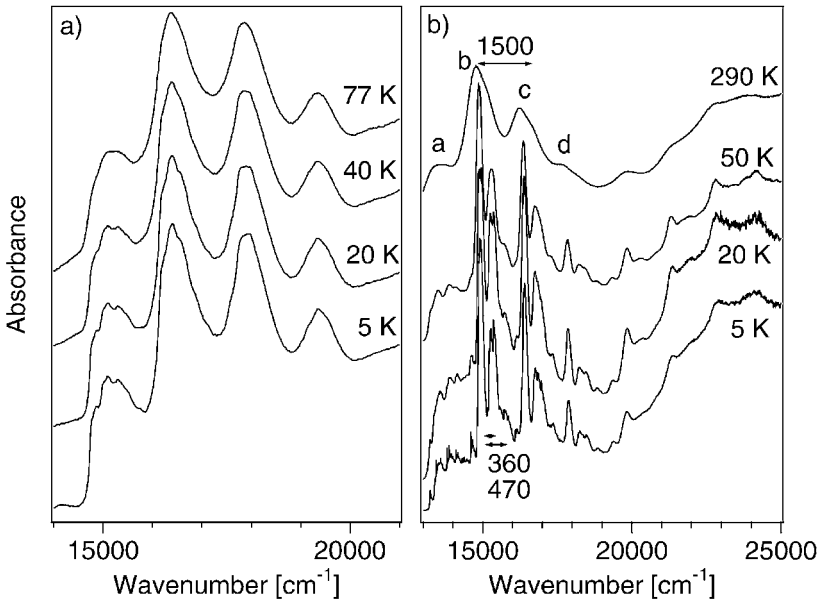

Fig. 3a, b Temperature dependence of the solid-state absorption spectra of: **a** NITBzImH; **b** NITCN. *Alphabetical labels* denote maxima summarized in Table 2. Energy intervals in wavenumber units are indicated by *horizontal double arrows*. Traces are offset along the ordinate for clarity

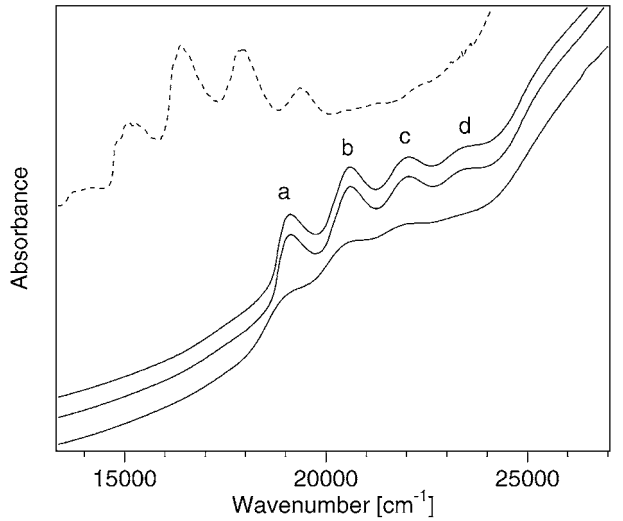

Fig. 4 Absorption spectra of NITBzImH (*top trace, dotted line*, 5 K) and IMBzImH (KBr disk, *solid lines*, measured at 5 K, 20 K and 290 K, *top to bottom*). *Alphabetical labels* denote maxima summarized in Table 2. Traces are offset along the ordinate for clarity

imately 1200 cm^{-1}, but a larger difference of approximately 1500 cm^{-1} is observed between the maxima at higher energy. These energy intervals indicate that the sequence of peaks in the absorption spectra does not correspond to a single vibronic progression, for which a constant energy separation is expected, therefore indicating that transitions to at least two excited states form the observed absorption band system. This conclusion is confirmed by the intensity distribution within the band sequences in the luminescence and absorption spectra. The absorption spectrum is expected to be a mirror image of the luminescence band, if only a single excited state is involved. The first member of the progression in the luminescence spectra has the highest intensity. In contrast, the experimental absorption spectra have a very different intensity distribution: the lowest energy peak is much less intense than the following higher energy bands. This is most evident in the spectra of NITPy in Fig. 2a, where the intensity of the first peak, labeled a, is lower by at least an order of magnitude than the intensity of the following bands, labeled b, c and d. To the best of our knowledge, the results in Fig. 2 are the only published comparisons of full luminescence and absorption spectra for uncoordinated nitronyl nitroxides and their lanthanide complexes [27, 28]. Their vibronic structure has been analyzed quantitatively for uncoordinated radicals and reveals offsets of the excited-state potential energy surfaces along several Raman-active modes [28]. Different excited states close in energy can be expected for nitroxide radicals, as they are observed for the diatomic NO molecule, where the lowest energy $^2\Sigma_g^+$ and $^2\Pi$ excited states occur within less than 2000 cm^{-1} in the ultraviolet wavelength range [36].

Figure 3 shows the absorption spectra throughout the visible wavelength range for the NITBzImH and NITCN radicals. These spectra again show clearly that the weak, lowest-energy absorption bands (labeled a) are not part of the intense progressions at higher energy, in support of the conclusion based on the comparison of absorption and luminescence spectra in Fig. 2. The higher-energy progressions are well resolved and have at least three members, labeled b, c, and d in Figs. 2 and 3. Figure 3a shows the temperature dependence of the absorption spectrum of NITBzImH. Low-frequency features at approximately 15,000 cm^{-1} are well resolved at 5 K, but this resolution disappears at 77 K and higher temperatures. The intensity distribution of the low-frequency resolved bands between 14,000 cm^{-1} and 16,000 cm^{-1} is different from the following higher-energy peaks between 16,000 cm^{-1} and 20,000 cm^{-1}. This difference again illustrates that two overlapping electronic transitions to different excited states are observed. The band maxima of the main vibronic progression shift by less than 15 cm^{-1} in this temperature range. The integrated intensities of the absorption band system in Fig. 3a are independent of temperature, indicating the absence of efficient vibronic intensity mechanisms, as expected for low-symmetry chromophores. The absorption spectrum of the NITCN radical in Fig. 3b

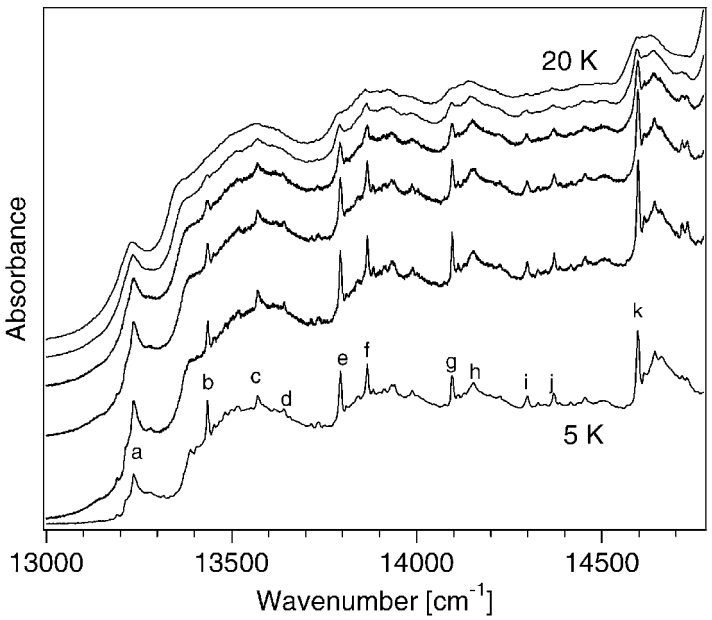

Fig. 5 Low-temperature absorption spectra of NITCN in the region of the lowest-energy electronic transition. Temperatures are 20 K, 15 K, 12 K, 9 K, 7 K, and 5 K (*top to bottom*). *Alphabetical labels* denote peak maxima summarized in Table 3. Traces are offset along the ordinate for clarity

shows higher energy peaks of the absorption band system with well-resolved vibronic structure involving at least three vibrational modes with frequencies of 1500 cm^{-1}, 470 cm^{-1}, and 360 cm^{-1}. The absorption spectrum in the region of bands b, c, and d has been analyzed quantitatively using these modes [28]. The 1500 cm^{-1} vibronic interval also appears prominently on the highest energy absorption band shown in Fig. 3b, starting at approximately 20,000 cm^{-1}. The intensity distribution within this progression indicates that a much larger distortion along the normal coordinate of this vibrational mode occurs in the higher-energy excited state.

Figure 4 shows that similar absorption spectra are observed for nitronyl nitroxide and imino nitroxide radicals, with the transitions for the imino nitroxides occurring higher in energy by approximately 4000 cm^{-1}. The average energy interval determined from bands a to d in the absorption spectra of the IMBzImH radical is 1450 cm^{-1}, a value similar to the NITBzImH radical, shown as the dotted trace in Fig. 4. All band maxima for the imino nitroxide radical are included in Table 2.

The best spectral resolution is observed for the NITCN radical, whose overall spectrum is shown in Fig. 3b. The region below 15,000 cm^{-1} is particularly well resolved and shown in detail in Fig. 5. A series of very sharp

Table 3 Energies of the resolved low-energy transitions in the absorption spectrum of the NITCN radical. Alphabetical labels are given in Fig. 5. Energy intervals ΔE are defined relative to the lowest-energy transition labeled *a* at 13236 cm^{-1}. Raman shifts corresponding to ground-state vibrational energies are included for comparison. All values are in wavenumber units (cm^{-1})

Transition	Energy	ΔE	Raman shift
a	13236	0	
b	13435	199	
c	13570	334	370
d	13641	405	500
e	13795	559	525
f	13868	632	610
g	14094	858	700
h	14154	918	1225
i	14300	1064	1260
j	14370	1134	1400
k	14596	1360	1435, 1450

peaks at 5 K is observed for the lowest-energy part of the spectrum, as denoted in Fig. 5 by the labels a to k. Their energies are given in Table 3 with the energy intervals measured from the lowest-energy absorption transition a. These intervals are similar to vibrational frequencies observed for the ground state by Raman spectroscopy [28], also included in Table 3, and can therefore be assigned as vibronic transitions. The bands denoted by labels a to k do not appear to be part of progressions with multiple members, such as the main progressions in Fig. 1, and their assignment based on the molecular orbital characteristics presented in the following section is not straightforward. Their temperature dependence in a narrow interval between 5 K and 20 K is striking, as widths increase and integrated intensities appear to decrease in this temperature range. No such effects are observed for other radicals, such as NITBzImH in Fig. 3a or for the higher energy absorption bands of NITCN in Fig. 3b. A phenomenological correlation can be made with the antiferromagnetic order in NITCN, whose onset occurs over the same temperature range [9]. The temperature-dependent lowest-energy absorption band of NITCN therefore appears to be an exceptional case showing effects of intermolecular phenomena.

4 Molecular Orbital Model for the Lowest-Energy One-Electron Excitations of Uncoordinated Nitronyl Nitroxide Radicals

The comparison of luminescence and absorption spectra in Fig. 2 shows that transitions to at least two excited states form the observed absorption band

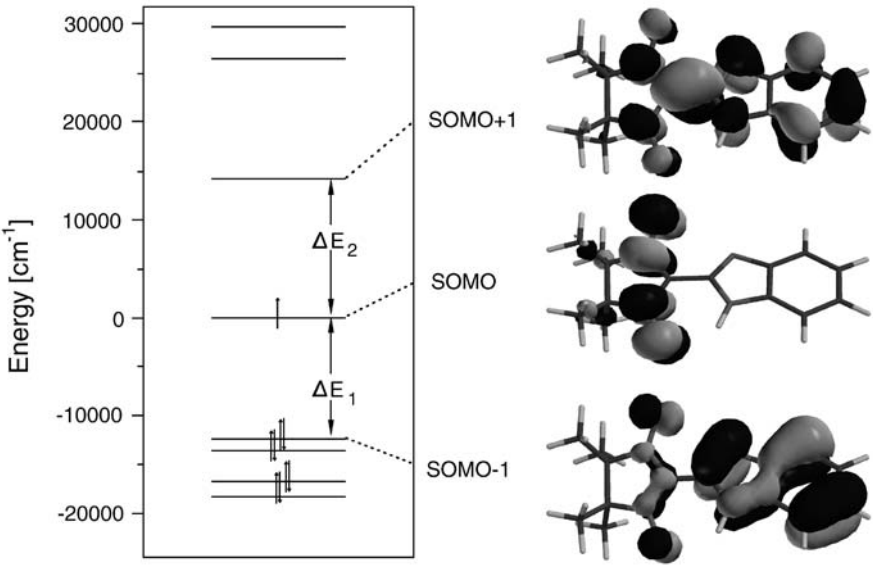

Fig. 6 Calculated molecular orbitals and energy levels of NITBzImH obtained with density-functional theory. The energy of the SOMO orbital is set to 0 for this diagram

system. This experimental conclusion is based on the luminescence and absorption spectra discussed in the preceding sections [27, 28]. Electronic structure calculations, as illustrated for NITBzImH in Fig. 6 and for other radicals in [28], further confirm the presence of several excitations in the range of the experimental absorption spectra. Density functional calculations [37] were carried out using the crystallographic structure of NITBzImH [38] in order to obtain the molecular orbitals and their energies in Fig. 6. The singly occupied molecular orbital (SOMO) is π antibonding and located on the nitroxide group, as has been characterized in detail by both theoretical calculations and experimental measurements of the unpaired spin density [3, 39–41]. The calculated energy differences ΔE_1 and ΔE_2 separating the SOMO from the SOMO−1 and SOMO+1 levels, respectively, are of comparable magnitude. It can therefore be expected that excited electronic states arising from the $(SOMO-1)^1(SOMO)^2$ and $(SOMO)^0(SOMO+1)^1$ excited electron configurations (using the labels in Fig. 6—strictly appropriate only for the ground state electron configuration—to identify molecular orbitals) are observed at similar energies and lead to overlapping absorption bands. Calculated transition energies and oscillator strengths confirm that two overlapping electronic transitions occur in the energy range of Figs. 2 and 3 [28, 42]. The main change in electron density for these two excited configurations occurs on the nitroxide group, as illustrated by the calculated shapes of the orbitals for NITBzImH. As a consequence, the O-N-C-N-O

bond lengths show the largest differences between the ground state and the low-energy excited states discussed here. It is intuitively appealing to assume that coordination of NITBzImH to a metal center decreases the π antibonding character along the O-N-C-N-O fragment, leading to a strengthening of these bonds. A spectroscopic manifestation of this effect is the increase of the main vibronic interval from 1450 cm^{-1} to 1570 cm^{-1} in the luminescence spectra of uncoordinated NITBzImH compared to [$Gd(hfac)_3$NITBzImH] in Fig. 2b,c.

It is important to emphasize that this comparison of molecular orbital calculations and experimental spectra is qualitative, as the limitation to a single molecule and the intrinsic precision of the computational approach used do not allow a quantitative comparison. Nevertheless, the characteristics of the orbitals, such as the electron density distribution, are very similar for different density functional and semiempirical calculations, indicating that the calculations are useful for a qualitative interpretation of the spectra. Detailed electronic structure calculations have been recently applied to the understanding of intermolecular magnetic interaction pathways in nitroxide radicals [43], underlining the importance of comparisons between computational data and spectroscopic results which provide a quantitative test for the theoretical models.

5
Absorption and Luminescence Spectra of Lanthanide Complexes with Chelating Nitronyl Nitroxide Ligands

Figure 2c shows the near-infrared luminescence spectrum of [$Gd(hfac)_3$NITBzImH] compared to its lowest-energy absorption band system. At 5 K, both spectra show well-resolved structure that is similar to the patterns observed for the uncoordinated radical, as summarized in Tables 1 and 2. The corresponding electronic transitions can be observed for many other complexes of lanthanide or d-block metal ions with radical ligands [24–27, 30]. In general, the spectra for lanthanide complexes are very similar to those of the uncoordinated radicals.

Figure 7 shows that the energy of the absorption band system in the visible spectral region varies significantly for gadolinium(III) complexes with different radical ligands, underlining again that these electronic transitions are centered on the radical. As expected, the lowest energy transition is observed for the complex of the blue nitronyl nitroxide radical NITBzImH, followed by those of the complexes of the red imino nitroxide radicals IMBzImH and IMPy, which show bands higher in energy than those of the NITBzImH ligand by approximately 3000 cm^{-1} and 5000 cm^{-1}, respectively. The spectra are less resolved at room temperature (dotted lines) than at 5 K (solid lines), but their overall band shape does not change, as shown in Fig. 7.

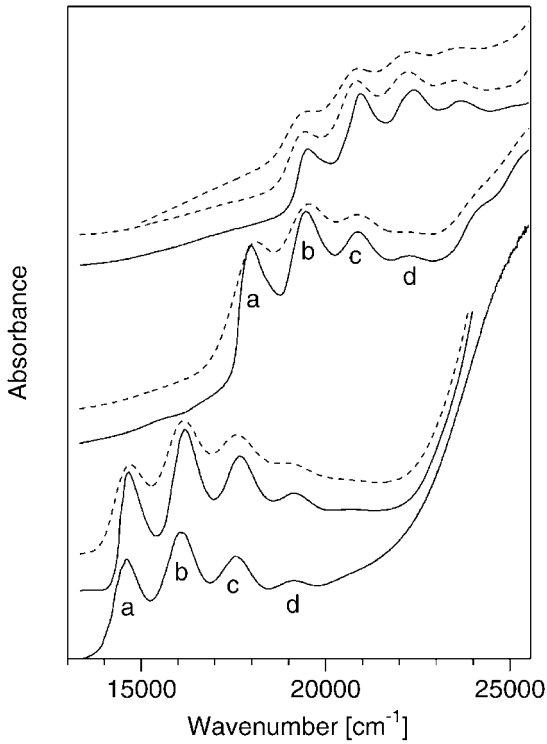

Fig. 7 Solid-state absorption spectra of lanthanide-radical complexes at 5 K (*solid lines*) and 290 K (*dotted lines*). *From top to bottom*: [Eu(hfac)$_3$IMPy] (290 K), [Gd(hfac)$_3$IMPy] (290 K, 5 K), [Gd(hfac)$_3$IMBzImH] (290 K, 5 K), [Gd(hfac)$_3$NITBzImH] (290 K, 5 K) and [Gd(NITBzImH)$_2$(NO$_3$)$_2$] (5 K). *Alphabetical labels* denote maxima summarized in Table 2. Traces are offset along the ordinate for clarity

The transitions labeled a to d for [Gd(hfac)$_3$IMBzImH] in Table 2 and Fig. 7 occur lower in energy by approximately 1000 cm^{-1} than those of the uncoordinated IMBzImH radical in Fig. 4. This red shift is larger by at least a factor of two than for NITBzImH and its [Gd(hfac)$_3$NITBzImH] complex, a difference possibly due to the different ligator atom on the radical ligand. The corresponding complexes of europium(III) also have very similar spectra, as illustrated by the comparison of the two top traces in Fig. 7, which indicate that band maxima vary by less than 50 cm^{-1} from those of the gadolinium(III) complex with an identical ligand sphere . Molar absorptivities (ϵ) on the order of 500 M^{-1} cm^{-1} have been reported for several lanthanide complexes with IMPy ligands in solution at room temperature [29]. At energies higher than shown in Fig. 7, the next absorption band has its onset at 26,310 cm^{-1} with a long progression in a 1540 cm^{-1} mode. This band is again shifted to higher energy than for nitronyl nitroxides, such as NITCN

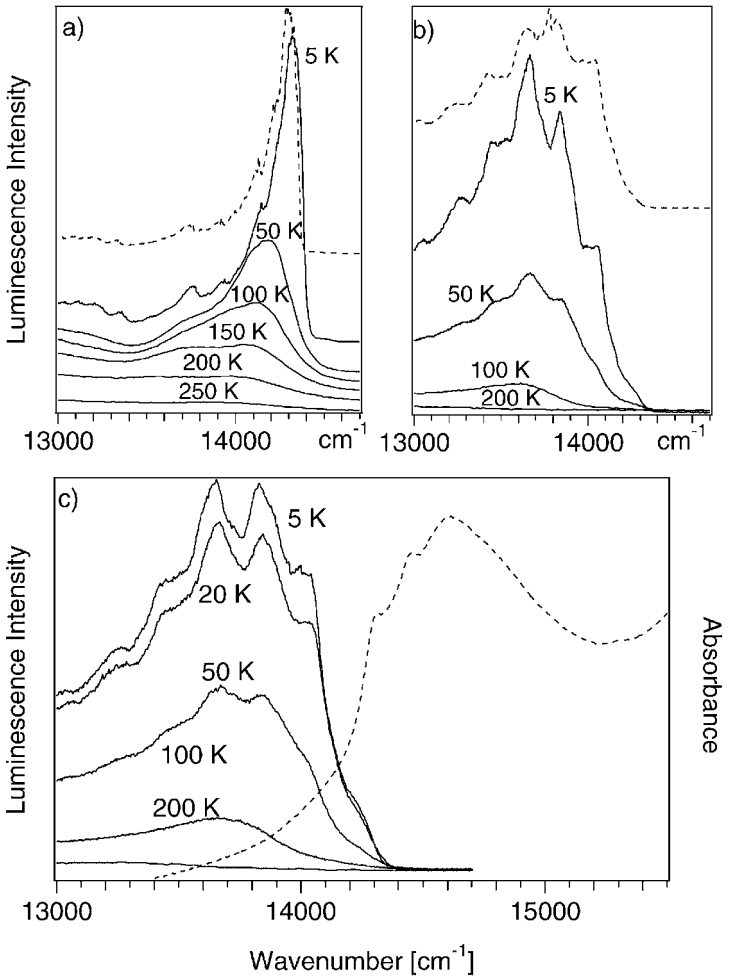

Fig. 8a–c Temperature dependence of the highest energy luminescence band of: **a** $[Gd(hfac)_3NITBzImH]$ (*solid lines*) and $[Eu(hfac)_3NITBzImH]$ (*dotted line*, 5 K); **b** $[Gd(NITBzImH)_2(NO_3)_3]$ (*solid lines*), $[La(NITBzImH)_2(NO_3)_3]$ (*dotted line*, 5 K); **c** $[Eu(NITBzImH)_2(NO_3)_3]$, absorption spectrum at 5 K shown as *dotted line*. Traces are offset along the ordinate for clarity

in Fig. 3b, where an onset lower by approximately 6000 cm^{-1} and a similar progression interval are observed. The higher energy excited states of imino nitroxide radicals and their metal complexes have yet to be investigated rigorously.

The luminescence transitions show an intriguing phenomenological dependence on the number of radical ligands, the ancillary ligands and the coordination number of the lanthanide ion. Figure 8a,b compare the highest

energy band of the luminescence spectra for $[Gd(hfac)_3(NITBzImH)]$ and $[Gd(NITBzImH)_2(NO_3)_3]$. A clear-cut difference appears: the nitrato complex in Fig. 8b has a larger band, consisting of a low-frequency progression with an average spacing of 190 cm^{-1}, which is absent in the complexes with hexafluoroacetylacetonato ancillary ligands in Fig. 8a. Complexes with different lanthanide ions are included for comparison in Fig. 8a,b. The spectra of $[Eu(hfac)_3(NITBzImH)]$ and $[La(NITBzImH)_2(NO_3)_3]$ are identical to those of their Gd(III) analogs. The presence of the low-frequency progression in $[La(NITBzImH)_2(NO_3)_3]$ indicates that it is not caused by lanthanide-radical exchange coupling. The Gd(III) and Eu(III) hexafluoroacetylacetonato complexes in Fig. 8a show a distinct red-shift of the band maximum with increasing temperature, possibly an indication of small structural changes occurring with temperature. In contrast, the nitrato complexes of these two lanthanide ions in Fig. 8b,c show a broader band at low temperature that does not change its shape, but becomes less resolved with increasing temperature. At temperatures above 100 K, the spectra from both types of compounds become similar. No hot bands at energies higher than the onset of the luminescence spectrum at 5 K are observed at any temperatures. Figure 8c compares absorption and luminescence spectra of $[Eu(NITBzImH)_2(NO_3)_3]$, indicating similar resolved structure in both spectra and the expected overlap in the region of the electronic origin. The spectra in Fig. 8 indicate that changes in the ligand sphere appear to have a larger influence on the optical spectra than changes of the lanthanide ions. These spectroscopic results illustrate the wide range of luminescence properties accessible to complexes of lanthanide ions with radical ligands. As the electronic transitions observed are ligand-centered, a model based on coupled chromophores[44] appears as a promising route towards the understanding of the spectroscopic effects observed for complexes with several nitroxide radical ligands, as illustrated in Fig. 8b,c.

Figure 9 shows a comparison of luminescence spectra of a series of europium(III) complexes. The Eu(III) ion shows a well studied f-f luminescence corresponding to the $^5D_0 \rightarrow {}^7F_J$ electronic transition at energies between 16,000 cm^{-1} and 16,500 cm^{-1}. Figure 9 illustrates that the luminescence behavior of these compounds can be tuned through the appropriate choice of radical ligand. The broad luminescence spectrum given as the top trace in Fig. 9 is observed for $[Eu(NITBzImH)_2(NO_3)_3]$, a complex with nitronyl nitroxide radical ligands which absorb at energies lower than the f-f transitions of Eu(III). For compounds with imino nitroxide radical ligands, the luminescence from the Eu(III) centered f-f transition is lower in energy than the first absorption band of the radical and it therefore dominates the spectrum, as shown in the bottom half of Fig. 9. The resolved structure of the f-f region is very similar for all compounds, illustrated in the inset to Fig. 9. Prominent energy intervals of 30 cm^{-1}, 120 cm^{-1}, and 360 cm^{-1} appear, independent of the types and numbers of radical ligands. Luminescence cen-

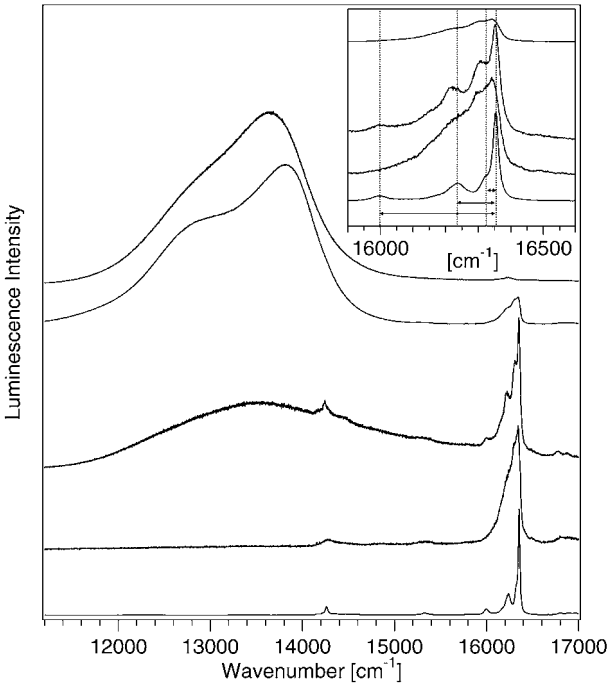

Fig. 9 Comparison of luminescence spectra of Eu(III) complexes with radical ligands. *Top to bottom*: $[Eu(NITBzimH)_2(NO_3)_3]$ (290 K), $[Eu(hfac)_3NITBzimH]$ (290 K), $[Eu(hfac)_3ImBzimH]$ (5 K) and $[Eu(hfac)_3IMPy]$ (5 K). The *lowest trace* is $Eu(hfac)_3{\cdot}2H_2O$ (5 K) and gives the f-f luminescence spectrum for a complex without radical ligands. *Inset*: enlarged view of the f-f transition for the *bottom four spectra in the main figure. Horizontal arrows* denote wavenumber intervals of 30 cm^{-1}, 120 cm^{-1} and 360 cm^{-1} (*top to bottom*). Traces are offset along the ordinate for clarity in both the main Figure and the inset

tered on the Eu(III) ion for a compound with IMPy ligands confirming our results was recently reported [29].

6 Phenomenological Correlations Between Optical Spectra and Magnetic Properties

The signatures of magnetic effects for the lanthanide complexes from the spectra in the preceding sections are not obvious, but the comparison of spectra nevertheless reveals some phenomenological trends. In contrast to a large number of d-block complexes with exchange coupling between paramagnetic metal centers, where quantities such as ground-state exchange

Table 4 Summary of magnetic data for selected Gd(III) and La(III) complexes with nitroxide radical ligands. Values are given for the exchange coupling constants using the Hamiltonian $H_{exc}=-2\Sigma J_{ij}S_iS_J$ For Gd(III) complexes, exchange coupling can occur between the lanthanide ion and the radical ligands ($J_{Gd\text{-}rad}$) and between radical ligands coordinated to the same metal center ($J_{rad\text{-}rad}$). Only the latter interaction can lead to nonzero coupling constants for the La(III) complex. Absorption energies are given for the lowest-energy band, denoted as peak a in Figs. 2, 4, and 7. All values are given in wavenumber units (cm^{-1})

Complex	$J_{Gd\text{-}rad}$	$J_{rad\text{-}rad}$	Absorption energy
$Gd(hfac)_3NITBzImH$	+1.7[a]		14470[a]
$Gd(NITBzImH)_2(NO_3)_3$	−4.05,[b] −0.80[b]	−1.1[b]	14600[e]
$Gd(hfac)_3NITPy$	+1.5[c]		
$Gd(hfac)_3IMBzImH$	−2.6[a]		18110[a]
$Gd(hfac)_3IMPy$	−3.0[d]		19860[a]
	−1.9[a]		
$La(NITBzImH)_2(NO_3)_3$		−1.1[b]	14600[e]

[a] [27] [b] [33] [c] [52] [d] [29] [e] [26]

splittings can be directly determined from luminescence and absorption spectra [18], no such energy differences are resolved in our spectra. This is not unexpected for lanthanide ions, as the exchange effects are much weaker than those of the d-block elements, illustrated by a large number of magnetic measurements for lanthanide complexes with nitroxide radical ligands [13, 32, 33]. A summary of magnetic exchange couplings for lanthanide complexes discussed in this overview is given in Table 4. A recent comprehensive review [4] of the magnetism of 3d metal ions with nitroxide radical ligands summarizes couplings for 22 complexes, varying from J=−219 cm^{-1} to J=71 cm^{-1} ($H_{exc}=-2JS_iS_j$), values larger by two orders of magnitude than those for the lanthanide complexes summarized in Table 4. These weak couplings are unlikely to be the cause of the variations observed in the absorption and luminescence spectra of different lanthanide complexes, as they are expected to lead to energy differences too small to be resolved. Nevertheless, two qualitative correlations can be made from the spectra:

1. The luminescence spectra in Fig. 8 show distinct differences between complexes with two (Fig. 8b,c) or only one radical ligand (Fig. 8a). The clearly visible progression illustrated in Fig. 8b,c observed in the spectra of the nitrato complexes with two radical ligands parallels an antiferromagnetic gadolinium-radical coupling and an antiferromagnetic radical-radical coupling similar in magnitude to the lanthanide-radical coupling [27, 32]. This progression indicates a significant distortion along a low-frequency normal coordinate at all temperatures, likely involving radical-lanthanide-radical modes, as it is not observed for complexes with only one radical ligand or for uncoordinated radicals. The shape of the spectrum does not change with temperature, indicating that the assumption of temperature-indepen-

dent exchange coupling parameters is justified. In contrast, narrower low-temperature spectra as shown in Fig. 8a are observed for complexes with only one radical ligand, where ferromagnetic Gd(III)-radical interactions occur in the ground state. At higher temperatures, the luminescence spectra of these compounds become broader, possibly indicating a structure change that could influence the exchange coupling. The assumption of temperature-independent exchange coupling constants is therefore not necessarily justified for these complexes. The luminescence spectra provide complementary information to the ground-state magnetic measurements.

2. Within the [Gd(hfac)$_3$radical] series in Fig. 7, where only the radical ligand is varied, the lanthanide-radical coupling becomes antiferromagnetic as the absorption bands shift to higher energy. It is not straightforward to quantitatively rationalize this trend, but it might indicate an influence of interactions between excited states and the ground state on the exchange interaction. Such effects are expected to become weaker as the energy separation between the ground and the excited states of the radical increases. The relatively small change of the absorption energy by 3000 cm^{-1} to 5000 cm^{-1} observed for the complexes in Fig. 7 is sufficient to go from ferromagnetic to antiferromagnetic coupling for the three related complexes. This phenomenological correlation is illustrated by the comparison of exchange couplings and absorption band positions in Table 4. The results presented here indicate that both the energy difference between ground and low-energy excited states and the detailed bandshape of the luminescence spectra can be qualitatively correlated with the sign of the lanthanide-radical exchange interaction.

In contrast to the lanthanide complexes, where the nature of the metal ion appears to have little influence on both the optical spectra and the exchange coupling, a distinct change from antiferromagnetic to ferromagnetic behavior has been reported for interactions between identical radical ligands coordinated to palladium(II) and platinum(II) centers [45], illustrating the fundamentally different magnetic properties that can be obtained with d-block metals. Additional optical spectroscopic measurements, including absorption spectra of charge-transfer bands in the ultraviolet region, are necessary for these compounds before a more quantitative correlation of optical spectra and magnetic properties becomes possible.

7
Optical Spectra of d-block Metals with Nitronyl Nitroxide Radical Ligands

Complexes of nitronyl nitroxide radicals with transition metal ions of the 3d series have been more thoroughly investigated by optical spectroscopic techniques than the lanthanide complexes or the uncoordinated radicals discussed in the preceding sections. We limit this section to a short summary

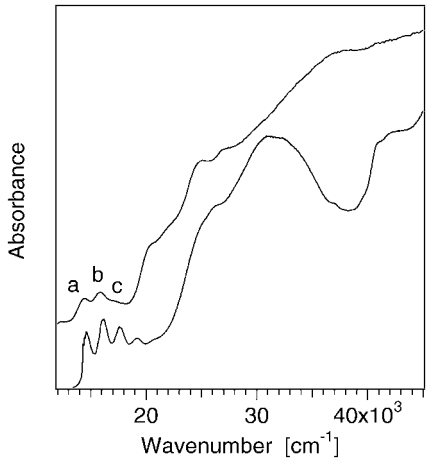

Fig. 10 Overview absorption spectra measured at 5 K of $PtCl_2(NITPy)_2$ (*top trace*) and $[Gd(NITBzImH)_2(NO_3)_3]$ (*bottom trace*). *Alphabetical labels* denote maxima summarized in Table 2. Traces are offset along the ordinate for clarity

of the reported work, in order not to duplicate material presented in a recent comprehensive review of nitroxide complexes with metal ions of the 3d series [4].

Chromium(III) complexes with radical ligands have received the most attention in the past. The absorption spectrum of a complex with a semiquinone ligand shows a significant enhancement of the lowest-energy spin-forbidden d-d band at approximately 14,000 cm^{-1} [46]. Unusually intense and surprisingly broad metal centered transitions in the same energy range have been reported for chromium(III) complexes with nitronyl nitroxide and imino nitroxide radicals [24, 25, 31]. At higher energy, ligand-centered bands which sometimes have resolved vibronic structure are observed [25, 31, 47]. Other transition metal complexes investigated involve manganese(II), cobalt(II), cobalt(III), nickel(II), and zinc(II) metal centers. Crystal structures, magnetic properties, absorption, magnetic circular dichroism (MCD), and resonance Raman spectra of these complexes have been reported [24–26, 30, 31, 33, 47]. Detailed investigations have been carried out on nickel(II) complexes with nitronyl nitroxide ligands, where MCD spectra show experimental evidence for weak d-d transitions superimposed on the more intense radical-centered absorption bands, which in general are the most prominent bands in the spectra [25]. As an example, the absorption spectrum of the $Pt(NITPy)_2Cl_2$ complex is shown in Fig. 10. This representative of the 5d elements, whose complexes with nitroxide radicals have not yet received much spectroscopic attention [45], shows again the typical ligand-centered band between 13,000 cm^{-1} and 17,000 cm^{-1}. The absorption maxima labeled a to c are summarized in Table 2. A red shift of approximately 1000 cm^{-1} is ob-

served for this platinum(II) complex compared to the uncoordinated NITPy radical. This shift is on the same order of magnitude as those described in the preceding sections for lanthanide complexes with nitroxide radical ligands. The more intense band at approximately 27,000 cm^{-1} has been observed for many other transition metal complexes with nitroxide radical ligands and corresponds most likely to a higher-energy electronic transition centered on the radical ligands [25].

A promising direction for future spectroscopic work is the application of external perturbations, such as pressure, which could affect the magnetic order of the title materials and simultaneously greatly enhance the luminescence intensity, as has been shown recently for diamagnetic complexes of palladium(II) and platinum(II) [48, 49]. Attractive compounds for future studies include recently described bimetallic complexes with radical ligands [50] and nickel(II) complexes where the imino nitroxide radical ligand shows linkage isomerism [51]. In the former compounds, intriguing spectroscopic properties influenced by both metal-metal and metal-ligand exchange interactions can be expected and in the latter complexes, the spectroscopic effects of the different ligand coordination can be studied quantitatively. Nitroxide radicals and their transition metal and lanthanide complexes provide a wide variety of new optical spectroscopic features, as illustrated by the absorption and luminescence spectra presented in this overview. They offer a vast field to explore in the search of novel molecular materials with interesting physical properties.

Acknowledgements Financial support from the Natural Sciences and Engineering Research Council (Canada), the Centre Jacques Cartier, and the Commission Permanente de Coopération Franco-Québécoise is gratefully acknowledged.

References

1. Kahn O (1996) Adv Inorg Chem 43:179
2. Luneau D (2001) Curr Opin Solid State Mater Sci 5:123
3. Benelli C, Gatteschi D (2002) Chem Rev 102:2369
4. Kaizaki S (2003) Bull Chem Soc Jpn 76:673
5. Kinoshita M, Turek P, Tamura M, Nozawa K, Shiomi D, Nakazawa Y, Ishikawa M, Takahashi M, Awaga K, Inabe T, Maruyama Y (1991) Chem Lett 1225
6. Cirujeda J, Mas M, Molins E, Lanfranc de Panthou F, Laugier J, Park JG, Paulsen C, Rey P, Rovira C, Veciana J (1995) Chem Commun 709
7. Caneschi A, Ferraro F, Gatteschi D, Le Lirzin A, Novak MA, Rentschler E, Sessoli R (1995) Adv Mater 7:476
8. Romero FM, Ziessel R, Drillon M, Tholence JL, Paulsen C, Kyritsakas N, Fisher J (1996) Adv Mater 8:826
9. Hirel C, Luneau D, Pécaut J, Öhrström L, Bussière G, Reber C (2002) Chem Eur J 8:3157
10. Inoue K, Iwamura H (1994) J Am Chem Soc 116:3173

11. Inoue K, Hayamizu T, Iwamura H, Hashizume D, Ohashi Y (1996) J Am Chem Soc 118:1803
12. Iwamura H, Inoue K, Koga N (1998) New J Chem 201
13. Luneau D, Romero FM, Ziessel R (1998) Inorg Chem 37:5078
14. Fegy K, Luneau D, Ohm T, Paulsen C, Rey P (1998) Angew Chem Int Ed 37:1270
15. Caneschi A, Gatteschi D, Sessoli R, Rey P (1989) Acc Chem Res 22:392
16. Matsuda K, Irie M (2000) J Am Chem Soc 122:7195
17. Nakano M, Yamada S, Yamagushi K (1998) Bull Chem Soc Jpn 71:845
18. McCarthy PJ, Güdel HU (1988) Coord Chem Rev 88:69
19. Mathonière C, Kahn O, Daran JC, Hilbig H, Kohler FH (1993) Inorg Chem 32:4057
20. Mathonière C, Kahn O (1994) Inorg Chem 33:2103
21. Ullman EF, Osiecki JH, Boocock DGB, Darcy R (1972) J Am Chem Soc 94:7049
22. Karayannis NM, Paleos CM, Mikulski CM, Pytlewski LL, Blum H, Labes MM (1973) Inorg Chim Acta 7:74
23. Richardson PF, Kreilick RW (1977) J Am Chem Soc 99:8183
24. Yoshida T, Kanamori K, Takamizawa S, Mori W, Kaizaki S (1997) Chem Lett 603
25. Yoshida T, Suzuki T, Kanamori K, Kaizaki S (1999) Inorg Chem 38:1059
26. Lescop C, Luneau D, Bussière G, Triest M, Reber C (2000) Inorg Chem 39:3740
27. Lescop C, Luneau D, Rey P, Bussière G, Reber C (2002) Inorg Chem 41:5566
28. Beaulac R, Bussière G, Reber C, Lescop C, Luneau D (2003) New J Chem 27:1200
29. Tsukuda T, Suzuki T, Kaizaki S (2002) J Chem Soc, Dalton Trans 1721
30. Ogita M, Yamamoto Y, Suzuki T, Kaizaki S (2002) Eur J Inorg Chem 886
31. Tsukahara Y, Iino A, Yoshida T, Suzuki T, Kaizaki S (2002) J Chem Soc Dalton Trans 181
32. Lescop C, Luneau D, Belorizky E, Fries P, Guillot M, Rey P (1999) Inorg Chem 38:5472
33. Lescop C, Belorizky E, Luneau D, Rey P (2002) Inorg Chem 42:3375
34. Davis MJ, Reber C (1995) Inorg Chem 34:4585
35. Bussière G, Beaulac R, Cardinal-David B, Reber C (2001) Coord Chem Rev 219/221:509
36. Herzberg G (1950) Molecular spectra and molecular structure I. Diatomic molecules. D. Van Nostrand Company, Toronto, New York, London, pp 421, 558
37. MacSpartan Pro, version 1.0.4 (2000) Wavefunction, Irvine, CA 92612. Molecular orbitals were calculated with the SVWN density functional method and the DN^* basis set
38. Yoshioka N, Irasawa M, Mochizuki Y, Kato T, Inoue H, Ohba S (1997) Chem Lett 251
39. Zheludev A, Barone V, Bonnet M, Delley B, Grand A, Ressouche E, Rey P, Subra R, Schweizer J (1994) J Am Chem Soc 116:2019
40. Zheludev A, Bonnet M, Luneau D, Ressouche E, Rey P, Schweizer J (1995) Phys B Condens Matter (Amsterdam) 213/214:268
41. Ressouche E, Boucherle JX, Gillon B, Rey P, Schweizer J (1993) J Am Chem Soc 115:3610
42. Zoppellaro G, Ivanova A, Enkelmann, V, Geies A, Baumgarten M (2003) Polyhedron 22:2099
43. Claiser N, Souhassou M, Lecomte C, Pontillon Y, Romero F, Ziessel R (2002) J Phys Chem B 106:12896
44. Wexler D, Zink JI, Reber C (1992) J Phys Chem 96:8757
45. Fettouhi M, Ali BE, Morsy M, Golhen S, Ouahab L, Guennic BL, Saillard J-Y, Daro N, Sutter J-P, Amouyal E (2003) Inorg Chem 42:1316
46. Benelli C, Dei A, Gatteschi D, Güdel HU, Pardi L (1989) Inorg Chem 28:3089

47. Yamamoto Y, Suzuki T, Kaizaki S (2001) J Chem Soc Dalton Trans 1566
48. Grey JK, Butler IS, Reber C (2002) J Am Chem Soc 224:9384
49. Grey JK, Butler IS, Reber C (2003) Inorg Chem 42:6503
50. Romanenko GV, Fokin SV, Vasilevskii SF, Tret'yakov EV, Shvedenkov YG, Ovcharenko VI (2001) Russ J Coord Chem 27:360
51. Tsukahara Y, Kamatani T, Suzuki T, Kaizaki S (2003) J Chem Soc Dalton Trans 1276
52. Benelli C, Caneschi A, Gatteschi D, Pardi L (1992) Inorg Chem 31:741

Top Curr Chem (2004) 241:119–165
DOI 10.1007/b96862

Electronic Spectroscopy and Photoreactivity of Transition Metal Complexes: Quantum Chemistry and Wave Packet Dynamics

Chantal Daniel (✉)

Laboratoire de Chimie Quantique, UMR 7551 CNRS/Université Louis Pasteur,
4 Rue Blaise Pascal, 67000 Strasbourg, France
daniel@quantix.u-strasbg.fr

Abstract The most significant developments in quantum chemistry and wave packet dynamics providing the theoretical tools to study the electronic spectroscopy and photoreactivity of transition metal complexes are presented. The difficulties inherent to this class of molecules as well as the degree of maturity of the computational methods are discussed. Recent applications in transition metal coordination chemistry are selected to outline and to illustrate the necessity for a strong interplay between theory and experiments.

Keywords Quantum chemistry · Potential energy surfaces · Wave packet propagations · Photodissociation dynamics

List of Abbreviations

B3LYP	Becke's three parameters Lee, Yang, Parr functional
CASPT2	Complete Active Space Perturbation Theory 2nd Order
CASSCF	Complete Active Space SCF
CCSD	Coupled Cluster Single Double
CCSD(T)	CCSD (Triple)
CI	Configuration Interaction
DFT	Density Functional Theory
EOM-CCSD	Equation of Motion CCSD
MC-SCF	Multiconfiguration-SCF
MP2	Moller Plesset 2nd Order
MR-CI	Multireference CI
MS-CASPT2	Multistate CASPT2
RASSCF	Restricted Active Space SCF
RHF	Restricted Hartree Fock
SAC-CI	Symmetry Adapted Cluster-CI
SCF	Self Consistent Field
SS-CASPT2	Singlestate CASPT2
TD-DFT	Time Dependent-Density Functional Theory
Δ-SCF	Delta-SCF

1 Introduction

The visible-UV absorption spectrum of transition metal complexes is characterized by a high density of various electronic excited states (Metal-Centred, Metal-to-Ligand-Charge-Transfer, Ligand-to-Ligand-Charge-Trans-

fer, Sigma-Bond-to-Ligand-Charge-Transfer, Intra-Ligand, Ligand-to-Metal-Charge-Transfer). The presence of electronic states of different nature, localisation, dynamics and reactivity in a limited domain of energy gives to this class of molecules unconventional photophysical and photochemical properties and explains the versatility and the richness of their photochemistry [1, 2]. Moreover these specific properties responsible for the occurrence under irradiation of fundamental physico-chemical processes such as electron/energy transfer, bonds breaking or formation, isomerisation, radicals formation, luminescence can be tailored chemically and more recently controlled by shaped laser pulses [3]. Two contrasted behaviours can be considered: after irradiation the molecular system can either be trapped in long-lived excited states of well defined structure leading to beautiful resolved absorption/emission spectroscopy or land on repulsive potential energy surfaces inducing extremely fast ligand dissociation in femtosecond time-scale. The bipyridine substituted complexes intensively studied over the last 30 years are representative of the first category [4] whereas transition metal carbonyls illustrate the second behaviour [5, 6]. Most of the time bound and repulsive electronic excited states coexist in a limited domain of energy and may interfere in the Franck-Condon region generating structureless absorption spectra. The interaction between various electronic states in different regions of the potential energy surfaces leads to critical geometrical structures such as saddle points, conical intersections or local minima. Consequently the observed response to the light of the molecular system is entirely governed by the sequence of many concurrent elementary processes. The development of short time resolved spectroscopy [7] (picoseconds–femtoseconds time-scale) in different domains (resonance Raman, FT-Infra-Red, FT-Electron Paramagnetic Resonance, emission, absorption UV/visible) has contributed to a better understanding of excited states structures and processes that are very fast even at low temperature. However several fundamental questions still remain to be solved. One important aspect is the differentiation between i) chemically active electronic states leading to bonds breaking or formation, isomerisation, radicals production and ii) long-lived excited states involved in the photophysics or subsequent secondary processes such as electron/energy transfer. The photo-induced reactivity in transition metal complexes is characterized by the occurrence of several schemes of fragmentation originated in complicated mechanisms. These mechanisms involve different electronic states and various reaction paths and elementary processes such as direct/indirect dissociation, internal conversion or intersystem crossing. The simulation of the dynamics following the photon absorption is not an easy task and two different situations have to be considered: i) ultra-fast direct dissociation from the absorbing state itself (adiabatic process); ii) indirect dissociation via internal conversion or intersystem crossing (non-adiabatic process). A third case, not contemplated

here, would be the trapping in long-life time excited states followed by emission to the electronic ground state, inhibiting reactivity.

The determination of the various channels and time scales of deactivation of the excited molecule is especially important. For this purpose a strong interplay between experiments and theory is mandatory. The first role of the theoretical study is to clarify the electronic structure of the complexes, to determine the low-lying electronic transitions and to assign the observed bands. This is probably the easiest task and several computational methods started to emerge in the 1990s able to describe with reasonable accuracy electronic spectroscopy in transition metal complexes (see next section). The second aspect related to the calculation of accurate multidimensional potential energy surfaces describing the reactivity of electronic excited states is the bottleneck of the theoretical study. In contrast to the impressive development in the past 15 years of methods based on the energy gradient formalism and adapted to the description of ground state reactivity [8], only a limited number of approaches can be contemplated to obtain a more or less complete characterization of the shape of several excited states potential energy surfaces. The main difficulty is related to the dimensionality of the problem which cannot be solved exactly due to the large number of nuclear coordinates. This implies a selective choice of a few degrees of freedom in the treatment of the dynamics which has to include several coupled electronic excited states, either non-adiabatically or by spin-orbit.

The next section devoted to the quantum chemical methods and concepts gives a survey of the computational schemes and theoretical tools adapted to the investigation of electronic spectroscopy and photoreactivity in transition metal complexes. The solvent and other environmental effects are not discussed here and are not taken into account in the selected applications described in the later sections dedicated to the electronic spectroscopy and photoreactivity, respectively.

2 Quantum Chemical Methods

The investigation of the electronic structure, the determination of the low-lying electronic transitions and the assignment of the observed bands is the first goal of the theoretical study. The second aspect of the theoretical study relates to the calculation of accurate multidimensional potential energy surfaces (PES) describing the reactivity of electronic excited states. The PES play a central role in the understanding of chemical/photochemical reactions mechanism, the quantum description of the nuclear motion being determined by the shape of the PES. When handling transition metal complexes the quantum chemical calculations giving access to the potential energy and to the properties involved in electronic spectroscopy and photochemical

reactivity (transition dipole moments, spin-orbit coupling, non-adiabatic coupling) cannot be routinely performed. However the development of efficient theories and algorithms combined with the availability of very fast computers has enabled such challenging computations which have to be carried out with care. The next sections aim at describing the theoretical procedures and the most significant developments in the field.

2.1 Basis Sets Effects and Effective Core Potentials

Despite the fact that exact atomic orbitals are inaccessible, atomic orbitals represent the most suitable set of functions for expanding molecular orbitals in the LCAO (Linear Combination of Atomic Orbitals) formalism. In nearly all ab initio calculations reported today basis sets of contracted Gaussians are used. In order to be adapted to excited states calculations in molecular systems containing transition metal atoms the basis sets have to be constructed taking into account several aspects: i) the various electronic configurations of the metal centre; ii) the level of calculation; iii) the description of the outer region of the charge density cloud. Basis sets required for an accurate description of ground state properties may be inadequate for the investigation of the electronic spectroscopy. Highly correlated methods such as MC-SCF, MR-CI or CCSD (T) will need more complete basis sets than single determinantal methods of Hartree-Fock (HF) type. In order to describe correctly the outer region of the charge density cloud diffuse functions will be necessary in the case of Rydberg states [9]. Polarization functions (basis functions with L-quantum numbers higher than the valence L-quantum number) may be important to describe significant displacement of electron density as in Metal-to-Ligand-Charge-Transfer states for instance. The difficulty is to find the best compromise between the computational cost and the accuracy. In this respect the scheme of contraction will be very important. For second- and third-row transition metal complexes the use of Effective Core Potentials (ECP) including relativistic effects and associated valence basis sets is a good compromise. For first-row transition metal complexes Atomic Natural Orbitals (ANO) [10, 11] constructed by averaging the corresponding density matrix over several electronic configurations (ground state, valence excited states, positive and negative ions) are required to obtain good structural properties, ionisation potentials, electron affinity and transition energies. Finally as in ground state molecular calculations the choice of the basis sets associated to the surrounding ligands has to be coherent with the basis sets chosen for the metal centre, especially for a good description of Metal-to-Ligand-, Sigma-Bond-to-Ligand- or Ligand-to-Metal Charge-Transfer states. The lower limit as far as the basis sets quality is concerned for standard correlated calculations (CASSCF, MR-CI, MS-CASPT2 or TD-DFT) in middle size transition metal complexes is at least Double-

Zeta with polarization functions for the second-row atoms and Triple-Zeta for the metal atoms. Highly correlated methods such as the CCSD theory are even more demanding in term of basis sets quality and this is one of the limiting steps for further applications in the field of transition metal complexes electronic spectroscopy [12].

In the calculations based on effective potentials the core electrons are replaced by an effective potential that is fitted to the solution of atomic relativistic calculations and only valence electrons are explicitly handled in the quantum chemical calculation. This approach is in line with the chemist's view that mainly valence electrons of an element determine its chemical behaviour. Several libraries of relativistic Effective Core Potentials (ECP) using the frozen-core approximation with associated optimised valence basis sets are available nowadays to perform efficient electronic structure calculations on large molecular systems. Among them the pseudo-potential methods [13–20] handling valence node less pseudo-orbitals and the model potentials such as AIMP (ab initio Model Potential) [21–24] dealing with node-showing valence orbitals are very popular for transition metal calculations. This economical method is very efficient for the study of electronic spectroscopy in transition metal complexes [25, 26], especially in third-row transition metal complexes.

2.2 Electron Correlation

Whatever physical reasons may exist for the correlated behaviour of the electrons—electron repulsion or Pauli anti symmetry principle—the effect is always to modify the electron-repulsion energy calculated from the electron distribution of the system. In the Hartree-Fock (HF) approximation one solves equations describing the behaviour of each electron in the averaged filed of the remaining (n−1) electrons. However the motions of the [n(n−1)]/2 pairs of electrons are correlated and the electron correlation energy is defined as

$$E_{corr} = E_{exact} - E_{HF} \quad (1)$$

The most obvious way to include the correlation effects is to go beyond the single configuration representation of the electronic wave function. For a stable molecule at the equilibrium geometry the need to go beyond the single-determinant approach is governed by the aim at describing correctly the detailed correlated motion of the electrons as induced by their instantaneous mutual repulsion. This effect is equally important in electronic ground and excited states. This is the dynamical correlation arising from the Coulomb repulsion.

Another reason for going beyond the single configuration scheme is related to near degeneracy effects which mean that several configurations will in-

teract strongly and cannot be treated separately from each other. This effects so-called static or non-dynamical correlation which is especially important in transition metals already at the atomic level where several electronic configurations are nearly degenerate. Moreover in transition metal complexes characterized by a high density of electronic states in a limited domain of energy the computation of reliable absorption spectra has to include this effect at the zero-order level, namely when computing the reference wave function. The static correlation energy is also very important at the molecular dissociation limit where several states may be necessary to describe the electronic structure of the products of dissociation. This is illustrated in Scheme 1 by the formation of di-radical fragments arising from metal-hy-

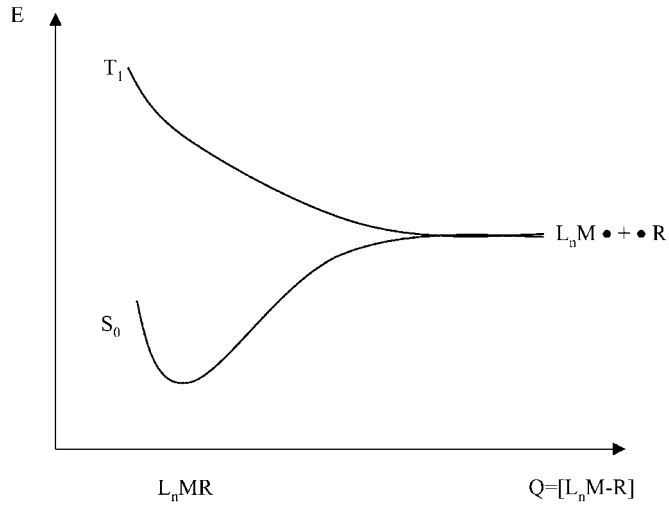

Scheme 1

drogen, metal-alkyl or metal-metal bonds homolysis (in L_nMR complexes) described by two degenerate states at dissociation, namely the triplet T_1 corresponding to the $(\sigma_g)^1(\sigma_u)^1$ electronic configuration and the singlet S_0 corresponding to the two-determinantal $(\sigma_g)^2(\sigma_u)^0-(\sigma_g)^0(\sigma_u)^2$ configuration (the σ_g and σ_u orbitals being the metal-hydrogen, metal-metal or metal-alkyl bonding and anti-bonding orbitals, respectively).

Finally, when handling photochemical reactions near degeneracy effects may also occur along the reactive pathways at critical geometries (avoided crossings, conical intersections) where the nature of the electronic wave function changes abruptly as a function of the nuclear displacement by mixing with upper electronic states. The multiconfiguration approach is necessary to describe correctly these areas of the potential energy surfaces (PES).

The difficulty for the quantum chemist interested by the description and the understanding of electronic spectroscopy and photoreactivity in transition metal complexes will be to take into account in a coherent and consistent way these different effects which are not always easily distinguishable from each other. It is noteworthy that a full CI approach which would include in the expansion the full set of determinants of the appropriate spin and space symmetry generated by distributing all electrons among all molecular orbitals would be impractical.

2.3 Relativistic and Spin-Orbit Effects

Molecules that contain heavy elements (in particular 5d transition metals) play an important role in the photochemistry and photophysics of coordination compounds for their luminescent properties as well as for their implication in catalysis and energy/electron transfer processes. Whereas molecular properties and electronic spectroscopy of light molecules can be studied in a non-relativistic quantum chemical model, one has to consider the theory of relativity when dealing with elements that belong to the lower region of the periodic table. As far as transition metal complexes are concerned one has to distinguish between different manifestations of relativity. Important but not directly observable manifestations of relativity are the mass velocity correction and the Darwin correction. These terms lead to the so-called *relativistic contraction* of the s- and p- shells and to the *relativistic expansion* of the d- and f- shells. A chemical consequence of this is for instance a destabilisation of the 5d shells with respect to the 3d shells in transition metals.

Another important evidence of relativity in electronic spectroscopy and photo- reactivity is the spin-orbit coupling. Indeed the coupling between the spin and orbital momentum breaks the strict spin selection rules deduced from non-relativistic quantum theory. The influence of this coupling between singlet and triplet electronic states on the spectra of transition metal complexes may be profound. The potential energy surfaces associated to the triplet states degenerate in the non-relativistic approximation are split according to the symmetry rules of the molecular point double group representation (Scheme 2). Consequently new critical geometries such as avoided crossing or conical intersection where non-radiative transitions may take place efficiently will appear leading to complicated shapes modifying drastically the photo- reactivity.

One fundamental aspect in the understanding of the photochemical behaviour of transition metal complexes is the role of the triplet states on the photoreactivity. The calculation of Spin-Orbit Coupling (SOC) effects is mandatory and should be performed in connection with highly correlated methods. The zero-field splitting of triplet molecular states can be calculated by the means of perturbation theory until the spin-orbit effects are not of

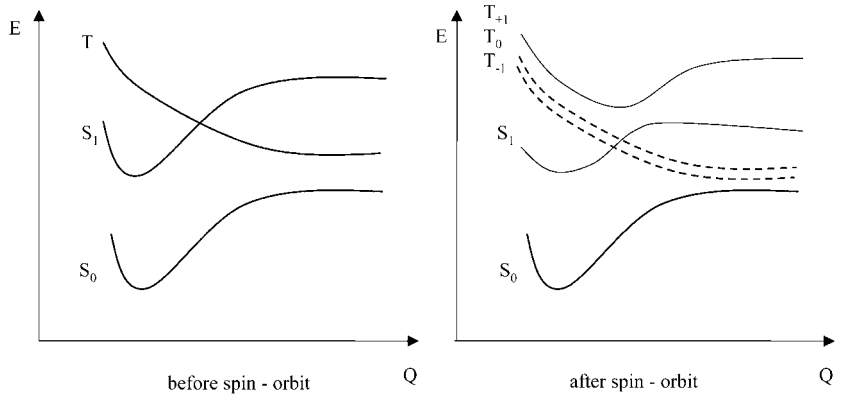

Scheme 2

equal size of the other electronic interactions [27]. When the treatment of SOC is required on the same footing with other interactions (heavy elements) it is necessary to go beyond the perturbation theory using a variational approach based on a spin-orbit Hamiltonian [28]. A very promising approach has been recently proposed accounting for spin-orbit polarization effects on multiconfigurational wave functions [29]. A sophisticated correlation treatment in a scalar relativistic approximation is carried out in a first step. A model space which includes a set of reference configurations able to represent all the wanted states along with singly excited configurations selected with the Spin-Orbit operator is defined in a second step. An extension of the combined DFT/MRCI method to spin-orbit effects has been proposed recently which is able to evaluate spin-dependent properties for excited electronic states in large molecular organic systems [30]. To the state of our knowledge this promising method has never been applied to the electronic spectroscopy of transition metal complexes.

2.4 Computational Methods

The goal is to obtain accurate transition energies (within 0.10 eV–0.15 eV) and reliable dipole transition moments in order to assign bands located in the UV-visible spectral domain of energy in various transition metal complexes. The size of the molecular system, its symmetry and the density of states as well as the saturation of the metal centre d shells or the metal-ligand interactions will generate particular difficulties. The choice of the method will be a compromise taking into account the following factors: i) the feasibility and computational cost; ii) the validity of some approximations; iii) the wanted level of accuracy; iv) the control that can be performed on the analysis of the results. Four types of methods based on different

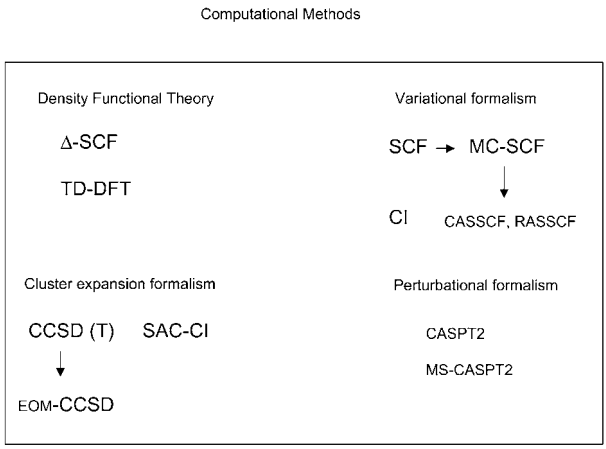

Scheme 3

mathematical formalisms are available for treating electronic spectroscopy in transition metal complexes (Scheme 3): i) the Density Functional Theory (DFT) like the Delta-Self-Consistent Field (Δ-SCF) [31–36] and Time-Dependent DFT (TD-DFT) [37–40]; ii) the variational approaches such as the Self-Consistent-Field (SCF) [41, 42], Configuration Interaction (CI) [43–46], Multi Configuration SCF (MC-SCF) [47–49], Multireference CI (MR-CI) [48, 50]; iii) the cluster expansion methods such as the Equation of Motion Coupled Cluster Single Double (EOM-CCSD) [51–55], the Symmetry Adapted Cluster CI (SAC-CI) [56–58]; iv) the Single State (SS) or Multistate (MS) 2nd Order perturbational approaches applied to zeroth-order variational wavefunctions and so-called SS-CASPT2 [59–61] and MS- CASPT2 [62]. Most of the methods discussed in the present chapter are present in the quantum chemical software: MOLCAS [63], GAUSSIAN [64], MOLPRO [65], TURBOMOLE [66], ACESII [67], ADF [68], HONDO [69].

2.4.1 Variational Methods

The few attempts at describing excited states in transition metal complexes within the Restricted Hartree Fock (RHF) formalism were rapidly abandoned due to the computational difficulties (convergence of the low-lying states in the open-shell formalism) and theoretical deficiencies (inherent lack of electronic correlation, inconsistent treatment of states of different multiplicities and d shell occupations). The simplest and most straightforward method to deal with correlation energy errors is the Configuration Interaction (CI) approach where the single determinant HF wave function is extended to a wave function composed of a linear combination of many de-

terminants in which the coefficients are variationally optimised. Within the CI formalism the configuration mixing is introduced (multi-determinantal approach) but the predetermined reference set of molecular orbitals is not reoptimised for the different electronic states. However most of the time and especially in transition metal complexes strong correlation effects affect the electron density. Therefore it is necessary to optimise the molecular orbitals according to a multi-configurational scheme including static electronic correlation effects which describe the interaction between two electrons in a pair at large separation space. The so-called MC-SCF method and its extension CASSCF (Complete Active Space SCF) [70, 71] or RASSCF (Restricted Active Space SCF) [72] methods have their origin in this fundamental problem. These methods provide zero-order wave functions used as references in subsequent CI, MR-CI or MS-CASPT2 calculations which take into account the dynamical correlation effects describing the interaction between two electrons at short inter-electronic distance (so-called cusp region). Obviously the MC-SCF approach is even more crucial in excited states calculations where electronic states mixing and dramatic changes of electron density during the excitation have to be taken into account. The large variation in the number of d electrons pairs among the various electronic states is one major difficulty when correlated methods are applied to transition metal complexes. The most widely used MC-SCF method is the CASSCF based on a partitioning of the occupied molecular orbitals into subsets corresponding to how they are used to build the wave function. The problem is reduced to the partition into sets of active and inactive orbitals and to a selection of correlated electrons. This discriminating strategy based on the physics and chemistry of the study includes all configuration state functions (CSFs) which are generated by distributing the active electrons among the active orbitals in all possible ways consistent with the spin and the symmetry of the wave function. In practical applications where the number of configurations may exceed 10^6 and the size of the active space may vary between 2e2a (where 2 electrons are correlated into 2 active orbitals) and 16e16a (where 16 electrons are correlated into 16 active orbitals) such a partitioning is not straightforward. The validity of the subsequent MR-CI or MS-CASPT2 treatments depends entirely on the quality of the CASSCF wave function and this strategy not easily automated cannot be used as a black-box. Most of the time the orbitals are optimised for the average energy of a number of excited states large enough to include the electronic spectrum of interest. This procedure avoids roots inversions as well as convergence problems and leads to a set of orthogonal wave functions of given spin and symmetry and to transition densities of reasonable accuracy used in properties calculation (dipole transition moments). The transition energies accuracy is obtained by the addition of the remaining correlation effects by means of MRCI or MS-CASPT2 calculations. If the active space can be chosen large enough according to the physico-chemical aspect of the problem results of high accu-

racy will be produced by the CASSCF/CI procedure where the configuration selection scheme on the top of the CASSCF wave function is performed by single and double replacement out of either a single reference (CI) or multi-reference space (MRCI). The slow convergence of the method, the size of which increases dramatically with the number of references and the default of size-extensivity leading to incorrect scaling of the energy with the number of correlated electrons are very limiting for a general use of the MR-CI formalism in non-trivial applications.

2.4.2 Second Order Perturbational Approach

An alternative to the fully variational approach depicted above is a mixed procedure where a multi-configurational variational method is used to build a zero-order wavefunction supplemented by a second order perturbational treatment of the dynamical correlation effects. The so-called CASPT2 and its multistate extension MS-CASPT2 methods [59–62] are size-extensive and give very accurate transition energies as soon as the variational wave function includes correctly at the zero-order the spectroscopy of the system under study. Otherwise the perturbational treatment is no longer valid due to the presence of intruder states interacting with the reference space and not included at the zero-order level. This leads to an erratic behaviour of the perturbation and to out of range transition energies by more than 2.0 eV. In these non-trivial cases either a level-shift technique has to be applied with care (weak intruder states) [73] or the CASSCF active space has to be increased (strong intruder states) as illustrated by the theoretical study of the spectroscopy of $Mn_2(CO)_{10}$ [74] or $HRe(CO)_5$ [25].

It is a general practice to evaluate the oscillator strength by combining the transition dipole moment calculated from the CASSCF wave functions and the transition energies computed at a higher correlated level (CASPT2). This approach relies on the hypothesis that dynamical correlation does not induce strong inter-state coupling between the various states. This condition does not hold when using a state-average zero-order CASSCF wavefunction extended over a wide range of states of different characters which affects the quality of the computed transition dipole moments. Therefore the transition dipole moment elements calculated with the multi-state CASPT2 eigenvectors turned out to be significantly better and more representative of the physics of the molecule.

2.4.3 Cluster Expansion Methods

The cluster expansion methods are based on an excitation operator which transforms an approximate wave function into the exact one according to the exponential ansatz

$$\Psi = \exp(\mathrm{T})|0\rangle \tag{2}$$

where T is a sum of single- to N-particles excitation operators (Coupled-Cluster theory) [75–77] or of symmetry adapted single- to N-particles excitation operators (Symmetry Adapted Cluster theory) [78]. The simplest truncation of T is to the 2nd Order where the single and double excitations are included in the cluster expansion (CCSD [79] or SAC) based on the HF single determinant $|0\rangle$. When electron correlation effects are dominated by pair effects these methods recover 90–95% of the exact correlation energy if the wave function is described by a dominant closed-shell determinant. The remaining correlation effects due to higher excitations are estimated by approximate methods like in the CCSD(T) approach [80] where the triple excitations are included perturbationally. These methods based on a separated electronic pairs approach in which pair clusters are used to describe the correlation between two electrons are size-extensive by definition and independent on the choice of reference orbitals. However, these methods which converge efficiently are hardly generalized to multi-reference starting wave functions. As far as the excited states and associated properties are concerned two cluster expansion based methods developed originally for open-shell situations have been proposed. The first one so-called SAC-CI method [56–58] supposes that the major part of electron correlation in the closed-shell ground state is transferable to the excited states since the excitation of interest involves only one and/or two electrons. These transferable dynamical correlation effects are expressed through an exponential operator and a linear operator is used to represent the non-transferable state-specific correlation effects such as quasi-degeneracy's. The absorption spectrum of $TiCl_4$ has been reinvestigated on the basis of this method leading to a perfect agreement with experimental data and a new assignment with an accuracy of the order of 0.15 eV [81]. In the CC based methods, so-called equation-of-motion CCSD (EOM-CCSD) [51–55] ionisation potentials, electron affinities and excitation energies are obtained directly from the equation of motion operating on the ground state wave function. This approach characterized by an unambiguous treatment of excited states where the only choices are the atomic basis sets and the excitation level of the operators is very demanding computationally and has been applied to only one transition metal complex, namely $FeCl_4^-$ leading to promising results for charge transfer transitions from the $^6A_1$ ground state [82]. A recent workable extension so-called extended similarity transformed EOM-CCSD (extended-STEOM-CC)

[12] has been applied with more or less success to a few transition metal compounds.

2.4.4 Density Functional Based Methods

The optical spectra of transition metal complexes have long been interpreted by means of DFT methods. However the Kohn-Sham orbitals calculated within the DFT formalism describe the electronic ground state in a single determinant scheme. While this method was well established for the ground state and the lowest states within a symmetry class from its early days its extension to excited states description is still in development. The first option proposed in 1977 by Ziegler and Baerends [83] within the framework of the time-independent formalism and generalized in 1994 by Daul [84] (so-called Δ-SCF method) is based on symmetry-dictated combinations of determinants able to evaluate in a non ambiguous way the space and spin multiplets. It has been applied with success to a variety of highly symmetric molecules [84]. However several limitations make this approach accessible to experts in the subject [85].

An alternative to the time-independent DFT method is the so-called time-dependent DFT (TD-DFT). This method based on the linear response theory is the subject of recent and promising theoretical developments [85–87]. The treatment of molecular properties by means of the linear response of the charge density to an applied field is based on a well founded formalism that allows direct computation of polarisabilities, excitation energies and oscillator strengths within the framework of the DFT. Only excitations corresponding to linear combinations of singly excited determinants are included like in single excitations Configuration Interactions (CIS) but taking into account additional electronic correlation effects. The accuracy of the response calculation is very sensitive to the approximation made for the exchange-correlation potential v_{xc} as well as to its repercussion on its derivative $\partial v_{xc}/\partial\rho$ (derivative discontinuity in the bulk region). Due to an underestimation of the attractive character of the exchange-correlation potential the charge density will be too diffuse. Consequently the ionisation threshold will be systematically too low with a dramatic effect on high excitation energies and polarisabilities which will be overestimated. Moreover excitations involving a substantial change in the charge density like charge transfer states will be described with difficulty by conventional functionals. In spite of these drawbacks the TD-DFT approach remains a computationally simple and efficient method able to treat practical problems in a reasonable time scale at a low cost as compared to highly correlated ab initio methods [88–93]. For medium size molecules or transition metal complexes TD-DFT results have been shown to be competitive with the highest level ab initio ap-

proaches but cases where current exchange-correlation functionals dramatically fail are known to exist [94, 95].

The calculated dipole transition moments are very sensitive to the quality of the calculation, namely the basis sets and the functional used [96]. Obviously they rely on the hypothesis that DFT excited states are well defined, an assumption which is not always true as explained above. Some functionals have been found to be more sensitive to the basis set quality than others.

2.5 Potential Energy Surfaces

In principle photochemical mechanisms are described by reaction paths on ground and excited states PES which can be determined according to the procedures developed for chemical reactivity. The new problem in photo-induced mechanisms is the complicated landscape of the PES characterized by the presence of a variety of critical geometries such as minima, transition states, high-order saddle points, avoided crossings, conical intersections resulting from non-adiabatic interactions between N-Dimensional PES. For a given atomic basis set the computational method used to solve the electronic problem has to be flexible enough to characterize correctly different regions of the molecular PES at the same level of accuracy. An inadequate wave function would result in a biased description of the different regions and such computed PES would not reproduce the exact BO potentials.

One of the most significant advances made in applied quantum chemistry in the past 20 years is the development of computationally workable schemes based on the analytical energy derivatives able to determine stationary points, transition states, high-order saddle points and conical intersections on multidimensional PES [8]. The determination of equilibrium geometries, transition states and reaction paths on ground state potentials has become almost a routine at many levels of calculation (SCF, MP2, DFT, MCSCF, CCSD, CI) for molecular systems of chemical interest [97, 98]. The availability of reliable and efficient analytic energy gradient procedures (first and second derivative) for the search of various critical points on several interacting complex surfaces at high correlated level (CASSCF, CCSD(T) and its extension EOM-CCSD, MR-CI) will have a significant impact in the theoretical study of transition metal photo-reactivity. Indeed, although reaction paths are uniquely defined in any coordinate system they cannot be determined unambiguously without the knowledge of reference points on the PES from which the analytical energy derivation procedure may start. Unfortunately the derivative formulation for highly correlated wave functions is very complex and if analytical first derivatives are available for the standard methods second derivatives calculations are even more complicated.

Density functional methods are competitive with the above traditional wave functions methods for numerous applications among them the compu-

tation of ground state PES. A few applications to transition metal photochemistry have been proposed on the basis of the Δ-SCF approach implying several approximations on the excited states reaction paths definition by symmetry constraints not always appropriate in a "coordinate driving" scheme [99]. Excited-state gradients have been recently implemented in DFT for various functionals, the feasibility of the approach having been tested for small molecules only [100]. The mathematical and computational machinery for structure optimisation is based on several various algorithms the complexity of which depends on the wanted accuracy at the electronic level. The application of these methods to photochemical problems raises serious practical difficulties as illustrated above. The computation of accurate multidimensional PES for several interacting electronic states in transition metal complexes is beyond the actual capabilities. For simple mechanisms involving the electronic ground state interacting with one excited state the global structure of the low-energy part of the PES can be visualized within a 3-D cross section plotting the energy on a grid while the critical points (minima, transition states, conical intersections) are fully optimised using rigorous ab initio correlated methods (MC-SCF) [101, 102].

However, the high density of electronic states which characterizes the absorption spectrum of transition metal complexes generates very complicated PES involving several singlet and triplet states (8 to 12 in standard molecules) in the UV/Visible domain of energy. A systematic investigation of the full PES being practically intractable the study of photochemical processes in transition metal complexes is generally based on several approximations: i) the nuclear dimensionality is reduced to $N \leq 2$; ii) the reaction path is approximated by metal-ligand bond elongation coordinates; iii) the highest symmetry is retained along the reaction path; iv) a limited evaluation of geometrical relaxation effects in excited states is performed. These approximations are based on the following criteria: i) the observed or calculated structural deformations on going from the electronic ground state to the excited state; ii) the observed or calculated structural deformations on going from the reactant to the products; iii) the hierarchy in time of the various elementary processes participating to the photochemical behaviour. The validity of these approximations is checked on the basis of the observables directly comparable with the experimental data such as the bond dissociation energies, the main spectral features or the time-scales of primary reactions as illustrated in the applications section. In contrast, the electronic problem is treated by means of the most accurate quantum chemical methods in order to get a semi-quantitative characterization of electronic spectroscopy in the Franck-Condon region and a correct description of the dissociative processes. The analysis of the main topological characteristics of the PES represented by contour maps (2-D) or profiles (1-D) of the potentials $V(q_i)$ is the first step towards a qualitative understanding of the photochemical mechanisms.

2.6
Non-Adiabatic Processes

In an electronically non-adiabatic process the description of the nuclear motion involves more than one PES. Electronic spectroscopy and photochemical reactions involve transitions between two or more PES in critical regions (avoided crossings, conical intersections, crossings) where the nature of the electronic wave function may change rapidly as a function of the nuclear displacement. This is illustrated in Scheme 4 which represents two different

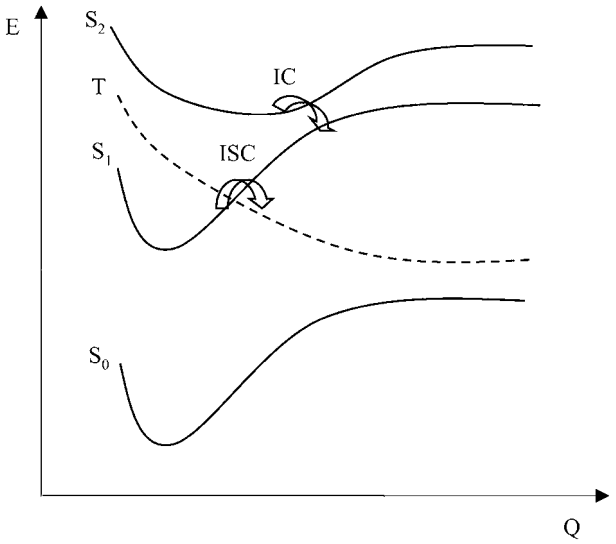

Scheme 4

situations, namely an internal conversion (IC) between electronic states of same multiplicity and an intersystem crossing (ISC) process between electronic states of different multiplicity.

The efficiency of the transition is governed by the non-zero interaction matrix elements between electronic states, the BO approximation being no longer valid. In order to determine the electronic structure aspects of an electronically non-adiabatic process it is necessary to determine: i) the critical regions of the PES; ii) the coupling between the states in these regions. The first point has been discussed in the previous section whereas the second point will be developed in the next section.

2.6.1 Adiabatic Representation

Within the Born-Oppenheimer approximation the adiabatic PES are obtained by calculating the electronic energy and wave function by the standard non-relativistic methods of quantum chemistry (see above) for a series of fixed nuclear geometries. This leads to avoided crossings (or conical intersections) between electronic states of same spin multiplicity and true crossings between electronic states of different spin multiplicity (Scheme 4). The non-adiabatic coupling between states of same multiplicity is given by the matrix elements of the kinetic energy operator. The calculation of the kinetic coupling terms requires the first and second derivatives of the electronic wave functions with respect to the nuclear coordinates. Although their determination is still delicate for polyatomic molecules, recent developments based on analytical derivatives techniques have allowed a direct computation of non-adiabatic couplings in the case of small triatomic molecules [103].

Apart from the calculation of the kinetic couplings, another difficulty arising in the adiabatic representation is the treatment at the same level of theory of the internal conversions (singlet to singlet or triplet to triplet transitions) and intersystem crossings (singlet to triplet transitions). Indeed, the adiabatic potentials are calculated in the non-relativistic approximation, the spin-orbit interaction being taken into account later on at a perturbational level of theory (see above). The singlet-singlet or triplet-triplet interactions characterized by avoided crossings are given by the matrix elements of the kinetic energy whereas the singlet-triplet interactions occurring at true crossings are determined by the spin-orbit potential coupling. Consequently when the transitions between states of same multiplicity are treated adiabatically the singlet-triplet transitions are described according to a '*quasi-diabatic*' picture.

2.6.2 Diabatic Representation

The sudden change of the adiabatic wave functions near an avoided crossing and the resultant large non adiabatic coupling elements in a narrow region of the PES make the adiabatic representation rather inconvenient for numerical applications. Moreover the 'non-adiabaticity' of the triplet potentials with respect to the non-relativistic Hamiltonian adds some difficulty in a coherent treatment of various non-radiative transitions. An electronic diabatic basis which changes smoothly across the region of avoided crossing can be obtained by unitary transformation of the electronic adiabatic basis. In the diabatic representation the kinetic couplings vanish exactly within the limit of a complete basis set. Unlike the adiabatic potentials, the diabatic potentials which are not eigenvalues of the electronic Schrödinger equation are allowed to cross (Fig. 1).

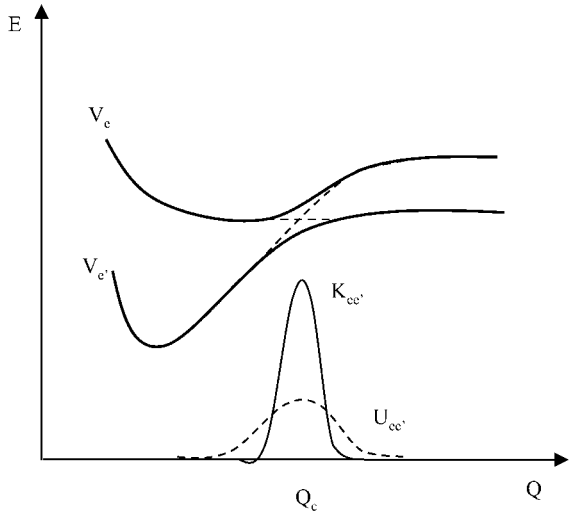

Fig. 1 Adiabatic potentials (*solid lines*) and diabatic potentials (*dashed lines*) corresponding to the electronic states e and e′. $K_{ee'}(Q)$ schematically represents the coordinate dependence of the non adiabatic coupling elements (adiabatic representation) whereas $U_{ee'}(Q)$ schematically represents the coordinate dependence of the non diabatic coupling elements (diabatic representation)

While the coupling between the adiabatic states is given by the off-diagonal elements of the matrix representation of T_{nu} (kinetic coupling) the coupling between the diabatic states arises from the off-diagonal elements of the matrix representation of H_{el} (potential coupling). At this stage transitions between states of same multiplicity and transitions between states of different multiplicity can be treated simultaneously in the diabatic representation considering that the triplet potentials are quasi-diabatic for the non-relativistic Hamiltonian. This approximation is valid only if the spin-orbit splitting of the triplet states is small as compared to the energy separation between the various electronic states

2.6.3 Diabatisation

The unitary transformation from a basis of adiabatic electronic states to a basis of diabatic electronic states is given by

$$V^d = U^+ V^a U \tag{3}$$

V^a being the matrix of the adiabatic electronic potentials (diagonal elements) and non-adiabatic couplings (off-diagonal elements) and V^d the matrix of the diabatic electronic potentials. The unitary matrix U is solution of the following equation:

$$\partial U/\partial Q + KU = 0 \tag{4}$$

where K is the matrix of the $K_{ee'}(Q)$ kinetic couplings between the adiabatic states e and e′ defined by (Q and q representing the nuclear and electronic coordinates, respectively)

$$K_{ee'}(Q) = \int dq \Psi_e^*(q,Q) \frac{\partial}{\partial Q} \Psi_{e'}(q,Q) \tag{5}$$

Since the numerical evaluation of these coupling terms on the basis of multiconfigurational wave functions is very demanding and is difficult to apply to polyatomic molecules the kinetic couplings have been approximate to asymmetric Lorentzian functions [104]

$$K_{ee'}(z) = \begin{cases} \dfrac{\Gamma^l_{ee'}}{4\left[z - z^c_{ee'}\right]^2 + \left(\Gamma^l_{ee'}\right)^2} \dfrac{\Gamma^l_{ee'}}{1/2\left(\Gamma^l_{ee'} + \Gamma^L_{ee'}\right)} & z \leqslant z^c_{ee'} \\ \dfrac{\Gamma^L_{ee'}}{4\left[z - z^c_{ee'}\right]^2 + \left(\Gamma^L_{ee'}\right)^2} \dfrac{\Gamma^L_{ee'}}{1/2\left(\Gamma^l_{ee'} + \Gamma^L_{ee'}\right)} & z \geqslant z^c_{ee'}. \end{cases} \tag{6}$$

with $\Gamma^l_{ee'}$ and $\Gamma^L_{ee'}$ being the parameters which define the shape of the Lorentzian function at mid-width and mid-height (Fig. 1) for a given nuclear coordinate z greater and smaller than the position of the avoided crossing (z^c). $\Gamma^l_{ee'}$ and $\Gamma^L_{ee'}$ are determined iteratively until coincidence between the diabatic and adiabatic potentials outside of the avoided crossing region. This simple procedure based on a crude estimation of the kinetic couplings has been applied with success to one-dimensional cuts of PES in transition metal complexes [104]. However, such a qualitative approach cannot be compared to exact calculations usually performed for describing highly resolved spectroscopy in small molecules.

2.7 Wave Packet Propagations

The motion of the molecular system under the influence of the potential is determined by the equations of dynamics. Consequently the shape of the computed PES governs entirely this motion. Since, as explained above, several approximations have to be made at the level of the dimensionality of the PES, it is very important to define clearly the initial conditions of the simulation and to estimate the hierarchy in time of the various elementary processes involved in the photochemical reactivity. In conventional photochemical experiments with long pulse duration and narrow frequency resolution only a few near-degenerate electronic states are directly populated. The energy is not large in excess and in a first approximation the reaction paths can be defined by the metal-ligand bond elongation coordinates corresponding to the observed photochemical reactions. In the case of very fast dissociative processes (10 fs to 1 ps) the system should not deviate signifi-

cantly from this 'pseudo minimum energy path' and the other many vibrational degrees of freedom can be frozen. Moreover there is no justification without any knowledge of the time scale of the dissociation for a full geometry optimisation along the excited states reaction paths as necessary in ground state reactivity studies. Typically one or two coordinates corresponding to the bond elongations describing the observed photochemical reactions (CO loss or Metal-R, R=H, Alkyl, Metal, X) are selected for building 1D or 2D PES, the other degrees of freedom being frozen to the Franck-Condon geometry [105, 106].

The quantum dynamics of photodissociation processes can be performed within the time-independent or time-dependent framework [107]. In the time-dependent picture used in the applications presented in the next section the time-dependent Schrödinger equation is solved:

$$i\hbar\frac{\partial}{\partial t}\varphi_e(t) = \hat{H}_e\varphi_e(t) \tag{7}$$

where $\varphi_e(t)$ is a wave packet (coherent superposition of all stationary eigenstates in the electronic excited state) evolving on the excited electronic state e potential. In order to describe the initial absorption followed by direct dissociation it is assumed that the initial vibrational state ϕ_{gi} in the electronic ground state multiplied by the transition dipole function μ_{eg} is instantaneously promoted by the photon to the upper electronic state (Scheme 5).

This initial wave packet that is not eigenstate of $\hat{H}_e$ starts to move under its action. The advantage of this approach is that the motion of the wave

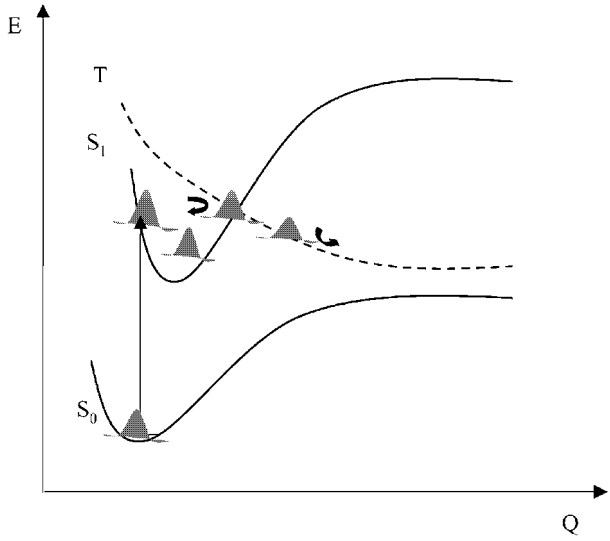

Scheme 5

packet, the centre of which remains close to a classical trajectory, can be followed in real time. The motion of the wave packet from the Franck-Condon region to the exit channel is described by the autocorrelation function

$$S(t) = \langle \varphi_e(0) | \varphi_e(t) \rangle \tag{8}$$

given by the overlap of the evolving wave packet with the initial wave packet at t=0. The absorption spectrum is calculated as the Fourier Transform of the autocorrelation function

$$\sigma_{\text{tot}}(\omega) \alpha \omega \int_{-\infty}^{+\infty} \text{dtS(t)} \, \text{e}^{\text{iEt}/\hbar} \tag{9}$$

where $E=E_i+\hbar\omega$ [108]. Wave packet calculations lead to the time-scale and probabilities of dissociation and to the branching ratio between concurrent primary processes occurring from a single electronic excited state. In the cases of indirect dissociative processes involving non-adiabatic transitions (jumps between different PES) a set of coupled time-dependent Schrödinger equations has to be solved:

$$\left.\begin{aligned} \text{i}\hbar \frac{\partial}{\partial \text{t}} \varphi_{\text{e}}(\text{t}) &= \hat{\text{H}}_{\text{e}} \varphi_{\text{e}}(\text{t}) + \text{V}_{\text{ee}'} \varphi_{\text{e}'}(\text{t}) \\ \text{i}\hbar \frac{\partial}{\partial \text{t}} \varphi_{\text{e}'}(\text{t}) &= \hat{\text{H}}_{\text{e}'} \varphi_{\text{e}'}(\text{t}) + \text{V}_{\text{e}'\text{e}} \varphi_{\text{e}}(\text{t}) \end{aligned}\right\} \tag{10}$$

with the same initial conditions than above but in a different basis so-called diabatic (see above) where the original adiabatic PES have been transformed in order to minimize the kinetic coupling between them and to introduce potential coupling terms $V_{ee'}$. This strategy is very efficient to describe simultaneously intersystem crossings and internal conversions, important processes in photo-induced reactivity in transition metal complexes. The wave packet approach yields to important quantities such as the time evolution of electronic states population, the dissociation probabilities or the branching ratio between concurrent processes.

3 Electronic Spectroscopy

The purpose of the next sub-sections devoted to the electronic spectroscopy of a variety of transition metal complexes is to illustrate the particularities characterizing this class of molecules and to outline the degree of methodological maturity in this field.

3.1
Electronic Spectroscopy of Transition Metal Carbonyls

3.1.1
$Ni(CO)_4$, $Cr(CO)_6$, $HM(CO)_5$ (M=Mn, Re) and $Mn_2(CO)_{10}$

Transition metal carbonyls constitute a very important class of complexes in laser chemistry as reactive precursors of catalytic processes, substitution reactions, chemical vapour deposition of thin films or layers on surfaces. They are among the most reactive transition metal complexes and their electronic structure has long been a matter of considerable interest stimulating theoretical research. Even though their experimental spectra have been known since the early 1970s, relatively little attention has been given to the electronic spectroscopy of the molecules reported in Table 1. A fundamental aspect of the theoretical study is related to the electronic correlation effects which are very important already at the electronic ground state level for a good description of the metal-CO bonding in these molecules. The results reported in Table 1 have been obtained by the means of correlated methods able to describe correctly the dπ-pπ back-bonding interaction in this class of molecules. The experimental spectrum in gas phase of $Ni(CO)_4$ (a d^{10} system) exhibits three bands attributed to MLCT $^1A_1 \rightarrow {}^1T_2$ transitions [109]. The TD-DFT [90], CASPT2 [110], SAC-CI [111] and EOM-CCSD [12] approaches give rise to three allowed transitions in the energy range of 4.0–6.5 eV in agreement with experiment leading to a reasonable assignment. The deviations on the transition energies never exceed 7%. The assignment of the upper bands in terms of one electron excitations in the principal configurations is quite sensitive to the level of calculation and is still a purpose of controversy.

The spectrum of $Cr(CO)_6$ (a d^6 system) is dominated by two very intense absorption bands assigned to MLCT $^1A_{1g} \rightarrow {}^1T_{1u}$ transitions and by low-lying shoulders originally attributed to weak MC transitions [112]. This assignment was confirmed by semi-empirical INDO/S CI [109] and SCF calculations [113, 114]. The more recent studies reported in Table 1 and based on ΔSCF [115], TD-DFT [88] and CASSCF/CASPT2 [110] methods reinterpreted the electronic spectrum of $Cr(CO)_6$. According to this new analysis the lowest part of the spectrum does not correspond to MC transitions but to orbitally and spin-forbidden MLCT states of low intensity not reported in Table 1 where only the intense bands observed at 4.43 eV and 5.41 eV are presented. If the TD-DFT and CASPT2 results are in excellent agreement with the experimental values the ΔSCF method overestimates by more than 20% the transition energies. These poor results are attributed to the inability of this approach to account for the configuration mixing which characterizes these two states.

The main features of the experimental spectra of $HMn(CO)_5$ and $HRe(CO)_5$ are alike with three main bands of increasing intensity when going from the low to the high energies: 4.31 eV [$HMn(CO)_5$] vs 4.63 eV [HRe

Table 1 Calculated electronic allowed transition energies (in eV) of $Ni(CO)_4$, $Cr(CO)_6$, $HM(CO)_5$ (M=Mn, Re) and $Mn_2(CO)_{10}$ by different methods

	ΔSCF[a] (DFT)	TD-DFT[b] (B3LYP)	CASSCF/ CASPT2[c]	MR-CI[d]	SAC-CI[e]	EOM-CCSD (Ext-STEOM)[f]	Exp.[g]
$Ni(CO)_4$							
1^1T_2		4.7	4.34		4.79	4.93 (4.24)	4.5–4.6
2^1T_2		4.82	5.22		5.51	5.35 (4.74)	5.4
3^1T_2		5.37	5.57		5.76	5.76 (5.03)	(5.2,5.5)
4^1T_2		5.84	6.28		-	6.39 (5.99)	6.0
5^1T_2		6.74	6.97		-		
$Cr(CO)_6$							
1^1T_{1u}	5.6	4.19 (3.91)	4.54–4.11				4.43
2^1T_{1u}	6.5	5.76 (5.37)	5.07–5.2				5.41
$HMn(CO)_5$							
1^1E ($3d_{Mn}\rightarrow 3d_{Mn}$)			4.27	4.51			4.31
2^1E ($3d_{Mn}\rightarrow \sigma^*_{Mn\text{-}H}$)			5.25	5.26			
3^1E ($3d_{Mn}\rightarrow \sigma^*_{Mn\text{-}H}$)			-	5.94			5.84
$HRe(CO)_5$							
1^1E ($5d_{Re}\rightarrow \pi^*_{CO}$)		4.67	4.72				4.63
2^1A_1 ($5d_{Re}\rightarrow \pi^*_{CO}$)		4.56	4.83				
3^1E ($\sigma_{Re\text{-}H}\rightarrow \pi^*_{CO}$)		5.49	6.31				5.91
4^1E ($5d_{Re}\rightarrow \pi^*_{CO}$)		5.91	6.21				6.33
5^1E ($5d_{Re}\rightarrow \pi^*_{CO}$)		-	6.34				
$Mn_2(CO)_{10}$							
1^1E_1	3.62	3.44	3.29				3.31
1^1B_2	3.42	4.01	3.43				3.69

[a] DFT (ΔSCF) $Cr(CO)_6$ [115] and $Mn_2(CO)_{10}$ [122]
[b] TD-DFT $Ni(CO)_4$ [90] $Cr(CO)_6$ [88] $HRe(CO)_5$ [25] and $Mn_2(CO)_{10}$ [90]
[c] CASSCF/CASPT2 $Ni(CO)_4$ [110], $Cr(CO)_6$ [110] $HRe(CO)_5$ [25] and $Mn_2(CO)_{10}$ [74]
[d] [9]
[e] [111]
[f] Extended similarity transformed EOM [12]
[g] Experimental absorption spectrum from [109] for $Ni(CO)_4$ and [112] for $Cr(CO)_6$, [116] for $HMn(CO)_5$ and $HRe(CO)_5$, [121] for$Mn_2(CO)_{10}$

$(CO)_5$] for the first weak band 5.84 eV [$HMn(CO)_5$] vs 5.91 eV ($HRe(CO)_5$) for the second band and 6.41 eV ($HMn(CO)_5$) vs 6.33 eV ($HRe(CO)_5$) for the highest strong band [116]. However, this similarity in the shape and energetics of the absorption spectra obscures the homogeneity of the spectrum of $HRe(CO)_5$ composed essentially of Metal-to-Ligand-Charge-Transfer (MLCT) states ($5d \rightarrow \pi^*_{CO}$) [25] in contrast to the variety of excited states contributing to the spectrum of $HMn(CO)_5$, namely Metal-Centred (MC) ($3d \rightarrow 3d$), Metal-to-Sigma-Bond-Charge-Transfer (MSBCT) ($3d \rightarrow \sigma^*_{Mn\text{-}H}$), MLCT ($3d \rightarrow \pi^*_{CO}$) and Sigma-Bond-to-Sigma-Bond-Charge-Transfer (SBSBCT) ($\sigma_{Mn\text{-}H} \rightarrow \sigma^*_{Mn\text{-}H}$) states [9]. In particular the low-lying singlet states responsible for the UV photochemistry of these molecules in low-temperature matrices of Ar, CH_4 or CO, namely the departure of a carbonyl ligand as the major primary reaction [117], correspond to MC and MSBCT states in $HMn(CO)_5$ whereas they are described by pure MLCT states in $HRe(CO)_5$. It is puzzling that different types of electronic excited states lead to rather similar photochemistry in the low energy domain. It has been shown that photodecarbonylation of transition metal hydrides occurs via the quasi-dissociative MSBCT ($3d \rightarrow \sigma^*_{M\text{-}H}$) states of $HCo(CO)_4$ [118] and $HMn(CO)_5$ [119].

$Mn_2(CO)_{10}$ prototype for bimetallic transition metal complexes has attracted considerable interest for its photochemical reactivity leading to competitive primary reactions, namely the CO loss and the homolytic cleavage of the Mn-Mn bond [120]. The quantum yield of these two reactive channels is controlled by the excitation wavelength. The lowest part of the absorption spectrum is characterized by one poorly resolved shoulder at 3.31 eV attributed to the $^1A_1 \rightarrow {}^1E_1$ ($d_\pi \rightarrow \sigma^*_{Mn\text{-}Mn}$) transition and one intense band at 3.69 eV assigned to the $^1A_1 \rightarrow a^1B_2$ transition corresponding to the $\sigma_{Mn\text{-}Mn} \rightarrow \sigma^*_{Mn\text{-}Mn}$ excitation ($\sigma_{Mn\text{-}Mn}$ and $\sigma^*_{Mn\text{-}Mn}$ are the metal-metal bonding and its antibonding counterpart orbitals). This early assignment by Gray et al. [121] was confirmed recently by CASSCF/CASPT2 [74] and TD-DFT [90] calculations, the results of which are in excellent agreement with the experiment (see Table 1). In contrast the ΔSCF results which have been shown to be extremely sensitive to the geometry agree with the characters of the two bands but differ by their relative ordering [122].

3.1.2 Mixed-Ligand Carbonyls $W(CO)_5L$ (L=Pyridine, CyanoPyridine)

The low-lying states responsible for the visible-near UV absorption and photo physical/chemical behaviour of mixed-ligand transition metal carbonyls $M(CO)_5L$ (Cr, Mo or W in d^6 configuration, L=pyridine derivative or piperidine) were usually interpreted in terms of interplaying low-lying MLCT and Metal Centred (MC) electronic transitions [6]. According to recent theoretical studies the interpretation based on the assignment of weak spectral features to MC transitions is not necessarily correct: DFT [88] and CASSCF/

Table 2 Calculated electronic allowed transition energies (in eV) for $[W(CO)_5(py)]$ and $[W(CO)_5(CNpy)]$ with oscillator strengths f larger than 0.001 (in parenthesis)

	MLCT Character	TD-DFT (B3LYP)	TD-DFT (BP86)	CASPT2	f	Exp.
$[W(CO)_5(py)]$						
a^1B_1	$5d_W \rightarrow \pi^*_{CO}$	3.02 (0.014)	2.95 (0.010)	3.40	0.034	2.81
b^1A_1	$5d_W \rightarrow \pi^*_{py}$	3.13 (0.135)	2.69 (0.124)	3.63	0.232	3.25
a^1B_2	$5d_W \rightarrow \pi^*_{CO}$	3.14 (0.013)	3.06 (0.011)	3.47	0.054	3.49
c^1A_1	$5d_W \rightarrow \pi^*_{CO}$	3.64 (0.019)	3.47 (0.004)	3.86	0.014	3.71
$[W(CO)_5(CNpy)]$						
b^1A_1	$5d_W \rightarrow \pi^*_{CNpy}$	2.50 (0.208)	2.14 (0.223)	2.84	0.179	2.72
a^1B_1	$5d_W \rightarrow \pi^*_{CO}$	3.07 (0.012)	3.13 (0.015)	3.16	0.042	3.07
a^1B_2	$5d_W \rightarrow \pi^*_{CO}$	3.14 (0.012)	3.18 (0.009)	3.21	0.033	3.34

CASPT2 [110] calculations on $M(CO)_6$ (M=Cr, Mo, W) and $Ni(CO)_4$ assigned the lowest states as MLCT ($d_M \rightarrow \pi^*_{CO}$) transitions while the MC states were calculated at much higher energies. Also TD-DFT calculations of $W(CO)_4$(phen) (phen=1,10-phenanthroline) and $W(CO)_4$(tmp) (tmp= 3,4,7,8-tetramethyl-1,10-phenanthroline) [123] and CASSCF/CASPT2 calculations of $Cr(CO)_4$(bpy) (bpy=2,2′-bipyridine) [124] have shown that the lowest MLCT ($d_M \rightarrow \pi^*_{diimine}$) are immediately followed in energy by several MLCT ($d_M \rightarrow \pi^*_{CO}$) states, the MC states lying higher in energy.

According to the results presented in Table 2 and in contrast to textbook interpretation, calculations on the model complexes $W(CO)_5$(py) and $W(CO)_5$(CNpy) show that no MC transitions are found below 4.0 eV in both molecules [125]. The most intense band which characterizes the spectrum of $W(CO)_5$(py) at 3.25 eV has been assigned to the $a^1A_1 \rightarrow b^1A_1$ MLCT ($5d_W \rightarrow \pi^*_{py}$) transition calculated at 3.13 eV at the TD-DFT (B3LYP) level and 3.63 eV by means of the CASPT2 method.

The lowest band observed at 2.81 eV is assigned to the $a^1A_1 \rightarrow a^1B_1$ MLCT transition corresponding to a $5d_W \rightarrow \pi^*_{CO}$ excitation accompanied by a charge reorganization among the remaining CO. This transition is calculated at 3.02 eV and 3.4 eV by TD-DFT (B3LYP) and CASPT2 methods, respectively. It is noteworthy that the use of different functionals may affect significantly the TD-DFT calculated excitation energies.

Both TD-DFT and CASPT2 methods assign the low-lying intense band observed at 2.72 eV in the absorption spectrum of $W(CO)_5$(CNpy) as the $a^1A_1 \rightarrow b^1A_1$ MLCT ($5d_W \rightarrow \pi^*_{CNpy}$) transition calculated at 2.50 eV (TD-DFT(B3LYP)) and 2.84 eV (CASPT2). As expected this transition is shifted to the lower energy when going from the pyridine to the cyano-pyridine substituted molecule and lies below the MLCT ($5d_W \rightarrow \pi^*_{CO}$) states calculated at 3.07 eV (3.16 eV) (a^1B_1) and 3.14 eV (3.21 eV) (a^1B_2) (Table 2). These results show that the lowest MLCT ($5d_W \rightarrow \pi^*_{CNpy}$) excited states are immedi-

ately followed in energy by MLCT ($5d_W \rightarrow \pi^*_{CO}$) states instead of MC states. Similar trends have been observed for the bidentate substituted complexes $W(CO)_4L$ (L=ethylenediamine, N,N′-di-alkyl-1,4-diazabutadiene) on the basis of TD-DFT and CASPT2 calculations [125].

3.2 Metal-to-Ligand-Charge-Transfer α-Diimine Complexes

In a series of structurally related transition metal α-diimine compounds, or even within the same molecule several different types of Charge Transfer (CT) transitions (from the metal M, from an halide ligand X or an axial $\sigma_{M\text{-}L}$ bond to the electron accepting α-diimine group) may be present in a limited domain of the absorption spectrum (visible-near UV). This gives to this class of molecules unconventional photo-chemical/physical properties which may be tailored acting on the electronic degree of delocalization between the metal centre, the α-diimine group and the heteroligands. In order to understand the differences of spectroscopy and photo-reactivity observed in a variety of molecules [126–135] a systematic quantum chemical study has been performed for several MLCT α-diimine model complexes [94, 136, 137]. A few examples are reported in the next following sub-sections.

3.2.1 Near UV-visible Absorption Spectra of $[Ru(E)(E')(CO)_2(iPr\text{-}DAB)]$ ($E=E'=SnPh_3$ or Cl; $E=SnPh_3$ or Cl, $E'=CH_3$; iPr-DAB=N,N′-diisopropyl-1,4-diaza-1,3-butadiene)

The near-UV/visible spectra of a series of $[Ru(E)(E')(CO)_2(iPr\text{-}DAB)]$ ($E=E'=SnPh_3$ or Cl; $E=SnPh_3$ or Cl, $E'=CH_3$; iPr-DAB=N,N′-diisopropyl-1,4-diaza-1,3-butadiene) have been investigated on the basis of theoretical and experimental analysis of model and real molecules, respectively [94].

The lowest-energy part of the absorption spectra of both $[Ru(SnH_3)_2(CO)_2(Me\text{-}DAB)]$ and $[Ru(SnH_3)(CH_3)(CO)_2(Me\text{-}DAB)]$ model complexes originates in an electronic transition that corresponds to excitation from an axial E-Ru-SnH_3 (E=SnH_3 or Me) $\sigma_{E\text{-}Ru\text{-}SnH3}$ orbital into the low-lying π^*_{DAB} orbital localized predominantly on Me-DAB (SBLCT transition) (Scheme 6).

The first intense band observed at 2.36 eV and 2.32 eV for $[Ru(SnPh_3)_2(CO)_2(iPr\text{-}DAB)]$ and $[Ru(SnPh_3)(Me)(CO)_2(iPr\text{-}DAB)]$, respectively have been assigned to SBLCT transitions calculated at 2.66 eV (b^1A_1) and 2.55 eV (b^1A') at the CASPT2 level (Table 3). The near-UV region dominated by weak shoulders at 3.12 eV $[Ru(SnPh_3)_2(CO)_2(iPr\text{-}DAB)]$ and at ~2.75 eV and 3.17 eV $[Ru(SnPh_3)(Me)(CO)_2(iPr\text{-}DAB)]$ consists mainly of MLCT ($4d_{Ru} \rightarrow \pi^*_{DAB}$) transitions calculated at 3.08 eV (a^1B_2) and 2.60 eV (a^1A'') / 3.21 eV (c^1A') for $[Ru(SnH_3)_2(CO)_2(Me\text{-}DAB)]$ and $[Ru(SnH_3)(CH_3)(CO)_2(Me\text{-}DAB)]$, respectively. This assignment is confirmed by the TD-DFT

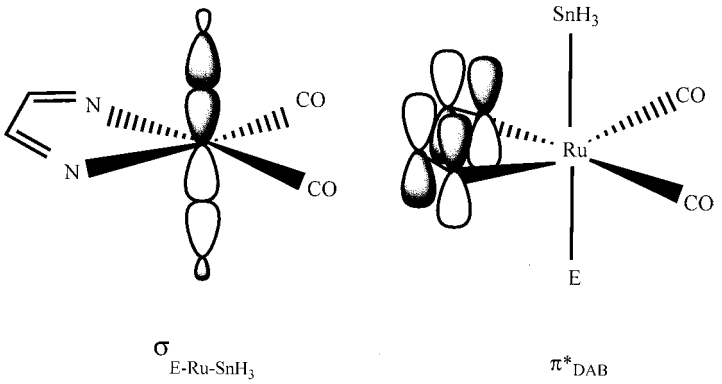

Scheme 6

(B3LYP) calculations. The agreement between the CASPT2 method and the Density Functional approach is remarkably good for these non-halide systems which have very similar absorption spectra.

In contrast CASPT2 and TD-DFT calculations lead to different descriptions of electronic transitions of the halide complexes [Ru(Cl)(Me)$(CO)_2$(Me-DAB)] and [Ru$(Cl)_2(CO)_2$(Me-DAB)]. The ab initio calculations assign the lowest intense bands observed at 2.72 eV [Ru(Cl)(Me)$(CO)_2$(iPr-DAB)] and 2.66 eV [Ru$(Cl)_2(CO)_2$(iPr-DAB)] to MLCT ($4d_{Ru}\rightarrow\pi^*_{DAB}$) transitions

Table 3 CASSCF/CASPT2 and TD-DFT excitation energies (in eV) and assignments of the low-lying electronic transitions of [Ru$(SnH_3)_2(CO)_2$(Me-DAB)], [Ru$(SnH_3)(CH_3)(CO)_2$(Me-DAB)], [Ru(Cl)$(CH_3)(CO)_2$(Me-DAB)] and [Ru$(Cl)_2(CO)_2$(Me-DAB)] [94]

	TD-DFT	CASSCF/CASPT2	Experiment[a]
Ru$(SnH_3)_2(CO)_2$(Me-DAB)			
$b^1A_1\ \sigma_{E\text{-}Ru\text{-}E'}\rightarrow\pi^*_{DAB}$	2.75	2.66	2.36
$a^1B_2\ 4d_{xy}\rightarrow\pi^*_{DAB}$	3.08	3.08	3.12
Ru$(SnH_3)(CH_3)(CO)_2$(Me-DAB)			
$b^1A'\ \sigma_{E\text{-}Ru\text{-}E'}\rightarrow\pi^*_{DAB}$	2.69	2.55	2.32
$a^1A''\ 4d_{xy}\rightarrow\pi^*_{DAB}$	2.71	2.60	2.75
$c^1A'\ 4d_{xz}\rightarrow\pi^*_{DAB}$	3.42	3.21	3.17
Ru(Cl)$(CH_3)(CO)_2$(Me-DAB)[b]			
$a^1A''\ 4d_{xy}\rightarrow\pi^*_{DAB}$	1.81	2.24	2.17
$b^1A'\ 4d_{xz}\rightarrow\pi^*_{DAB}$	2.03	2.83	2.72
Ru$(Cl)_2(CO)_2$(Me-DAB)[b]			
$a^1B_2\ 4d_{xy}\rightarrow\pi^*_{DAB}$	1.86	2.45	2.23
$b^1A_1\ 4d_{xz}\rightarrow\pi^*_{DAB}$	2.07	2.84	2.66

[a] [94]

[b] The one-electron excitation in the main configuration is given for the CASSCF/CASPT2 calculation as explained in the text it may differ significantly from the TD-DFT assignment

calculated at 2.83 eV (b^1A') and 2.84 eV (b^1A_1), respectively in the model systems. The shoulders present at ~2.19 eV in both molecules is attributed to MLCT transitions as well. The CASPT2 transition energies get along the experimental values with a blue shift on going from the non-halide to the halide complexes. The presence of these low-lying MLCT states quenches the photo-reactivity of the halide substituted complexes in accordance with the experimental features. However, the beautiful agreement between the CASPT2 and TD-DFT results observed in the non-halide systems is destroyed here and the low-lying excited states in both molecules are attributed to XLCT ($p_{Cl}\rightarrow\pi^*_{DAB}$) transitions by the TD-DFT method which under estimates the transition energies in this case. Recent calculations [138] showed that these states have a mixed MLCT/XLCT character which is more MLCT pronounced in Cl substituted complexes in agreement with absorption and Resonance Raman experiments [130]. The TD-DFT approach tends towards an overestimation of the XLCT character. The present results illustrate the difficulty for the DFT approach in describing excited states in systems containing bonding between a halide and a low-valent metal atom.

3.2.2 Electronic Spectroscopy of [M(R)(CO)$_3$(H-DAB)] (M=Mn, Re; R=H, Ethyl, H-DAB=1,4-diaza-1,3-butadiene)

The visible part of the absorption spectrum of this class of molecules consists of several MLCT states corresponding to $d_{Metal}\rightarrow\pi^*_{DAB}$ excitations between 17,500 cm^{-1} and 25,000 cm^{-1} [136, 137]. Regarding the values of the oscillator strengths f reported in Table 4 the b^1MLCT (c^1A') state corre-

Table 4 MR-CCI calculated electronically allowed transition energies (in cm^{-1}) for [Mn(R)(CO)$_3$(H-DAB)] (R=H, ethyl) and [Re(R)(CO)$_3$(H-DAB)] (R=H, ethyl) with oscillator strengths (in parenthesis)

	Character	R=H[a]	R=ethyl[a]	Exp.[b]
[Mn(R)(CO)$_3$(H-DAB)]				
a^1A''	$3d_{Mn}\rightarrow\pi^*_{H\text{-}DAB}$	18,000 (0.04)	-	
b^1A'	$3d_{Mn}\rightarrow\pi^*_{H\text{-}DAB}$	21,060 (0.03) **18,700**	17,600 (0.012)	20,000
c^1A'	$3d_{Mn}\rightarrow\pi^*_{H\text{-}DAB}$	23,020 (0.39)	20,000 (0.13)	
d^1A'	$3d_{Mn}\rightarrow 3d_{Mn}$	33,400 (0.02)	34,200 (0.01)	30,000(sh)
e^1A'	$\sigma_{Mn\text{-}H}\rightarrow\pi^*_{H\text{-}DAB}$	35,600 (0.11)	27,400 (0.26)	
[Re(R)(CO)$_3$(H-DAB)]				
a^1A''	$5d_{Re}\rightarrow\pi^*_{H\text{-}DAB}$	15,800 ($<10^{-5}$)	-	
b^1A'	$5d_{Re}\rightarrow\pi^*_{H\text{-}DAB}$	17,440 ($<10^{-5}$) **15,900**	20,570 (0.0) **20,500**	20,500
c^1A'	$5d_{Re}\rightarrow\pi^*_{H\text{-}DAB}$	22,470 (0.38) **19,400**	30,370 (0.46) **24,420**	
d^1A'	$\sigma_{Re\text{-}H}\rightarrow\pi^*_{H\text{-}DAB}$	33,490 (0.15) **31,600**	25,520 (0.06) **26,700**	

[a] The MS-CASPT2 values are reported in bold
[b] From the UV-visible spectrum of Mn(Me)(CO)$_3$(iPr-DAB) at 183°K in solution (dimethyl-2,2-butane/n-pentane) and of Re(Me)(CO)$_3$(iPr-DAB) at room temperature in THF

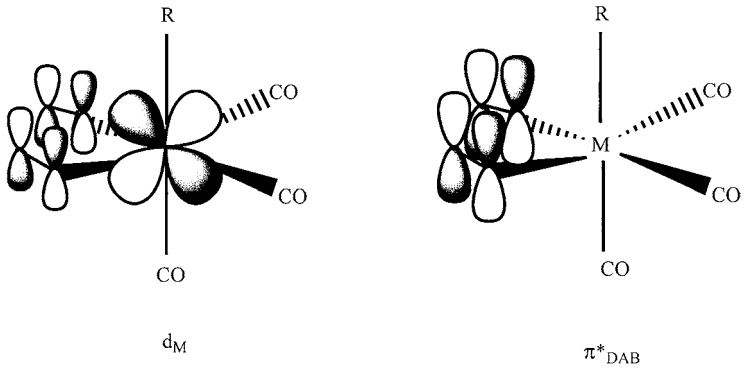

Scheme 7

sponding to an excitation to the π^*_{DAB} orbital from the d orbital which interacts with this π^* of the H-DAB group (Scheme 7) is the only one contributing to the intense band at ~500 nm (20,000 cm^{-1}) characterizing these transition metal complexes.

The upper part of the absorption spectrum (UV energy domain) is composed essentially of the SBLCT state corresponding to the $\sigma_{Metal\text{-}R} \rightarrow \pi^*_{DAB}$ excitation. On going from the first-row transition metal complex $Mn(R)(CO)_3(H\text{-}DAB)$ to the rhenium analogue the Metal-Centred states are destabilized and do not contribute to the UV part of the absorption spectrum. When replacing the hydrogen by an ethyl ligand the metal-R bond weakening is accompanied by a stabilization of the SBLCT observed in the Mn and Re complexes. The transition energies reported in Table 4 for the four model complexes have been obtained at the MRCI level. CASPT2 values are also reported when available for comparison. A general trend is an overestimation of the transitions energies by the pure variational approach. The dynamical correlation effects included at the MS-CASPT2 level and underestimated by the MRCI method may be important especially for the states interacting strongly with the electronic ground state or other excited states (b^1MLCT state in Re(R) $(CO)_3$(H-DAB) for instance). This illustrates the degree of difficulties of such ab initio calculations in this class of molecules. Despite the similarity of the absorption spectra within this series of complexes, the photo-reactivity is very different going from ultra-fast direct and efficient CO loss observed in $Mn(Me)(CO)_3$(iPr-DAB) to the homolytic cleavage of the metal-ethyl or metal-benzyl bond in $Re(R)(CO)_3$(iPr-DAB) (R=ethyl, benzyl). The computation of accurate potential energy surfaces describing the various photo-reactive pathways will be the key for the understanding of the photochemical reactivity as illustrated in section 4.

3.3 Cyclometalated Complexes

3.3.1 Electronic Spectra of M(2-thienylpyridine)$_2$ (M=Pd, Pt) Complexes: a CASSCF/CASPT2 Study

Photo-chemical and photo-physical investigations based on highly resolved emission and excitation spectra of cyclometalated complexes [139, 141] revealed that the lowest excited states are Ligand Centred (LC) corresponding to $\pi \rightarrow \pi^*$ excitations with a large degree of MLCT admixture in contrast to the compounds discussed in the previous sub-sections which are characterized by low-lying MLCT, SBLCT and MC states.

A careful theoretical analysis based on CASSCF/CASPT2 calculations of transition energies and oscillator strengths of two cyclometalated complexes Pd(thpy)$_2$ and Pt(thpy)$_2$ containing either Pd(II) or Pt(II) as the central metal coordinated to two *cis*-conjugated C-protonated 2-(2-thienyl) pyridine (thpy$^-$) ligands (Scheme 8) has been reported [142]. The purpose of this

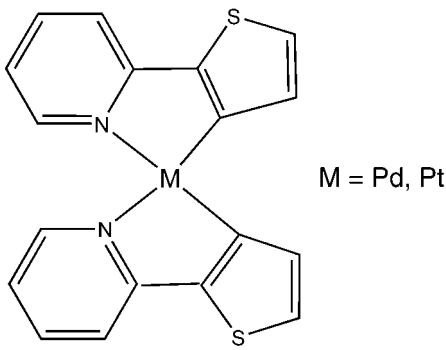

Scheme 8

study was an analysis of the excitation and emission spectra and the search for some trends on modifying the metal centre. The calculated excitation energies to the low-lying triplet and singlet states are reported in Table 5. The a^3A_1 and a^3B_2 states, almost purely LC with very limited MLCT contribution in Pd(thpy)$_2$ are about 1500 cm^{-1} lower for Pt(thpy)$_2$ (18,170 cm^{-1}, 18,830 cm^{-1}) than for Pd(thpy)$_2$ (19,690 cm^{-1}, 19,960 cm^{-1}), both being considerably lower than the calculated vertical excitation energies for the free thpy ligands (~23,000 cm^{-1}). The calculated values are in perfect agreement with the experimental data which establish these states at 17,160 cm^{-1} (Pt(thpy)$_2$) and 18,420 cm^{-1} (Pd(thpy)$_2$) [143, 144]. However, one interesting question which illustrates the complementarity's between experiments and

Table 5 Calculated electronic spectra of $M(2\text{-thpy})_2$ (M=Pd, Pt) at the CASPT2 level (in cm^{-1}) with oscillator strengths (in parenthesis)

	Character	CASPT2
$Pd(2\text{-thpy})_2$		
a^3A_1	LC	19,689
a^3B_2	LC	19,957
A^1A_1	MLCT	24,432 (0.0306)
A^1B_2	MLCT	26,052 (0.1994)
A^1B_1	MLCT	27,960 (0.0298)
B^1B_2	LC	31,240 (0.0324)
B^1A_1	LC	32,022 (0.2985)
$Pt(2\text{-thpy})_2$		
a^3A_1	LC	18,168
a^3B_2	LC	18,829
A^1A_1	MLCT	20,441 (0.0116)
A^1B_2	MLCT	23,454 (0.2342)
B^1B_2	MLCT	26,397 (0.0268)
A^1B_1	MLCT	26,550 (0.0340)
C^1B_2	LC	29,718 (0.0173)
B^1A_1	LC	31,010 (0.3038)

theory and which remains to be solved is the presence of two low-lying triplet states below the S_1 state in the theoretical spectrum when only one triplet state is put in evidence experimentally.

The calculations predict a significantly larger a^3B_2-a^3A_1 energy splitting in $Pt(thpy)_2$ than in $Pd(thpy)_2$, 661 cm^{-1} vs 268 cm^{-1}. The most intense band in both spectra found below 340 nm (29,000 cm^{-1}) has been assigned to metal-perturbed B^1A_1 LC transition calculated at 32,022 cm^{-1} ($Pd(thpy)_2$) and 31,010 cm^{-1} ($Pt(thpy)_2$) about 2000 cm^{-1} lower than the experimental band maximum. The A^1B_2 CT state may also contribute to this band. The neglect of chromophore-solvent interactions in this theoretical study might be responsible for the discrepancy between the calculated and experimental band maxima.

3.3.2 Excited Electronic States in Phenylpyridine Ir (III) Complexes: A TD-DFT Study

Absorption spectra and emissive properties of $Ir(ppy)_3$ and related Ir(III) complexes (where ppy=2-phenyl-pyridine) have been extensively studied in solution and in solid state [145–149]. The size of the ligands together with the presence of a heavy metal atom has made the theoretical study of such molecules challenging until recently. In a recent TD-DFT (B3LYP) study [150] the low-lying triplet and singlet excited states of three related Ir(III) complexes $Ir(ppy)_3$, $Ir(ppy)_2(acac)$ and $Ir(ppy)_2(bza)$ (where acac=acetoy-

Table 6 TD-DFT calculated excitation energies E (in eV) to the low-lying triplet and singlet states of $Ir(ppy)_3$, $Ir(ppy)_2(acac)$ and $Ir(ppy)_2(bza)$ and associated oscillator strengths f

	E	f	Experiment[a]
$Ir(ppy)_3$			
T_1 (^{3}A)	2.59		2.7
T_2 (^{3}E)	2.60		
S_1 (^{1}A)	2.80	0.0044	2.9
S_2 (^{1}E)	2.85	0.0019	
	2.85	0.0022	
S_3 (^{1}E)	3.03	0.0207	
	3.04	0.0186	
S_4 (^{1}A)	3.04	0.0058	
$Ir(ppy)_2(acac)$			
T_1 (^{3}A)	2.47		2.49
T_2 (^{3}E)	2.48		
S_1 (^{1}A)	2.70	0.0314	
S_2 (^{1}E)	2.73	0.0003	
$Ir(ppy)_2(bza)$			
T_1 (^{3}A)	2.42		2.41
T_2 (^{3}E)	2.48		
T_3 (^{3}A)	2.49		
S_1 (^{1}A)	2.59	0.0026	
S_2 (^{1}E)	2.71	0.0312	
S_3 (^{1}E)	2.75	0.0006	

[a] [145–148]

lacetonate, bza=benzyolacetonate) used in organic light emitting diode devices (OLEDS) [151] have been determined at the zero-order (neglect of spin-orbit coupling effects). The calculated transition energies to the lowest triplet states (2.4 eV–2.6 eV) and singlet states (2.6 eV–2.8 eV) in the three complexes are in good agreement with experimental absorption spectra and luminescence studies (Table 6). The low-lying transitions are assigned to MLCT states, although the Kohn-Sham metal orbitals have significant mixture of ligand character.

The lowest triplet states T_1 in $Ir(ppy)_3$ is calculated at 2.59 eV compared to 2.70 eV observed absorption and 2.50 eV (observed emission). For $Ir(ppy)_2(acac)$ and $Ir(ppy)_2(bza)$ the T_1 states are found at 2.47 eV (absorption) and 2.41 eV (emission) and 2.42 eV (2.41 eV), respectively. Nearby triplet lie within 0.1 eV and the lowest singlet states occur within 0.1–0.2 eV. These molecules are characterized by a high density of states between 2.42 eV and 3.65 eV, corresponding mainly to $d_{Ir} \rightarrow \pi^*_{ppy}$, π^*_{acac}, π^*_{bza} excitations. The most intense transitions are found in the upper part of the absorption spectrum of $Ir(ppy)_2(bza)$ beyond 3.50 eV.

3.4 Spin-Orbit Effects on the Electronic Spectroscopy

3.4.1 The Octahedral $RhCl_6^{3-}$ Complex

The $RhCl_6^{3-}$ complex is typical of octahedral transition metal compounds playing an important role as doping agents for manufacturing AgX photographic emulsions, affecting their sensitivities and gradation [152, 153]. The spin-orbit states of $RhCl_6^{3-}$ in the three lattices NaCl, Cs_2NaYCl_6 and water solution have been investigated by means of CASSCF/CASPT2 calculations within the ab initio model potential (AIMP) approach (Table 7) [154].

The main effect of the surrounding lattice acts on the Rh-Cl equilibrium distance which may vary from 2.34 Å in the free $RhCl_6^{3-}$ complex to 2.42 Å in vacuum (2.35 Å in NaCl, 2.37 Å in Cs_2NaYCl_6 and water). The excitations energies in different environment are affected accordingly.

The spin-orbit effects on the electronic ground state $^1A_{1g}$ and the lowest excited states $^3T_{1g}$, $^3T_{2g}$, $^1T_{1g}$ and $^1T_{2g}$ corresponding to $4d_{Rh} \rightarrow 4d_{Rh}$ excitations were calculated with an effective one-electron operator [155]. Transition energies shifts of more than 1000 cm^{-1} have been found for the low-lying triplets. The total splitting of the $^3T_{1g}$ state amounts to 2000 cm^{-1} and the $^3T_{2g}$ state is split by 1500 cm^{-1}. The $^1T_{1g}$ and $^1T_{2g}$ are not perturbed too much with a shift of 800 cm^{-1} and 470 cm^{-1} to the blue, respectively. For some of the triplet states the singlet-triplet mixing may reach 10%.

Most of the optical spectra of $RhCl_6^{3-}$ complexes are not well enough resolved to reveal details of the spin-orbit splitting pattern due to line broad-

Table 7 CASPT2 calculated excitation energies (in cm^{-1}) to the low-lying triplet and singlet states of the $RhCl_6^{3-}$ complex without spin-orbit interaction in vacuum and different host lattices and with spin-orbit interaction for the free $RhCl_6^{3-}$ complex[a]

	Electronic states			
Without spin-orbit	$^3T_{1g}$	$^3T_{2g}$	$^1T_{1g}$	$^1T_{2g}$
In vacuum	10,600	13,000	15,400	20,300
Free $RhCl_6^{3-}$	**13,830**	**16,320**	**18,340**	**23,320**
NaCl	13,900	16,800	18,500	24,000
Cs_2NaYCl_6	12,900	15,600	17,500	22,900
Water	13,200	15,900	18,000	23,400
With spin-orbit	$E_g\ T_{2g}\ T_{1g}\ A_{1g}$	$E_g\ T_{2g}\ T_{1g}\ A_{1g}$	T_{1g}	T_{2g}
Free $RhCl_6^{3-}$	**13,390**	16,650	**19,140**	**23,790**
	13,600	17,300		
	14,250	16,200		
	15,340	17,690		
Experiment	**14,000**		**20,000**	**24,800**

[a] With a Rh-Cl distance of 2.34 Å (experimental value in K_3RhCl_6) close to the equilibrium distance in NaCl (2.35 Å)

ening and vibrational progression. Furthermore the $^1A_{1g} \rightarrow {}^1T_{1g}$ and $^1A_{1g} \rightarrow {}^1T_{2g}$ transitions are more intense. In diffuse reflectance measurements transitions with small extinction coefficients appear enhanced compared to more intense transitions with a lot of fine structure in the region below 20,000 cm^{-1} [156]. Three bands are observed at 20,000 cm^{-1}, 24,800 cm^{-1} and 14,000 cm^{-1} which can be assigned to T_{1g} ($^1T_{1g}$), T_{2g} ($^1T_{2g}$) and E_g ($^3T_{1g}$) components calculated at the CASPT2/SO level at 19,140 cm^{-1}, 23,790 cm^{-1} and 13,390 cm^{-1}, respectively.

3.4.2 Trischelated Diketonato Complexes of Trivalent Chromium

The tris(acetylacetonato)chromium(III) complex $Cr(acac)_3$ has been the subject of a number of spectroscopic and theoretical studies [157]. Of special interest are the trigonal splittings of the $^4T_{2g}$ and $^4T_{1g}$ states. For the lowest $^4T_{2g}$ state the experimental splitting amounts to 800 cm^{-1} with the $^4A_1$ component below the ^4E component. The ground and excited states of the neutral tris (1,3-propanedionato) chromium (III) d^3 complex ($Cr(PDO)_3$) model for $Cr(acac)_3$ have been investigated with CASSCF/CASPT2 methods [158] the spin-orbit being included in a perturbative approach [155].

The transition energies to the quartet and doublet metal centred states calculated at the CASPT2 level are compared to the experimental values in Table 8.

The absolute positions of the doublet states are overestimated by about 2500 cm^{-1}. The spin-orbit coupled emitting doublet states is predicted to be the 2A(3/2) component of the ^2E_g state in agreement with spectral assignment but in conflict with excited state EPR experiments. Despite the quality of the calculations the large zero-field splitting (ZFS) of the ^2E_g (220–290 cm^{-1}) has not been reproduced with theoretical values less than 100 cm^{-1}.

Table 8 CASPT2 calculated excitation energies (in cm^{-1}) to the low-lying doublet and quartet states of $Cr(PDO)_3$ including the spin-orbit interactions

Transition	Electronic states	Excitation energies	Experiment[a]
$^4A_{2g} \rightarrow {}^2E_g$	^2E	15540	12940 (^2E)
			13200 (^2E)
$^4A_{2g} \rightarrow {}^2T_{1g}$	$^2A_2$	16270	
	^2E	16660	
$^4A_{2g} \rightarrow {}^2T_{2g}$	$^2A_1$	22170	
	^2E	21470	
$^4A_{2g} \rightarrow {}^4T_{2g}$	$^4A_1$	16090	17700 ($^4A_1$)
	^4E	17410	18,500 (^4E)
$^4A_{2g} \rightarrow {}^4T_{1g}$	$^4A_2$	25760	
	^4E	24760	22700 (^4E)

[a] From [159–161]

This work illustrates the complexity of the theoretical analysis when introducing the spin-orbit coupling effects at the level of the five lowest excited states for a symmetric molecule. However the unusually large ZFS of the ground state has been reproduced and attributed to an anisotropic spin-orbit mechanism. The cause of this anisotropy has been clearly identified as orbital mixing between the t_{2g} and e_g shells. In addition a significant trigonal splitting of the $^4T_{2g}$ parent state is reproduced with the correct sign for a perfectly octahedral first coordination sphere. The shape of the molecular orbitals indicates the presence of a phase-coupling effect from the unsaturated chelating bridge.

4 Photoreactivity

In order to illustrate the complexity of excited states reactivity in transition metal complexes two selected examples are reported in the next section dedicated to the ab initio (CASSCF/MR-CI or MS-CASPT2) study of the photodissociation of $M(R)(CO)_3$(H-DAB) (M=Mn, R=H; M=Re, R=H, Ethyl) complexes. Despite the apparent complexity and richness of the electronic spectroscopy, invaluable information regarding the photodissociation dynamics can be obtained on the basis of wave packet propagations on selected 1-Dim or 2-Dim cuts in the PES, restricting the dimensionality to the bonds broken upon visible irradiation (Metal-CO or Metal-R). The importance of the intersystem crossing processes in the photoreactivity of this class of molecules will be illustrated by the theoretical study of the rhenium compound.

4.1 Dissociative vs Non-dissociative Metal-to-Ligand-Charge-Transfer (MLCT) States in $M(H)(CO)_3$(α-diimine) Complexes (M=Mn, Re)

The photodissociation dynamics of $M(H)(CO)_3$(H-DAB) (M=Mn, Re), model systems for $M(R)(CO)_3$(α-diimine) complexes (with M=Mn, Re, R representing a metal fragment or alkyl or halide groups bound to the metal by high-lying $\sigma_{M\text{-}R}$ orbitals) have been investigated in two recent studies [136, 137]. The main purpose was to understand the change of photochemical behaviour upon visible irradiation, namely from the CO loss and/or Mn-R bond homolysis to the Re-R bond homolysis and/or emission when going

Fig. 2 **a** CASSCF/MR-CI Potential energy surface of the ^{1}MLCT absorbing state of $Mn(H)(CO)_3$(H-DAB) as a function of q_a=[Mn-H] and q_b=[Mn-COax]. **b** Time evolution of the wavepacket (*solid lines*) on the ^{1}MLCT potential (*dashed lines*)

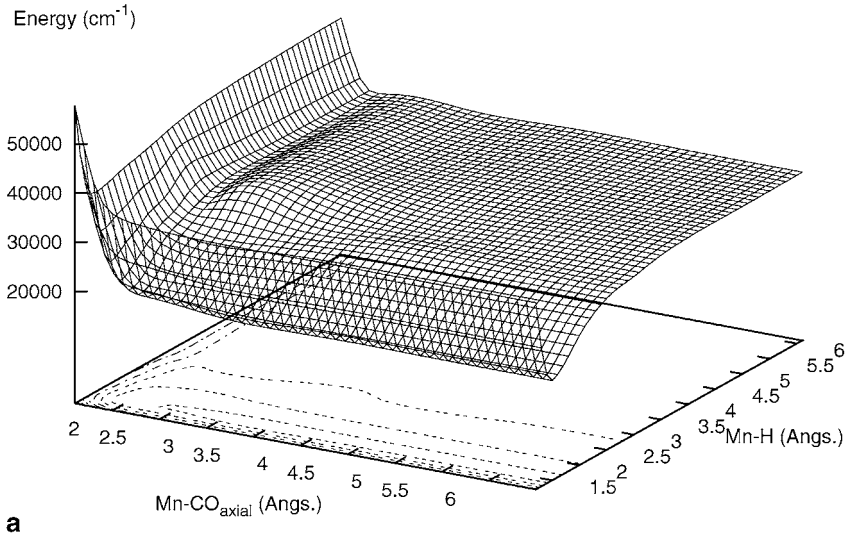
Energy (cm-1)
50000
40000
30000
20000
2
2.5
3
3.5
4
4.5
5
5.5
6
Mn-CO axial (Angs.)
1.5
2
2.5
3
3.5
4
4.5
5
5.5
6
Mn-H (Angs.)

a

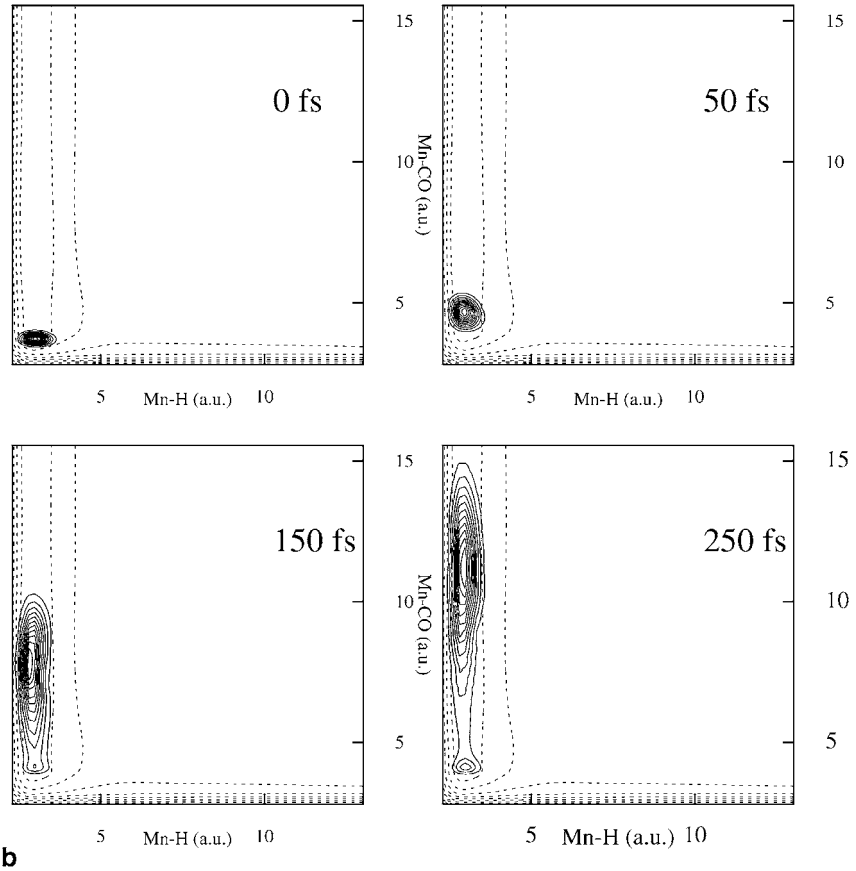
0 fs
50 fs
150 fs
250 fs
Mn-CO (a.u.)
Mn-H (a.u.)
5
10
15

b

from the first-row to the third-row transition metal complexes [131–135]. Despite the presence of many low-lying singlet and triplet excited states potentially photoactive (nine for the manganese complex and seven for the rhenium one) it has been shown that only two states, the ^{1}MLCT ($d_M \rightarrow \pi^*_{DAB}$) absorbing state and the ^{3}SBLCT ($\sigma_{M\text{-}R} \rightarrow \pi^*_{DAB}$) state, will control the photochemistry of this class of molecules. As illustrated by the contour plot of the 2D PES calculated as a function of q_a=[Mn-H] and q_b=[Mn-CO_{ax}] the ^{1}MLCT absorbing state itself is dissociative for the CO loss in $Mn(H)(CO)_3$(H-DAB) (Fig. 2a).

The dissociative character of the MLCT state in the first-row transition metal complexes is due to the weakening of the Mn-CO_{axial} bond when exciting an electron from the d_{Mn} orbital which is responsible for the $d\pi p\pi$ Mn-CO_{ax} back bonding interaction to the π^*_{DAB} localized on the acceptor group. This effect is less important in the third-row transition metal complexes where the metal-CO_{axial} interaction occurs mainly through the interaction with the diffuse p of the metal. Moreover the ^{3}SBLCT state presents a valley of dissociation for the metal-hydrogen bond breaking in both molecules. However after absorption to the ^{1}MLCT in the visible energy domain $Mn(H)(CO)_3$(H-DAB) will completely dissociate within 450 fs according to an ultra-fast direct dissociative process (Fig. 2b) leading exclusively to the departure of the axial CO ligand. This theoretical study was the first evidence of the MLCT reactivity of some transition metal α-diimine complexes currently observed experimentally [162].

4.2 Role of the Triplet Sigma-Bond-to-Ligand-Charge-Transfer (SBLCT) State in the Photoreactivity of $Re(R)(CO)_3$(α-diimine) (R=H, Ethyl)

As illustrated by the contour plot of the 2D PES depicted in Fig. 3a and in contrast to the manganese analogue, the ^{1}MLCT absorbing state is bound along both channels (axial CO loss and Re-H bond homolysis) in $Re(H)(CO)_3$(H-DAB).

Within the 2-Dim approximation ($q_{a=}$Re-H, q_b=Re-CO_{ax}) one possibility of deactivation of $[Re(H)(CO)_3(H\text{-}DAB)]^*$ is via intersystem crossing to the ^{3}SBLCT state, this potential being repulsive for the homolytic cleavage which is observed in a series of analogues like $Re(R)(CO)_3$(iPr-DAB) (R=methyl, ethyl, metal fragment) with various quantum yields ($\phi=10^{-2}$ for

Fig. 3 **a** CASSCF/MR-CI Potential energy surface of the ^{1}MLCT absorbing state of $Re(H)(CO)_3$(H-DAB) as a function of q_a=[Re-H] and q_b=[Re-CO_{ax}]. **b** Time evolution of the wavepacket (*solid lines*) on the ^{1}MLCT (*left side*) and ^{3}SBLCT (*right side*) potentials (*dashed lines*) coupled by spin-orbit

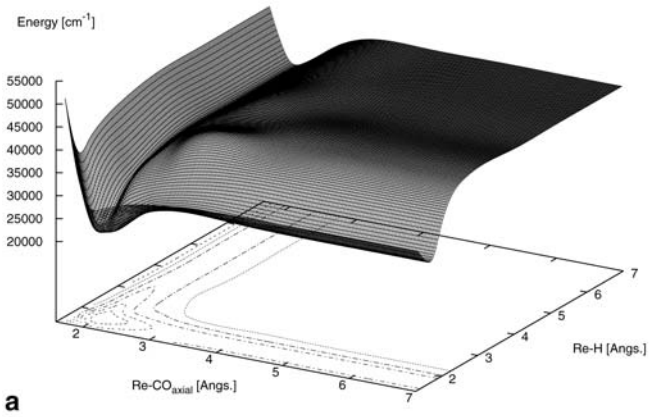
Energy [cm-1]
55000
50000
45000
40000
35000
30000
25000
20000
2
3
4
5
6
7
Re-CO axial [Angs.]
Re-H [Angs.]

a

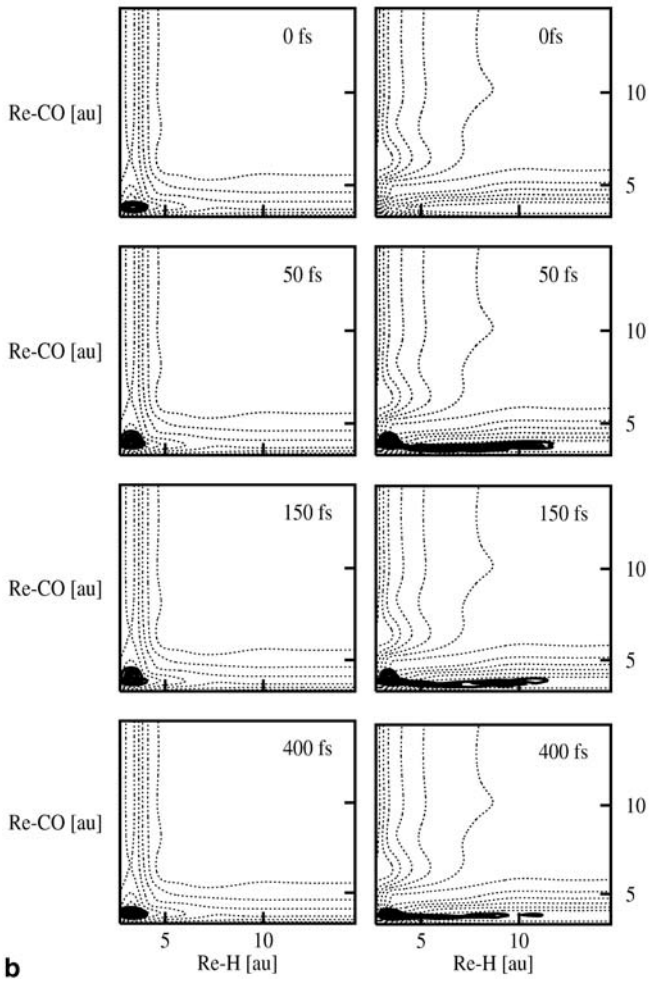
0 fs
0fs
50 fs
50 fs
150 fs
150 fs
400 fs
400 fs
Re-CO [au]
10
5
5
10
Re-H [au]

b

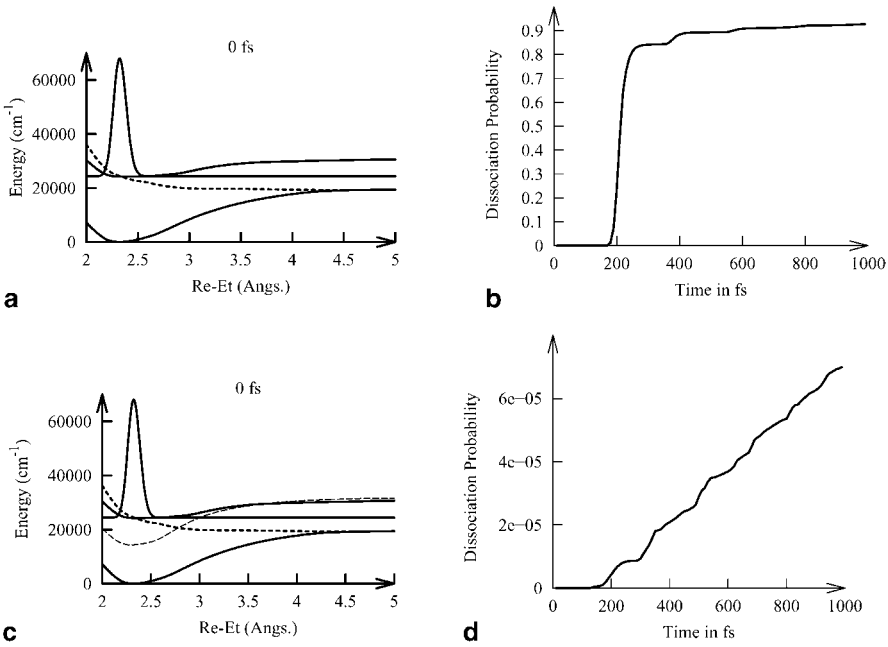

Fig. 4 **(a)** Initial wave packet (*continuous line*) on the ^{1}MLCT absorbing state coupled to the ^{3}SBLCT state (*dashed line*) by spin-orbit. **(b)** Dissociation probability of the ethyl group along the ^{3}SBLCT potential in Re(ethyl)$(CO)_3$(H-DAB) as function of time resulting from the wave packet propagation starting from this initial condition. **(c)** Initial wave packet (*continuous line*) on the ^{1}MLCT absorbing state coupled to the ^{3}SBLCT state (*bold dashed line*) and to the lowest ^{3}MLCT (*dashed line*) by spin-orbit. **(d)** Dissociation probability of the ethyl group along the ^{3}SBLCT potential in Re(ethyl)$(CO)_3$(H-DAB) as function of time resulting from the wave packet propagation starting from this initial condition

R=methyl, $\phi \approx 1.0$ for R=ethyl or benzyl) [136, 163, 164]. After initial excitation under visible irradiation the system gets trapped in the potential well of the MLCT state (Fig. 3b, left side). Within a very short time scale (50 fs) the ^{3}SBLCT state is populated via ^{1}MLCT$\rightarrow$^{3}SBLCT intersystem crossing (Fig. 3b, right side). As soon as the wavepacket reaches the ^{3}SBLCT potential it evolves along the dissociation channel towards the formation of the diradicals $H^{\cdot}$+$^{\cdot}$[Re$(CO)_3$(H-DAB)]. The reaction is rather slow and inefficient in this model complex with a probability of dissociation less than 2% within 2 ps.

In order to follow the trends when replacing the hydrogen atom by the ethyl group 1-Dim potential energy curves have been computed for Re(Et)$(CO)_3$(H-DAB) as a function of the Re-ethyl bond elongation. A preliminary 1-Dim wavepacket simulation has been performed on the potentials corresponding to the ^{1}MLCT absorbing state and ^{3}SBLCT states coupled by spin-orbit (Fig. 4a). Due to the favourable position of the crossing (around 2.4 Å)

the intersystem crossing is extremely efficient and the probability of dissociation reaches 90% in 1 ps (Fig. 4b) in agreement with recent fs experiments reported for $Re(Et)(CO)_3(dmb)$ (dmb=4,4′-dimethyl-2,2′-bipyridyl) in solution [164, 165]. However, when introducing the low-lying ^{3}MLCT states in the 1-Dim simulation this probability decreases dramatically from 70% when one triplet is included to a nearly total quenching (probability of 8.0 10^{-5}) when the lowest ^{3}MLCT state is taken into account in the simulation (Fig. 4c,d).

This example illustrates the complexity of the excited states dynamics in this class of molecules. The early stage dynamical behaviour (in the first ps) may be tailored by the metal centre, the α-diimine group or the surrounding ligands. These chemical factors govern the character and electronic localization of the excited states, their relative position, the presence of critical geometries. Moreover the shape and relative positions of the PES may be also modified by the other experimental conditions like solvent effects. Obviously the development of new theoretical tools able to compute accurate multidimensional PES is needed to investigate the dynamics of photochemical reactions in transition metal coordination compounds.

5 Concluding Remarks

Until the beginning of the 1980s, the date of the expansion of the electronic correlated methods (whereas the electronic spectroscopy and photochemistry of transition metal complexes were largely investigated experimentally), the theoretical knowledge of the excited states properties was mainly based on a qualitative scheme in term of molecular orbitals analysis. The development of efficient theories and algorithms able to take into account the electronic correlation effects and the multi-states problem combined with a new generation of computers (fast, vector oriented or parallel, with huge memory and storage capacities) has made challenging computations possible providing transition energies within 0.15 eV of accuracy even on large molecular systems at different levels of theory based either on wave function or on density functional formalism. On one hand, in the latter case the expertise is not yet sufficient with respect to the ability of the current functionals at describing a variety of excited states and additional validation calculations have to be performed. On the other hand, highly correlated wave functions are limited to middle size molecules due to the basis set and Multi- Configurational-SCF expansions.

With the spectacular development of the very popular Kohn-Sham DFT method in the last decade ground state chemical properties can be accurately predicted and reactivity interpreted on the basis of a simple and convenient analysis. Recent research devoted to implementation that scales only

linearly with the system size opens the route to the treatment of systems with hundreds, may be even thousands of atoms. The solvent effects can be already be taken into account in a number of algorithms and the hybrid methods such as Quantum Mechanics/Molecular Mechanics (QM/MM) bring within reach the treatment of other environment effects on systems of chemical/biological interest. The ground state reactivity can be analysed in terms of a single energy profile along a well defined reaction path characterized by a few critical geometries such as minima or transition states accessible through the standard quantum chemical methods. In contrast the photo-induced reactivity follows very complicated mechanisms involving non-adiabatic processes with jumps between different PES. The bottleneck of the theoretical study is the computation of refined multi-dimensional PES of consistent accuracy in the various domains of potential energy (Franck-Condon, Asymptotic region, critical geometries). Alternative methods based on molecular dynamics so-called 'on the fly' which avoid the computation of such complicated PES cannot be used actually for studying photo-reactivity in transition metal complexes mainly due to the difficulty at converging the energy and it's gradient in the presence of several near-degenerate electronic excited states. On the basis of ab initio two-dimensional PES it is possible to deduce from wave packet simulations several important photo-physical/photo-chemical properties like the time-scale of photo-dissociation, non-radiative processes such as intersystem crossings. The main features of the absorption spectra or the branching ratio between different primary reactions are also accessible. Within the limit of the theoretical model it is mandatory to perform such simulations in close collaboration with experimentalists.

References

1. Campagna S, Serroni S, Barigelletti F, Guest editors (2000) Coord Chem Rev Special Issue 13th International Symposium on Photochemistry and Photophysics of Coordination Compounds (Lipari, Italy 1999)
2. Coord Chem Rev (2002) Dick Stufkens Special Issue (Amsterdam, 2001) 230
3. Assion A, Baumert T, Bergt M, Brixner T, Kiefer B, Seyfried V, Strehle M, Gerber G (1998) Science 282:919
4. Meyer TJ (1986) Pure Appl Chem 58:1193
5. Wrighton MS (1974) Chem Rev 74:401
6. Geoffroy GL, Wrighton MS (1979) In: Organometallic photochemistry. Academic Press, New York
7. Montiel-Palma V, Perutz RN, George MW, Jina OS, Sabo-Etienne S (2000) Chem Commun 13:1175; Abbott LC, Arnold CJ, Gordon KC, Hester RE, Moore JN, Perutz RN, Ye TQ (1999) Laser Chem 19:279; Bell SEJ, Rice JH, McGarvey JJ, Hester RE, Moore JN, Perutz RN, Ye TQ, Mizutani Y, Kitagawa T (1999) Laser Chem 19:271
8. Schlegel HB (1995) In: Yarkony DR (ed) Modern electronic structure theory. World Scientific, Singapore, p 459

9. Hachey MRD, Daniel C (1998) Inorg Chem 37:1387
10. Pierloot K, Dumez B, Widmark P-O, Roos BO (1995) Theor Chim Acta 90:87
11. Pou-Amérigo R, Merchan M, Nebot-Gill I, Widmark P-O, Roos BO (1995) Theor Chim Acta 92:149
12. Nooijen M, Lotrich V (2000) J Chem Phys 113:494
13. Andrae D, Häussermann U, Dolg M, Stoll H, Preuss H (1990) Theor Chim Acta 77:123
14. Hay PJ, Wadt WR (1985) J Chem Phys 82:270
15. Hay PJ, Wadt WR (1985) J Chem Phys 82:299
16. Hurley MM, Pacios LF, Christiansen PA, Ross RB, Ermler WC (1986) J Chem Phys 84:6840
17. Küche W, Dolg M, Stoll H, Preuss H (1991) Mol Phys 74:1245
18. LaJohn LA, Christiansen PA, Ross RB, Atashroo T, Ermler WCJ (1987) Chem Phys 87:2812
19. Ross RB, Powers JM, Atashroo T, Ermler WC, LaJohn LA, Christiansen PA (1990) J Chem Phys 93:6654
20. Stevens WJ, Krauss M, Basch H, Jasien PG (1992) Can J Chem 70:612
21. Barandiaran Z, Seijo L (1992) Can J Chem 70:409
22. Casarubios M, Seijo L (1998) J Mol Struct (THEOCHEM) 59:426
23. Casarubios M, Seijo L (1999) Chem Phys 110:784
24. Seijo L (1995) J Chem Phys 102:8078
25. Bossert J, Ben Amor N, Strich A, Daniel C (2001) Chem Phys Lett 342:617
26. Vallet V, Bossert J, Strich A, Daniel C (2003) Phys Chem Chem Phys 5:2948
27. Daniel C, Guillaumont D, Ribbing C, Minaev B (1999) J Phys Chem A 103:5766
28. Visscher L, Nieuwport WC (1994) Theor Chim Acta 88:447
29. EPCISO software: Vallet V, Maron L, Teichteil C, Flament JP (2000) J Chem Phys 113:1391
30. Kleinschmidt M, Tatchen J, Marian CM (2002) J Comp Chem 23:824
31. von Barth U (1979) Phys Rev A20:1693
32. von Barth U (1980) Phys Scr 21:585
33. Daul C, Güdel H-U, Weber J (1992) J Chem Phys 98:4023
34. Daul C, Baerends EJ, Vernooijs P (1994) Inorg Chem 33:3543
35. Lannoo M, Baraff GA, Schlüter M (1981) Phys Rev B24:943
36. Wood JH (1980) J Phys B At Mol Phys 13:1
37. Runge E, Gross EKU (1984) Phys Rev Lett 52:997
38. Gross EKU, Kohn W (1990) Adv Quantum Chem 21:255
39. Gross EKU, Dobson JF, Petersilka M (1996) Density functional theory. Springer, Berlin Heidelberg New York
40. Casida ME (1995) Recent advances in density functional methods. World Scientific, Singapore
41. Roothan CCJ (1951) Rev Mod Phys 23:69
42. Roothan CCJ (1960) J Chem Phys 51:363
43. Roos BO (1972) Chem Phys Lett 15:153
44. Roos BO, Siegbahn PEM (1977) In: Schaefer HF III (ed) Methods of electronic structure theory. Plenum Press, New York, p 277
45. Shavitt I (1977) In: Schaefer HF III (ed) Methods of electronic structure theory. Plenum Press, New York, p 189
46. Siegbahn PEM (1977) Chem Phys 25:197
47. Roos BO (1983) In: Diercksen GHF, Wilson S (eds) Methods in computational physics. Reidel, Dordrecht, p 161

48. Werner H-J (1987) In: Prigogine I, Rice SA (eds) Advances in chemical physics. Wiley, Chichester, p 1
49. Shepard R (1987) In: Lawley KP (ed) Ab initio methods in quantum chemistry part II: the multiconfiguration SCF method. Wiley, Chichester
50. Werner H-J, Knowles PJ (1988) J Chem Phys 89:5803
51. Comeau DC, Bartlett RJ (1993) Chem Phys Lett 207:414
52. Geertsen J, Rittby M, Bartlett RJ (1989) Chem Phys Lett 164:57
53. Sekino H, Bartlett RJ (1984) Int J Quantum Chem Symp 18:255
54. Stanton JF, Bartlett RJ (1993) J Chem Phys 98:7029
55. Stanton JF, Bartlett RJ (1993) J Chem Phys 98:9335
56. Nakatsuji H (1978) Chem Phys Lett 59:362
57. Nakatsuji H (1979) Chem Phys Lett 67:329
58. Nakatsuji H (1979) Chem Phys Lett 67:334
59. Andersson K, Malmqvist P-Å, Roos BO, Sadlej AJ, Wolinski K (1990) J Phys Chem 94:5483
60. Andersson K, Malmqvist P-Å, Roos BO (1992) J Chem Phys 96:1218
61. Andersson K, Roos BO, Malmqvist P-Å, Widmark P-O (1994) Chem Phys Lett 230:391
62. Finley J, Malmqvist P-Å, Roos BO, Serrano-Andrés L (1998) Chem Phys Lett 288:299
63. MOLCAS 5.0 software (2000) University of Lund
64. GAUSSIAN software (1998) Carnegie Office Park, Pittsburgh PA USA
65. Werner H-J, Knowles PJ, Amos RD (2002) MOLPRO version 2002.1 software
66. Ahlrichs R et al. (2002) TURBOMOLE Program Package for ab initio electronic structure calculations version 5.5. Universität Karlsruhe, Physical Chemist, Karlsruhe, Germany
67. ACES II software: Stanton JF, Gauss J, Perera SA, Yau A, Watts JD, Nooijen M, Oliphant N, Szalay PG, Lauderdale WJ, Gwaltney SR, Beck S, Balkova A, Bernholdt DE, Baeck K-K, Rozyczko P, Sekino H, Hober C, Pittner J, Bartlett RJ (2002) Quantum Theory Project, University of Florida
68. Baerends EJ, Bickelhaupt FM, v Gisbergen SJA, Guerra CF, Snijders JG, Velde G, Ziegler T (2002) ADF version 2002.21 SCM Theoretical Chemistry. Vrije Universiteit, Amsterdam, The Netherlands
69. HONDO 8.5 software: Dupuis M et al. (1994) Electronic Structure System
70. Roos BO, Taylor PR, Siegbahn PEM (1980) Chem Phys 48:157
71. Roos BO (1987) In: Lawley KP (ed) Advances in chemical physics; ab initio methods in quantum chemistry. Wiley, Chichester, p 399
72. Malmqvist P-Å, Rendell A, Roos BO (1990) J Phys Chem 94:5477
73. Roos BO, Andersson K (1995) Chem Phys Lett 245:215
74. Kühn O, Hachey MRD, Rohmer MM, Daniel C (2000) Chem Phys Lett 322:199
75. Cizek J (1969) J Chem Phys 45:4256
76. Coester F (1966) Nucl Phys 7:421
77. Paldus J, Cizek J, Shavitt I (1972) Phys Rev A 5:50
78. Nakatsuji H, Hirao K (1978) J Chem Phys 68:2035
79. Bartlett RJ (1981) Ann Rev Phys Chem 32:359
80. Watts JD, Gauss J, Bartlett RJ (1993) J Chem Phys 98:8718
81. Nakatsuji H, Ehara M, Palmer MH, Guest MF (1992) J Chem Phys 97:2561
82. Oliphant N, Bartlett RJ (1994) J Am Chem Soc 116:4091
83. Ziegler T, Rauk A, Baerends EJ (1977) Theor Chim Acta 43:261
84. Daul C (1994) Int J Quantum Chem Symp 52:867
85. Jamorski C, Casida ME, Salahub DR (1996) J Chem Phys 104:5134

86. Casida ME (1996) In: Recent advances in density functional methods. World Scientific, Singapore
87. Casida ME (1996) In: Recent developments and applications of modern DFT. Elsevier Science, Amsterdam, p 391
88. Rosa A, Baerends EJ, Gisbergen SJA, van Lenthe E, Groeneveld JA, Snijders JG (1999) J Am Chem Soc 121:10356
89. Wakamatsu K, Nishimito K, Shibahara T (2000) Inorg Chem Commun 3:677
90. Van Gisbergen SJA, Groeneveld JA, Rosa A, Snijders JG, Baerends EJ (1999) J Phys Chem A 103:6835
91. Ricciardi G, Rosa A, van Gisbergen SJA, Baerends EJ (2000) J Phys Chem A 104:635
92. Rosa A, Ricciardi G, Baerends EJ, van Gisbergen SJA (2001) J Phys Chem A 105:3311
93. Ricciardi G, Rosa A, Baerends EJ (2001) J Phys Chem A 105:5242
94. Turki M, Daniel C, Záliš S, Vlček A Jr, van Slageren J, Stufkens DJ (2001) J Am Chem Soc 123:11431
95. Full J, Gonzalez L, Daniel C (2001) J Phys Chem A 105:184
96. Chermette H (1998) Coord Chem Rev 178/180:699
97. Pulay P (1995) In: Yarkony DR (ed) Modern electronic structure theory. World Scientific, Singapore, p 1191
98. Shepard R (1995) In: Yarkony DR (ed) Modern electronic structure theory. World Scientific, Singapore, p 345
99. Baerends EJ, Rosa A (1998) Coord Chem Rev 177:97
100. Caillie CV, Amos RD (2000) Chem Phys Lett 317:159
101. Worth GA, Hunt P, Robb MA (2003) J Phys Chem A 107:621
102. Sobolewski AL, Domcke W (2000) Chem Phys 259:181
103. Matsika S, Yarkony DR (2002) J Phys Chem A 106:2580
104. Finger K, Daniel C, Saalfranck P, Schmidt B (1996) J Phys Chem 100:3368
105. Heitz MC, Daniel C (1997) J Am Chem Soc 119:8269
106. Guillaumont D, Vlček A Jr, Daniel C (2001) J Phys Chem A 105:1107
107. Schinke R (1993) In: Photodissociation dynamics. Cambridge University Press, Cambridge
108. Heller EJ (1981) Acc Chem Res 14:368
109. Kotzian M, Rösch N, Schröder H, Zerner MC (1989) J Am Chem Soc 111:7687
110. Pierloot K, Tsokos E, Vanquickenborne LG (1996) J Phys Chem 100:16545
111. Nakai H, Ohmari Y, Nakatsuji H (1991) J Chem Phys 95:8287
112. Sohn YS, Hendrickson DN, Gray HB (1971) J Am Chem Soc 93:3603
113. Vanquickenborne LG, Verhulst J (1983) J Am Chem Soc 105:1769
114. Pierloot K, Verhulst J, Verbeke P, Vanquickenborne LG (1989) Inorg Chem 28:3059
115. Pollak C, Rosa A, Baerends EJ (1997) J Am Chem Soc 121:10356
116. Blackney GB, Allen WF (1971) Inorg Chem 12:2763
117. Church SP, Poliakoff M, Timney JA, Turner JJ (1983) 22:3259
118. Heitz MC, Ribbing C, Daniel C (1997) J Chem Phys 106:1421
119. Daniel C (1992) J Am Chem Soc 114:1625
120. Meyer TJ, Caspar JV (1985) Chem Rev 85:187
121. Levenson RA, Gray HB (1975) J Am Chem Soc 97:6042
122. Rosa A, Ricciardi G, Baerends EJ, Stufkens DJ (1995) Inorg Chem 34:3425
123. Farrell IR, van Slageren J, Záliš S, Vlček A Jr (2001) Inorg Chim Acta 315:44
124. Guillaumont D, Daniel C, Vlček A Jr (2001) J Phys Chem A 105:1107
125. Záliš S, Vlček A Jr, Daniel C (2003) Collect Czech Commun 68:89
126. Stufkens DJ (1992) Comments Inorg Chem 13:359

127. Aarnts MP, Wilms MP, Peleen K, Fraanje J, Goubitz K, Hartl G, Stufkens DJ, Baerends EJ, Vlček A Jr (1996) Inorg Chem 35:5468
128. Aarnts MP, Stufkens DJ, Wilms MP, Baerends EJ, Vlček A Jr, Clark IP, George MW, Turner JJ (1996) Chem Eur J 2:1556
129. Nieuwenhuis HA, Stufkens DJ, Oskam A (1994) Inorg Chem 33:3212
130. Nieuwenhuis HA, Stufkens DJ, Oskam A, Vlček A Jr (1995) Inorg Chem 34:3879
131. Kleverlaan CJ, Martino DM, van Willigen H, Stufkens DJ, Oskam A (1996) J Phys Chem 100:18607
132. Kleverlaan CJ, Stufkens DJ, Clark IP, George MW, Turner JJ, Martino DM, van Willigen H, Vlček A Jr (1998) J Am Chem Soc 120:10871
133. Kleverlaan CJ, Stufkens DJ (1999) Inorg Chim Acta 284:61
134. Rossenaar BD, Lindsay E, Stufkens DJ, Vlček A Jr (1996) Inorg Chim Acta 250:5
135. Rossenaar BD, Stufkens DJ, Oskam A, Fraanje J, Goubitz K (1996) Inorg Chim Acta 247:215
136. Guillaumont D, Daniel C (1999) J Am Chem Soc 121:11733
137. Bruand-Cote I, Daniel C (2002) Chem A Eur J 8:1361
138. Ben Amor N, Záliš S, Daniel C (2004) J Phys Chem A (submitted)
139. Maestri M, Balzani V, Deuschel-Cornioley C, von Zelewsky A (1992) Adv Photo Chem 17:1
140. Yersin H, Huber P, Wiedenhofer H (1994) Coord Chem Rev 132:35
141. Yersin H, Donges D (2001) In: Top Curr Chem, vol 214. Springer, Berlin Heidelberg New York
142. Pierloot K, Ceulemans A, Merchan M, Serrano-Andrés L (2000) J Phys Chem A 104:4374
143. Yersin H, Schützenmeier S, Wiedenhofer H, von Zelewsky A (1993) J Phys Chem 97:13496
144. Wiedenhofer H, Schützenmeier S, von Zelewsky A, Yersin H (1995) J Phys Chem 99:13385
145. King KA, Spellane PJ, Watts RJ (1985) J Am Chem Soc 107:1431
146. Colombo MG, Brunold TC, Riedener T, Gudel HU, Fortsch M, Burgi HB (1994) Inorg Chem 33:545
147. Lamansky S, Djurovich P, Murphy D, Abdel-Razzaq F, Kwong R, Tsyba I, Bortz M, Mui B, Bau R, Thompson ME (2001) Inorg Chem 40:1704
148. Lamansky S, Djurovich P, Murphy D, Abdel-Razzaq F, Lee HE, Adachi C, Burrows PE, Forrest SR, Thompson ME (2001) J Am Chem Soc 123:4304
149. Finkenzeller WJ, Yersin H (2003) Chem Phys Lett 377:299
150. Hay PJ (2002) J Phys Chem A 106:1634
151. Baldo MA, O'Brien DF, You Y, Shoustikov A, Sibley S, Thompson ME, Forrest SR (1998) Nature 395:151
152. Beck MT, Kiss P, Szalay T, Porzsolt EC, Bazsa G (1976) J Signal Am 4:131
153. Endo K, Saikawa M (1990) J Photo Sci 38:210
154. Ribbing C, Gilliams B, Pierloot K, Roos BO, Karlström G (1998) J Chem Phys 109:3145
155. Ribbing C, Daniel C (1994) J Chem Phys 100:6591
156. Eyring G, Schönherr T, Schmidtke HH (1983) Theor Chim Acta 64:83
157. Schönherr T (1997) Top Curr Chem 191:87
158. Ribbing C, Pierloot C, Ceulemans A (1998) Inorg Chem 37:5227
159. Atanasov MA, Schönherr T, Schmidtke HH (1987) Theor Chim Acta 71:59
160. Schönherr T, Eyring G, Linder R (1983) Z Naturforsch 38:736
161. Fatta AM, Lintvedt RL (1971) Inorg Chem 10:478

162. Stufkens DJ, van Outerstep JMW, Oskam A, Rossenaar BD, Stor GJ (1994) Coord Chem Rev 132:147
163. Rossenaar BD, Kleverlaan CJ, van de Ven MCE, Stufkens DJ, Vlček A Jr (1996) Chem Eur J 2:228
164. Farrell IR, Matousek P, Kleverlaan CJ, Vlček A Jr (2000) Chem Eur J 6:1386
165. Farrell IR, Vlček A Jr (2000) Coord Chem Rev 208:87

Top Curr Chem (2004) 241:167–278
DOI 10.1007/b96863

Spectra, Energy Levels and Energy Transfer in High Symmetry Lanthanide Compounds

Peter A. Tanner (✉)

Department of Biology and Chemistry, City University of Hong Kong, Tat Chee Avenue, Kowloon, Hong Kong S.A.R. P.R. China
bhtan@cityu.edu.hk; http://personal.cityu.edu.hk/~bhtan

Abstract The Ln^{3+} ion is situated at a site of octahedral symmetry in crystals of the lanthanide elpasolites, M_2ALnX_6. The syntheses and crystal structures of M_2ALnX_6 are described, with particular reference to phase transitions. The centrosymmetric environment of Ln^{3+} confers different spectral properties than are observed for most solid-state lanthanide ion systems, and the selection rules are deduced. The vibrational, electronic Raman and electronic spectra of the lanthanide elpasolite systems are presented and discussed. The electronic spectra are described in terms of the $4f^N$-$4f^N$ zero phonon line and the vibronic sideband structure and the success of intensity calculations is evaluated. The synergy of one- and two-photon studies is emphasized. The differences with the $4f^N$-$4f^{N-1}5d$ spectra of M_2ALnX_6 are illustrated. The parametrization of the energy level datasets is assessed and the success of recent refinements is analysed. Following a brief review of the theory of energy transfer in crystals, experimental studies of quenching, cross-relaxation, upconversion and photon avalanche in neat and doped elpasolite systems are reviewed. Physical mechanisms are given for spectral features and for energy transfer pathways.

Keywords Cubic crystal · Vibrational Spectra · Luminescence · Absorption · Crystal Field · Vibronic

List of Abbreviations

CF	Crystal field
ED	Electric dipole
EDV	Electric dipole vibronic
EQ	Electric quadrupole
ESA	Excited state absorption
ET	Energy transfer
IR	Infrared
irrep	Irreducible representation
MCD	Magnetic circular dichroism
MCPE	Magnetic circularly polarized emission
TP	Two-photon
ZPL	Zero phonon line

1 Introduction

This review covers the series La^{3+} ($4f^0$) to Lu^{3+} ($4f^{14}$), including also Y^{3+}, which are collectively denoted by Ln^{3+}. It focuses upon neat and doped hexahalide compounds with Ln^{3+} situated at equilibrium sites of octahedral symmetry with the elpasolite structure, M_2ALnX_6 (M^+, A^+ are univalent cat-

ions and X^- is a halide anion). Ln^{2+} and Ln^{4+} systems; other high symmetry systems such as hexanitritolanthanates(III) [1]; lanthanide ions (Ln^{3+}) at cubic sites in MF_2 (M=Ca, Sr) [2–6] or $MCaF_3$ [7] crystals where charge compensation is required; as well as lower symmetry elpasolite systems, are mostly not included. This review covers the synthesis, structures, spectra and ET phenomena of lanthanide elpasolites. It is written for chemists so mathematical treatments and details of instrumentation have been omitted but can be consulted from the references.

The aims of the study of the electronic spectra of M_2ALnX_6 systems are to obtain information about the interaction of the vibrational part of the CF with the paramagnetic ion, and to determine the energies and symmetry properties of the vibrational modes. One of the outcomes of the spectral analysis is a CF energy level diagram, which can test theoretical models of lanthanide ion systems. The detailed knowledge of the energy level schemes and of the vibrational properties is then essential for an understanding of the ET phenomena between lanthanide ions. A distant hope remains for the ability to tailor-make materials, aided by CF calculations, which are efficient phosphors, upconverters and solid-state laser materials. The rationale for studying lanthanide elpasolites is that they comprise the most symmetric crystal system available for Ln^{3+}, and serve as model systems for our understanding of static and dynamic processes in the solid-state. Although the structural simplicity is manifested by highly degenerate electronic energy levels of Ln^{3+}, it is not evident in the electronic spectra and ET phenomena of these systems, which as yet, require more detailed understanding.

2 Synthesis

Meyer [8] reviewed the synthesis and structure of elpasolites in 1982. The preparation of the precursors, the anhydrous lanthanide halides has been reviewed by Taylor [9], Taylor and Carter [10] and Corbett [11, 12]. A versatile solid-state method to the synthesis of LnX_3 (X=Cl, Br, I) is the ammonium chloride route [13, 14]. The phase diagram of the ternary system CsCl-NaCl-$LaCl_3$ has been investigated by differential thermal analysis and X-ray diffraction and only one congruently melting compound $Cs_2NaLaCl_6$ was found [15].The chloroelpasolites $Cs_2NaLnCl_6$ are conveniently prepared by the dissolution of the appropriate lanthanide oxide in hot, concentrated HCl, followed by the addition of solid CsCl and NaCl, and then evaporation to dryness [16]. The powdered product is hygroscopic and may be converted to the anhydrous form by pumping under vacuum, or with the passage of dry HCl gas, at about 450 °C. The powder is then sealed inside a quartz tube and passed through a Bridgman furnace at the appropriate temperature. The melting points of $Cs_2NaLnCl_6$ are generally >800 °C. As an alternative prepa-

ration, the stoichiometric quantities of dry $LnCl_3$, CsCl and NaCl are sealed into a quartz tube, which is passed through the Bridgman furnace [8]. The resulting crystals are deliquescent and should be handled in a dry box, where they can be cut, polished and sealed in resin. Coating the crystal with liquid paraffin oil or vacuum grease affords temporary prevention from moisture attack. Baud et al. [17] have utilized the solid-state reaction of a mixture of constituent chlorides to prepare the series Cs_2KLnCl_6. The series $Cs_2LiLnCl_6$ have been prepared from the dissolution of CsCl, LiCl (or Li_2CO_3) and the lanthanide oxide in concentrated HCl, and then by the passage of HCl gas for two days at 500 °C over the resulting powder after evaporation [18]. The series $Rb_2NaLnCl_6$ [19] and $Cs_2AgLnCl_6$ [20] were prepared similarly. Alternatively, the reaction of $CsLu_2Cl_7$ with Li in a Ta tube for 19 days at 500 °C gives $Cs_2LiLuCl_6$ [21]. The solid-state halide method is equally applicable for the synthesis of complex bromides [22] and fluorides [23, 24], provided that the appropriate container and temperature are selected [8]. Bromides are hygroscopic but the fluorides are harder crystals and more stable in air. A lower temperature route to hexafluoroelpasolites is available by the hydrothermal method [25], in which aqueous solutions of the fluorides MF and AF, together with the lanthanide oxide, are heated at about 480 °C and pressures of 100–150 MPa. The fluorides Cs_2ALnF_6 have also been prepared by direct fluorination [26, 27] or hydrofluorination [28] of the corresponding chlorides or oxides. The flux [29, 30] and bifluoride [31] methods which have been employed for d- and p-block hexafluoroelpasolites have not been utilized for the corresponding lanthanide ion complexes. The series Cs_2ALnI_6 (A=Na, Li) was prepared by the solid-state reaction of CsI, AI, Ln metal and I_2 at 300 °C [32].

3 Structure

The structure of the mineral elpasolite, K_2NaAlF_6 (M_2ALnX_6 type, [33]) occupies an intermediate position between perovskite ($MLnX_3$, where Ln=A) and antifluorite (M_2LnX_6, where there are no A^+ ions) types. The elpasolite system M_2ALnX_6, where $r(M^+)>r(A^+)$, crystallizes in the face-centred cubic space group *Fm3m* (No. 225). The $4Ln^{3+}$ are located at (a) (0,0,0) at an octahedral (O_h) site in 6-coordination with Cl^-, with the $4A^+$ at (b) (½,½,½), also at an O_h site. The $8M^+$ are situated at (c) (¼,¼,¼) in a simple cubic lattice; and $24X^-$ are at (e) (x00), being shared by Ln^{3+} and A^+ so that the LnX_6 and AX_6 octahedra are interconnected (Fig. 1a–c). The free parameter x depends mostly upon the relation between the A^+ and Ln^{3+} radii and is in the range from 0.225 to 0.275 [28]. The lattice spacing is large (about 1 nm) so that the closest Ln-Ln distance is about 0.7 nm, being much larger than in dimeric systems (e.g. 0.38 nm in $Cs_3Yb_2Br_9$ [34]) where Ln-Ln interactions

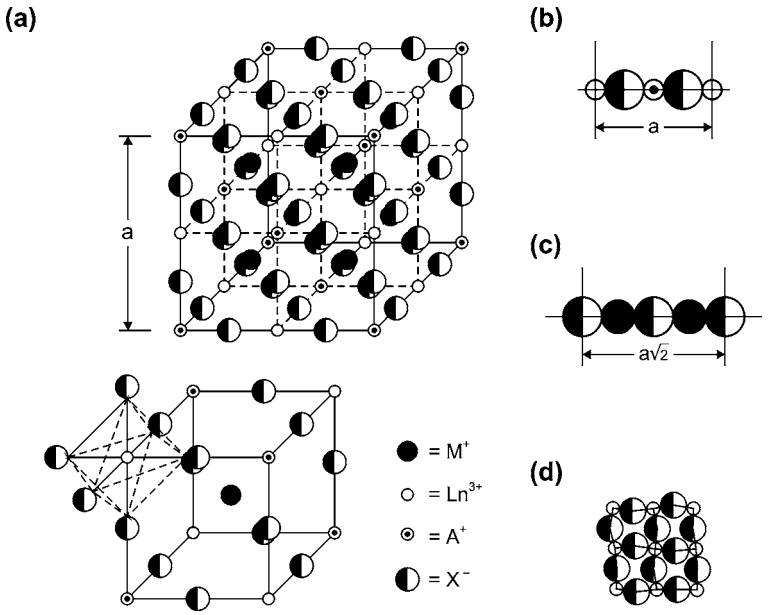

Fig. 1a–d Crystal structure of M_2ALnX_6 and coordination environment of Ln^{3+}: **a** packing of ions in the crystal lattice, showing the octahedral coordination of Ln^{3+} and A^+; **b** packing along the **c** axis in the **ab** plane; **c** packing in the **ab** plane along the [110] direction at **c**=1/4; **d** rotation of the LnX_6^{3-} octahedra in the distorted phase

have ramifications in the electronic spectra. The local environment of Ln^{3+} in $Cs_2NaLnCl_6$ has been compared with that in $Cs_3Ln_2Cl_9$ [35], since both systems have six Cl^- nearest neighbours at about 0.25 nm distant. However, a further Ln^{3+} ion is the second nearest neighbour in the latter system, but only the fourth nearest in $Cs_2NaLnCl_6$. Figure 2a shows the variation of the lattice parameter, $|\mathbf{a}|$, of the unit cell of Cs_2NaLnX_6 with the 6-coordinate ionic radius (r) of Ln^{3+}. In each case the r=0 intercept differs by no more than 5% from $2r(Na^+)+4r(X^-)$.

The major structural interest concerning elpasolites concerns the wide variety of phase transitions which these systems undergo. Usually the structural distortions are associated either with rotations of the octahedra LnX_6^{3-} to give a tetragonal phase (space group $I4/m$-C_{4h}^5), or with a combination of octahedron rotations and M^+ ion displacements from their equilibrium positions in the tetragonal phase to give a monoclinic phase ($P12_1/n1$) [36]. For the series $Cs_2NaLnCl_6$, investigations of the cubic to tetragonal phase transition have been carried out by heat capacity measurements [37–39], inelastic neutron scattering [40, 41], electron spin resonance [42, 43], nuclear magnetic resonance [44] and X-ray diffraction [45]. The results show that the early members of the series $Cs_2NaLnCl_6$ undergo this phase transition at

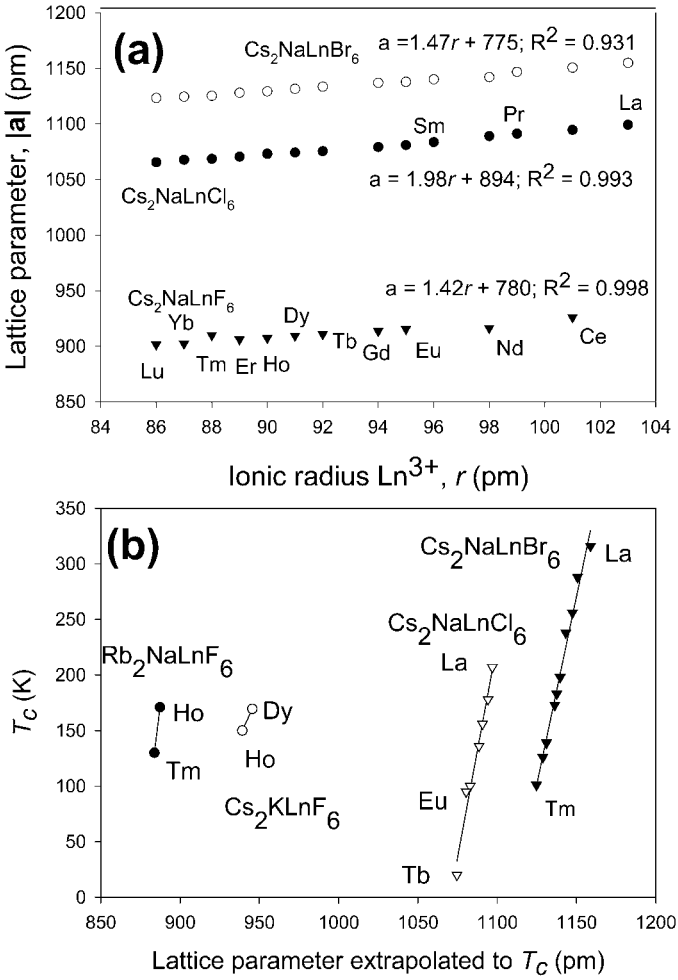

Fig. 2 **a** Plot of lattice parameter of Cs_2NaLnX_6 (X=Cl, Br, F) against 6-coordinate ionic radius of Ln^{3+} (data from [8]). **b** Plot of cubic to tetragonal phase transition temperature, T_C, against lattice parameter extrapolated to T_C (data from [8, 37, 41, 43, 50, 60]). The linear regressions in **b** are shown as a guide to the eye

higher temperatures (for example, 207 K for La [43]), but later members are more resistant to it. The Goldschmidt tolerance factor, *t*, derived from the consideration of hard-packing of spherical ions [8], is successful in identifying the stable range (when *t* is in the range 0.8 to 1.0) for the cubic structure of MAX_3 compounds from the ionic ratios of the constituent ions. The modified tolerance factor is deduced by the hard sphere packing in the unit cell of M_2ALnX_6, from Fig. 1b,c [24]:

$$t' = \frac{[r(M_{12}^{+}) + r(X^{-})]}{\sqrt{2}\{0.5[r(A_6^{+}) + r(Ln_6^{3+})] + r(X^{-})\}} \quad (1)$$

where the subscript denotes the coordination number. Although t' is capable of predicting the stability ranges of M_2ALnF_6, it fails for the series M_2ALnCl_6 [8]. This is because the polarizability of X^- increases by a factor of 4 from F^- to Cl^- [8], so that the hard sphere model is not applicable. Meyer has provided an alternative classification of the stability ranges of M_2ALnCl_6 in terms of structure field maps, employing differences in molar volumes with respect to a particular compound [8]. A large number of studies using solid-state nuclear magnetic resonance [46] X-ray diffraction [47–50], heat capacity [51] on lanthanide ion systems, as well as electron spin resonance [52, 53], Raman [54, 55], hydrostatic pressure [56] and calorimetric studies [57] on other systems, have concerned the phase transitions of M_2ALnF_6. Cubic to tetragonal phase transitions for the series $Cs_2NaLnBr_6$ occur in the range 316 K (Ln=La) to 173 K (Ln=Gd) [58].

The number of formula units per unit cell is unchanged in the initial displacive phase transition, and the space group is reduced to the $I4/m\text{-}C_{4h}^5$ tetragonal subgroup. The only phonons affected by a transition involving no change in the number of molecules per unit cell are those of infinite wavelength in the cubic structure. The transition is associated with the instability of only one lattice vibration, with all other vibrations showing no changes, and the determination of the particular vibration is discussed by Ihringer [50]. In fact, the τ_{1g} lattice vibration (see Sect. 5) in the low temperature structure effectively collapses at T_c, and is called a soft mode, i.e. the single zone centre mode i for which the frequency vanishes at the phase transition temperature, obeying an equation of the type

$$\omega_i^2 = \text{constant} \times (T - T_c) \quad (2)$$

with temperature T. This produces a rotation of the LnX_6^{3-} octahedra, by about 5° at 17 K in the case of Rb_2NaHoF_6 [50], and brings four of the 12 X^- ions surrounding each M^+ into contact with it, thereby reducing the unit cell volume by a few percent. The tetragonal domains are long range and randomly oriented in the crystal along the four-fold cubic axes [59], Fig. 1d. The τ_{1g} (O_h) soft mode is inactive in the Raman spectrum of the cubic phase, but is potentially active [α_g+$\epsilon_g(C_{4h})$] in the Raman spectrum below T_c [55].

The $Fm3m \rightarrow I4/m$ transition is second order since it is characterized by discontinuities in the second derivatives of the free energy, such as heat capacity [37]. Figure 2b shows that for some Ln^{3+}, a linear relation exists between T_c and the lattice constant extrapolated to the phase transition temperature. Actually, the T_c=0 intercept from linear regression in Fig. 2b for the $Cs_2NaLnCl_6$ series is 1070.4 pm, which suggests that these compounds

with smaller unit cells than this value (i.e. Ln^{3+}=Er^{3+}, Tm^{3+}, Yb^{3+}, Lu^{3+}) do not undergo the phase transition. However, apparent exceptions to this behaviour are $Cs_2NaGdCl_6$ [59] (not shown in Fig. 2b), and $Cs_2NaTmCl_6$ [44] which are stable down to the mK range. Krupski has calculated the phase transition temperatures, and the slopes in Fig. 2b from a rigid sphere model, in which the M^+ cation sits inside a rhombic dodecahedral cavity of 12 neighbouring X^- anions. In the rigid sphere model, the T_C=0 intercept in Fig. 2b represents the case when M^+ and X^- are in mutual contact, i.e.

$$|\mathbf{a}|(T_C = 0) = 2\sqrt{2}[(R(M^+) + R(X^-))] \tag{3}$$

where R is the Pauling 12-fold coordination radius. In agreement with this, from Fig. 2b, the derived sum of the radii of the Cs^+ and X^- ions from the intercepts of the plots of Cs_2NaLnX_6 (X=Cl, Br) are <0.62% greater than the sum of the corresponding 12-coordinate ionic radii.

In some cases, the above cubic to tetragonal transition is followed by other types, such as the ${O_h}^5 \rightarrow {C_{4h}}^5 \rightarrow {C_{2h}}^3 \rightarrow {C_{2h}}^5$ phase transitions of Cs_2RbDyF_6 [49, 54]. A first-order phase transition, involving a cooperative Jahn-Teller distortion has been reported for $Cs_2NaHoCl_6$ at low temperature, 150 mK [61].

4 Spectral Selection Rules

The various optical spectra caused by the interaction of electromagnetic radiation with wavevector $|\mathbf{k_i}|=2\pi/\lambda$ with a crystal are governed by corresponding spectral selection rules. The scalar quantity k_i ranges from 10 to 50,000 cm^{-1} for infrared to ultraviolet radiation. On the other hand the range of values of $|\mathbf{k}|$ of the crystal lattice (vibration) wave in the first Brillouin zone, i.e. the unit cell of the reciprocal lattice is $[1/|\mathbf{a}| \sim 1/(10^{-7}$ cm)]. The changes in wavevector (or momentum) of the lattice wave which accompany Raman scattering or infrared absorption are thus very small compared to the size of the Brillouin zone. To a first approximation we then have the selection rules $\mathbf{k}$=0, i.e. only the phonons at the zone centre, or the in-phase motions in all primitive unit cells of the crystal can be involved. The situation corresponds to a lattice wave phonon having infinite wavelength.

The intensity of a spectral transition is calculated from matrix elements involving the initial and final state wavefunctions and the transition operator. This leads to selection rules, as for multielectron atoms, in terms of restrictions upon the values of S, L and J in the transition (Table 1). Considering the selection rules for vibrational spectra, the $\mathbf{k}$=0 phonons of the initial and terminal states transform as Γ_i and Γ_f, respectively, of the point group

Table 1 Transformation properties under point group O_h of operators for interaction of radiation with single crystals, and related selection rules

Type of spectrum	Operator	Irrep(s) in O_h	Ref.	*SLJ* selection rules[a]	Allowed terminal states[b] from	
					Γ_{1g} initial state	Γ_{8g} initial state
Vibrational infrared	ED	Γ_{4u}	[62]	-	$\Gamma_{4u} \equiv \tau_{1u}$ (v)	$\Gamma_{4u} \equiv \tau_{1u}$ (v)
Vibrational Raman	Polarizability	Γ_{1g}, Γ_{3g}, Γ_{5g}	[62]	-	$\Gamma_{1g} \equiv \alpha_{1g}$, $\Gamma_{3g} \equiv \epsilon_g$, $\Gamma_{5g} \equiv \tau_{2g}$ (v)	
Electronic Raman	Polarizability	$[\Gamma_{1g}, \Gamma_{3g}, \Gamma_{5g}]^s$ $[\Gamma_{4g}]^{as}$	[63]	$\Delta S=0$; $\lvert\Delta L\rvert \leq 2$; $\Delta J \leq 2$;	Γ_{1g}, Γ_{3g}, Γ_{5g}, Γ_{4g} (e)	Γ_{6g}, Γ_{7g}, Γ_{8g} (e)
One photon electronic transition	ED	Γ_{4u}	[64]	$\Delta S=0$; $\lvert\Delta L\rvert \leq 1$; $\lvert\Delta J\rvert \leq 1$; $J=0 \leftrightarrow J=0$ and $L=0 \leftrightarrow L=0$ are forbidden	Γ_{4u} (e)	Γ_{6u}, Γ_{7u}, Γ_{8u} (e)
	Induced ED	Not applicable in O_h symmetry	[64, 65]	$\Delta S=0$; $\lvert\Delta L\rvert \leq 6$; $\lvert\Delta J\rvert \leq 6$; if $J=0$ or $J'=0$, $\lvert\Delta J\rvert=2,4,6$; $J=0 \leftrightarrow J=0$ and $L=0 \leftrightarrow L=0$ are forbidden	Not applicable in O_h symmetry	Not applicable in O_h symmetry
	MD	Γ_{4g}	[65]	$\Delta S=0$; $\Delta L=0$; $\lvert\Delta J\rvert \leq 1$; $J=0 \leftrightarrow J=0$ and $L=0 \leftrightarrow L=0$ are forbidden	Γ_{4g} (e)	Γ_{6g}, Γ_{7g}, Γ_{8g} (e)
	EQ	Γ_{3g}, Γ_{5g}	[66]	$\Delta S=0$; $\lvert\Delta L\rvert \leq 2$; $\lvert\Delta J\rvert \leq 2$; $J=0 \leftrightarrow J=0$ and $L=0 \leftrightarrow L=0$ are forbidden	Γ_{3g}, Γ_{5g} (e)	Γ_{6g}, Γ_{7g}, Γ_{8g} (e)
	ED Vibronic	Γ_{4u} (see Sect. 7.4)	[67, 68]	$\Delta S=0$; $\lvert\Delta J\rvert \leq 6$; $\lvert\Delta L\rvert \leq 6$; if $J=0$ or $J'=0$, $\lvert\Delta J\rvert=2$, 4, 6; $J=0 \leftrightarrow J=0$ and $L=0 \leftrightarrow L=0$ are forbidden	See Table 4	See Table 4
One colour TP electronic transition	TP	$[\Gamma_{1g}, \Gamma_{3g}, \Gamma_{5g}]^s$	[69–71]	Depends upon approximation order, e.g. $\Delta S=0$; $\lvert\Delta J\rvert \leq 2$; $\lvert\Delta L\rvert \leq 2$; for second-order Axe process (see Sect. 10)	Γ_{1g}, Γ_{3g}, Γ_{5g} (e)	Γ_{6g}, Γ_{7g}, Γ_{8g} (e)

[a] Additional one-electron quantum number selection rules are not included here, see for example [65]

[b] v=vibrational, e=electronic state. s from symmetric; as from antisymmetric direct product of $\Gamma_{4u} \times \Gamma_{4u}$

O_h for elpasolites.[1] The transition operator also transforms according to a particular irrep, Γ_o, of O_h (Table 1), so that simple group theoretical selection rules may be formulated to identify whether a particular type of transition is potentially allowed or forbidden. Then the point group selection rule for an allowed vibrational transition is

$$\Gamma_i \times \Gamma_f \quad \text{contains} \quad \Gamma_o \tag{4}$$

Examples are given in lines 1 and 2 of Table 1 for allowed IR and Raman transitions, respectively.

5 Vibrational Spectra

In order to understand the electronic spectra of the lanthanide hexahaloelpasolites, which are mainly vibronic in character, it is essential to have a firm understanding of the vibrational spectra. The vibrations of elpasolites may be classified in terms of the moiety modes [ν_i (i=1 to 6)] of the LnX_6^{3-} ion [74], or the vibrations [S_i (i=1 to 10)] of the (Bravais) unit cell [75, 76], which are all of the **k**=0 optical vibrations. The Cartesian displacements of these normal vibrations of M_2ALnX_6 are shown in Fig. 3. From Table 1, it is observed that only τ_{1u} modes are IR active, whilst α_{1g}, ϵ_g and τ_{2g} modes are Raman active. Several studies have concerned the room temperature IR spectra of $Cs_2NaLnCl_6$ [77–81], M_2ALnBr_6 [82] and M_2ALnF_6 [83–85]. Raman spectra at temperatures from 300 to 10 K have been reported for $Cs_2NaLnCl_6$ [86–94], M_2ALnBr_6 [95–96] and M_2ALnF_6 [25, 83, 97, 98]. The room temperature Raman and IR spectra of $Cs_2NaYbCl_6$ are shown in Fig. 4a,b. The four Raman bands are assigned to the S_5, S_4, S_2 and S_1 modes, in order of increasing energy, whereas the four IR bands correspond to the S_9, S_7, S_8 and S_6 τ_{1u} modes. The spectra of $Cs_2NaLnCl_6$ (Ln=Nd, La) in [79] show an additional IR band at 215 cm^{-1}, and since it is not present in the spectrum of ref. [78] it is due to another species. The corresponding spectra of Cs_2KYbF_6 are shown in Fig. 4e,f. The vibrational assignments are collected in Table 2. The energy of S_{10}, and of the low temperature ungerade modes are taken from the vibronic spectra, discussed in Sect. 7.4. Polar vibrations can be longitudinal optic (LO) or transverse optic (TO) (with the energy LO>TO), depending upon the direction of the displacement with respect to the phonon wavevector. The TO-LO splittings are not resolved in the room temperature IR spectra, and there has been some discussion in the literature

[1] The O_h point group character table and the O (and O^* double group) multiplication table are given in the Appendix. The irreps are labelled Γ_1, Γ_2... herein [72], corresponding to A_1, A_2.... The subscript g or u is usually not included in the labelling of $4f^N$ crystal field states since it is even (odd) for even (odd) N, respectively [73].

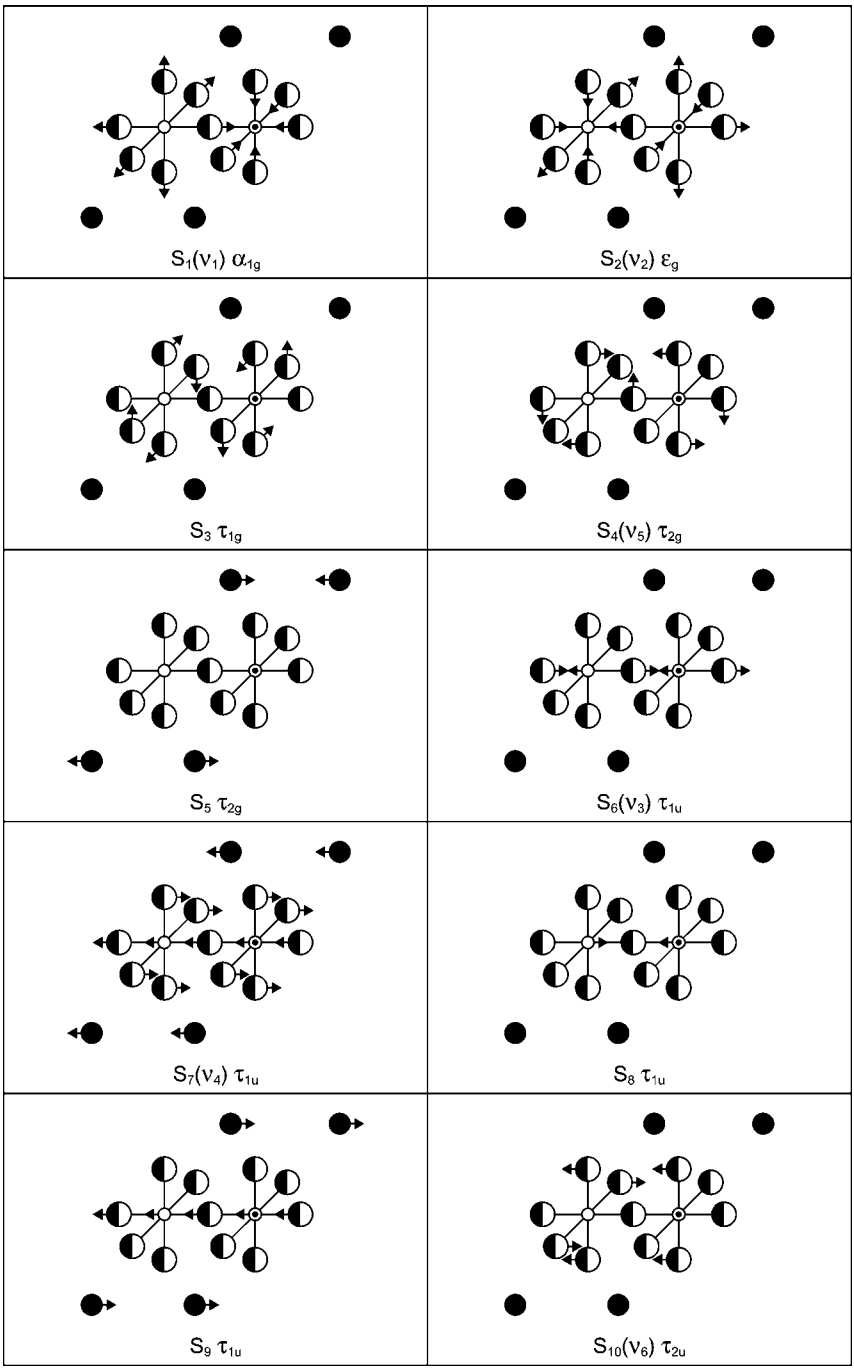

Fig. 3 Cartesian symmetry coordinate displacements (not to scale) in the normal vibrations of M_2ALnX_6. The labelling of nuclei is the same as Fig. 1. (After [75])

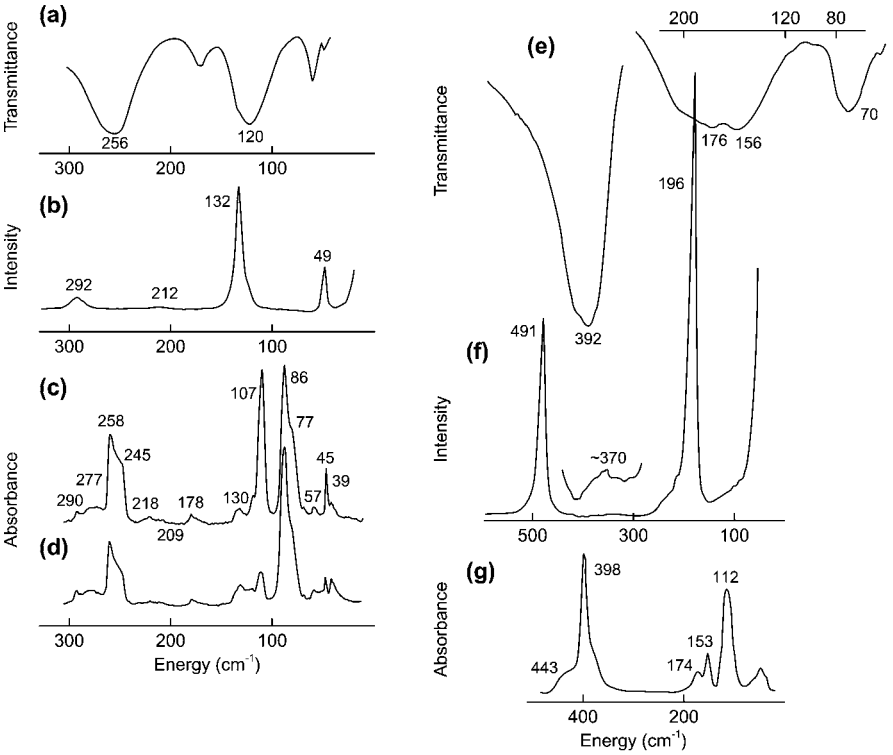

Fig. 4a–g Infrared, Raman and vibronic spectra of $Cs_2NaYbCl_6$ (**a–d**) and Cs_2KYbF_6 (**e–g**): **a** 300 K IR spectrum; **b** 338 K Raman spectrum; **c**, **d** 20 K absorption spectrum of $(^2F_{7/2})\Gamma_6 \rightarrow \Gamma_7$, $\Gamma_8(^2F_{5/2})$, respectively; **e** 300 K IR spectrum, **f** 300 K Raman spectrum, **g** 20 K $(^2F_{7/2})\Gamma_6 \rightarrow \Gamma_7(^2F_{5/2})$ absorption spectrum of Cs_2KYbF_6. (Adapted from [77, 83, 86, 97])

as to which vibronic features correspond to these modes (see Sects. 6 and 7.4). The tabulated values for τ_{1u} vibrations are averaged over the longitudinal and transverse components.

Normal coordinate analyses of the six LnX_6^{3-} moiety vibrations employing several different force fields have been performed using the **GF** matrix method approach [62], which involves the solution of the matrix equation, for a particular symmetry species of vibration:

$$\mathbf{GFL} = \mathbf{L}\Lambda \tag{5}$$

where the **G** and **F** matrices are the inverse kinetic energy matrix and the potential energy matrix, respectively; the **L** matrix is composed of eigenvectors of the matrix **GF**, which describe the normal vibrations; and the diagonal Λ matrix contains the eigenvalues, λ_i, which are related to the vibrational wavenumbers, $\bar{\nu}_i$, by

Table 2 Vibrational energy data (cm^{-1}) for M_2ALnX_6 (adapted from [76])

Ln	Unit cell group mode (S_i, i=1–10) energy (cm^{-1})									
	S_1 (ν_1)α_{1g}	S_2 (ν_2)ϵ_g	S_3(-)τ_{1g}	S_4 (ν_5)τ_{2g}	S_5(-)τ_{2g}	S_6 (ν_3)τ_{1u}	S_7 (ν_4)τ_{1u}	S_8(-)τ_{1u}	S_9(-)τ_{1u}	S_{10} (ν_6)τ_{2u}
	$Cs_2NaLnCl_6$ at 120–10 K, except [a]at 300 K; [b][99]									
La[a]	274	218	-	111	42					
Ce	279	222	-	112	46	257	106	-	-	75
Pr	282	220	16[b]	114	46	255	105	173	59	77
calc. 1	*282*	*221*	-	*112*	-	*255*	*105*	-	-	*79*
calc. 2	*288*	*226*	*21*	*124*	*48*	*262*	*115*	*165*	*55*	*85*
Nd	285	228	20	116	46	258	107	177	53[a]	78
Sm	287	230	-	118	45	264	107	180	-	80
Eu	290	228	(21)	118	47	260	105	176	(58)	79
calc. 2	*295*	*231*	*20*	*126*	*47*	*266*	*116*	*165*	*53*	*86*
Gd	290	232	-	118	45	270	109	175	-	82
Tb	292	233	-	123	45	268	111	182	56	82
Dy	295	235	-	124	45	266	111	181	-	80
Ho	297	239	-	127	47	267	114	176	61	83
Er	297	236	(21)	126	47	268	116	182	62	86
calc. 2	*295*	*233*	*21*	*132*	*49*	*263*	*126*	*173*	*56*	*88*
Tm	297	237	228[a]	127	47	268	118	182	63	88
Yb	296	-	-	128	48	266	119	181	-	89
Y[a]	284	223	-	128	47	270	-	-	-	-
calc. 3	*296*	*240*	*39 i*	*138*	*40*	*315 TO*	*137 TO*	*185 TO*	*45 TO*	47
						360 LO	*165 LO*	*211 LO*	*75 LO*	
	$Cs_2LiLnCl_6$ at 300 K, except [a]20 K; [b]85 K									
Pr	-	-	-	-	48[a]	262[a]	111[a]	219[a]	59[a]	89[a]
Eu	288[b]	212[b]	(20)	132[b]	(50)	263[a]	119[a]	(215)	(59)	95[a]
calc. 1	*288*	*211*	-	*138*	-	*263*	*119*	-	-	*97*
calc. 2	*274*	*194*	*20*	*145*	*57*	*293*	*105*	*178*	*59*	*101*
Er	285	219	-	140	52	261[b]	124[b]	209[b]	-	102[b]
Yb	288	-	-	144	56	259[a]	129[a]	215[a]	-	109[a]

Table 2 (continued)

Ln	Unit cell group mode (S_i, i=1–10) energy (cm^{-1})									
	S_1 (ν_1)α_{1g}	S_2 (ν_2)ϵ_g	S_3(-)τ_{1g}	S_4 (ν_5)τ_{2g}	S_5(-)τ_{2g}	S_6 (ν_3)τ_{1u}	S_7 (ν_4)τ_{1u}	S_8(-)τ_{1u}	S_9(-)τ_{1u}	S_{10} (ν_6)τ_{2u}
Tm	289	220	-	146	-	-	-	-	-	-
M,A,Ln,X	M_2ALnX_6 and M_2AYX_6:Ln^{3+} at 300 K, except where stated; [a]20 K; [b]85 K									
Cs,Na,Pr,Br	175	139	(15)	79	32[a]	183[a]	72[a]	150[a]	44[a]	56[a]
calc. 1	*175*	*139*	-	*79*	-	*174*	*72*	-	-	*56*
calc. 2	*178*	*143*	*13*	*76*	*35*	*197*	*72*	*135*	*39*	*50*
Cs,Na,Nd,Br	174	137	-	74	38	-	-	-	-	-
Cs,Na,Gd,Br	178	140	-	77	39	-	-	-	-	-
Cs,Na,Tm,Br	-	-	15	-	38[b]	181[b]	79[b]	156[b]	50[b]*	55[b]
Cs,Na,Ho,Br	-	-	-	-	-	178[a]	80[a]	154[a]	-	55[a]
Cs,Na,Yb,Br	178	134	-	84	43	180	94	150	-	53
Cs,Na,Y,Br	182	142	-	81	42	-	-	-	-	-
Cs,Na,La,Br	170	134	-	71	38	-	-	-	-	-
Cs,Li,Tm,Br	185	140	-	98*	-	-	-	-	-	
Cs,Li,Tm,I	127	100	-	70*	-	-	-	-	-	-
M,A,Ln	*neat* M_2ALnF_6 and M_2AYF_6:Ln^{3+} at 300 K; [a]120–10 K									
Cs,K,Pr	456[a]	352[a]	(50)	174[a]	53[a]	(370)	(137)	(170)	72[a]	98[a]
calc. 1	*456*	*342*	-	*152*	-	*372*	*150*	-	-	*108*
calc. 2	*457*	*355*	*49*	*172*	*52*	*376*	*154*	*201*	*63*	*91*
Cs,K,Y:Eu	-	-	-	-	-	372[a]	139[a]	174[a]	-	99[a]
Cs,K,Gd	473	380	-	185	-	372	140	165	72	-
Cs,K,Yb	490[a]	370	-	195	54[a]	413[a]	153[a]	174[a]	72[a]	115[a]
Cs,K,La	443	334	-	-	-	357	130	170	65	-
Cs,K,Y	476	382	-	194	-	412	160	200	75	-
calc. 4	*363*	*270*	-	*178*	-	*305*	*190*	-	-	*96*
Rb,K,Y	470	-	-	210	60	-	-	-	-	-
Cs,Na,Tm	473	373	(50)	203	65[a]*	401[a]	173[a]	249[a]	92[a]*	137[a]
calc. 2	*468*	*362*	*49*	*218*	*68*	*397*	*178*	*238*	*79*	*134*
Cs,Na,Y:Eu	-	-	-	-	65[a]	373[a]	162[a]	252[a]	55[a]*	123[a]

Table 2 (continued)

Ln	Unit cell group mode (S_i, i=1–10) energy (cm^{-1})									
	S_1 (ν_1)α_{1g}	S_2 (ν_2)ϵ_g	S_3(-)τ_{1g}	S_4 (ν_5)τ_{2g}	S_5(-)τ_{2g}	S_6 (ν_3)τ_{1u}	S_7 (ν_4)τ_{1u}	S_8(-)τ_{1u}	S_9(-)τ_{1u}	S_{10} (ν_6)τ_{2u}
Cs,Na,Y	467	363	-	200	69	-	-	-	-	-
Cs,Na,Tb	468	362	-	194	69	-	-	-	-	-
Rb,Na,Eu	-	-	-	-	-	388	150	140*	72	110
Rb,Na,Ho	498[a]	396[a]	50	205[a]	75[a]	-	-	-	-	-
Rb,Na,Tm	500	404	(50)	210	76	420	161	222	87	125
calc. 2	*500*	*402*	*50*	*213*	*76*	*423*	*158*	*227*	*84*	*124*

Values in parentheses were assumed for the fitting calculation. The calculated values (*calc*), rounded to nearest integers, are in italics. *Uncertain experimental data. *calc*. 1 is a 5-parameter General Valence Force-Field [74]. Some of the fitted frequencies are slightly different from those given here; *calc.* 2 is a 9-parameter unit cell group calculation employing a modified General Valence Force-Field [76]; *calc.* 3 is a lattice dynamics calculation [100]. TO transverse optic mode; LO longitudinal optic mode. i imaginary. *calc.* 4 for YF_6^{3-} is at MP2 level of theory using the SBKJ pseudopotentials and extended one-electron basis sets [101]

Table 3 Comparison of selected force constants (N m^{-1}) from the vibrational datafits to M_2ALnX_6

	120–10 K $Cs_2NaPrCl_6$		120–10 K $Cs_2NaPrBr_6$		120–20 K $Cs_2LiEuCl_6$		300 K Cs_2KPrF_6	
	calc. 1	*calc.* 2	*calc.* 1	*calc.* 2	*calc.* 1	*calc.* 2	*calc.* 1	*calc.* 2
K_1	109.1	68.0	96.9	60.3	101.9	59.6	142.3	92.9
K_2	-	29.3	-	21.1	-	20.9	-	38.5
k_1	10.7	10.9	8.9	8.7	13.4	13.1	17.0	15.4
H_1	6.7	5.8	6.9	5.4	10.1	9.3	7.8	4.8

calc. 1 is a 5-parameter General Valence Force-Field [74]. Some of the fitted frequencies are slightly different from those given here; *calc.* 2 is a 9-parameter unit cell group calculation employing a modified General Valence Force-Field [76].

$$\lambda_i = (2\pi c\bar{\nu}_i)^2 \tag{6}$$

Tabulations have been given of the relevant **G** and **F** matrix elements [74, 76]. Some results from the General Valence Force Field (*calc.* 1) are compared with experimental observations in Table 2. The principal bond stretching (K_1) and bending (H_1) force constants both increase across the series of $Cs_2NaLnCl_6$ from Ce to Yb, and in Cs_2ALnX_6 from X=Br<Cl<F. Members of the series $Cs_2LiLnCl_6$ have higher values of H_1 (but lower values of K_1) for $LnCl_6^{3-}$ than the corresponding ones in $Cs_2NaLnCl_6$, due to the constraint of the Cl^- nuclei by the polarizing Li^+ cation. The self-consistent field (SCF) model, with refinements such as the inclusion of electron correlation effects at the second-order Møller-Plesset (MP2) level of theory, has also been employed for the calculation of vibrational frequencies of hexafluoroelpasolites [101]. *Calc.* 4 in Table 2 lists these calculated frequencies for YF_6^{3-}.

A more complete analysis of the vibrational spectra includes all of the unit cell vibrations, and some typical results (*calc.* 2) are included in Table 2. The fitted values of K_1 are only about 60% of those when considering the LnX_6^{3-} moiety alone, and also the X-Ln-X bending force constants are also slightly smaller (Table 3). The magnitudes of the Ln-X (*cis*-) bond-bond stretching interaction force constant (k_1) are generally similar in both analyses, being about 9–16% of the values of K_1 for Cs_2NaLnX_6 (X=Cl, Br), but rather greater for Cs_2LiLnX_6. The unit cell group analysis serves to show the importance of the mixing of the symmetry coordinates of internal and external vibrations. This is most noticeable for the four τ_{1u} modes, especially for S_7 and S_8 in hexafluoroelpasolites [76].

6 Lattice Dynamics

The unit cell group description of the normal modes of vibration within a unit cell, many of which are degenerate, given above is adequate for the interpretation of IR or Raman spectra. The complete interpretation of vibronic spectra or neutron inelastic scattering data requires a more generalized type of analysis that can handle $30N$ (N=number of unit cells) normal modes of the crystal. The vibrations, resulting from interactions between different unit cells, correspond to running lattice waves, in which the motions of the elementary unit cells may not be in phase, if $\mathbf{k}\neq 0$. Vibrational wavefunctions of the crystal at vector position ($\mathbf{r}+\mathbf{t_n}$) are described by Bloch wavefunctions of the form [102]

$$\Psi^i_{\mathbf{k}}(\mathbf{r}+\mathbf{t_n}) = \exp(i\mathbf{k}\cdot\mathbf{t_n})\Psi^i_{\mathbf{k}}(\mathbf{r}) \tag{7}$$

where $\mathbf{t_n}$ is a general crystal lattice translation vector, and the wavevector $\mathbf{k}$ also describes the phase relationship between the Bravais cells, in addition to designating the lattice wave modes related to it. Due to the translational symmetry of the crystal, it is sufficient to consider all of the $\mathbf{k}$ within the first Brillouin zone of the reciprocal lattice. This is shown for the case of a cubic crystal in Fig. 5, in which the high-symmetry points Γ, Λ, L... are la-

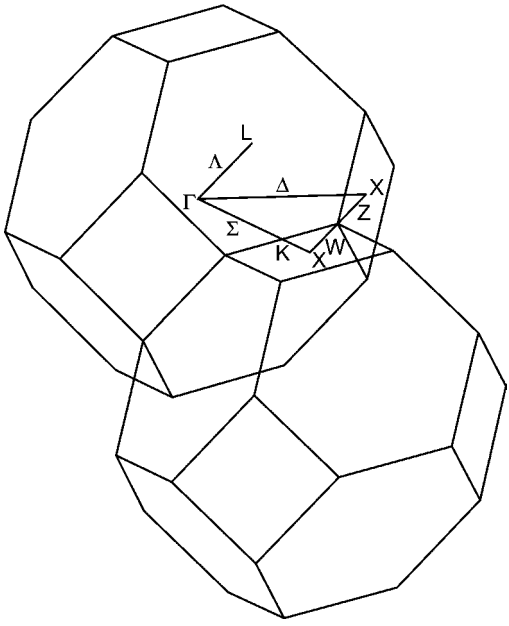

Fig. 5 Two unit cells of the reciprocal lattice for the face-centred cubic lattice of Cs_2NaYCl_6, showing major symmetry points and directions (from [100] with permission)

belled. The unit cell group model thus refers to optical phonons of infinite wavelength, **k**=0, where the exponential factor becomes unity. When we carry out the crystallographic point-group, G_0, operations on a **k** vector we generate the star of **k**. For a general **k** vector, the star has h wings (where h=point group G_0 order). The star has fewer wings if the **k** vector lies along a symmetry line or plane (since some of the symmetry operations then leave it unchanged), or if the **k** vector touches the zone boundary (some of the G_0 operators produce a **k** related to the original one by a reciprocal lattice vector, so that they are equivalent). The operations which leave **k** invariant or equivalent comprise a subgroup $P_{\mathbf{k}}$ of the entire point group G_0. All of the elementary operators related to elements of the point group $P_{\mathbf{k}}$, combined with the translation subgroup T_l of the space group S describing all the symmetry of the crystal structure, give a subgroup $S_{\mathbf{k}}$ of the group S, called the group of the wave vector **k**. Under this group $S_{\mathbf{k}}$, some wave functions of $\Psi^i_{\mathbf{k}}$ (or other physical quantities) transform among themselves according to an irrep Γ of the group of **k**. This irrep Γ of the group $S_{\mathbf{k}}$ is also called a *small* representation of the space group S.

The appropriate symmetry group for the analysis of $Fm3m$ crystal vibrational normal coordinates is the **k** group [102]. At **k**=0, all point-group (G_0=O_h) operations leave this point invariant so that we can use the O_h point group operations. For a nonzero **k**-vector along the k_x-axis in reciprocal space (i.e. at the point Δ, Fig. 5) the symmetry is reduced to C_{4v}, and the symmetries $\Delta_1+\Delta_5$ (i.e. A_1+E) are compatible, for example, with the symmetry Γ_{4u} (T_{1u}) of the group O_h at **k**=0. Other compatibility relations exist for other special points in the reciprocal lattice, so that the symmetry is reduced from O_h at **k**=0 (Γ point) to C_{2v} at Σ, C_{3v} at Λ, D_{4h} at X, for example. The consideration of the crystal, rather than the unit cell, vibrations thus produces splittings of degeneracies of phonon modes, and the vibration frequency depends upon the irrep Γ corresponding to different points **k** of the reciprocal lattice. These phenomena are represented in dispersion curves by plotting the vibration frequency as a function of **k** in the first Brillouin zone (i.e. $-\pi/a \leq k \leq \pi/a$).

The lattice dynamics of several halogenoelpasolites has been modelled to include both short (nearest-neighbour) and long-range (electrostatic, due to ionic charges) interactions between rigid (unpolarizable) ions [100]. The results for Cs_2NaYCl_6 are shown in Fig. 6. Since the diagram is rather complicated, the irreps of modes at the point Γ are given, together with the energies, in Table 2, *calc.* 3. There are three gaps in the phonon density of states, roughly between 236–239, 274–284 and 297–309 cm^{-1}. The S_3 τ_{1g} mode is shown as an imaginary (negative) frequency. The τ_{1u} transverse (lower energy) and longitudinal (higher energy) acoustic phonons have energy 0 cm^{-1} at the Γ point (the three acoustic phonons with **k**=0 correspond to in-phase translation of all unit cells, and therefore to translation of the crystal), but

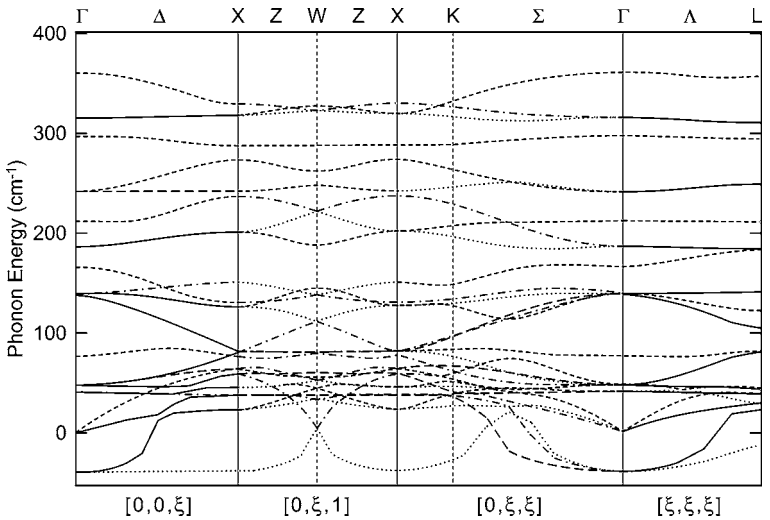

Fig. 6 Calculated phonon dispersion curves for Cs_2NaYCl_6, with the irreps of vibrational modes denoted by line styles: *short dashed lines* Δ_1, Z_1, Σ_1, Λ_1;*dotted lines* Δ_2, Z_2, Σ_2, Λ_2; *long dashed lines* Δ_3, Z_3, Σ_3; *dotted dashed lines* Δ_4, Z_4, Σ_4; *continuous lines* Δ_5, Σ_3. (from [100] with permission)

show considerable dispersion for nonzero **k** in Cs_2NaYCl_6. The phonon dispersion curve region below 100 cm^{-1} is very complex (Fig. 6). At highest energy, although the TO branch of S_6 (τ_{1u}) is fairly flat, the S_6 LO branch shows considerably more dispersion. We infer that the density of states per unit frequency interval for the TO mode is greater than for the LO mode, so that the spectral peak should be sharper. The calculated dispersion curves from [100] show some qualitative similarities to the dispersion curves for Cs_2UBr_6 [103], K_2ReCl_6 [104] and K_2NaAlF_6 [105]. The quantitative description of normal modes at the Γ point can be assessed from Table 2, *calc*. 3, by comparison with experimental data. Notably, the calculated energies of several modes (S_6, S_7) are rather high, and the $S_1(\alpha_{1g})$ mode is calculated to be at higher energy than $S_6(\tau_{1u})$. The energy of $S_{10}(\tau_{2u})$ is too low. The calculated TO-LO splittings of τ_{1u} modes are rather large (e.g. 45 cm^{-1} and 30 cm^{-1} for S_6 and S_9, respectively), which arises from setting the ionic charges to those of the free ions.

The experimental investigation of the phonon dispersion curves of elpasolites has been rather limited, partly because features due to electronic inelastic scattering of neutrons occur with greater intensity than phonon peaks. The energy of the S_3 mode has been determined from neutron inelastic scattering data [40, 48]. The Γ-point minimum becomes more distinct in the dispersion relation of this mode as the temperature is lowered [40]. Bührer and Güdel [106] have measured and calculated the phonon disper-

sion curve for this Γ-point mode in $Cs_2NaTmBr_6$ along the Δ-direction, where it splits into an almost dispersionless (and unique) Δ_2 mode, and a doubly-degenerate (originally transverse rotatory mode) Δ_3 mode with strong dispersion. The energy spectra of neutrons scattered from $Cs_2NaLaCl_6$ at 8 K showed only one identifiable phonon peak at ca. 230 cm^{-1}, which corresponds to the S_2 mode [107]. Three peaks at ca. 48, 145 and 306 cm^{-1} were attributed to phonon scattering in the inelastic neutron scattering spectrum of $Cs_2NaLnBr_6$ [60]. The first two of these features presumably correspond to S_5 and S_2, but assignment of the highest energy band is obscure. The measured phonon dispersion curves of $Cs_2NaBiCl_6$ along the directions Δ, Σ and Λ [108] are in qualitative agreement with Fig. 6.

7
One-photon $4f^N$-$4f^N$ Electronic Spectra

7.1
Electronic Hamiltonian and States of $4f^N$ Systems

The electronic states of rare earth ions in crystals are N-body localized states, since the N electrons of $4f^N$ are coupled strongly, and move around the corresponding ion core without extending far away. The semiempirical calculations for the $4f^N$ energy level systems employ a parametrized Hamiltonian H under the appropriate site symmetry for Ln^{3+}:

$$\mathrm{H} = \mathrm{H}_{AT} + \mathrm{H}_{CF} + \mathrm{H}_{ADD} \tag{8}$$

where H_{AT} comprises the atomic Hamiltonian, which includes all interactions which are spherically symmetric; H_{CF} is the operator comprising the nonspherically symmetric CF; H_{ADD} contains other interactions. The atomic Hamiltonian is expressed:

$$\mathrm{H}_{AT} = E_{AV} + \sum_k F^k \mathrm{f}_k + \sum_i \zeta_f \mathrm{s_i} \cdot \mathrm{l_i} + \alpha \mathrm{L}(\mathrm{L}+1) + \beta \mathrm{G}(G_2) + \gamma \mathrm{G}(R_7) + \sum_s T^s \mathrm{t}_s + \sum_k P^k \mathrm{p}_k + \sum_j M^j \mathrm{m}_j \tag{9}$$

where k=2,4,6; s=2,3,4,6,7,8; j=0,2,4. The first term E_{AV} (containing F^0) adjusts the configuration barycentre energy with respect to other configurations. The Slater parameters F^k represent the electron-electron repulsion interactions and are two-electron radial integrals, where the f_k represent the angular operator part of the interaction. The spin orbit magnetic coupling constant, ζ_f, controls the interaction and the mixing of states from different *SL* terms with the same *J* manifold. These two parameters are the most im-

portant in determining the atomic energies. Note that the terms $\sum_{i}^{N} e_{4f}(i) = Ne_{4f}$ involving the kinetic energy of the electrons and their nuclear attraction do not give rise to a splitting of the $4f^N$ levels and are contained in E_{AV}. The two-body configuration interaction parameters α, β, γ parametrize the second-order Coulomb interactions with higher configurations of the same parity. For f^N and f^{14-N}, N>2 the three body parameters T^s are employed to represent Coulomb interactions with configurations that differ by only one electron from f^N. With the inclusion of these parameters, the free ion energy levels can usually be fitted to within 100 cm^{-1}. The magnetic parameters M^j describe the spin-spin and spin-other orbit interactions between electrons, and the electrostatically correlated spin-orbit interaction P^k allows for the effect of additional configurations upon the spin-orbit interaction. Usually the ratios $M^0{:}M^2{:}M^4$ and those of $P^2{:}P^4{:}P^6$ are constrained to minimize the number of parameters, which otherwise already total 20.

The H_{CF} operator represents the nonspherically symmetric components of the one-electron CF interactions, i.e. the perturbation of the Ln^{3+} $4f^N$ electron system by all the other ions. The states arising from the $4f^N$ configuration are well-shielded from the oscillating crystalline field (so that spectral lines are sharp) but a static field penetrates the ion and produces a Stark splitting of energy levels. The general form of the CF Hamiltonian H_{CF} is given by

$$H_{CF} = \sum_{i;k=0}^{\infty} \left[B_0^k C_0^k(i) + \sum_{q=1}^{k} \left(B_q^k \left(C_{-q}^k(i) + (-1)^q C_q^k(i) \right) + B'^k_q i \left(C_{-q}^k(i) - (-1)^q C_q^k(i) \right) \right) \right] \tag{10}$$

where the B_q^k are parameters and the $C_q^k(i)$ are tensor operators related to the spherical harmonics, see Eq. (19c); and the sum on i is over all electrons of the $4f^N$ configuration. Since the Hamiltonian is a totally symmetric operator, for the case of O_h site symmetry, only those values of k whose angular momentum irreps contain Γ_{1g} give nonzero B_q^k, i.e. k=4 and 6. The nonzero CF parameters for the O_h group reduce to $B_0^4, B_4^4, B_0^6, B_4^6$. The unit tensor normalized CF parameters $B_q^{(k)}$ (used by Richardson) are related to the spherical tensor CF parameters B_q^k (used by Wybourne) by

$$B_q^{(k)} = B_q^k \langle f || C^{(k)} || f \rangle = B_q^k (-7) \begin{pmatrix} 3 & k & 3 \\ 0 & 0 & 0 \end{pmatrix} \tag{11}$$

so that $B_0^{(4)} = 1.128B_0^4$, and $B_0^{(6)} = -1.277B_0^6$. However, the B_4^k parameters are related to B_0^k, and in the Wybourne spherical tensorial notation [64] adopted herein, and in the cubic environment, $B_4^4 = B_0^4\,(5/14)^{1/2}$ and $B_4^6 = -B_0^6\,(7/2)^{1/2}$. Thus only 2 additional parameters are required to model the CF splittings of J terms by the octahedral CF, and this presents a more severe test for theory than for low symmetry systems where up to 27 parameters may be employed.

The labelling of electronic states of the rare earth ions in a CF differs from that of the transition elements with outer d-electrons where the CF is much larger. For the lanthanide ions, the spin-orbit interaction is larger than the CF acting upon Ln^{3+}. The comparison is misleading from the inspection of the relevant parameters, since ζ_f has the magnitude from 623 to 2903 cm^{-1} for Ce^{3+} to Yb^{3+} in M_2ALnCl_6, whereas the largest of the CF parameters, B_0^4, ranges from 2119 to 1471 cm^{-1} in the same series [72]. However, the comparison is actually made by looking at the splitting of states, since the CF splitting is up to several hundred cm^{-1} for these ions, whereas spin-orbit interaction produces a splitting of many thousands of cm^{-1}. Therefore we consider basis state wavefunctions of free ions first, which in the $[SL]$ coupling scheme of the f^N electron system are written as combinations of $|\alpha' S' L' JM\rangle$ states:

$$\left|f^N \psi JM\right\rangle = \sum_{\alpha' S' L'} C_\psi(\alpha' S' L') \left|f^N \alpha' S' L' JM\right\rangle \tag{12}$$

where $C_\psi(\alpha' S' L')$ are the intermediate coupling coefficients and α' represents extra quantum numbers that are necessary to describe the state completely. The state is usually specified by the symbol ψ=$[\alpha SL]$ since the term αSL makes the largest contribution to the eigenvector, and only J and M are good quantum numbers. The basis for the CF wavefunction for the irrep $\Gamma\gamma$ is expressed as linear combinations of $|JM\rangle$ kets:

$$\left|f^N \psi J \Gamma\gamma\right\rangle = \sum_{M'} S_{J\Gamma\gamma}(M') \left|f^N \psi JM'\right\rangle \tag{13}$$

where the coefficients $S_{J\Gamma\gamma}(M')$ are given for example, in Table A19 of [68]. Several J' terms, with different $\psi' J'$ values but which correspond to the same symmetry irrep of the CF point group, can mix under the influence of the CF Hamiltonian as follows:

$$\left|f^N [\psi J] \Gamma\gamma\right\rangle = \sum_{\psi' J'} D_{\psi' J'} \left|f^N \psi' J' \Gamma\gamma\right\rangle \tag{14}$$

Taking $|f^N \alpha SLJM\rangle$ as matrix bases, and diagonalizing the Hamiltonian H in Eq. (8) to fit the experimental electronic energy levels, the values of the parameters in Eqs. (9) and (10), and of the mixing coefficients in Eqs. (12)–

(14) can be determined. Prof. M. Reid has written a suite of computer programs for this type of fitting.

7.2
Zero Phonon Lines and Vibronic Sideband

The energy levels of *SLJ*-multiplets of f^N configurations are depicted in many texts concerning lanthanide ions, in the form of Dieke diagrams. The intra-configurational electronic spectra of Ln^{3+} comprise sharp lines, since the ion is shielded from external fluctuating electric fields by the full outer-shell electrons $5s^25p^6$. The transition intensity between states i and f is measured independently of concentration by the oscillator strength [109], which for a cubic elpasolite crystal is given by [97]

$$P_{if} = 6.50 \times 10^{-19} \frac{a^3}{b} \int A(\bar{\nu}) d\bar{\nu} \tag{15}$$

where a is the magnitude of the lattice parameter in pm, b is the crystal thickness in cm, and the integral is over absorbance $A(\bar{\nu})$ with respect to the energy in wavenumbers. For simplicity, in this equation and in the following, we assume that unpolarized radiation is incident upon an isotropic crystal. The measured oscillator strength of a ZPL (although more often, relative values are employed with respect to a certain transition) may be compared with the calculated value in order to confirm the assignment of a particular electronic transition. The oscillator strength of the transition may be defined with respect to the matrix element of the transition multipole moment, and is approximately given by [68]

$$P_{if} = \frac{8\pi^2 m \bar{\nu}_{if} c}{3hg_i} \left| M_{if} \right|^2 \tag{16}$$

where m is the electron mass, $\bar{\nu}_{if}$ is the transition energy in cm^{-1} and c is the velocity of light in cm s^{-1}. g_i is the degeneracy of the initial state, and this is frequently omitted from the definition, but (as well as η below), taken into account when comparing calculation and experiment [65]. In general the matrix element $|M_{if}|$ refers to vibronic states, which may be factored out by the Herzberg-Teller expansion [110, 111]:

$$\begin{aligned} |M_{if}| = {} & \langle \psi_f | \mathrm{M}_e | \psi_i \rangle \langle \chi_{fk} | \chi_{in} \rangle + \sum_m (\langle \psi_f | \mathrm{M}_e | \psi_m \rangle \langle \chi_{fk} | c_{mi} | \chi_{in} \rangle \\ & + \langle \psi_m | \mathrm{M}_e | \psi_i \rangle \langle \chi_{fk} | c^*_{mf} | \chi_{in} \rangle) \end{aligned} \tag{17}$$

where ψ_f, ψ_i and ψ_m refer to final, initial and intermediate electronic state wave functions, and M_e contains the sum over f electrons only. The vibrational wave functions χ refer to n or k quanta and depend upon the nuclear

coordinates. One of the coefficients, c_{mi}, for a particular normal mode of vibration, Q_v, is given by

$$c_{mi} = \frac{\langle \psi_m | (\partial \mathrm{H}/\partial Q_v)_{Q_0} Q_v | \psi_i \rangle}{-(E_m - E_i)} = -\Delta E_{mi}^{-1} \langle \psi_m | (\partial \mathrm{H}/\partial Q_v)_{Q_0} Q_v | \psi_i \rangle \tag{18}$$

where $(\partial \mathrm{H}/\partial Q_v)_{Q_0}$ is the change in potential energy with nuclear displacement, evaluated at the equilibrium nuclear geometry. The introduction of the phonon normal coordinate Q_v leads to a change in phonon number between the initial and final electronic states.

When the first term is nonzero the electronic transition is allowed by a particular mechanism, whereas it is forbidden when zero. It contributes mainly zero phonon line intensity when the shift in equilibrium positions of the nuclei between the two states can be ignored, so that $\langle \chi_{fk} | \chi_{in} \rangle \neq 0$ only for the $k=n$ case in Eq. (17). The second and third terms contribute mainly one-phonon sideband vibronic intensity to the transition. $|\langle \psi_f | \mathrm{M}_e | \psi_i \rangle|^2$ is given by [68]

$$|\langle \psi_f | \mathrm{M}_e | \psi_i \rangle|^2 = \left\{ \eta \sum_q |\langle \psi_f | \mathrm{D}_q^{(1)} | \psi_i \rangle|^2 + \eta' a \sum_q |\langle \psi_f | \mathrm{m}_q | \psi_i \rangle|^2 + \eta'' b \sum_q |\langle \psi_f | \mathrm{D}_q^{(2)} | \psi_i \rangle|^2 \right\} \tag{19a}$$

where the spherical tensor

$$\mathrm{D}_q^{(k)} = \sum_i r_i^k \mathrm{C}_q^{(k)}(\theta_i, \phi_i) \tag{19b}$$

m_q is the magnetic dipole operator and

$$\mathrm{C}_q^{(k)}(\theta_i, \phi_i) = \sqrt{\frac{4\pi}{2k+1}} Y_q^{(k)}(\theta_i, \phi_i) \tag{19c}$$

where $Y_q^{(k)}$ is a spherical harmonic function of rank k. In Eq. (19a), a and b are constants expressed in terms of fundamental constants [68].

The three terms in brackets represent contributions from ED, MD and EQ transitions, respectively, and the matrix elements in terms of reduced matrix elements, 3-j and 6-j symbols are given elsewhere for MD [65, 112] and EQ [113, 114] transitions. The dimensionless factors η, η', η'' [115] in Eq. (19a) correct the vacuum linestrengths to those appropriate for the crystal, by correcting the polarizability of the medium and/or the density of radiative modes. The ZPL (i.e. electronic origin) of a transition refers to the 0–0′ transition, i.e. from the v=0 vibrational level of one state to the v′=0 level of the other in the case of absorption.

The selection rules of angular momenta S, L, J for the above transitions are listed in Table 1. The point group selection rule for an allowed transition

(in addition to the *S*, *L* and *J* etc., selection rules) is the same as Eq. (4). Examples are given in Table 1 for allowed transitions: of an even-electron f^N system, to terminal states from a nondegenerate Γ_{1g} initial state (column 6); and of an odd-electron f^N system (where the O^* double group is used [73]) from a Γ_{8g} initial state (column 7). The mechanism for the three types of transition in M_2ALnX_6 is shown schematically by the operator M_e in Fig. 7a, but it is noted that the ED process is forbidden due to the selection rule (Eq. 4), since Γ_o corresponds to Γ_{4u} (Table 1) and Γ_i, Γ_f have the same parity for f-electron states.

More generally, it has been noted [116] that the oscillator strengths for fully allowed ED:MD:EQ transitions are in the approximate ratio of $1{:}10^{-5}{:}10^{-6}$, respectively. However, ED transitions are parity forbidden in the case of f-f intraconfigurational transitions, so that the mechanism which enables such transitions for rare earth ions is via crystal-field mixing of f^N wave functions with opposite parity wave functions such as $f^{N-1}d$ due to the odd terms $H'_{CF} = \sum_{i,t,p} B_p^t C_p^t(i)$ with t=1,3,5,7 (which are usually ignored when calculating energies) of the CF when the ion is situated at a noncentrosymmetric site. Following Judd [117], this type of transition is called induced (forced) electric dipole in Table 1. The f^N wave function then becomes

$$\psi_i = |f^N \psi_i\rangle + \sum_m c_{mi} |f^{N-1} d \psi_m^i\rangle \tag{20}$$

where

$$c_{mi} = \langle \psi_m^i | H'_{CF} | \psi_i \rangle / (E_i - E_m) \tag{21}$$

The mechanism is shown schematically in Fig. 7b, corresponding to the product of matrix elements of the type

$$\Delta E_{im}^{-1} \langle f^N \psi_f | D^{(1)} | \psi_m^i \rangle \langle \psi_m^i | H'_{CF} | f^N \psi_i \rangle \tag{22}$$

where ψ_i and ψ_f denote the initial and final f^N states of the intraconfigurational transition, ψ_m^i denotes an opposite-parity state, and H'_{CF} is the CF operator connecting this state to the f^N state.

When the CF is centrosymmetric, as for Ln^{3+} in elpasolites, it is not H'_{CF} itself, but its increment $\sum_v \left(\frac{\partial H'_{CF}}{\partial Q_v}\right)_{Q_0} Q_v$ caused by the odd-parity vibration Q_v which introduces non-zero c_{mi}, and therefore induces an EDV transition.

Based upon an approximate assumption that all the energies E_m lie within a definite intermediate configuration, $4f^{N-1}5d$ for example, Judd [117] completed the summation over m, with closure over the operators $D^{(1)}$ and H'_{CF} to give the following formula:

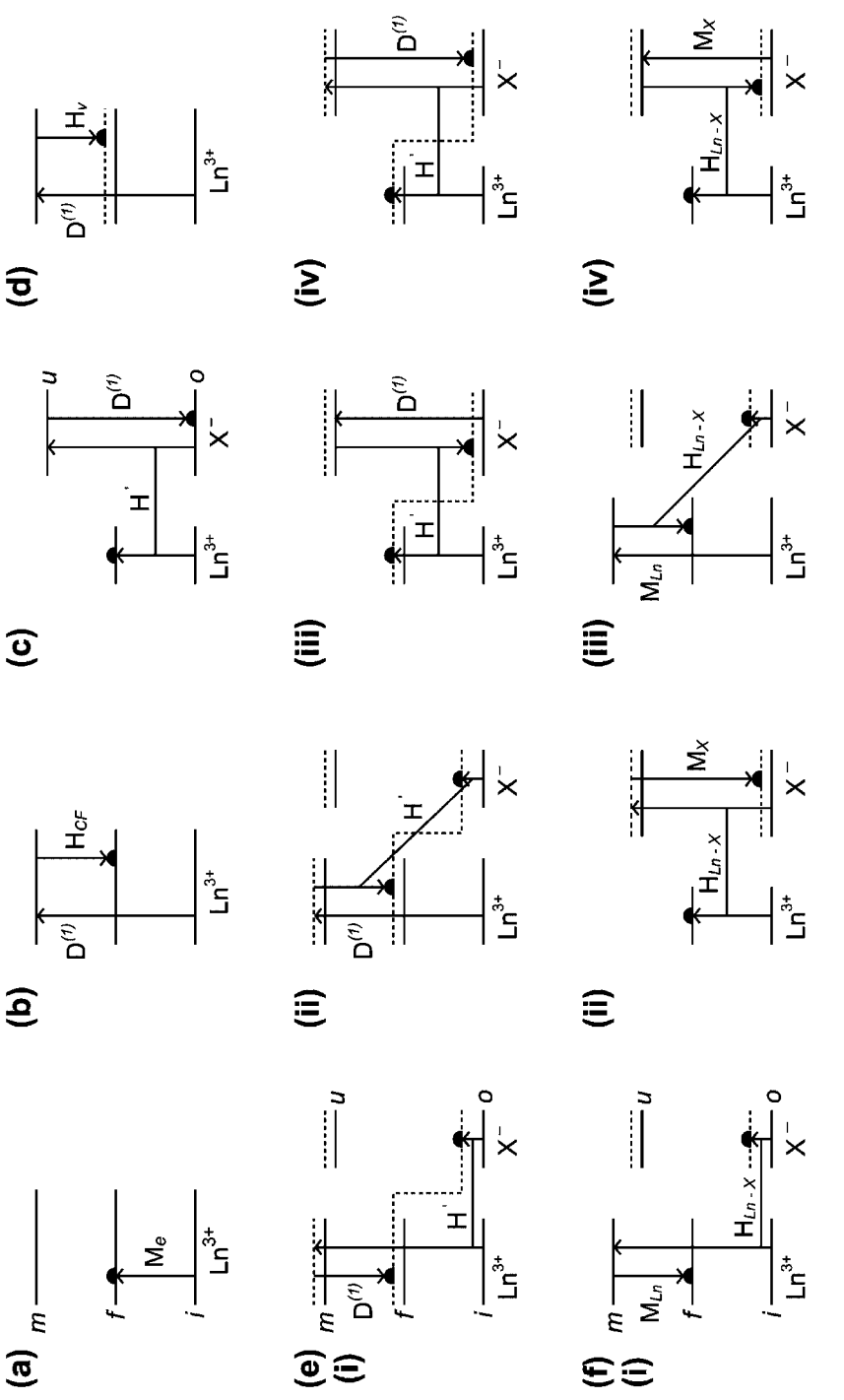
(a)
m
f
i
Me
Ln3+
(b)
D(1)
HCF
Ln3+
(c)
u
D(1)
H'
o
Ln3+
X−
(d)
D(1)
Hv
Ln3+
(e)
(i)
m
u
D(1)
H'
f
i
Ln3+
X−
o
(ii)
D(1)
H'
Ln3+
X−
(iii)
D(1)
H'
Ln3+
X−
(iv)
D(1)
H'
Ln3+
X−
(f)
(i)
m
MLn
f
HLn - X
i
Ln3+
u
X−
o
(ii)
MX
HLn - X
Ln3+
X−
(iii)
MLn
HLn - X
Ln3+
X−
(iv)
MX
HLn - X
Ln3+
X−

$$\langle \mathrm{f}^{\mathrm{N}}\psi_f J_f M_f|\mathrm{D}_q^{(1)}|\mathrm{f}^{\mathrm{N}}\psi_i J_i M_i\rangle = \sum_{\lambda}\langle \mathrm{f}^{\mathrm{N}}\psi_f J_f M_f|\mathrm{U}_{p+q}^{(\lambda)}|\mathrm{f}^{\mathrm{N}}\psi_i J_i M_i\rangle \times\left[\sum_{tp}(-1)^{p+q}[\lambda]\begin{pmatrix}1 & \lambda & t\\ q & -(p+q) & p\end{pmatrix}A_p^t\Xi(t,\lambda)\right] \tag{23}$$

in which $\Xi(t,\lambda)$, λ=2,4,6) is a summation over intermediate configurations involving $\langle 4\mathrm{f}||r\mathrm{C}^{(1)}||5\mathrm{d}\rangle\langle 5\mathrm{d}||r^t\mathrm{C}^t||5\mathrm{d}\rangle$ etc., and average energies of these configurations; and $A_p^t = B_p^t/\langle 4\mathrm{f}|r^t|4\mathrm{f}\rangle$. Actually, Eq. (23) (which is the same as Eq. (133) given with detailed explanation in [65]) usually serves as a parametrization formula in which the $A_{tp}^{\lambda} = A_p^t\Xi(t,\lambda)$ are experimentally-fitted intensity parameters, since matrix elements of the unit tensor operators $\mathrm{U}_{p+q}^{(\lambda)}$ can be calculated from [121], whilst the coefficients $C_{\psi}(\alpha' S' L')$ and $D_{\psi' J'}$ in Eqs. (12)–(14) for the initial and final CF states can be obtained from the CF fitting calculation.

Most publications have simply considered multiplet $\psi_i J_i$ to multiplet $\psi_f J_f$ transitions because the number of intensity parameters can be considerably decreased: to three. Approximately assuming that the populations of all CF states within the initial (ground) multiplet are equal, Judd gave a simple formula, as follows:

$$\sum_{\Gamma\gamma}\left|\langle \mathrm{f}^{\mathrm{N}}\psi_f J_f\Gamma_f\gamma_f|\mathrm{D}_q^{(1)}|\mathrm{f}^{\mathrm{N}}\psi_i J_i\Gamma_i\gamma_i\rangle\right|^2 = \sum_{\lambda}\Omega_{\lambda}\left|\langle \mathrm{f}^{\mathrm{N}}\psi_f J_f\|\mathrm{U}^{(\lambda)}\|\mathrm{f}^{\mathrm{N}}\psi_i J_i\rangle\right|^2 \tag{24}$$

Fig. 7a–f Some mechanisms for f-f pure electronic (**a**–**c**) and vibronic (**d**–**f**) absorption transitions for Ln^{3+} systems: **a** MD, EQ pure electronic transitions (the operator M_e refers to the MD or EQ transition moment operators, Sect. 7.2); **b** Induced ED transition (one of the two mechanisms; H_{CF} is the CF operator connecting opposite parity configurations, $D^{(1)}$ is the electric dipole moment operator, Sect. 7.2); **c** Coulombic correlation of transient ED moments in the ligands by the EQ transition of the lanthanide ion [145] (one of the two mechanisms, with H′ representing the metal quadrupole-ligand multipole moment operator, Sect. 7.2); **d** Judd vibronic mechanism, with H_v representing the vibronic coupling operator; **e** Faulkner-Richardson [67] static (i), (ii) and dynamic (iii), (iv) coupling mechanisms. H′ is a vibronic coupling operator, Eq. (37); **f** Stavola-Dexter two-centre vibronic transition, (i)–(iv) [175]. M_{Ln} and M_X are electric dipole transition moment operators and H_{Ln-X} represents the metal multipole-ligand multipole interactions, (Eqs. 48b–48e). **b** and **c** are not applicable also to centrosymmetric sites in M_2ALnX_6. *Dotted lines* represent vibrational energy levels, which are linked between Ln^{3+} and X^- in **e** to show that the vibration is that of the LnX_6^{3-} moiety, but unlinked in **f** where X^- is a vibrating ligand; *horizontal bars* represent correlated interactions; *i*, *f* are f^N states, *m* is an opposite-parity Ln^{3+} state; *o* is the ligand ground electronic state, *u* is a ligand opposite-parity state. The initial states are ground states in all cases, and final states are marked by *semicircles*

where

$$\Omega_\lambda = [\lambda]\sum_{tp} |A^\lambda_{tp}|^2/[t] \tag{25}$$

In this case, only Ω_2, Ω_4 and Ω_6 (or only Ω_4 and Ω_6 for elpasolites) are fitting parameters, and the reduced elements of $U^{(\lambda)}$ in Eq. (24) can be calculated [121] and the coefficients $C_\psi(\alpha' S' L')$ obtained from energy level fitting.

The programs of Prof. Reid can also fit $4f^N$-$4f^N$ transition intensities to obtain A^λ_{tp} or Ω_λ, and the former intensity fitting is helpful to assign (and fit) CF energy levels.

The oscillator strength for entire multiplet-multiplet transitions enabled by the forced ED mechanism is in the region of 10^{-5} to 10^{-8} for Nd^{3+} at a C_s site [118]; 10^{-5} to 10^{-6} for Pr^{3+} at a C_s site [119]; or ca. 10^{-6} for Er^{3+} at an S_4 site [120].

We now arrive at the major factor which distinguishes the electronic spectra of centrosymmetric M_2ALnX_6 systems from those of most other lanthanide ion systems. This results from the vanishing of the second bracket of Eq. (22), since $\Gamma_m \times \Gamma_i$ is odd parity and $\Gamma(H'_{CF})$ is only even parity. Forced dipole pure electronic transitions are thus forbidden for these lanthanide systems.

Generally, the MD oscillator strengths are in the region 10^{-7} to 10^{-11} [122] for individual ZPL transitions of Ln^{3+}. Considering M_2ALnX_6, the MD ZPL of transitions with $|\Delta J|=\pm 1$, such as the $^4I_{13/2} \rightarrow {}^4I_{15/2}$ transition of Er^{3+} in $Cs_2NaErCl_6$ and the $^5I_8 \rightarrow {}^5I_7$ transition of Ho^{3+} in $Cs_2NaHoCl_6$, often dominate their respective spectral regions [112] since the vibronic transitions are generally weak. For the purpose of spectral assignments, the calculated MD relative intensities are generally in good agreement with experiment (e.g. [123]) as long as CF induced *J*-mixing is taken into account [112], except for cases where the composition of the wave function is especially sensitive to parameter values and inaccurately determined. Orbital reduction factors, which parametrize covalency contributions, have not been included in the calculations. MCD and MCPE have sometimes been employed to provide assignments of the irreps of terminal CF levels of MD transitions (e.g. [124]). Figure 8 shows the $^5D_4 \rightarrow {}^7F_5$ MCPE and emission spectra of Tb^{3+} in $Cs_2NaTbCl_6$, with the MD transitions between CF levels marked and shown in the energy level diagram. The selection rules identify that the MD intensity results from the contributions of both $^7F_5$ and $^5F_5$ to the final $^7F_5$ state, and of both $^7F_4$ and $^5F_4$ to the initial $^5D_4$ state. All bands shown in this figure are due to MD transitions. The ordinate *I* is the total emission intensity, whereas ΔI is the difference in emission intensity between left and right circularly polarized radiation. With some assumptions, ΔI_{fi} may be calculated from

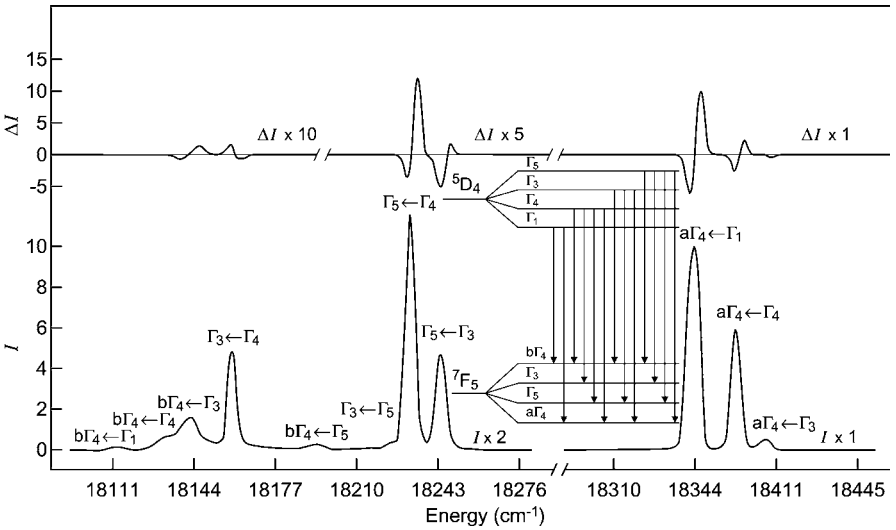

Fig. 8 MCPE (ΔI) and emission (I) spectra for the $^7F_5 \leftarrow {}^5D_4$ transition of Tb^{3+} in $Cs_2NaTbCl_6$ at 20 K with a magnetic field strength of 0.86 T. The individual crystal field transitions are labelled, and *vertical lines* in the energy level diagram show the MD transitions. The ←notation is as [124].

$$\Delta I_{fi} \propto B_i(T)\bar{\nu}_{if}^4[|\langle\psi_i|\mathrm{m}_-|\psi_f\rangle|^2 - |\langle\psi_i|\mathrm{m}_+|\psi_f\rangle|^2] \tag{26}$$

where $B_i(T)$ is a Boltzmann factor for the emitting state; $\bar{\nu}_{if}$ is the transition energy (cm^{-1}); and $m_\pm$ are the MD operators for left and right circularly polarized radiation. In Fig. 8, the six prominent *A* terms [125] in the MCPE spectra were unambiguously assigned to six zero phonon lines [124]. When the CF interaction is larger than the magnetic interaction, then the first order Zeeman effect produces a symmetric splitting of Γ_4 and Γ_5 states, which is independent of the relative orientation of the crystal axis to the applied magnetic field. When the CF splitting is of the same order of magnitude as the Zeeman splitting, more complex second order effects occur such as the splitting of Γ_3 states and the appearance of forbidden transitions.

Care must be taken to avoid saturation effects when measuring the oscillator strengths of intense MD transitions [126]. It has been assumed that MD oscillator strengths are rather insensitive to the site symmetry of a particular rare earth ion [127], and this may be the case for some particular transitions. However, the ED contribution to the zero phonon line intensity of an ion at a noncentrosymmetric site may be comparable to, or greater than the MD contribution, so that the measured intensity arises from both contributions.

Some major differences between the electronic spectra of Ln^{3+} in a noncentrosymmetric system and in cubic elpasolites are evident from Fig. 9, where a

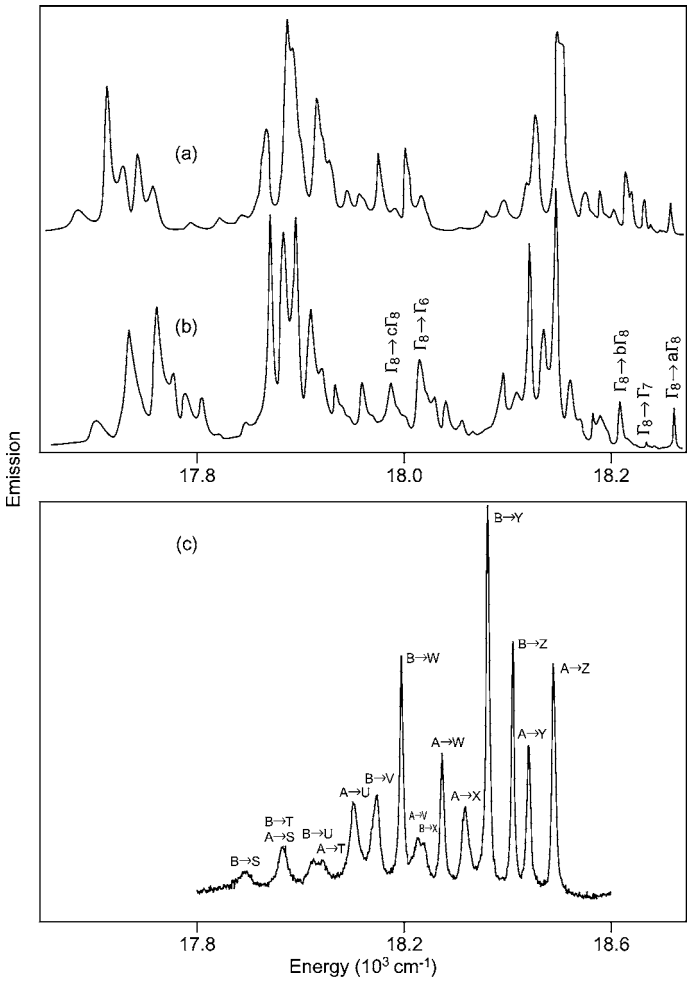
(a)
(b)
Γ8→cΓ8
Γ8→Γ6
Γ8→bΓ8
Γ8→Γ7
Γ8→aΓ8
Emission
17.8
18.0
18.2
(c)
B→Y
B→W
B→Z
A→Z
A→W
A→Y
B→V
A→U
A→X
B→T
A→S
B→U
A→T
A→V
B→X
B→S
17.8
18.2
18.6
Energy (10³ cm⁻¹)

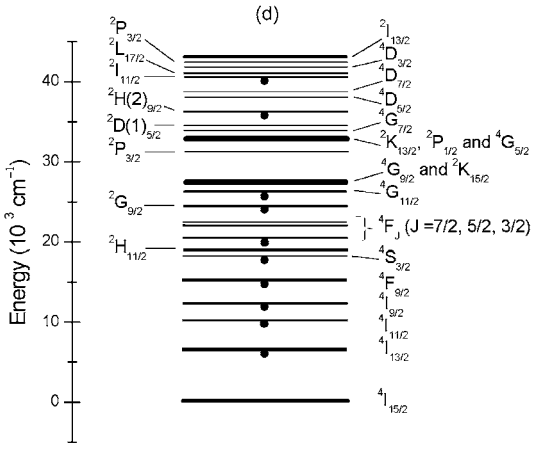
(d)
Energy (10³ cm⁻¹)
40
30
20
10
0
²P3/2
²L17/2
²I11/2
²H(2)9/2
²D(1)5/2
²P3/2
²G9/2
²H11/2
²I13/2
⁴D3/2
⁴D7/2
⁴D5/2
⁴G7/2
²K13/2, ²P1/2 and ⁴G5/2
⁴G9/2 and ²K15/2
⁴G11/2
⁴F (J =7/2, 5/2, 3/2)
⁴S3/2
⁴F9/2
⁴I9/2
⁴I11/2
⁴I13/2
⁴I15/2

comparison is given of the $^4S_{3/2} \rightarrow {}^4I_{15/2}$ spectra of $YAlO_3:Er^{3+}$ and Cs_2AErCl_6 (A=Li, Na), with the pure electronic transitions being identified in each case. The *SLJ* energy levels of Er^{3+} in $Cs_2NaErCl_6$ are also shown for clarity. The site symmetry of Er^{3+} in $YAlO_3$ is C_s so that pure electronic transitions are allowed by the forced ED mechanism, Fig. 7b, in which the CF mixes $4f^{10}5d^1$ character into $4f^{11}$ electronic states. All 15 features correspond to electronic transitions between Kramers doublet electronic states and the bands are relatively sharp even at 300 K. As mentioned above, the forced dipole pure electronic transitions are forbidden in cubic M_2ALnX_6 systems. Thus, by contrast, in Fig. 9a,b, there are fewer (5) zero phonon lines and their MD intensity contribution in the centrosymmetric system Cs_2AErCl_6 is overlapped and dwarfed by the broader, more intense vibronic structure. The spectra Fig. 9a,b become broad, with unresolved features at 300 K. In general, whereas the intensities of individual vibronic bands are quite small (oscillator strengths usually in the region of 10^{-10} to 10^{-8}), the summation of vibronic intensities for a particular transition between CF states can give a total sideband oscillator strength of up to 10^{-7} to 10^{-6} for the case of M_2ALnCl_6 [97, 128].

The EQ oscillator strengths are calculated to be between 10^{-10} to 10^{-13} [113] for individual ZPL transitions of Ln^{3+} in Cs_2NaMX_6. Much attention has previously been paid to the relationship of hypersensitive and EQ transitions. It appears, however, that the spectra of many such transitions were usually recorded (in solution) at room temperature so that the distinction was not possible between vibronic and pure electronic structure (see for example [129–132]), with the total oscillator strengths being of the order 10^{-5}. Indeed, the only conclusive resolution of the electric quadrupole mechanism in contributing the entire ZPL intensity in a crystal concerns the uranyl ion.

Many theories concerning the origin of hypersensitivity explained the large changes in intensity for certain transitions of rare earth ions in different environments in terms of purely electronic effects (e.g. the inhomogeneous dielectric and dynamic coupling (ligand polarization) mechanisms [133, 134] including the screening of outer electron shells [135]; the anisotropic polarizability contributions [136]; and the role of linear CF terms [137]). One of the mechanisms of the coulombic correlation of transient

Fig. 9a–d 488-nm excited emission spectra of Er^{3+} in different crystal environments. 20 K spectra of: **a** $Cs_2NaErCl_6$ and **b** $Cs_2LiErCl_6$; **c** 300 K spectrum of $YAlO_3:Er^{3+}$. The (one) emitting level in **a** and **b** is $^4S_{3/2}\Gamma_8$, whereas this splits into two Kramers doublets, labelled A and B, in $YAlO_3:Er^{3+}$. This transition terminates upon the electronic ground state, where there are 5 CF levels in the cubic elpasolite systems (a,b,cΓ_8, Γ_7, Γ_6), but 8 (labelled S through Z) for Er^{3+} at the C_s site in $YAlO_3$. (Adapted from [72] and unpublished data); **d** *SLJ* Energy levels of Er^{3+} in $Cs_2NaErCl_6$. The *semicircles* indicate terms from which luminescence has been observed for Er^{3+} in neat or diluted elpasolite hosts

electric dipole moments in the ligands by the EQ transition of the lanthanide ion is shown in Fig. 7c. Peacock [138] considered that the vibronic intensity mechanism is not important for molecular complexes. On the other hand, Henrie et al. [139], and also Judd [140], recognized the importance of the vibronic contribution to the intensity of hypersensitive transitions. Henrie et al. envisaged the occurrence of odd-parity vibrations via a covalency (charge transfer) model. Judd [140] noted that in the case of large Ln-X distances compared to the ligand displacements, all of the vibronic intensity should reside in the hypersensitive transitions, and subsequently gave an illustrative treatment for τ_{1u} vibrational modes [141].

The measured oscillator strength of the $(^6H_{5/2})\Gamma_7 \rightarrow \Gamma_6(^6F_{1/2})$ pure EQ allowed transition of Sm^{3+} in $Cs_2NaSmCl_6$ [142], at 6355 cm^{-1}, is 3×10^{-10} (Fig. 10) in agreement with calculation [113, 143]. Using an oriented crystal, linear polarization measurements in different directions (in the absence of a magnetic field) of an MD allowed ZPL do not show a variation in intensity for the cubic M_2ALnX_6 systems. This is not the case for EQ ZPL, where the explicit polarization dependence has been given by Hellwege [144] for transitions between various CF levels in cubic systems.

The dynamic coupling mechanism (Fig. 7c) only makes a contribution to the intensity of an EQ transition for a system with point group symmetry

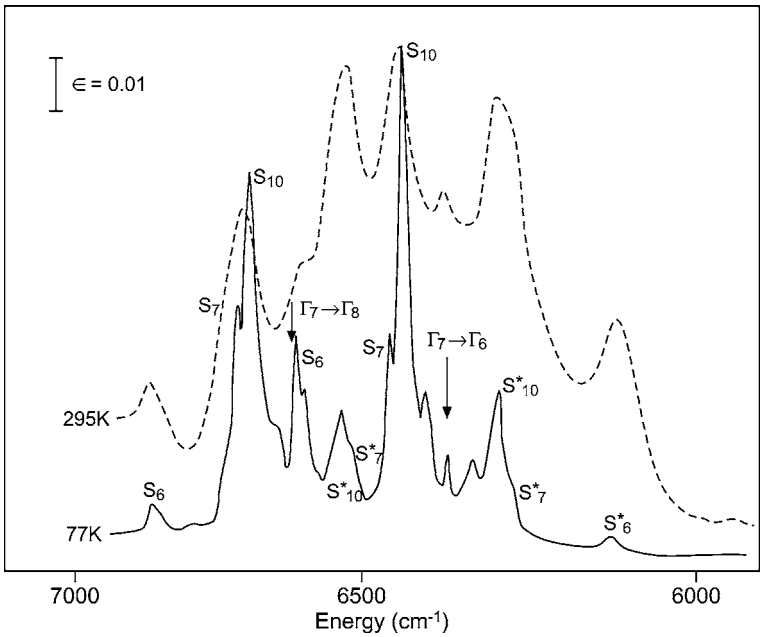

Fig. 10 295 K and 77 K absorption spectra of $Cs_2NaSmCl_6$ between 6000 and 7000 cm^{-1}. The $(^6H_{5/2})\Gamma_7 \rightarrow \Gamma_6(^6F_{1/2})$ pure EQ transition is marked, together with associated Stokes and anti-Stokes (*starred*) vibronic structure. (Adapted from [142])

such that one of the components of the ED operator transforms as the same irrep as one of the components of the EQ operator [145]. This is not the case for the O_h molecular symmetry point group, so that that the feature assigned to the EQ ZPL in the 300 K and 77 K spectra of $Cs_2NaSmCl_6$, Fig. 10, is much weaker than the associated vibronic structure. The electronic origin is identified by Stokes and anti-Stokes structure in the notation of Table 2. In conclusion it appears that nearly all of the intensity of hypersensitive transitions in M_2ALnCl_6 is vibronic in character. We have further observed that a non-centrosymmetric perturbation (for example, at crystal defect sites) introduces ED character into the pure electronic transition, which then becomes considerably enhanced.

7.3 Vibronic Spectra: Vibrational Progressions Caused by Displacement in Equilibrium Position

For an allowed transition, the intensity is distributed between the ZPL and vibrational progressions, since the first term in Eq. (17) can be nonzero for $k \neq n$ when the displacement in equilibrium position cannot be ignored, especially for the strong electron-phonon coupling case. This is quantified for Ln^{3+} electronic transitions by weak linear coupling (small Huang-Rhys parameter, $S=0$ inferring that all intensity is contributed by the electronic origin, the vibrational quantum v=0); or stronger linear coupling (e.g. $S=w$, where w (>0) phonons correspond to the intensity maximum of the sideband) [116]. The first situation corresponds to a very small displacement along the vibrational normal coordinate during the electronic transition (as in MD $f^N \leftrightarrow f^N$ transitions), whereas the second case is illustrated by a greater change, as in ED $f^N \leftrightarrow f^{N-1}d$ electronic transitions. In the absence of Jahn-Teller effects, considering the case at low temperature, when only the $n=0$ vibrational level initial state is populated (i.e. $\Gamma(\chi_{in}) \equiv \Gamma_{1g}$), the symmetry selection rule for the first term of Eq. (17) to be nonzero for the first member $k=1$ of a given vibrational mode Q_v is that $\Gamma(\chi_{fk=1}) \times \Gamma(\chi_{in=0})$ contains Γ_{1g}. Thus the progression forming-mode is a totally-symmetric vibration.

The intensity ratio of the ZPL intensity ($I^{0,0}$) to that of the p-th member of the progression in the emission (Eq. 27) or the q-th in absorption (Eq. 28) spectra is given by

$$\frac{I^{0,p}}{I^{0,0}} = \left[\frac{E(ZPL) - p\bar{\nu}_1}{E(ZPL)}\right]^4 \left[\frac{R_{0,p}}{R_{0,0}}\right]^2 \tag{27}$$

$$\frac{I^{q,0}}{I^{0,0}} = \left[\frac{E(ZPL) + q\bar{\nu}_1}{E(ZPL)}\right] \left[\frac{R_{q,0}}{R_{0,0}}\right]^2 \tag{28}$$

respectively, where the wave function overlap integrals $R_{0,p}$ and $R_{q,0}$ can be related to the displacement ΔS of the minimum of the potential surface of the excited electronic state along the α_{1g} normal coordinate [146]. Furthermore, for the case of hexacoordinated species, the individual Ln-X bond length change, $\Delta r = \Delta S/\sqrt{6}$.

Totally symmetric vibrational progressions in the $\nu(\mathrm{Ln}-\mathrm{Cl})$ stretching mode have been reported very weak at the long wavelength tails of certain emission transitions, for example, for Pr^{3+} in the $^3P_0 \rightarrow {}^3H_4$, $^3H_5$, $^3F_2$ transitions [147]; for Dy^{3+} in the $^4F_{9/2} \rightarrow {}^6H_{13/2}$ transition [123]; for Ho^{3+} in the $^5F_5 \rightarrow {}^5I_8$ transition [148]; and for Yb^{3+} in the $^2F_{5/2} \rightarrow {}^2F_{7/2}$ transition [149]. The maximum bond length change along the α_{1g} coordinate is ca. 1.4 pm. Jahn-Teller effects are common in the spectra of d-block elements but are much less important for f^N systems, where progressions in nontotally symmetric modes have rarely been observed in $4f^N$-$4f^N$ electronic spectra [149].

7.4 Vibronic Spectra: One-phonon Sideband

The doped (guest) Ln^{3+} ion destroys the translational symmetry of the crystal and the $4f^N$ electronic states of Ln^{3+} are very localized, so that vibronic states are classified according to irreps of the site group. The vibrational irreps have been described as those of the LnX_6^{3-} complex ion point group, or more accurately as those of the Ln^{3+} site group contained in the space group. The second and third terms of (17) refer to the vibrational sideband structure of the transition caused by the electron-phonon coupling Hamiltonian $\left(\frac{\partial \mathrm{H}}{\partial \mathrm{Q}_\nu}\right)_{Q_0} Q_\nu$, and they are nonzero when [110, 150]

$$\Gamma(\psi_f^*) \times \Gamma(\mathrm{M}_e) \times \Gamma(\psi_m) \quad \text{contains} \quad \Gamma_{1g} \tag{29a}$$

$$\Gamma(\chi_{fk}^*) \times \Gamma(Q_\nu) \times \Gamma(\chi_{in}) \quad \text{contains} \quad \Gamma_{1g} \tag{29b}$$

and

$$\Gamma(\psi_m) \times \Gamma(Q_\nu) \times \Gamma(\psi_i) \quad \text{contains} \quad \Gamma_{1g} \tag{29c}$$

The vibrational states χ_{fk} and χ_{in} differ by one quantum of Q_ν, i.e. the two $4f^N$ vibronic states differ by one quantum of a vibration. Usually M_e is the ED operator, so that the Q_ν has odd-parity for centrosymmetric systems, and ψ_m corresponds to an opposite-parity ($4f^{N-1}5d$) intermediate state.[2] Based on Eq. (29), from the **k**=0 unit cell vibrations identified in Table 2, the symmetry species of vibrational modes enabled in specific EDV transitions between the CF levels of $4f^N$ rare earth ions in elpasolite lattices are therefore

[2] Both theoretically [151] and experimentally (e.g. [152]) it is evident that MD vibronic intensity contributions are small for M_2ALnX_6 systems.

Table 4 **k**=0 Selection rules for one-phonon sideband structure of the $i \rightarrow f$ transition in the EDV spectra of octahedral symmetry compounds (from [110]). The M_2ALnX_6 unit cell group modes contain $\tau_{1u}+\tau_{2u}$, but not ϵ_u or α_{1u}

$\Gamma_i \backslash \Gamma_f$	Γ_1	Γ_2	Γ_3	Γ_4	Γ_5
Γ_1	τ_{1u}	τ_{2u}	$\tau_{1u}+\tau_{2u}$	$\alpha_{1u}+\epsilon_u+\tau_{1u}+\tau_{2u}$	$\alpha_{1u}+\epsilon_u+\tau_{1u}+\tau_{2u}$
Γ_2		τ_{1u}	$\tau_{1u}+\tau_{2u}$	$\alpha_{1u}+\epsilon_u+\tau_{1u}+\tau_{2u}$	$\alpha_{1u}+\epsilon_u+\tau_{1u}+\tau_{2u}$
Γ_3			$\tau_{1u}+\tau_{2u}$	All u	All u
Γ_4				All u	All u
Γ_5					All u
$\Gamma_i \backslash \Gamma_f$	Γ_6			Γ_7	Γ_8
Γ_6	$\alpha_{1u}+\epsilon_u+\tau_{1u}+\tau_{2u}$			$\alpha_{1u}+\epsilon_u+\tau_{1u}+\tau_{2u}$	All u
Γ_7				$\alpha_{1u}+\epsilon_u+\tau_{1u}+\tau_{2u}$	All u
Γ_8					All u

subject to the selection rules given in Table 4, in which only τ_{1u} type ($S_6=\nu_3$ and $S_7=\nu_4$) and τ_{2u} type ($S_{10}=\nu_6$) are active moiety modes. The oscillator strengths of entire vibronic sidebands of Cs_2NaYCl_6:Ln^{3+} do not vary significantly with the concentration of Ln^{3+} in the crystal, although some individual vibronic origins do exhibit minor changes attributed to the change in mixing of vibrational symmetry coordinates with change in Ln-Cl bond distance with concentration [153, 154]. The vibronic sideband intensity at temperature T, $I(T)$ shows a coth law dependence with temperature [155]:

$$I(T) = \sum_i I_i(0)\coth(\mathrm{hc}\bar{\nu}_i/2k_BT) \tag{30}$$

where the sum is over all the component vibrations ν_i in the sideband, and k_B is the Boltzmann constant.

The model which has been most widely applied to the calculation of vibronic intensities of the $Cs_2NaLnCl_6$ systems is the vibronic coupling model of Faulkner and Richardson [67]. Prior to the introduction of this model, it was customary to analyse one-phonon vibronic transitions using Judd closure theory, Fig. 7d, [117] (see, for example, [156]) with the replacement of the $T_\lambda^{electronic}$ (which is proportional to the above Ω_λ) parameters by $T_\lambda^{vibronic}$, which include the vibrational integral and the derivative of the CF with respect to the relevant normal coordinate. The selection rules for vibronic transitions under this scheme therefore parallel those for forced electric dipole transitions (e.g. $|\Delta J| \leq 6$; and in particular when the initial or final state is $J=0$, then $|\Delta J|=2, 4, 6$).

Because the general features of the Faulkner-Richardson model are representative and convey a simple physical picture, and it is the only model that has been extensively and fairly successfully applied to the interpretation of the vibronic spectra of $Cs_2NaLnCl_6$ systems, it will be described in slightly

modified form in more detail herein. It is assumed that the Ln^{3+} ion and six ligands X^- interact by Coulomb, and not exchange forces. Only the (odd-parity) LnX_6^{3-} vibrations, the so-called moiety modes, are considered to be responsible for vibronic perturbations. The Hamiltonian for the complete system is partitioned into three parts: free ion (H_A^0), ligand (H_B^0) and lanthanide ion-ligand interaction. Each charge distribution is expanded as a multipolar series about the appropriate centre. The latter lanthanide ion-ligand part of the Hamiltonian is then further partitioned into operators representing electrostatic interactions between the metal ion multipoles and the monopoles (static coupling operator, V) and higher multipoles (dynamic coupling operator, U) of the ligands. Both operators are expanded in the normal coordinates Q_v about the equilibrium geometry, and retaining the linear terms in Q_v, the vibronic Hamiltonian is

$$\mathrm{H} = \mathrm{H}_A^0 + \mathrm{H}_B^0 + \mathrm{V}^0 + \mathrm{U}^0 + \sum_v \mathrm{V}'_v Q_v + \sum_v \mathrm{U}'_v Q_v \tag{31}$$

where the $'$ signifies differentiation with respect to Q_v at the equilibrium position.

The operators U^0 and V^0 are expressed in terms of the interaction potential:

$$\mathrm{V}^0 = \sum_X \sum_{l_{Ln}} \mathrm{V}_X(l_{Ln}, 0) = \sum_X \sum_{l_{Ln}} \sum_{m_{Ln}} \mathrm{T}^{(l_{Ln},0)}_{m_{Ln},0}(X)\mathrm{D}^{(l_{Ln})}_{m_{Ln}}(Ln)\mathrm{D}^{(0)}_0(X) \tag{32}$$

$$\mathrm{U}^0 = \sum_X \sum_{l_{Ln}} \sum_{m_{Ln}} \sum_{m_X} \mathrm{T}^{(l_{Ln},1)}_{m_{Ln},m_X}(X)\mathrm{D}^{(l_{Ln})}_{m_{Ln}}(Ln)\mathrm{D}^{(1)}_{m_X}(X) \tag{33}$$

with

$$\mathrm{T}^{(l_{Ln},l_X)}_{m_{Ln},m_X}(X) = \frac{(-1)^{l_X+m_X+m_{Ln}}}{R_X^{l_{Ln}+l_X+1}} \cdot \cdot \left[\frac{(l_{Ln}+l_X+m_{Ln}+m_X)!(l_{Ln}+l_X-m_{Ln}-m_X)!}{(l_{Ln}+m_{Ln})!(l_{Ln}-m_{Ln})!(l_X+m_X)!(l_X-m_X)!}\right]^{1/2} \mathrm{C}^{(l_{Ln}+l_X)}_{-(m_{Ln}+m_X)}(\Theta_X, \Phi_X) \tag{34}$$

where l is the rank of the multipole and m specifies its component; (R_X, Θ_X, Φ_X) are the ligand X^- coordinates with respect to the rare earth ion Ln^{3+}. The $\mathrm{D}^{(0)}_0(X) = q_X$ in Eq. (32) is the net charge on X, and the U^0 in Eq. (33) is approximated by only taking l_X=1 terms, the dipole $\mathrm{D}^{(1)}_{m_X}$ ones, from the sum over $l_X \geq 1$. Differentiation gives

$$\mathrm{V}'_v = \sum_{l_{Ln},m_{Ln}} \left[\sum_X \left(\partial \mathrm{T}^{(l_{Ln},0)}_{m_{Ln},0}(X)/\partial Q_v\right)_0 q_X\right] \mathrm{D}^{(l_{Ln})}_{m_{Ln}}(Ln) \tag{35}$$

$$U'_v = \sum_{l_{Ln},m_{Ln}} \left[\sum_{X,m_X} \left(\partial T^{l_{Ln},1}_{m_{Ln},m_X}(X)/\partial Q_v \right)_0 D^{(1)}_{m_X}(X) \right] D^{(l_{Ln})}_{m_{Ln}}(Ln) \tag{36}$$

For the centrosymmetric elpasolite systems, the last three terms of Eq. (31) (denoted in brief by U^0, V_1 and U_1) are chosen as the perturbation Hamiltonian (H′) upon the zeroth order Hamiltonian operator. Then V_1 is a vibronic coupling operator, arising from the interactions between the f-electrons of Ln^{3+} and the vibrating point-charge distributions of the ligands. Since U_0+U_1 involves higher multipoles (approximately only the dipole is considered here) of the ligand charges, it involves dynamic coupling between Ln^{3+} and X^-. The last two perturbation operators (V_1 and U_1) produce the EDV intensity, with the participation of opposite-parity lanthanide ion states, abbreviated as Ln_m, and ligand excited states X_u.

The ground-state $|Ln_{00}X_0)$ wavefunction is utilized as the zeroth order basis set (using rounded kets), and using the singly- and doubly-excited state functions, the perturbed wavefunctions of the LnX_6^{3-} system are written to first order in H′. Then the EDV transition moment for the $|Ln_{00}X_0\rangle \rightarrow |Ln_{f1}X_0\rangle$ transition is given by

$$\begin{aligned} M_{00,f1}(Q) = & (Ln_{00}X_0|D^{(1)}|Ln_{00}X_0)(Ln_{f1}X_0|H'|Ln_{00}X_0)/(E_{f1}) \\ & - {\sum}'_{m\neq f} (Ln_{m0}|D^{(1)}|Ln_{00})(Ln_{m0}X_0|H'|Ln_{f1}X_0)^{\dagger}/(E_{m0}-E_{f1}) \\ & - {\sum}'_{m} Ln_{f1}|D^{(1)}|Ln_{m1}(Ln_{00}X_0|H'|Ln_{m1}X_0)^{\dagger}/(E_{m1}) \\ & + {\sum}'_{u} \left(X_u|D^{(1)}|X_0\right)(Ln_{00}X_u|H'|Ln_{f1}X_0)^{\dagger} \left[\frac{2E_u}{(E_{f1})^2-(E_u)^2}\right] \end{aligned} \tag{37}$$

of which the first term is zero for a centrosymmetric system, and the dipole strength is

$$D_{00,f1} = |M_{00,f1}|^2 \tag{38}$$

The vibronic wave functions for the LnX_6^{3-} system are written as Herzberg-Teller products of harmonic oscillator wave functions and electronic wave functions. We consider an absorption transition from the zeroth vibrational level of the electronic ground state to the *f*-th electronic excited state accompanied by the excitation of one quantum of the *v*-th odd-parity normal mode Q_v (i.e. the occupation number $k(v)$=1). The vibrational wavefunctions are then χ_{00} and χ_{f1} for the ground and *f*-th excited electronic state, respectively. The EDV transition element of the *q*-th component of the moment $M_{00,f1}$ in Eq. (37) for the 00→*f*1 transition can be written in terms of static and dynamic coupling parts:

$$M_{00,f1;q} = \sum_{v} [\langle \chi_{00} | M^{(s)}_{0f;q}(Q_v) | \chi_{f1} \rangle + \langle \chi_{00} | M^{(d)}_{0f;q}(Q_v) | \chi_{f1} \rangle] \tag{39}$$

This partitioning gives rise to the occurrence of interference terms between the static and dynamic coupling contributions in the expression for the dipole strength Eq. (38), Eq. (46).

The vibrational integral is separated

$$M_{00,f1;q} = \langle \chi_{00} | Q_v | \chi_{f1} \rangle \sum_{l_{Ln}, m_{Ln}} [A'_v(l_{Ln}, m_{Ln}) Z^{(s)}_{0f;q}(l_{Ln}, m_{Ln}) + B'_v(l_{Ln}, m_{Ln}; q) Z^{(d)}_{0f;q}(l_{Ln}, m_{Ln})] \tag{40}$$

where

$$A'_v(l_{Ln}, m_{Ln}) = \sum_X q_X [\partial \mathrm{T}^{(l_{Ln},0)}_{m_{Ln},0}(X) / \partial Q_v]_0 \tag{41}$$

$$B'_v(l_{Ln}, m_{Ln}; q) = \sum_X \bar{\alpha}_X(v_f) [\partial \mathrm{T}^{(l_{Ln},1)}_{m_{Ln},q}(X) / \partial Q_v]_0 \tag{42}$$

in which $\bar{\alpha}_X(v_f)$ is the average ligand polarizability,

$$Z^{(s)}_{0f;q}(l_{Ln}, m_{Ln}) = -{\sum_m}' \{ (Ln_0 | \mathrm{D}^{(1)}_q | Ln_m)^\dagger (Ln_m | \mathrm{D}^{(l_{Ln})}_{m_{Ln}} | Ln_f)^\dagger / E_{fm} - (Ln_f | \mathrm{D}^{(1)}_q | Ln_m) (Ln_0 | \mathrm{D}^{(l_{Ln})}_{m_{Ln}} | Ln_m)^\dagger / E_{m0} \} \tag{43}$$

$$Z^{(d)}_{0f}(l_{Ln}, m_{Ln}) = (Ln_0 | \mathrm{D}^{(l_{Ln})}_{m_{Ln}} | Ln_f)^\dagger \tag{44}$$

The electronic multipolar factor $Z^{(s)}_{0f;q}$ in Eq. (43) may be evaluated in terms of reduced matrix elements and 3-j and 6-j symbols following the closure arguments of Judd [117] mentioned before. The vibrational integral is given by

$$\langle \chi_{00} | Q_v | \chi_{f1} \rangle = \sqrt{\frac{\hbar}{4\pi c \bar{\nu}_v}} \tag{45}$$

where $\bar{\nu}_v$ is the harmonic wavenumber of the v-th normal mode. The evaluation of the vibronic coupling factors $A'_v(l_{Ln}, m_{Ln})$ and $B'_v(l_{Ln}, m_{Ln}; q)$ was carried out by numerical differentiation. The first of these quantities depends upon the X^- charge, q_X, and the ligand positional displacements of the v-th normal mode. The second quantity depends upon the ligand polarizability, $\bar{\alpha}_X(v_f)$, and positional displacements.

The evaluation of the electronic factors, by way of the 3-j and 6-j symbols, leads to selection rules for the vibronic spectra. In the formula for $\Xi(l_{Ln},\lambda)$

Table 5 EDV dipole strengths and relative intensities for the $^7F_0 \rightarrow {}^5D_2$ transition of Eu^{3+} in $Cs_2NaEuCl_6$ (from [67])

Transition	Dipole strength[a]	Relative intensity	
		Calculated	Observed[b]
$\Gamma_{1g} \rightarrow \Gamma_{3g}+\nu_3$	2.4	0.88	0.82
$\Gamma_{1g} \rightarrow \Gamma_{3g}+\nu_4$	2.7	1.0	1.0
$\Gamma_{1g} \rightarrow \Gamma_{3g}+\nu_6$	0.6	0.22	0.19
$\Gamma_{1g} \rightarrow \Gamma_{5g}+\nu_3$	3.0	1.0	1.0
$\Gamma_{1g} \rightarrow \Gamma_{5g}+\nu_4$	2.1	0.7	0.56
$\Gamma_{1g} \rightarrow \Gamma_{5g}+\nu_6$	1.2	0.4	[c]

[a] In units of 10^{-43} e.s.u.^{2} cm^2. The total electric dipole strength is calculated (observed) to be 12 (48); [b]Measurement error ±20%; [c]Overlapped by other bands

in the approximate Judd expression for $Z^{(s)}_{0f;q}(l_{Ln}, m_{Ln})$ the values of l_{Ln} and λ are limited (λ=2, 4, 6; $l_{Ln}=\lambda\pm1$); and there are triangle conditions limiting the intermediate Ln^{3+} configuration to an opposite parity $f^{N-1}d$ or $f^{N-1}g$ configuration (with only the latter if l_{Ln}=7). For the $Z^{(d)}_{0f}(l_{Ln}, m_{Ln})$ in Eq. (44), the value of l_{Ln}=2,4,6. Also, other selection rules on *S*, *L* and *J* from the Faulkner-Richardson model are given in Table 1.

The Faulkner-Richardson vibronic intensity model has been used to rationalize the vibronic sidebands in many $LnCl_6^{3-}$ systems [157–164]. The radial integral and $\Xi(l_{Ln},\lambda)$ parameter values were not fitted, but taken from the literature. Generally, the agreement with experimental vibronic intensities has been of a semiquantitative nature, but the relative magnitudes of the ED vs MD contributions to the total dipole strengths of multiplet-multiplet transitions are fairly well-reproduced. In some cases, for example Eu^{3+} in $Cs_2NaEuCl_6$ [67], the agreement of both absolute and relative intensities is remarkable (Table 5). Furthermore, the vibronic intensities of several hypersensitive transitions (e.g. $^4I_{15/2} \rightarrow {}^2H_{11/2}$, $^4G_{11/2}$ of Er^{3+} in $Cs_2NaErCl_6$, [163] and $^4G_{7/2} \rightarrow {}^4I_{11/2}$ of Nd^{3+} in Cs_2NaYCl_6:Nd^{3+} [158]) are calculated to be very large, due to transition quadrupole (Ln^{3+})-transition dipole (Cl^-) interactions incorporated in the dynamic coupling part of the intensity model. More generally, one of the main features of the model has been that the static coupling (SC) and dynamic coupling (DC) terms usually make comparable contributions, and that signed interference terms may play an important role in determining vibronic intensities:

$$D_{00,f1} = |M_{00,f1}(SC)|^2 + M^*_{00,f1}(SC) \times M_{00,f1}(DC) + M^*_{00,f1}(DC) \times M_{00,f1}(SC) + |M_{00,f1}(DC)|^2 \quad (46)$$

The sign of the interference terms in Eq. (46) has been the subject of discussion which has been clarified by Xia and Reid [165].

Some further modifications have been suggested since the first use of the model, although no detailed calculations have been forthcoming. In the Faulkner-Richardson model, the vibronic factor $A_{\nu}^{'}(l_{Ln}, m_{Ln})$ was calculated by numerical partial differentiation. In a manuscript focusing upon the vibronic structure of EQ transitions, Judd [141] subsequently pointed out that this can be avoided by using the appropriate bipolar expansions. In addition, Judd included a further mechanism in the static coupling term, not only to account for the interaction between metal ion multipoles and ligand charges, but also the induced charges on the ligands (which are polarized by Ln^{3+}). The dynamic coupling mechanism, represented by the last term of Eq. (37) where the $4f^N$ electrons polarize the ligands, which then interact with the radiation field, was represented by Judd in an alternative manner where the radiation field induces dipoles in the ligands which then re-radiate and interact with the $4f^N$ electrons. A factor was also introduced in the dynamic coupling term to account for the screening of the quadrupole fields by the fifth shell electrons of Ln^{3+}. Stewart [166] further modified the dynamic coupling term by including polarizability derivatives as well as anisotropic polarizabilities and found that these terms were important for the vibronic structure of the hypersensitive $^5D_0 \rightarrow {}^7F_2$ transition of Eu^{3+}. On the same subject, Malta [167] utilized a ligand field model and included the dependence of the effective charges and polarizabilities upon the Ln^{3+}-Cl^- distance.

More general calculations have not been forthcoming from the above refinements due to lack of knowledge about some of the parameters involved. An alternative more general parametrization approach was presented by Reid and Richardson for vibronic intensities [168], based upon linear vibronic coupling, but independent of the detailed nature of the Ln^{3+}-ligand-radiation field interactions under the electric dipole approximation. The general parametrization scheme for vibronic intensities, which also includes the contributions from vibrational progressions to the vibronic intensity, utilizes the point group notation of Butler. An electronic operator called the effective vibronic transition operator is introduced for one-phonon electric dipole vibronic processes. It contains rank 2, 4 and 6 unit tensor operators which act within the $4f^N$ configuration, and parameters $A^{\lambda^+}_{t^-c*\nu*}(d\nu*)$ which represent the vibronic mixing of CF states with opposite-parity configurations. For the $LnCl_6^{3-}$ moiety, the parameters are derivatives with respect to the 3 odd-parity normal modes, with up to 11 parameters each for the τ_{1u} modes and 10 for τ_{2u}. The parameters may be reduced in number when expressed in terms of the intrinsic parameters of the superposition model, $\bar{A}_t^{\lambda}$, where each Ln-Cl interaction is cylindrically symmetric and independent. The Herzberg-Teller formalism is applied to calculate the electric dipole

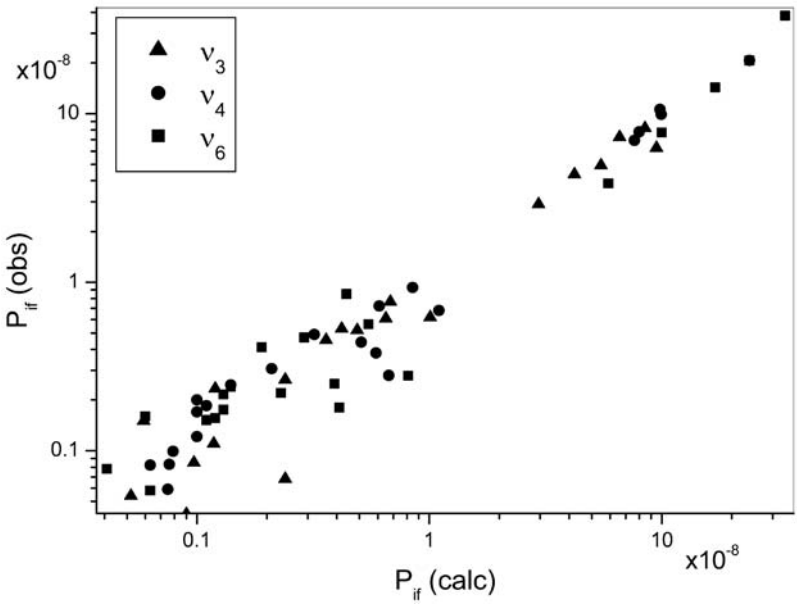

Fig. 11 Comparison of calculated and observed vibronic oscillator strengths for absorption transitions from the $(^4I_{15/2})a\Gamma_8$ level of Er^{3+} in $Cs_2NaErCl_6$. (Data from [128])

strength of the vibronic transition by using the initial and final $4f^N$ electronic wavefunctions with the effective vibronic transition operator, including the product with the vibrational integral. The latter assumes a harmonic force-field. The results of calculated and experimental oscillator strengths for the ν_3, ν_4 and ν_6 vibronic intensities in the electronic absorption spectra of Er^{3+} in $Cs_2NaErCl_6$ are shown in Fig. 11, where 68 vibronic transitions were fitted [128]. The signs of the derived intensity parameters were taken to indicate the importance of both the static and dynamic coupling mechanisms. The agreement with experimental data is good, although a large number (18) of parameters were employed and the descriptions of physical mechanisms are not forthcoming. More recently [169], it has been found that different sets of parameter values may provide a similar goodness-of-fit to the experimental vibronic intensities, due to the presence of multiple local minima in the nonlinear fitting process. Furthermore the parameter signs may not be uniquely determined because intensities depend upon the squares of these values.

An attempt to elucidate the physical mechanisms of vibronic transitions and to avoid excessive parametrization has been made in the vibronic intensity calculations of Acevedo et al. [97, 170–173] which have been performed for individual vibronic transitions between CF states, with and without the Judd closure approximation, following the point group symme-

try notation of Griffith [174]. Particular care has been given to the vibrational analysis of the moiety modes, which was largely based upon the normal coordinate analyses of solid pyridinium complexes in the studies of Richardson and co-workers. However, the direct calculations have only employed the major $^{2S+1}L_J$ components of states, and a selected intermediate state. This is probably the reason for the rather poor agreement with calculation in some cases, due to the delicate balance and interference between the signed contributions from dynamic and static coupling terms. The agreement for overall multiplet-multiplet vibronic intensities is found to be generally good.

It is relevant here to mention the treatment of vibronic intensities by the two-centre theory of Stavola and Dexter [175, 176], which leads to the expression for the ED transition matrix element for the vibronic absorption of a coupled rare earth-ligand system. In the present case of M_2ALnX_6 the ligand is monatomic, but more generally, we consider the case where X is not monatomic in Ln^{3+}-X^- (e.g. X=OH, NO_2, etc). Following Stavola and Dexter, the ED strength for the q-th polarized component of the transition in which the Ln^{3+} ion undergoes an intraconfigurational $4f^N$ transition, $Ln_i \rightarrow Ln_f$, and one quantum of vibration within ligand X^- is simultaneously excited i.e. $X_0 \rightarrow X_1$, is

$$D_{Ln_iX_0,Ln_fX_1} = \left|\langle Ln_iX_0|\mathrm{M}^q_{Ln} + \mathrm{M}^q_X|Ln_fX_1\rangle\right|^2 \tag{47}$$

where M_{Ln} and M_X operate over the coordinates of Ln and X respectively. Dropping the superscript q in the following, assuming that Ln_0 and X_0 refer to ground states with reference energy zero, and denoting lanthanide and ligand (opposite parity) intermediate states by the subscripts m and u, respectively, the matrix element in Eq. (47) is expanded, with rounded kets denoting zeroth-order states [175]:

$$\langle Ln_0X_0|\mathrm{M}_{Ln} + \mathrm{M}_X|Ln_fX_1\rangle = \big(Ln_0X_0|\mathrm{M}_{Ln} + \mathrm{M}_X|Ln_fX_1\big) \tag{48a}$$

$$-\sum_{m\neq f}\big(Ln_m|\mathrm{M}_{Ln}|Ln_f\big)\big(Ln_0X_0|\mathrm{H}_{Ln-X}|Ln_mX_1\big)\big(E_{Ln_m} + E_{X_1}\big)^{-1} \tag{48b}$$

$$-\sum_{u\neq 1}\big(X_u|\mathrm{M}_X|X_1\big)\big(Ln_0X_0|\mathrm{H}_{Ln-X}|Ln_fX_u\big)\big(E_{Ln_f} + E_{X_u}\big)^{-1} \tag{48c}$$

$$-\sum_{m\neq f}\big(Ln_0|\mathrm{M}_{Ln}|Ln_m\big)\big(Ln_mX_0|\mathrm{H}_{Ln-X}|Ln_fX_1\big)\big(E_{Ln_f} + E_{X_1} - E_{Ln_m}\big)^{-1} \tag{48d}$$

$$-\sum_{u\neq 0}\big(X_0|\mathrm{M}_X|X_u\big)\big(Ln_0X_u|\mathrm{H}_{Ln-X}|Ln_fX_1\big)\big(E_{Ln_f} + E_{X_1} - E_{X_u}\big)^{-1} \tag{48e}$$

The first term (Eq. 48a) is nonzero in the presence of odd CF terms (but zero in the present case for Ln^{3+} at an O_h site). By including several assumptions, such as the neglect of terms at Eqs (48c) and (48e), and of in-

terference effects when squaring matrix elements, and the restriction of the Ln-X interaction Hamiltonian $H_{Ln\text{-}X}$ to dipole-dipole coupling interactions; and approximations such as the averaging over polarization directions and over *SLJ*-multiplet states of Ln^{3+}, a simple expression for the dipole strength of the cooperative absorption $Ln_0X_0 \rightarrow Ln_fX_1$ was derived [175].

Modifying the diagrams of Dexpert-Ghys and Auzel [177], it is instructive to compare the mechanisms of vibronic transitions enabled by the Faulkner-Richardson [67] and Stavola-Dexter mechanisms. Figure 7e shows the static (i), (ii) and dynamic (iii), (iv) coupling mechanisms of Faulkner and Richardson [67], involving the excitation of one quantum of a certain LnX_6^{3-} moiety mode in an f^N excited state. Notice that the mechanism is vibronic and not electronic in nature. In the Stavola-Dexter mechanism, Fig. 7f, the vibration is excited within a (separate) ligand and the excitation at the lanthanide ion, M_{Ln}, is purely electronic dipolar. The Ln^{3+}-X^- interaction is ligand dipole-metal dipole or ligand dipole-metal quadrupole.

All of the above vibronic intensity calculations of M_2ALnX_6 systems have employed the LnX_6^{3-} moiety model. By contrast, the earlier studies of the electronic spectra of rare earth ions interpreted the vibronic sidebands in terms of crystal, rather than moiety mode or unit cell vibrations. This is because more than one elementary excitation occurs in vibronic spectroscopy, so whereas the conservation of wavevector restricts the sum of the momenta of the electronic and vibrational excitations: $\mathbf{k}_{photon}=\mathbf{k}_e+\mathbf{k}_{vib}=0$, then $\mathbf{k}_e$ or $\mathbf{k}_{vib}$ can be nonzero [110]. This means that $\mathbf{k}\neq 0$ vibrational modes (i.e. due to dispersion, with consequent reduction in symmetry and maybe also degeneracy, and with change in energy) can produce vibronic intensity. This is particularly so for acoustic modes (which have zero energy at $\mathbf{k}=0$) which show greater dispersion than optical modes (Fig. 6). Although all vibrational modes can therefore contribute to the intensity of a vibronic band, only those points of high density of vibrational states in fact produce sufficient spectral intensity [178], and these points lie near special points of the Brillouin zone (Fig. 5). The method for obtaining the vibronic selection rules at points other than $\mathbf{k}=0$ has been the focus of several studies [for example, 179–182]. In conclusion, it is observed that the major spectral features in a vibronic sideband can be explained under $\mathbf{k}=0$ selection rules, sometimes particularly well [183], but the interpretation of fine structure requires a more detailed lattice dynamics model [184], and we return to this in the next section. The description of the vibrational states of the guest ion in the crystal is not made in terms of a single $\mathbf{k}$ vector (running or plane wave) but in terms of linear combinations (standing waves) since the translational symmetry is destroyed.

Finally, it is noted that for transitions such as $\Gamma_1 \rightarrow \Gamma_i + \nu_3(\tau_{1u})$, where i=3, 4 or 5, in the absence of electron-vibrational interaction, the terminal vibronic state irreps are degenerate. In fact, various experimental studies have shown that the splitting of these states is <1 cm^{-1} for Ln^{3+} systems. The major broadening mechanisms of the linewidths of ZPL transitions to the electronic ground state (e.g. Fig. 9b, $\Gamma_8 \rightarrow a\Gamma_8$), are (i) inhomogeneous broadening due to random microscopic crystal strain, and (ii) homogeneous broadening due to ion-ion interactions, as well as Raman broadening *within* the excited state. Doppler and lifetime broadenings are very much smaller. Vibrational sequences can also contribute to line broadening, due to the slight change in vibrational frequencies between the ground and excited states. Other pure electronic transitions in Fig. 9b are *additionally* broadened by the short lifetimes of the terminal electronic states. This effect is more evident in Fig. 9c. The vibronic transitions in Fig. 9b are also *additionally* broadened due to the phonon dispersion and to the shorter lifetimes of terminal vibronic states.

7.5 Interpretation and Assignment of $4f^N$-$4f^N$ Spectra

The electronic spectra of M_2ALnX_6 systems are particularly complex because they are mainly vibronic, and many transitions overlap. So how can the spectral features be reliably assigned? First, the electronic origin of each transition needs to be identified. Selection rules foretell if the transition is MD or EQ allowed, and the MD selection rules are rather less restrictive for odd-electron systems (Table 1). If the band is MD allowed, its oscillator strength (or intensity ratio) can be compared with calculation. For absorption transitions from nondegenerate ground states, the splitting of ZPL for earlier members of the $Cs_2NaLnCl_6$ series below T_c (see above), not apparent in Cs_2NaYCl_6:Ln^{3+}, can indicate the presence of a degenerate excited state.

If the ZPL is weak, then variable temperature studies can identify its location from hot electronic and vibronic structure, with the latter illustrated in Fig. 10. The vibronic structure can be used to identify certain symmetry types of transition, for example Γ_1-Γ_2 (Table 4). One viewpoint has been put forward that the spectral interpretation is confused by phonon dispersion in the vibronic sidebands of transitions. However, this complexity of the vibronic structure can in fact be utilized to provide a fingerprint to identify the location of the electronic origin. Where possible, it is more certain to compare both emission and absorption (or excitation) spectra for a particular transition in order to locate the electronic origin. Otherwise, transitions from different emissive states (with different state irreps) can be employed to confirm the symmetries and locations of terminal levels. Whereas other neat systems such as $PrCl_3$ show additional features not present in the electronic spectra of the diluted crystal ($LaCl_3$:Pr^{3+}) due to interactions between

Pr^{3+} ions [183], this is generally not the case for M_2ALnX_6 systems because the Ln^{3+}-Ln^{3+} separation is large (>ca. 0.7 nm).

The problem of resolving an individual transition from overlapping emission transitions, or of populating a certain electronic state of Ln^{3+} in M_2ALnX_6 may in some cases be simplified by quenching the emission from a certain state by doping with another lanthanide ion. Thus the infrared emission of Yb^{3+} has been studied by doping $Cs_2NaLnCl_6$ (Ln=Ho, Nd) with Yb^{3+} [149]; the emission transitions from the Ho^{3+} $^5S_2$ level have been quenched [185]; and the $^5I_4$ level of Ho^{3+} has been populated in $Cs_2NaHo_{0.99}Er_{0.01}Cl_6$ [186].

We turn now to the use of vibronic fine structure in aiding spectral assignments. Dilution of $Cs_2NaLnCl_6$ into the transparent host crystal Cs_2NaYCl_6 leads to a closer approximation to **k**=0 selection rules, with the disappearance of certain features which are present in the vibronic spectra of $Cs_2NaLnCl_6$. By contrast, the guest $Cs_2NaLnCl_6$ modes lie within the bands of host $Cs_2NaGdCl_6$ modes, so that the vibronic spectra of $Cs_2NaGdCl_6$:Ln^{3+} and $Cs_2NaLnCl_6$ are very similar except for minor energy shifts of features. This phenomenon is observed more clearly for the later members of $Cs_2NaLnCl_6$ which retain the cubic structure at low temperature, for example, the $^5S_2 \rightarrow {}^5I_7$ emission spectra of Ho^{3+} in (a) Cs_2NaYCl_6:Ho^{3+} and (b) $Cs_2NaGdCl_6$:Ho^{3+} are displayed in Fig. 12 [185]. The Ho^{3+} $^5S_2(\Gamma_3)$ level is at 18365 cm^{-1}. Several transitions to the $^5I_7$ CF levels (located between 5118–5270 cm^{-1}) overlap in the spectral region 13300–12800 cm^{-1}, but we do not discuss these in detail [185], and focus on the individual vibronic band shapes. The band marked 0–0 is the electronic origin $^5S_2(\Gamma_3) \rightarrow {}^5I_7(a\Gamma_4)$. The ν_6 vibronic origin (labelled 6) of this transition has a more prominent high energy shoulder (6′) in the $Cs_2NaGdCl_6$ host. Similarly, ν_4 (4) also has a more prominent low energy shoulder (4′), and ν_3 [(3)—also shown in the lowest energy band, $\Gamma_3 \rightarrow b\Gamma_4+\nu_3$] has two accompanying bands (3′ and 3″) in the $Cs_2NaGdCl_6$ host. The characteristic (changes in) band shapes thus aid the assignments of vibronic structure. By contrast, the electronic spectra of $Cs_2LiLnCl_6$ and $Cs_2NaLnCl_6$ show considerable differences in the *displacement energies* of vibronic structure from a particular electronic origin (Fig. 9a,b) because the $LnCl_6^{3-}$ vibrational frequencies are rather different, particularly for S_8 (Table 2). Since these systems differ only by changes in the Ln^{3+} third-nearest neighbour, the changes in the electronic energy levels of Er^{3+} are minor. Thus, chemical modification techniques have been used to locate and identify electronic energy levels by subtle differences in vibronic fingerprints. The comparison of analogous vibronic structure in the luminescence and absorption spectra of Cs_2NaLnX_6 (X=Cl, Br, F) has also been employed to aid spectral assignments (see, for example, [185, 187]). Vibronic intensity calculations have seldom been used to assign electronic transitions, but rather for comparison of their agreement with observed spectral intensity assignments.

The actual assignment of *individual* fine structure within vibronic peaks in the spectra of M_2ALnX_6 is by no means clear at present. Comparison of the vibronic spectra of $Cs_2NaYbCl_6$ (Fig. 4d) and $Cs_2NaErCl_6$ (Fig. 9a) shows that more detailed structure is observed in the former case, due to greater phonon dispersion. Chodos and Satten calculated the dispersion curves and phonon density of states for Cs_2UBr_6, and used these to model the Γ_{4u} (T_{1u}) and Γ_{5u} (T_{2u}) vibronic sidebands. It is interesting to compare the results for this system [184, 188] with the elpasolite dispersion curves [100] and vibronic spectra, because both systems crystallize in the *Fm3m* space group and comprise LX_6 units. However the electron-phonon coupling for the actinide system is about an order of magnitude greater than for the lanthanide system. Bron [189] has pointed out that in general, intraconfigurational f^N-f^N transitions are coupled to nonlocalized vibrations as well as to localized vibrations. The τ_{1u} vibrational fields are longer range than τ_{2u}, (or α_{2u}, ϵ_u [190]) so that the model of Chodos and Satten confined the τ_{2u} field to motions of the 6 nearest Br and 8 next-nearest Cs nuclei. First, we consider the similarities between the results for Cs_2UBr_6 and the vibronic spectra of elpasolites, with $Cs_2NaYbCl_6$ as an example. At high energy, in Fig. 4c,d, the features at 258, 277 cm^{-1} correspond to TO and LO modes, with the latter exhibiting greater dispersion. Weak bands at 209, 219 cm^{-1} in Fig. 4c, d are similar to the weak double-hump in Cs_2UBr_6 from the **k**=0 ϵ_g mode at points Z_1, W_2'. There are three major features both in Cs_2UBr_6 and $Cs_2NaYbCl_6$ in the region of ν_4. The highest energy band (130 cm^{-1}) has previously been assigned to the LO mode, but the calculated LO-TO splitting is rather smaller [191] and the band can gain intensity from the **k**=0 ν_5 mode at special points in the reciprocal lattice. The major peak in the τ_{2u} projected density of states in Cs_2UBr_6 has four components, with the lowest energy of these being associated with the **k**=0 mode in [184]. In the elpasolite vibronic sideband, the ν_6 **k**=0 band has been assigned to the stronger peak, which has a prominent low energy shoulder. This weakens in the Cs_2NaYCl_6:Ln^{3+} systems, but becomes stronger in systems which undergo the phase transition to $C_{4h}{}^5$. The major problem in the assignment of structure is whether the peaks in the vibronic spectra correspond to **k**=0 modes, with the work of Satten concluding that this is not the case. The assignments of the ν_4 and ν_6 vibrations in Table 2, from the vibronic spectra of $Cs_2NaLnCl_6$ would be ca. 5 cm^{-1} and 8 cm^{-1} too high, respectively if we follow the model assignments of Chodos and Satten.

Some differences in the vibronic sidebands of $Cs_2NaLnCl_6$ and Cs_2UBr_6 are the sharp peak at 290 cm^{-1} in the former spectrum (Fig. 4c,d) which corresponds to the flat ν_1 mode at special points, and the weak feature at 178 cm^{-1} due to third shell motion. The low-vibrational-energy shoulder on ν_3 (at 245 cm^{-1}, Fig. 4c,d and 3′ in Fig. 12) is characteristic of $Cs_2NaLnCl_6$ systems and could correspond to τ_{1u} modes at special points such as X_4^-, X_5^-. The assumption has been made that the vibronic sideband is one-pho-

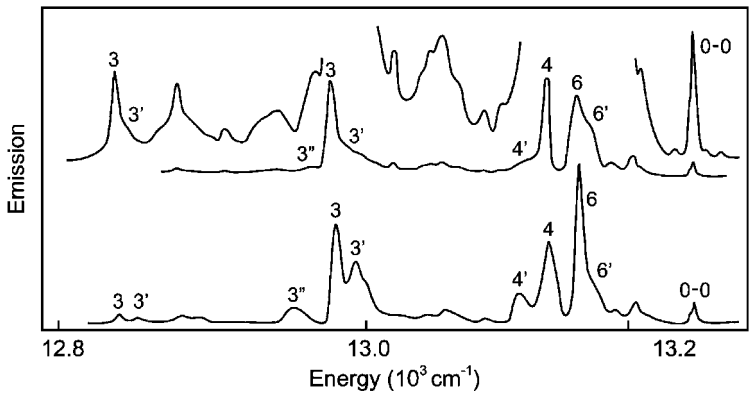

Fig. 12 488 nm excited 12–15 K luminescence spectra of $Cs_2NaYCl_6:Ho^{3+}$ (*top*) and $Cs_2NaGdCl_6:Ho^{3+}$ (*bottom*) between 13,300 and 12,800 cm^{-1}. The zero phonon lines are marked 0–0. The numbers i=3,4,6 indicate the vibrational modes ν_i in the sidebands. (Adapted from [185])

non in nature [179]. Otherwise, the 245 cm^{-1} band could be associated with several two-phonon modes.

Finally, the assignment of electronic energy levels from f^N-f^N electronic spectra can strengthened by techniques such as the vibronic Zeeman effect [192], MCD, MCPE, and the use of high pressure, but these have not been systematically employed. ESA measurements could be employed to locate (congested) levels at energies >20,000 cm^{-1}. Ground state term energies have been determined from complementary techniques such as electronic Raman spectra [91], inelastic scattering of neutrons [60, 106, 107], magnetic measurements [28, 193, 194], electron spin resonance [42, 195, 196], nuclear magnetic resonance [44, 197] and electron spin-lattice relaxation [198] for comparison with the results from electronic spectroscopy. TP spectroscopy (see Sect. 10) has proved to be a valuable tool in extending the energy level datasets of rare earth ions. Generally, the assignment of energy levels goes hand-in-hand with the refinement of the energy level calculations.

8
Electronic Raman Spectra

At room temperature, the Raman spectra of cubic lanthanide elpasolites comprise four bands, corresponding to the S_1, S_2, S_4 and S_5 modes of vibration. On cooling, the very broad, unresolved features due to electronic transitions between CF levels of Ln^{3+}, sharpen and reveal the locations of $4f^N$ excited states. The first studies of the electronic Raman spectra therefore focused upon the determination of the CF levels of the lower multiplet terms

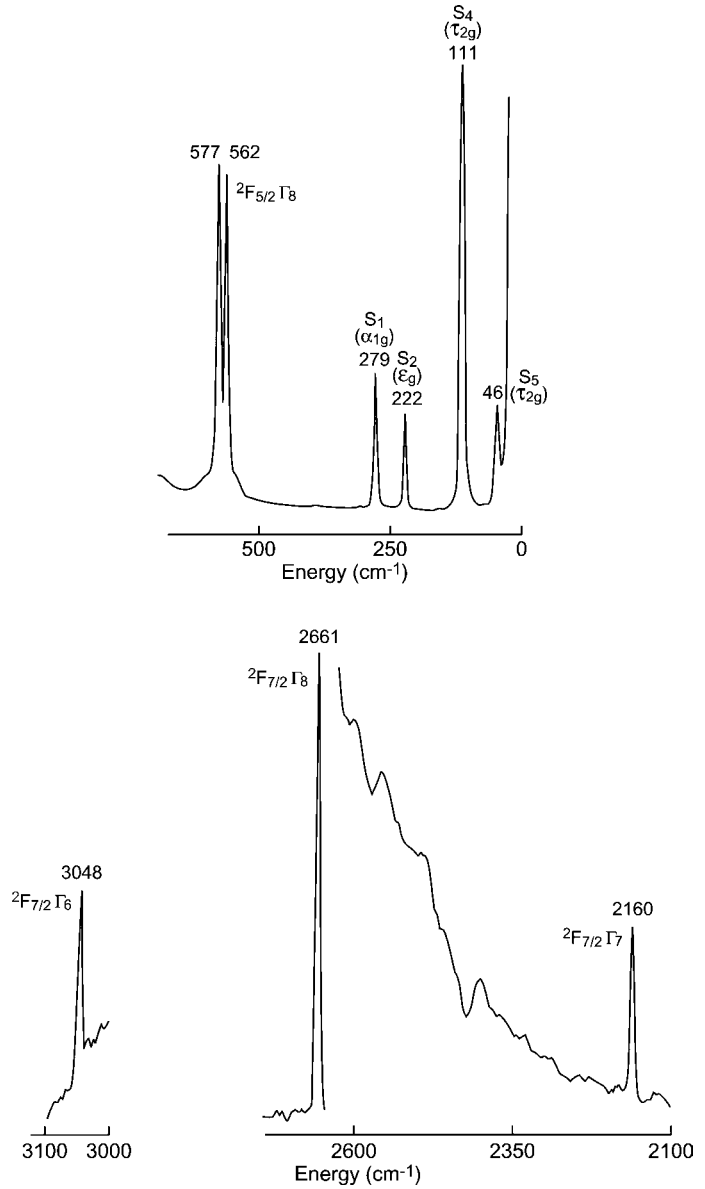

Fig. 13 35 K Raman spectrum of $Cs_2NaCeCl_6$ using argon ion laser excitation. Note the change of scale for the 2661 cm^{-1} band. (Adapted from [92])

of Ln^{3+} in the elpasolite lattices, and the fitting of these levels by CF theory [88, 93, 94, 147, 199–201]. Figure 13 shows the usefulness of the electronic Raman technique in completely and unambiguously identifying the f^1 energy level structure of Ce^{3+} in $Cs_2NaCeCl_6$ [92] (shown in Table 6 and subse-

Table 6 Experimental and calculated electronic Raman transition intensity ratios for Ce^{3+} in $Cs_2NaCeCl_6$

Transition from $^2F_{5/2}\Gamma_7$	Energy (cm^{-1})	Electronic Raman scattering intensity[a]				
		Observed	Theoretical	JOA-1	JOA-2	Direct
$^2F_{5/2}\Gamma_8$	562,580	4.2±0.5	$0.2449\|F_2\|^2+0.2073\|F_1\|^2$	4.2	4.2	4.2
$^2F_{7/2}\Gamma_7$	2161	0.16±0.01	$0.0078\|F_1\|^2$	0.00	0.04	0.25
$^2F_{7/2}\Gamma_8$	2662	0.86±0.07	$0.0227\|F_2\|^2+0.0058\|F_1\|^2$	0.39	0.31	1.52
$^2F_{7/2}\Gamma_6$	3050	1.00	$0.0181\|F_2\|^2$	0.31	0.22	1.27

Data taken from [203] and [91]. JOA-1, standard Judd-Ofelt-Axe calculation using F_1=0.00, F_2=4.13; JOA-2, standard JOA calculation using F_1=2.38, F_2=3.5; Direct, direct calculation

quently discussed in Fig. 17), since all intraconfigurational electronic Raman transitions are allowed from the Γ_7 electronic ground state. Note that although $Cs_2NaCeCl_6$ undergoes the phase transition at 178 K [41], no vibrational splittings are observed at 35 K, and only the electronic level $^2F_{5/2}$ Γ_8 exhibits a resolved splitting into two Kramers doublet levels.

More recent interest has focused upon the interpretation of the relative intensities of the electronic Raman transitions. The theory of electronic Raman spectroscopy has been well-summarized elsewhere [63, 202], and the electronic Raman scattering amplitude from an initial $|\psi_i\rangle$ to a final $|\psi_f\rangle$ vibronic state (where the phonon states are the same, and usually zero-phonon (i.e. electronic) states) is given by $\langle\psi_f|\alpha_{\rho\sigma}|\psi_i\rangle$. In this expression, the cartesian polarizations of the incident photon $(hc\bar{\nu})$ and the scattered photon $(hc\bar{\nu}_s)$ are σ and ρ, respectively. The Cartesian electronic Raman scattering tensor is written as

$$\alpha_{\rho\sigma} = -\sum_r \left[\frac{D_\rho^{(1)}|\psi_r\rangle\langle\psi_r|D_\sigma^{(1)}}{hc(\bar{\nu}_r - \bar{\nu})} + \frac{D_\sigma^{(1)}|\psi_r\rangle\langle\psi_r|D_\rho^{(1)}}{hc(\bar{\nu}_r + \bar{\nu}_s)} \right] \tag{49}$$

where ψ_r is a vibronic state [63] with opposite-parity to the f^N states ψ_i and ψ_f, usually taken from the $4f^{N-1}5d$ and $4f^{N-1}5g$ configurations. The Cartesian tensor is expressed as a linear combination of spherical tensors, which in turn may be expressed in terms of unit tensors and scattering parameters [91]. By invoking the Judd closure approximation in the Judd-Ofelt-Axe formalism, the relative electronic Raman scattering intensities can be expressed in terms of just two parameters, F_1 and F_2, which are further inter-related if the intensity is entirely contributed by the $4f^{N-1}5d$ configuration. Based upon this simple model, the relative intensities of electronic Raman bands were calculated for various $Cs_2NaLnCl_6$ systems (Ln=Ce, Pr, Eu, Er, Tm and Yb). The observed and calculated relative intensities for Ln=Ce are shown in Table 6 and are reasonably well-fitted by the two parameters. The experimental values are from integrated band intensities using polycrystalline ma-

terial, so that the calculated intensities are averaged over all polarizations. For some other Ln^{3+} elpasolite systems, the electronic Raman band relative intensities were considerably over-estimated, and this was attributed to the matching of the energy gap between the upper level ψ_f and the next lower f^N level with (multiple) quanta of phonons of the appropriate symmetry [91]. Fast multiphonon relaxation can then occur which shortens the excited state lifetime.

Other features of interest in the electronic Raman spectra of these systems [91] are the occurrence of an excited-state electronic Raman transition in $Cs_2NaTmCl_6$ when the excited state is thermally populated; and of *D*-term [63] resonance electronic Raman scattering.

The validity of the Judd closure approximation, where an entire configuration degeneracy is taken, with an effective energy barycentre, is more stringently tested in the electronic Raman calculations than in the conventional electric dipole intensity calculations because only two variable parameters are employed. However, the use of this approximation serves as a 'black box' approach and does not give insight into the intensity mechanisms of electronic Raman transitions. The direct calculation, presented first for $TmPO_4$ by Xia [204], utilizes the detailed energy eigenvectors and eigenvalues of intermediate CF states, and the results for the electronic Raman relative intensities of Ce^{3+} are somewhat improved from the JOA calculation [203] (Table 6). However, the performance of the direct calculation suffers from the problem that the opposite parity intermediate states have not yet been well-characterized for Ln^{3+} systems. A strategy has therefore been employed in which, for example for Pr^{3+} in $Cs_2NaPrCl_6$ [205], the direct products of the CF $4f^1$ core states and $5d^1$ CF states are employed, but the electrostatic interaction between the $4f^1$ core and the $5d^1$ electron is neglected. The appropriate energies may be estimated from the CF levels of Ce^{3+} in $Cs_2NaCeCl_6$. Some serious discrepancies between experimental and calculated intensities remain when using this approach [205], which are more likely to be due to the inaccurate wave functions employed for the $4f^15d^1$ intermediate states, rather than to the failure to include states from $4f^15g^1$. Neglecting the latter configuration, then for the electronic Raman transitions from the $^3H_4\Gamma_{1g}$ electronic ground state of Pr^{3+}, it follows from the consideration of the selection rule for the ED allowed transition to the intermediate state Γ_r (i.e. $\Gamma_{1g}\times\Gamma_{4u}\times\Gamma_r$ contains Γ_{1g}) that the r is one or more of the 18 Γ_{4u} $4f^15d^1$ CF states. A detailed energy level calculation of the $4f^15d^1$ configuration which includes electrostatic interactions [206] shows that the large CF leads to more extensive mixing of *SLJ* states than is the case for the $4f^2$ configuration [207]. However, when utilizing these more accurate intermediate state wave functions for some transitions, specific intensity sources can be pinpointed for certain electronic Raman transitions [208].

9
Electron-phonon Mixing of States

Chodos [103] said that the electron-phonon interaction can be thought of as the changing crystalline field due to the neighbouring nuclear vibrations. Thus, Henderson and Imbusch [116] write the electron-phonon interaction as the first term in the power series the crystal strain, and show how it modifies a $4f^N$ electron wavefunction by introducing opposite-parity ones. Actually, the electron-phonon coupling takes part in many phenomena, including the shapes and widths of spectral lines, and relaxation rates, in addition to vibronic sidebands. However, the vibronic coupling between the lanthanide ion and the lattice is generally weak [116].

Malta [167] has described the case when a vibronic state is in resonance with a pure electronic state, and it was found that depending upon the strength of the vibronic interaction, the admixture between these levels can lead to nearly equal spectral intensities. In fact this phenomenon was observed previously in the $^3P_0(\Gamma_1) \rightarrow {}^3F_2$ luminescence spectra of $PrCl_6^{3-}$ [147], where an apparent doubling of features occurred. It is also responsible for the anomalous behaviour in the Raman spectrum of $Cs_2NaYbCl_6$ [91]. We consider here only the $Cs_2NaTmCl_6$ system, where it has contributed to the disputed assignments of the $^3H_6$ ground term of Tm^{3+} in $TmCl_6^{3-}$, so that the experimental and calculated energy level schemes were apparently in disagreement [209–213].

The experimentally measured $^3H_6$ energy levels are located (in cm^{-1}) at 0, 56, 108, 148, 261, 370 and 394 (Fig. 14a) from the low temperature $TmCl_6^{3-}$ luminescence spectra of transitions terminating upon the electronic ground state. The two energy levels (measured at 10 K at 108 and 148 cm^{-1}) are in fact derived from the resonance of the $^3H_6 a\Gamma_5$ (T_{2g}) CF level, through electron-phonon coupling with the vibronic level $^3H_6\Gamma_1+\nu_5(\tau_{2g})$. This resonance can be turned on or off by the action of heat [91] or pressure [214]. At room temperature, the energy of ν_5 is 132 cm^{-1}. At 120 K, the band in the Ar^+ ion laser excited Raman spectrum at 128 cm^{-1} develops a high energy shoulder at 144 cm^{-1} [91], and on further cooling these features become more widely separated and clearly resolved. The simplest model of the interaction of the $a\Gamma_5$ electronic and $\Gamma_1+\nu_5$ vibronic states utilizes first order perturbation theory (a more accurate theoretical treatment of these phenomena is given in [215]) and the corrected electronic energy at 10 K is shown at 123 cm^{-1} in Fig. 14a, with the experimental energies as dotted lines. The interaction matrix element is some tens of cm^{-1} [91]. This interaction has also been probed by the use of high pressure at ambient temperature [214], but in this case only one band is observed—for example, at 2.7 GPa, the blue-shifted $\Gamma_1+\nu_5(\tau_{2g})$ coupled mode is at 143 cm^{-1}. The lower-energy coupled mode, mainly of electronic character, is line-broadened at room temperature and not resolved from the background. Figure 14b shows the shifts to high ener-

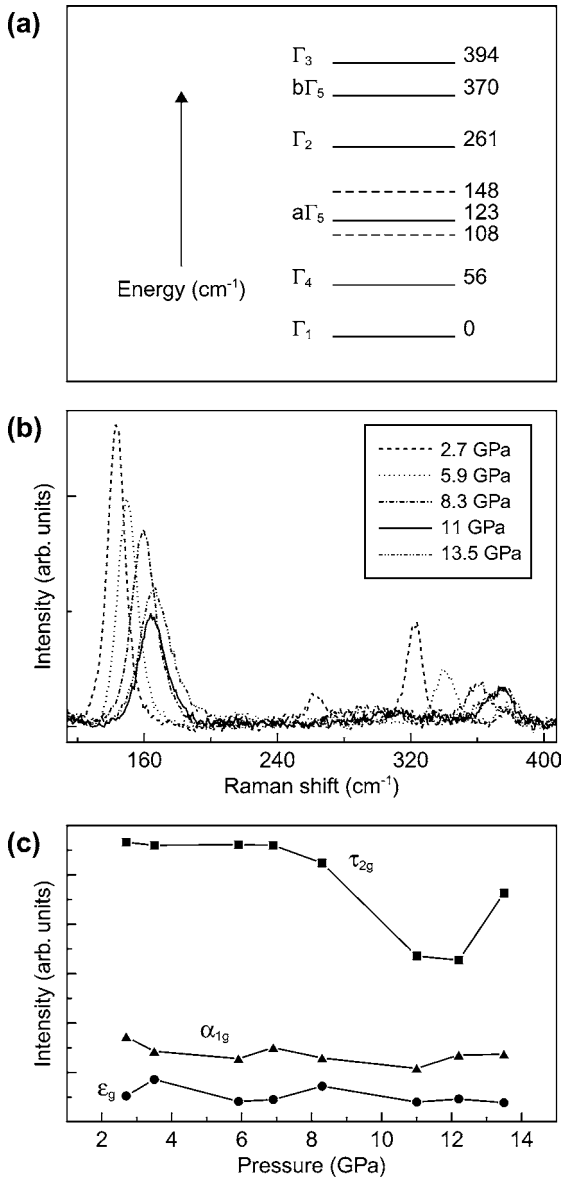

Fig. 14a–c Electron-phonon coupling in $Cs_2NaTmCl_6$: **a** energy levels of Tm^{3+} at 10 K (see Sect. 9); **b** 295 K Raman spectra at stated pressures; **c** integrated areas of moiety mode Raman bands as a function of pressure. (Adapted from [214])

gy of the three Raman-active moiety modes of $TmCl_6^{3-}$ as the pressure is increased. The integrated areas of the bands at different pressures are plotted in Fig. 14c, and the band areas of the $\nu_2(\epsilon_g)$ and $\nu_1(\alpha_{1g})$ modes do not show a noticeable change. The area of the coupled $\Gamma_1+\nu_5(\tau_{2g})$ mode decreases at 11–

12 GPa, but then increases at 13 GPa. This has been attributed to a redistribution of intensity between the resonant vibronic and electronic states when the electron-phonon coupling is greater (between 11–12 GPa), followed by the commencement of decoupling of the electronic and vibronic states, at 13 GPa. A further example of the resonance between pure electronic and vibronic states has been found for the $^3H_4\Gamma_4$ CF level of this system, which couples with $^3H_4\Gamma_5+\nu_2(\epsilon_g)$ [213].

Further examples of the coupling of vibronic states involving gerade moiety modes with CF states have been found in studies of the TP spectra of $Cs_2NaTbCl_6$ [216].

10 One and Two Colour Two-photon $4f^N$-$4f^N$ Spectra

The CF energy levels of some M_2ALnX_6 systems become congested above ~20,000 cm^{-1}, so that the overlapping of electronic and vibronic transitions in the ultraviolet absorption spectrum makes assignments ambiguous in many cases. The use of TP excitation in several cases, using spectral regions where one-photon excitation corresponds to an open window, has enabled detailed energy level datasets to be assigned. The assignments are especially clarified by the use of single crystals with plane-polarized radiation and applied magnetic fields.

TP transitions within a $4f^N$ configuration involve intermediate states belonging to opposite parity configurations, such as $4f^{N-1}5d$, $4f^{N+1}4d^9$, $4f^{N-1}5g$ configurations, etc., but usually only the first of these is considered because it lies at a much lower energy than any other opposite parity configuration.

In general for two-colour TP transitions, where $hc\bar{\nu}_1$ and $hc\bar{\nu}_2$ are the photon energies, with cartesian polarizations ρ and σ, the relevant second- (i.e. the lowest), third- and fourth-order terms for the transition elements M_{if} between the ground state and the final state are as follows respectively [217–220]:

$$-\sum_n \left[\frac{\langle \psi_f | D_\rho^{(1)} | \psi_n \rangle \langle \psi_n | D_\sigma^{(1)} | \psi_i \rangle}{hc(\bar{\nu}_n - \bar{\nu}_2)} + \frac{\langle \psi_f | D_\sigma^{(1)} | \psi_n \rangle \langle \psi_n | D_\rho^{(1)} | \psi_i \rangle}{hc(\bar{\nu}_n - \bar{\nu}_1)} \right] \tag{50}$$

$$\sum_{m,n} \left[\frac{\langle \psi_f | D_\rho^{(1)} | \psi_m \rangle \langle \psi_m | V' | \psi_n \rangle \langle \psi_n | D_\sigma^{(1)} | \psi_i \rangle}{(hc)^2 (\bar{\nu}_m - \bar{\nu}_2)(\bar{\nu}_n - \bar{\nu}_2)} + \frac{\langle \psi_f | D_\sigma^{(1)} | \psi_m \rangle \langle \psi_m | V' | \psi_n \rangle \langle \psi_n | D_\rho^{(1)} | \psi_i \rangle}{(hc)^2 (\bar{\nu}_m - \bar{\nu}_1)(\bar{\nu}_n - \bar{\nu}_1)} \right] \tag{51}$$

$$-\sum_{l,m,n}\left[\begin{array}{l}\dfrac{\langle\psi_f|\mathrm{D}^{(1)}_{\rho}|\psi_l\rangle\langle\psi_l|\mathrm{V}''|\psi_m\rangle\langle\psi_m|\mathrm{V}'|\psi_n\rangle\langle\psi_n|\mathrm{D}^{(1)}_{\sigma}|\psi_i\rangle}{(hc)^3(\bar{\nu}_l-\bar{\nu}_2)(\bar{\nu}_m-\bar{\nu}_2)(\bar{\nu}_n-\bar{\nu}_2)}\\ +\dfrac{\langle\psi_f|\mathrm{D}^{(1)}_{\sigma}|\psi_l\rangle\langle\psi_l|\mathrm{V}''|\psi_m\rangle\langle\psi_m|\mathrm{V}'|\psi_n\rangle\langle\psi_n|\mathrm{D}^{(1)}_{\rho}|\psi_i\rangle}{(hc)^3(\bar{\nu}_l-\bar{\nu}_1)(\bar{\nu}_m-\bar{\nu}_1)(\bar{\nu}_n-\bar{\nu}_1)}\\ +\dfrac{\langle\psi_f|\mathrm{D}^{(1)}_{\rho}|\psi_l\rangle\langle\psi_l|\mathrm{V}'|\psi_m\rangle\langle\psi_m|\mathrm{V}''|\psi_n\rangle\langle\psi_n|\mathrm{D}^{(1)}_{\sigma}|\psi_i\rangle}{(hc)^3(\bar{\nu}_l-\bar{\nu}_2)(\bar{\nu}_m-\bar{\nu}_2)(\bar{\nu}_n-\bar{\nu}_2)}\\ \dfrac{\langle\psi_f|\mathrm{D}^{(1)}_{\sigma}|\psi_l\rangle\langle\psi_l|\mathrm{V}'|\psi_m\rangle\langle\psi_m|\mathrm{V}''|\psi_n\rangle\langle\psi_n|\mathrm{D}^{(1)}_{\rho}|\psi_i\rangle}{(hc)^3(\bar{\nu}_l-\bar{\nu}_1)(\bar{\nu}_m-\bar{\nu}_1)(\bar{\nu}_n-\bar{\nu}_1)}\end{array}\right] \tag{52}$$

In these expressions, $|\psi_i\rangle(i=l,m,n)$ refer to intermediate states within the $4f^{N-1}5d$ configuration; and $hc\bar{\nu}_i$ (i=l, m, n) are the energies of these states above the ground state energy; V′ and V″ can be the spin-orbit or the CF operator, acting between intermediate states.

The mechanism of the TP transition, which is principally a second-order process, involves an ED transition from the initial state to an intermediate state (with or without resonance), and thence another from the intermediate state to the final state [221]. However, the states and energies in Eqs. (50)–(52) are only eigenstates and eigenvalues of the zero-order Hamiltonian H_0 in a stationary perturbation treatment, in which the complete Hamiltonian is

$$\mathrm{H}=\mathrm{H}_0+\mathrm{V}'+\mathrm{V}''+\ldots \tag{53}$$

where H_0 includes the central field Hamiltonian and the Coulomb interaction between the 4f electrons, V=V′+V″+... is the perturbation Hamiltonian which includes the spin-orbit and CF interactions, and the electrostatic interaction between the (N−1) 4f electrons and the 5d electron which is often ignored. The Judd-Pooler [218] type perturbation calculation (50, 51) and Judd-Pooler-Downer [220] type perturbation calculation (50–52), both use eigenstates of the zeroth-order Hamiltonian H_0 within the $4f^{N-1}5d$ configuration, but the relevant energies $hc\bar{\nu}_i$ (i=m, l...) are approximately taken to be degenerate, somehow like using the closure approximation. By contrast, in the direct calculation, the intermediate eigenstates $|\phi_N\rangle$ and eigenvalues $hc\bar{\nu}_N$ of the complete Hamiltonian, H, are used within the $4f^{N-1}5d$ configuration, as well as within the $4f^N$ configuration, and only the second-order expression (obtained from Eq. 50 by changing $|\psi_n\rangle$ and $hc\bar{\nu}_n$ to be $|\phi_N\rangle$ and $hc\bar{\nu}_N$, respectively) needs to be evaluated.

The *SLJ* selection rules for the second-order Axe process are listed in Table 1. Note that by the contraction of the expression at Eq. (50) using Judd closure, the transitions of the type $\Gamma_{1g}\rightarrow\Gamma_{1g}$ become forbidden. Inclusion of the CF operator in the third-order expression [V′=H_{CF}, (Eq. 51)] widens the *SLJ* selection rule to ΔS=0; $|\Delta J|\leq 6$; $|\Delta L|\leq 6$, whereas for V′=H_{SO} in (51), ΔS=1; $|\Delta J|\leq 2$; $|\Delta L|\leq 3$. The 4th-order expression at Eq. (52) leads to the selection rules ΔS=1; $|\Delta J|\leq 6$; $|\Delta L|\leq 6$.

Thus far, the experimental investigations of TP spectra of $\mathrm{M_2ALnX_6}$ have utilized the more sensitive technique of excitation spectra rather than ab-

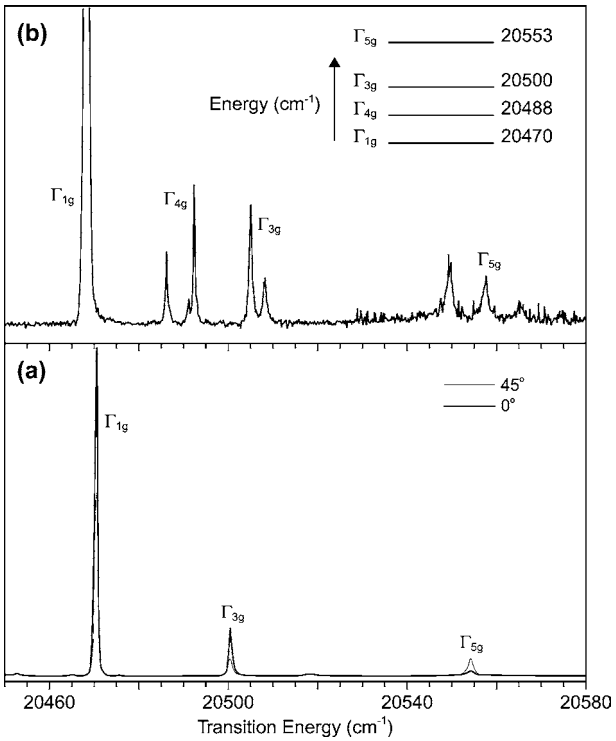

Fig. 15a, b Two-photon excitation spectra of a single crystal of $Cs_2NaTbCl_6$ at ca. 6 K: **a** in two linear polarizations making the angle indicated to [100]; **b** in the presence of a 4.5 T field along [110]. The *inset* shows the $^5D_4$ energy level scheme of Tb^{3+} in this system. (Adapted from [223])

sorption spectra, and have used one colour. Nevertheless, unlike the one-photon spectra of these cubic systems, studies employing TP excitation can distinguish the symmetry of the terminal state in a particular transition. In the case of a nondegenerate Γ_{1g} electronic ground state, transitions are allowed to Γ_{1g}, Γ_{3g} and Γ_{5g} terminal states for one-colour TP excitation (Table 1), with additional transitions to Γ_{4g} excited states for the two-colour case [221, 222]. Using one-colour radiation along the *z* axis, linearly polarized along the *x* axis, $\Gamma_{1g} \rightarrow \Gamma_{1g}$ transitions do not show a polarization dependence; $\Gamma_{1g} \rightarrow \Gamma_{5g}$ transitions are forbidden, and $\Gamma_{1g} \rightarrow \Gamma_{3g}$ transitions exhibit maximum intensity. With *xy* polarized radiation, the intensity of $\Gamma_{1g} \rightarrow \Gamma_{5g}$ is at a maximum, whereas that of $\Gamma_{1g} \rightarrow \Gamma_{3g}$ transitions decreases by a factor of four. Figure 15a shows the experimental polarization dependence of the $(^7F_6)\Gamma_{1g} \rightarrow (^5D_4)\Gamma_{1g}$, Γ_{3g}, Γ_{5g} one-colour TP transitions of Tb^{3+} in $Cs_2NaTbCl_6$ [223]. Although $\Gamma_{1g} \rightarrow \Gamma_{2g}$ transitions are forbidden, the hot transitions such as those from Γ_{4g} initial states of the ground multiplet term to Γ_{2g} states are

allowed, and in variable temperature studies the relevant states can be populated. Figure 15b shows that the application of a magnetic field can confirm the degeneracy of excited states (first order Zeeman effect) and introduce intensity into transitions that are forbidden in the absence of the magnetic field (second order Zeeman effect) [221]. For even-electron systems, first-order Zeeman splittings only occur in Γ_4 and Γ_5 states. The second-order effect is sensitive to the orientation of the crystal axes relative to the magnetic field direction [224]. When second-order interactions are small, experimental g-values can be used to distinguish between states of the same symmetry [224].

From Fig. 15 it is evident that the TP spectra of M_2ALnX_6 consist of a few sharp lines, due to transitions between CF states, which are uncluttered by vibronic structure. This situation is distinct from, and complementary to, one-photon studies. Sztucki [225, 226] has presented a theory of TP vibronic transitions and anticipated the observation of some weak lines in TP spectra induced by even-parity vibrations in the case of ED-ED TP absorption, and odd-parity vibrations for ED-MD TP transitions. The observation of the former is clear from the studies of Denning et al. [212, 216, 227–230], but the observation of the latter is less certain [231]. Certainly, the appearance of vibronic structure can complicate the assignments of spectral features in TP spectra, especially when resonances occur between vibronic and pure electronic levels, as discussed in the previous section [216]. When polarization or Zeeman studies cannot be performed, it may be difficult to assign the bands in TP spectra because they lack the confirmatory vibronic fingerprints of one-photon spectra. Furthermore, since the excitation spectral technique is utilized, absorption by an impurity ion might occur and subsequently lead to emission in the (broad) spectral range being monitored. In fact, the impurity ion might otherwise transfer the excitation to the majority species by ET. Alternatively, ESA might occur at the pump energy. Such problems have been encountered in the TP excitation spectra of Cs_2NaYCl_6:Sm^{3+} [229], $Cs_2NaTbCl_6$ [216] and Cs_2NaYCl_6:Tm^{3+} [212], where some spectral features are unexplained.

The first studies of the TP spectra of M_2ALnX_6 systems were carried out on neat $Cs_2NaGdCl_6$, since the energy level scheme of the f^7 ion Gd^{3+} has a transparent window up to almost 32000 cm^{-1} [232–234]. This was followed by more extensive studies of Cs_2NaTbX_6 (X=F, Cl, Br) [216, 223, 227, 230], $Cs_2NaEuCl_6$ and Cs_2NaYF_6:Eu^{3+} [228], Cs_2NaYCl_6:Sm^{3+} [229] and Cs_2NaYCl_6:Tm^{3+} [212] by Denning's group.

The theoretical calculation of TP intensities has been called unreliable [224], but semiquantitative agreement with experiment has recently been achieved. A particular difficulty was experienced with $\Gamma_1 \rightarrow \Gamma_1$ transitions since the calculated intensity is zero under second-order treatments. Ceulemans and Vandenberghe [71, 235, 236] considered the third and fourth-order analyses of TP transitions in cubic lattices, and utilized a fourth-order

scheme incorporating spin-orbit coupling and CF interactions to analyse the $^7F_6 \rightarrow {}^5D_4$ transition of Tb^{3+} in $Cs_2NaTbCl_6$. Subsequently it was proposed from a direct calculation that the $(^7F_6)\Gamma_1 \rightarrow (^5D_4)\Gamma_1$ TP transition is actually a third-order rather than a fourth-order process [237], and the calculated line strength was found to be sensitive to the location of the intermediate levels. Reid et al. [238] have previously demonstrated the equivalence of direct and Judd-Pooler -type perturbation calculations for calculating TP transition intensities, provided that the appropriate eigenstates and eigenvalues are employed. In the direct calculation of the $^7F_6 \rightarrow {}^5D_4$ transition intensity [237] the pure Russell-Saunders multiplets for the initial and terminal state wavefunctions were employed (thereby neglecting the *SL*- and *J*- admixtures), and only the lowest-energy intermediate states of $4f^7 5d^1$ were considered. Ligand-metal couplings were not included [239, 240]. More recently, a second-order direct calculation of 18 TP transitions of Tb^{3+} in $Cs_2NaTbCl_6$ has been performed, and closer agreement with experiment was obtained for the intensity of the $\Gamma_{1g} \rightarrow \Gamma_{1g}$ TP transition, because CF wavefunctions were used for the $4f^8$ states, and rather exact wavefunctions for $4f^7 5d$ states [241]. The wavefunctions of the initial and final states of the $4f^8$ system were expressed in terms of Russell-Saunders coupled wavefunctions, with one f-electron coupled to the $4f^7$ core. For the $4f^7 5d$ intermediate configuration, the free ion and CF wavefunctions of $4f^7$ (Gd^{3+}) were employed, and combined with the CF wavefunctions of the excited $5d^1$ configuration of Ce^{3+}, to give direct product type intermediate state wavefunctions. This treatment neglects the electrostatic interaction between the $4f^7$ core and the 5d-electron. The results of this calculation for the $^7F_6 \rightarrow {}^5D_4$ transition are shown in Table 7, which compares the calculated transition linestrengths for two polarizations with the experimental values. It is observed that a considerable difference exists for the calculations using free ion and CF wavefunctions for the $4f^7$ core configuration, with the latter giving better agreement.

In previous calculations [235, 237] only the $^7F_6 \rightarrow {}^5D_4$ transition channel was considered, but other wavefunctions are admixed (to small extents) into $^7F_6$ and $^5D_4$, so that *other* channels $^7F_6 \rightarrow {}^7F_4$, $^5F_4$, $^3F_4$; $^5G_6 \rightarrow {}^5D_4$, $^7F_4$, $^5F_4$, $^3F_4$; and $^7F_4 \rightarrow {}^5D_4$, $^7F_4$, $^5F_4$, $^3F_4$ may contribute to the intensity. In fact, the dominant contributions are found to be $^7F_4 \rightarrow {}^7F_4$ and $^7F_6 \rightarrow {}^7F_4$, and *not* the nominal $^7F_6 \rightarrow {}^5D_4$. As mentioned above for the vibronic intensity calculations, the accuracy of the wavefunctions and energies employed is the key factor in obtaining agreement between theory and calculation.

The direct calculation method has also been applied to the calculation of transition linestrengths and intensity ratios of the $(^7F_0)\Gamma_{1g} \rightarrow (^5D_2)\Gamma_{3g}$, Γ_{5g} and $(^7F_0)\Gamma_{1g} \rightarrow (^5L_6)\Gamma_{1g}$, $a\Gamma_{5g}$ TP transitions of Eu^{3+} in the cubic Cs_2NaYF_6 host [70, 243]. The calculated relative intensities for the former transition were in reasonable agreement with experiment and the neglect of *J*-mixing in the initial state only had a minor effect. However, the neglect of spin-orbit

Table 7 Calculated and experimental two-photon transition intensities for the $^7F_6 \rightarrow {}^5D_4$ transition of Tb^{3+} in $Cs_2NaTbCl_6$ (from [241])

$^5D_4$ final state[a]	Energy (cm^{-1})	Calculated (relative) transition linestrength[b]				Observed intensities for incident radiation propagating along [100]		
		Using free-ion wavefunctions for $4f^7$ configuration		Using CF wave-functions for $4f^7$ configuration		Relative[c]		Polarization orientation averaged, corrected for depolarization[d]
		θ=0°	θ=45°	θ=0°	θ=45°	θ=0°	θ=45°	Absolute ($\times 10^5$)
Γ_{1g}	20,470	60(11.0)	60(11.0)	77(11.0)	77(11.00)	11.0	11.0	11.0
Γ_{3g}	20,500	2.89(0.53)	0.73(0.13)	77(11.0)	20(2.86)	1.87	1.10	2.1
Γ_{5g}	20,553	0(0.0)	26(4.77)	0(0.0)	8(1.14)	0.33	0.99	1.5

[a] The initial state is $(^7F_6)\Gamma_{1g}$ in all cases

[b] In units of $(10^{-14}\ cm^2\langle 4f|r|5d\rangle^4/h^2c^2)$. θ is the angle that the radiation electric vector makes with [001]

[c] Measured by integration of the hard copy spectra in [242]. These results are semi-quantitative

[d] Intensities tabulated in [242]

couplings within the initial and terminal states drastically reduced the transition linestrengths, but did not significantly change the transition intensity ratios. In the case of the latter $(^7F_0)\Gamma_{1g} \rightarrow (^5L_6)\Gamma_{1g}$, $a\Gamma_{5g}$ TP transitions, it is necessary to use intermediate states built from $5d^1$ CF states and $4f^5$ core CF (rather than free ion) states in order to obtain satisfactory agreement with experiment.

11
$4f^N$-$4f^{N-1}5d$ Electronic Spectra

In contrast to intraconfigurational f^N-f^N transitions of Ln^{3+}, the interconfigurational f^N-$f^{N-1}d$ electronic transitions are ED allowed in the first order, with the selection rules given in Table 1. There have been relatively few reports of the f-d electronic spectra of Ln^{3+} although the characterization of $4f^{N-1}5d^1$ states, in terms of eigenvalues and eigenvectors is essential for accurate calculations of vibronic, electronic Raman scattering and TP transition intensities. Following earlier studies of the absorption spectra of lanthanide hexahalides [244, 245], Ionova et al. [246] systematized the energies of f-d and charge transfer transitions of LnX_6^{3-} species, with the lowest energies (determined from broad spectral bands of these species in solution at ambient temperatures) for the transitions of $LnCl_6^{3-}$ being shown in Fig. 16.

Theoretical developments [250], the requirements for vacuum ultraviolet phosphors, the search for blue and ultraviolet solid-state lasers, coupled with improvements in the construction of vacuum ultraviolet spectrometers [251] and the easier access to synchrotron radiation, have led to a recent upsurge of interest in $4f^N$-$4f^{N-1}5d^1$ spectra of rare earths. Just as in the case of $4f^N$-$4f^N$ spectra [207], the $4f^N$-$4f^{N-1}5d^1$ spectra of lanthanide ions in octahedral symmetry environments comprise much more detailed structure than in the case of low symmetry systems.

The elpasolite system which has received the most attention is Ce^{3+}, and the results of this simplest $5d^1$ system are now reviewed. Unlike the 4f configuration, the 5d configuration experiences a CF interaction that is considerably larger than the 5d spin-orbit coupling. In octahedral (O_h) symmetry, the CF splits the $5d^1$ configuration into two levels, a triply degenerate $T_{2g}(\Gamma_{5g})$ lower state and a doubly degenerate $E_g(\Gamma_{3g})$ upper state. With the inclusion of the spin-orbit interaction, the splitting of the T_{2g} and E_g states is as shown in Fig. 17. Schwartz and Schatz [252] reported the absorption and MCD spectra of octahedral Ce^{3+} (in the Cs_2NaYCl_6 host) at 6 K. Two electronic transitions were observed in the region between 28,150 to 31,000 cm^{-1}, assigned, in order of increasing energy, to $(^2F_{5/2})\Gamma_{7u} \rightarrow \Gamma_{8g}(^2T_{2g})$ and $(^2F_{5/2})\Gamma_{7u} \rightarrow \Gamma_{7g}(^2T_{2g})$. The transition to the $5d^1(^2E_g)$ state was not detected up to 50,000 cm^{-1}, so that $\Delta = 10Dq \geq 20{,}000$ cm^{-1}. van't Spijker et al. [253] did not comment upon these results in their more recent study of Ce^{3+}-

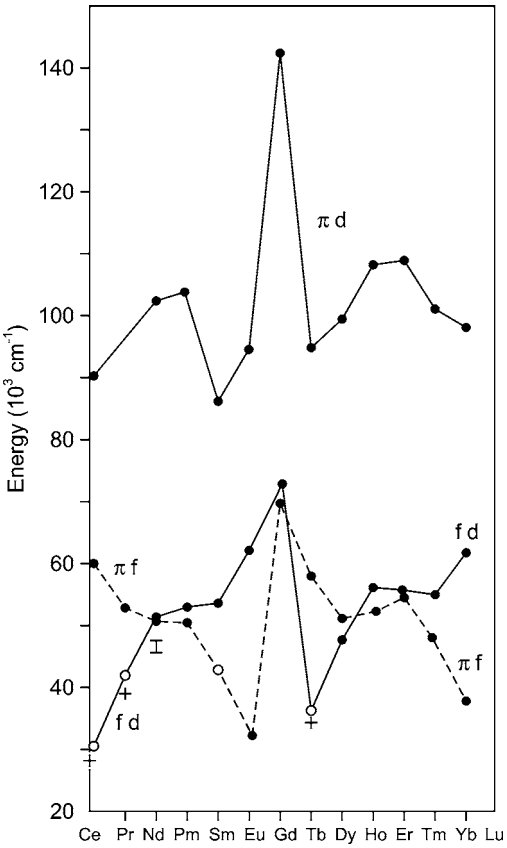

Fig. 16 Lowest f-d, charge transfer π-f and π-d transition energies of $LnCl_6^{3-}$ (Adapted from [246]). The *crosses* for Ce, Pr, Nd and Tb represent the lowest $4f^{N-1}5d$ electronic state in the crystalline elpasolite lattices. (Data from [206, 247–249])

doped elpasolites using room-temperature X-ray excitation, where two room-temperature bands at 48,780 cm^{-1} and 46,512 cm^{-1} in $Cs_2NaLuCl_6:Ce^{3+}$ were assigned to absorption to the $5d^1(^2E_g)$ state. Features were reported at similar energies in $Cs_2NaLnCl_6:Ce^{3+}$ (Ln=Gd, Y) [254]. Since the state ^2E_g transforms as a Kramer's quartet, Γ_{8g}, in O_h symmetry, these bands presumably correspond to the unresolved electronic transitions from the ground $^2F_{7/2}$ and excited $^2F_{5/2}$ terms. Otherwise one of the bands does not correspond to single Ce^{3+} ions in octahedral symmetry. The assignment of higher energy structure, and of features in the synchrotron excitation spectra of $Cs_2LiLnCl_6$ (Ln=Y, La) [255–257] is not clear. Broad features have been observed in the absorption and emission spectra of Ce^{3+} doped into hexafluoroelpasolites [258, 259], attributed to the presence of several Ce^{3+} sites.

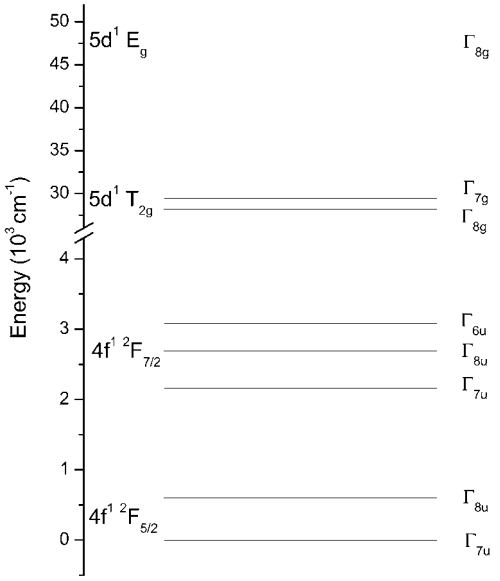

Fig. 17 Energy levels of Ce^{3+} in a $Cs_2NaLnCl_6$ host crystal (Adapted from [248])

Recently, Laroche et al. [260] have obtained the $4f^{N-1}5d^1 \rightarrow 4f^N$ emission spectra of Cs_2NaYCl_6:Ce^{3+} and Pr^{3+} at 77 K by pumping the $^3H_4 \rightarrow {}^3P_0$ f^2-electron absorption bands of Pr^{3+}. The absorption and $(^2T_{2g})\Gamma_{8g}$ emission spectra at 10 K have recently been reported [248] and are shown in Fig. 18a. The electronic origin is coincident in both spectra, but is strongly self-absorbed in the emission spectrum. The lack of mirror-image symmetry between absorption and emission is due to the presence of further transitions, as marked, in emission and absorption. The spectra differ considerably from the $4f^N$-$4f^N$ spectra of M_2ALnCl_6 and each transition consists of two strong vibrational progressions (see Sect. 7.3), which in the absence of Jahn-Teller effects, from Table 1 must correspond to totally symmetric modes. The first progression is in the ν_1(Ln-Cl) breathing mode (299±2 cm^{-1}). The second is in a mode of energy 48±2 cm^{-1}, and comparison with the f-d spectra of other systems shows that the energy does not change greatly in the spectra of $Cs_2NaTbCl_6$, Cs_2NaYCl_6:U^{3+} or Cs_2LiYCl_6:Ce^{3+}. This energy is similar to that of the $S_5(\tau_{2g})$ mode, so that the motion is mainly of the second shell $LnCs_8$.

The bond length change in the f-d excitation process can be calculated for the Ln-Cl and Ln-Cs coordinates by application of Eqs. (27) and (28). It is not clear whether or not to subtract the broad underlying continuum when integrating spectral features (e.g. in Fig. 18a, the maximum for the $n\nu_1$ replicas on the zero phonon line is at n=1, but the peak intensity of the groups of bands is at n=2). With subtraction of the continuous background from the spectrum, the bond length change along the Ce-Cl coordinate from

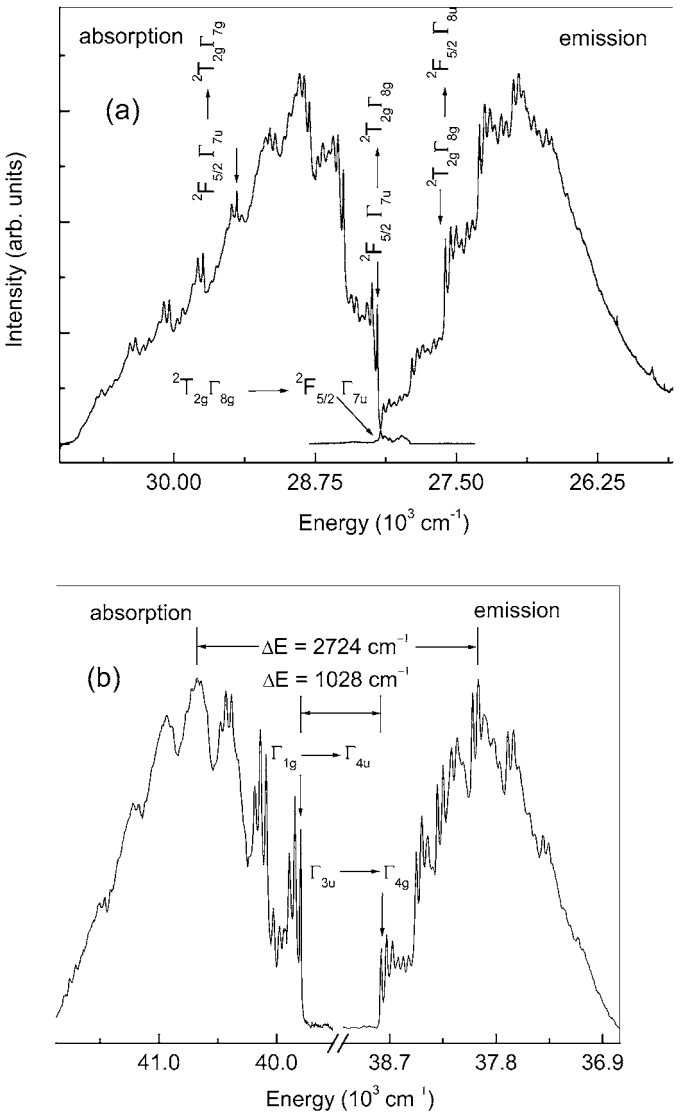

Fig. 18a, b 10 K f-d absorption and emission spectra of Cs_2NaYCl_6 doped with: **a** Ce^{3+}; **b** Pr^{3+}. Refer to Fig. 17 for the identification of the Ce^{3+} transitions. Only the lowest energy absorption and highest energy emission transitions are marked for Pr^{3+}. (Adapted from [206, 248])

the f-electron ground state to the 5d-electron $^2T_{2g}$ state is calculated to be 0.06 Å, which is <2% of the bond distance. An ab initio calculation based upon the $CeCl_6^{3-}$ cluster [248] gives a similar value, 0.05 Å, and it predicts a bond length contraction in the $^2T_{2g}$ state.

Table 8 Energy level calculations for Pr^{3+} in the $Cs_2NaPrCl_6$ elpasolite lattice [207]

N	*SLJ*	Irrep	Energy (cm^{-1})		
			Expt	Calculated	
				$4f^2$	$4f^2/4f6p$
1	$^3H_4$	Γ_1	0	38	8
2	$^3H_4$	Γ_4	242	257	247
3	$^3H_4$	Γ_3	422	408	411
4	$^3H_4$	Γ_5	702	683	721
5	$^3H_5$	aΓ_4	2300	2310	2297
6	$^3H_5$	Γ_5	2399	2413	2395
7	$^3H_5$	Γ_3	2645	2625	2650
8	$^3H_5$	bΓ_4	2763	2718	2750
9	$^3H_6$	Γ_3	4386	4406	4373
10	$^3H_6$	aΓ_5	4437	4456	4429
12	$^3H_6$	Γ_2	4591	4643	4616
13	$^3H_6$	bΓ_5	4807	4798	4809
14	$^3H_6$	Γ_4	4881	4867	4887
11	$^3H_6$	Γ_1	4942	4897	4922
15	$^3F_2$	Γ_3	5203	5224	5195
16	$^3F_2$	Γ_5	5297	5282	5305
17	$^3F_3$	Γ_4	6616	6634	6605
18	$^3F_3$	Γ_5	6621	6628	6621
19	$^3F_3$	Γ_2	6682	6686	6703
22	$^3F_4$	Γ_1	6902	6913	6909
20	$^3F_4$	Γ_3	6965	6994	6982
21	$^3F_4$	Γ_4	7012	6967	6979
23	$^3F_4$	Γ_5	7278	7260	7265
24	$^1G_4$	Γ_1	9847	9766	9841
25	$^1G_4$	Γ_4	9895	9852	9897
26	$^1G_4$	Γ_3	9910	9901	9921
27	$^1G_4$	Γ_5	10,327	10,441	10,328
28	$^1D_2$	Γ_5	16,666	16,705	16,670
29	$^1D_2$	Γ_3	17,254	17,209	17,248
30	$^3P_0$	Γ_1	20,625	20,611	20,611
31	$^1I_6$	Γ_1	21,166	21,163	21,169
32	$^3P_1$	Γ_4	21,218	21,225	21,218
33	$^1I_6$	Γ_4	21,255	21,263	21,254
34	$^1I_6$	aΓ_5	(21,343[a])	21,380	21,360
35	$^1I_6$	Γ_2	21,788	21,793	21,777
36	$^1I_6$	bΓ_5	21,967	21,971	21,975
37	$^1I_6$	Γ_3	22,035	22,024	22,032
38	$^3P_2$	Γ_5	22,367	22,387	22,375
39	$^3P_2$	Γ_3	22,494	22,491	22,500
40	$^1S_0$	Γ_1	(>39,017[a])	45,759	44,880

[a] From Cs_2NaYCl_6:Pr^{3+}

It is interesting that the emission from the $5d^1\ ^2E_g$ state of Ce^{3+} (Fig. 17) has never been reported, and was not observed (near 47,000 cm^{-1}) upon ultraviolet excitation of Cs_2NaYCl_6:Ce^{3+} [248]. However, a group of bands was observed in (neat) $Cs_2NaErCl_6$ which has been assigned to the $^2E_g \rightarrow {}^2F_{5/2}$, $^2F_{7/2}$ transitions of Ce^{3+} impurity [248]. One possibility [248] is that the emission is quenched by transfer to killer sites (such as by transfer to $f^{N-1}d$ electronic states of Nd^{3+} or Pr^{3+} ions) in Cs_2NaYCl_6, which are not as numerous in $Cs_2NaErCl_6$. Otherwise, it could be that the excited Ce^{3+} ion is oxidized to Ce^{4+} by transfer of an electron to the host conduction band. Presumably this does not occur for the trace concentration of Ce^{3+} present in the $Cs_2NaErCl_6$ host.

In contrast to Ce^{3+}, the first bands in the 10 K f-d emission and absorption spectra of Pr^{3+} [206] are separated by more than 1000 cm^{-1}, and the band maxima by 2724 cm^{-1}, Fig. 18b. In this case, the lowest excited f^1d^1 state, Γ_{3u} (of mainly $^3F_2$ and $^3H_4$ character [206, 261]), is not accessible by absorption or emission from/to the $(^3H_4)\Gamma_{1g}$ f^2 ground state. The assignment of the labelled transitions in Fig. 18b: $(f^1d^1)\Gamma_{3u} \rightarrow (f^2)\Gamma_{4g}$ (emission) and $(f^2)\Gamma_{1g} \rightarrow (f^1d^1)\Gamma_{4u}$, is evident from the f^2 energy levels of Pr^{3+} (Table 8) and the selection rules in Table 1. Transitions from Γ_{3u} are allowed to terminal Γ_{4g} and Γ_{5g} CF states only, whereas transitions from Γ_{1g} are allowed only to the 18 Γ_{4u} levels of f^1d^1. The $4f^15d^1 \rightarrow 4f^2$ emission spectra are extensive over a wide spectral range because transitions are observed from the $(f^1d^1)\Gamma_{3u}$

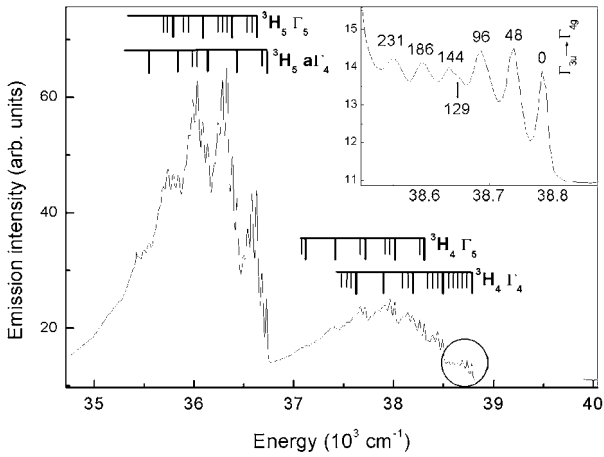

Fig. 19 First four groups of bands in the 252.7-nm excited 10 K emission spectrum of $Cs_2NaY_{0.99}Pr_{0.01}Cl_6$. The progressions in ν_1 and in the lattice mode are indicated. Zero-phonon lines are assigned to terminal *SLJ* states, and the electronic transitions are indicated by *horizontal bars* above the spectra. The *inset* shows the first (*circled*) group of bands in greater detail, with the displacements from the $\Gamma_{3u} \rightarrow \Gamma_{4g}$ origin marked. (Adapted from [206])

state to the ladder of f^2 levels in Table 8. The first groups of bands are shown in Fig. 19, with the inset enlarging the initial $\Gamma_{3u} \rightarrow \Gamma_{4g}(^3H_4)$ structure. The relative intensities of these ED transitions were evaluated by the first term in Eq. (17), taking into account the mixing of the f^2 and f^1p^1 configurations [206, 207, 261] and are in reasonable agreement with experiment.

The first $4f^3 \rightarrow 4f^25d$ bands of Nd^{3+} in $Cs_2NaYCl_6:Nd^{3+}$ have been investigated by ground-state absorption, as well as by excited-state absorption from the $(^4F_{3/2})\Gamma_8$ level at 11,348 cm^{-1} [247]. The onset of absorption in the former spectrum is above 45,600 cm^{-1}, with the first maximum at 47,600 cm^{-1}. However, unlike the cases of Ce^{3+} and Pr^{3+}, no d-f emission is observed for Nd^{3+} in hexachloroelpasolite hosts, because the lowest $4f^25d$ level is rapidly depopulated by nonradiative relaxation to the f^3 levels directly below. This situation differs from $YPO_4:Nd^{3+}$ [262–264] and $MYF_4:Nd^{3+}$ [246, 265, 266] where $4f^25d \rightarrow 4f^3$ emission is observed.

12
Variation Across the Lanthanide Series of Energy Level Parameter Values

One of the outcomes of the spectral analyses is an energy level dataset, as in Table 8, column 'Expt.'. Clearly the most important criterion for the energy level dataset is that no incorrect assignments are included, which lead to spurious parameter values and possibly a poor datafit. Systematic errors between different energy level datasets have often been due to the calibration from "standard air" wavelengths to vacuum wavelengths. These errors are small in the infrared spectral region, but are up to 10–15 cm^{-1} in the ultraviolet. Since the symmetry representations of energy levels are frequently ill-defined, often an experimentally-determined energy level is matched with the closest calculated energy level, and this is more permissible when all levels of a given multiplet term have been identified. However, different fits have often switched certain symmetry irreps for levels of incompletely-assigned terms. The second criterion for the energy level dataset is completeness. Extensive datasets have been presented for a few other systems, such as for the garnets and $LaX_3:Ln^{3+}$, where about 100 levels have been fitted, but it has been pointed out that the assignments have not always been secure [267]. In the energy level parametrizations of $Cs_2NaLnCl_6$, neglecting Yb^{3+} and Ce^{3+}, only 7–30 (in 1980, [268]), 19–45 (in 1985, [269]), and 23–61 (in 1994, [72]) CF levels were fitted. The data for other M_2ALnX_6 systems has generally been scarce. More recently, the use of TP excitation spectroscopy [216, 227–230] and ultraviolet emission and absorption spectroscopy [35, 207, 213, 270] have enabled more complete energy level datasets to be tested. Taking into account the high degeneracies (up to 3) of many of the energy levels, in several cases the datasets are now among the most extensive of those available for Ln^{3+} systems. Table 9 lists some of the previous energy

Table 9 Selected energy level parametrizations of M_2ALnX_6 and $M_2AM'X_6$:Ln^{3+} systems[a]

System (*N*:*s*)	Ref.	Comments
$Cs_2NaLnCl_6$; Ln=Ce(5:*1*),Pr(30:*19*), Nd(7:*9*),Eu(16:*13*),Tb(27:*8*)	[268]	g-values and MD linestrengths also calculated
$Cs_2NaLnCl_6$; Ln=Ce (5:1), Pr (33:16), Nd (32:25), Sm (28:9), Eu (19:12), Tb (27:11), Dy (42:17), Ho (45:18), Er (35:23), Tm(22:21), Yb (5:40)	[269, 271]	Mixed datasets of $Cs_2NaLnCl_6$ and Cs_2NaYCl_6:Ln^{3+}. SCCF fits for Sm, Dy, Ho. Superposition model analysis
$Cs_2NaPrCl_6$ (27:15); Cs_2NaYX_6:Pr^{3+}, X=Cl (27:14), Br (24:16)	[272]	SCCF fits also carried out
Cs_2NaHoX_6, X=Cl (61:15,**14**), Br (34:7)	[273]	Fits with and without SCCF; mixed datasets with diluted systems
$Cs_2NaDyCl_6$ (43:14)	[123]	Mixed dataset with $Cs_2NaGdCl_6$:Dy^{3+}
$Cs_2NaGdCl_6$:Nd^{3+} (41:15)	[274]	3 levels from $Cs_2NaNdCl_6$ included
$Cs_2NaLnCl_6$: Ln=Ce (5:0), Pr (28:39), Nd (33:21), Eu (27:12), Gd (35:25), Tb (23:8), Dy (40:15), Ho (61:13), Er (41:18), Tm (30:33), Yb (5:19); Cs_2NaYCl_6:Ln^{3+}: Ln=Pr (25:26), Sm (25:10); Eu (19:12); $Cs_2NaGdCl_6$:Ln^{3+}: Ln=Nd (41:15), Ho (33:5) $Cs_2LiErCl_6$ (29:14) $Cs_2NaLnBr_6$ Ln=Pr (24:39); Ho (37:6); Tm (22:40); Yb (5:43) Cs_2KPrF_6 (4:6); Cs_2KYF_6:Eu^{3+} (9:9); Rb_2NaEuF_6 (9:10)	[72]	Mixed datasets with diluted systems
$Cs_2NaLnCl_6$ Ln=Er (35:*21*); Nd (33:*25*); Tm (25:*32*)	[275, 276]	Relativistic crystal field
$Cs_2NaLnBr_6$: Ln=Ce (2), Pr (4); Nd (3); Tb (3); Dy (5); Ho (5); Er (5); Tm (3); Yb (3)	[60]	C_{4h} symmetry Hamiltonian
$Cs_2NaErCl_6$ (40:***10***)	[277]	SCCF fit
$Cs_2NaPrCl_6$ (27:10, 27:**8**); Cs_2NaYCl_6:Pr^{3+} (27:9,27:**7**)	[278]	With and without SCCF
Cs_2NaYCl_6:Tm^{3+} (36:55, 36:**28**)	[212]	With and without SCCF
Cs_2NaYCl_6:Sm^{3+} (67:21; 67:**20**); $Cs_2NaEuCl_6$ (77:19;77:**16**); Cs_2NaYF_6:Eu^{3+} (57:27;57:**23**); Cs_2NaTbX_6: X=Cl (100:19;100:**18**); Br (91:21; 91:**15**)	[216, 279]	With and without SCCF
Cs_2NaTbX_6 X=F (86:26); Cl (125:22;125:**20**); Br (28:12)	[223]	Chloride with and without SCCF
$Cs_2NaEuCl_6$ (77:16); Cs_2NaYF_6:Eu^{3+} (57:22)	[228]	
Cs_2NaYCl_6:Sm^{3+} (67:17)	[229]	
Cs_2NaTbX_6: X=F (90:27); Cl (100:19); Br (90:19)	[227, 280, 281]	
$Cs_2NaPrCl_6$ (38:38,38:**14**); $Cs_2LiPrCl_6$ (32:34,32:**15**); Cs_2NaYCl_6:Pr^{3+} (36:39,36:**14**)	[207]	With and without CI
$Cs_2NaTmCl_6$; (38:55;38:**11**)	[213]	With and without CI
$Cs_2NaErCl_6$; (58:20;58:<u>17</u>,	[35]	With and without modified matrix element
$Cs_2NaErCl_6$; (75:20;75:**11**)	[282]	With and without CI

[a] The standard deviation, s (cm^{-1}), is defined in [269] as $[\Sigma(E_{calc.}-E_{expt.})^2/(N-p)]^{0.5}$, where $E_{calc.}$ and $E_{expt.}$ are the calculated and experimental energies, N is the number of energy levels fitted, and p is the number of parameters. Values are rounded to the nearest integer. Values in italics represent the mean deviation, which does not take into account the number of parameters employed (p=0). Bold values refer to SCCF or CI fits. The underlined value refers to the inclusion of a multiplying factor for the matrix element $\langle {}^2H(2)\|U^4\|{}^2H(2)\rangle$

level parametrizations for M_2ALnX_6 systems but is not exhaustive. The number of levels fitted, and the resulting standard deviation, are also included in the table. Apparently very good energy level fits in some cases may result from over-parametrization, omission of energy level outliers in the fit, inclusion of incorrect assignments, or from the fit of only one or two *SLJ* terms. The standard deviations of the fits are generally not as good as those obtained in the analysis of Ln^{3+} at low symmetry sites, since the presence of a much larger number of CF parameters in the latter case can absorb some of the deficiencies in the model [271].

Often the energy level fitting process is performed by first fitting the energy level *SLJ* baricenters, and then fitting the CF parameters to the splitting of the *J* levels [283, 284]. Certain parameter values can vary wildly if not constrained in the early stages of fitting [207, 230].

12.1 Atomic Hamiltonian Parameters

Figure 20 shows a plot of the Slater parameters against atomic number, with data from the most extensive fits of each lanthanide ion in the series $Cs_2NaLnCl_6$. Most of the parameters from the fit of 77 energy levels for Eu [228] are far from the general trend (as marked for the F^4 graph, for example). The lower points for Eu (not labelled) in the F^k plots are from the 27-level fit [72]. The ratios F^2/F^4 and F^4/F^6 are 1.36±0.10 and 1.48±0.08, respectively, and are fairly close to those expected for a Coulomb field. The log-log plot of the spin-orbit coupling constant, ζ_f, against atomic number, Z, shows a slight curvature (Fig. 21), and from the plot of ζ_f against Z, the empirical relationship between these two quantities is

$$\zeta_f = (18,704 \pm 614) - (725 \pm 19)Z + (7.13 \pm 0.15)Z^2; \mathrm{R}^2 = 0.9999 \qquad (54)$$

The parameter α generally lies in the range 15–25 cm^{-1}, with apparently anomalous values in the fits of Eu^{3+} [228] and Gd^{3+}, Tm^{3+} [72], and does not exhibit a clear trend. The parameter β generally lies between −500 to −800 cm^{-1}, and γ generally needs to be constrained in the fits, to within a reasonable range. In some of the energy level fits, the parameters M^j, P^k or T^i were constrained, but there are no clear trends for these parameter values across the series $Cs_2NaLnCl_6$.

The effects upon the free ion parameters through the replacement of Na by Li, or Ln by Y or Gd, are negligible. There are small, systematic differences in the energy level schemes of these systems which, within the experimental errors, do not translate into significant parameter differences for the Cs_2ALnCl_6 systems studied [72, 207]. Even the replacement of the first nearest neighbour Cl in $LnCl_6^{3-}$ by Br leads to the following four (Br/Cl) parameter ratios near unity for four different Ln^{3+} systems [72, 223]: F^2 0.999±0.005; F^4 1.015±0.030; F^6 1.010±0.035; ζ_f 0.999±0.003. The data are

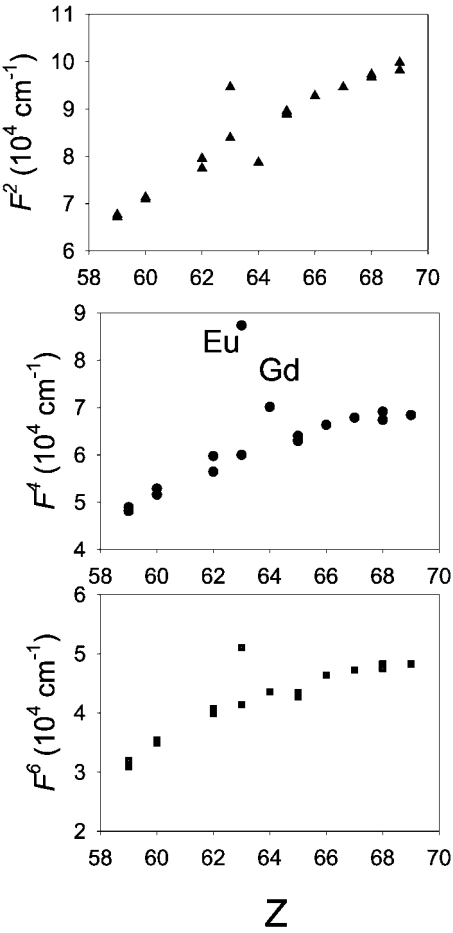

Fig. 20 Plots of Slater parameters F^k against atomic number for $Cs_2NaLnCl_6$, from Pr (Z=59) to Tm (Z=69). (Data from [35, 72, 207, 213, 216, 223, 229, 270])

scarce for M_2ALnF_6 systems [72, 223], but the ratios (Cl/F) are found to be: F^2 0.995±0.006; ζ_f 0.997±0.006.

12.2 One-electron Crystal Field Parameters

The fourth and sixth degree CF parameters from some previous energy level fits for $Cs_2NaLnCl_6$ systems are plotted against atomic number of Ln in Fig. 22, and it is evident that considerable data scatter results. Indeed, it has been realized for some time for the system $Cs_2NaLnCl_6$ [147] that the CF parameters exhibit a *SLJ*-term dependence (see Sect. 12.3), so that different

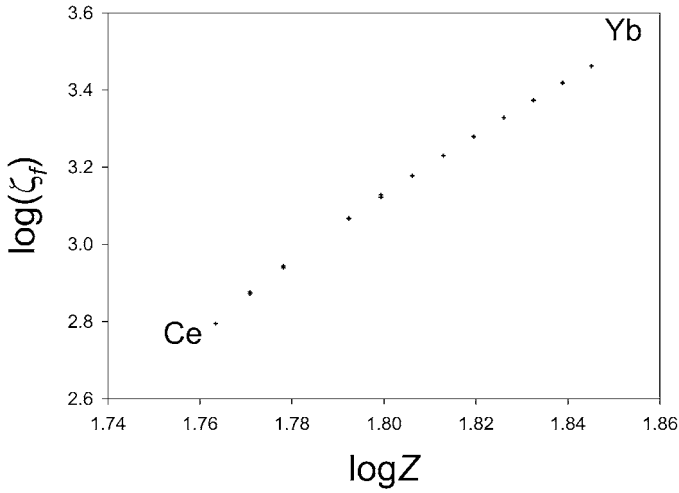

Fig. 21 Plot of log(spin-orbit coupling constant, ζ_f, in cm^{-1}) against log(atomic number) for $Cs_2NaLnCl_6$. (Data as in Fig. 20)

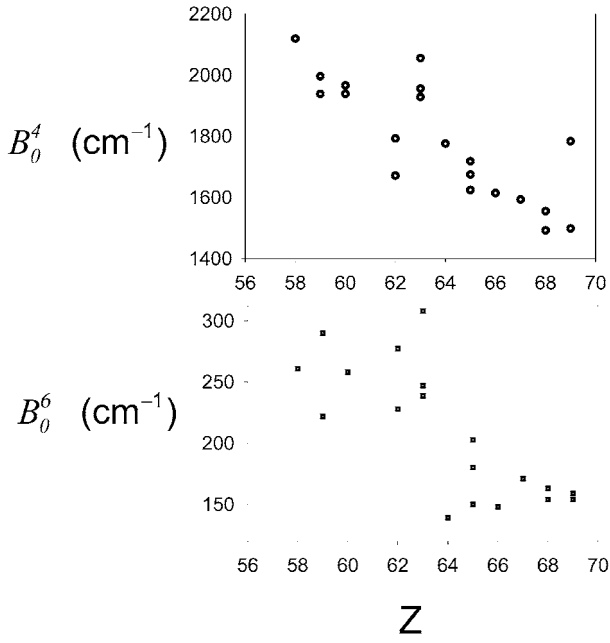

Fig. 22 Plots of fourth and sixth degree crystal field parameters against atomic number from Ce (Z=58) to Tm (Z=69) for $Cs_2NaLnCl_6$. (Data as in Fig. 20)

values are obtained when fitting different numbers of levels, different multiplets, or by differently weighting the levels in the fits. The linear regression lines (not shown) for Fig. 22 are

$$B_0^4 = (4701 \pm 479) - (45.8 \pm 7.5)Z; R^2 = 0.674 \tag{55}$$

$$B_0^6 = (992 \pm 150) - (12.3 \pm 2.4)Z; R^2 = 0.601 \tag{56}$$

Generally, but with notable exceptions, the CF parameters are greater for larger lattice parameters, as for the earlier members of the lanthanide series in $Cs_2NaLnCl_6$. The most comprehensive comparison of CF parameters for Cs_2NaLnX_6 systems has been made for Ln=Tb, X=halide. The approximate values (in cm^{-1}) of B_0^4 were 3163, 1718, 1383; and of B_0^6 were 242, 180, 121 for F, Cl, Br, respectively [223, 230]. In this case, the CF parameters are smaller for increasing lattice parameter in Cs_2NaTbX_6.

The comparison of the energy level datafits with those for other systems should take into account the fact that only two CF parameters have been employed for M_2ALnX_6, whereas the number is considerably greater for other systems where Ln^{3+} is doped, for example: 9 for $Y_3Al_5O_{12}$ (YAG) and LaF_3; 6 for $CsCdBr_3$ and $Cs_3Lu_2X_9$ (X=Cl, Br). As an example, the CF parameters from the $Cs_2NaErCl_6$ datafit [35] are compared with those for Er^{3+} in several lattices in Table 10, using the CF strength, S^k, which is a spherical parameter independent of the crystal symmetry:

$$S^k = \left[7/(2k+1) \begin{pmatrix} 3 & 3 & k \\ 0 & 0 & 0 \end{pmatrix}^2 \sum_{q=-k,k} (B_q^k)^2 \right]^{1/2} \tag{57}$$

The comparison is made with respect to uncorrected CF parameters, i.e. without empirical correction or correlated CF (CCF) contributions. The inclusion of this second-order CF effect does not, at least in the studies of oth-

Table 10 Fourth- and sixth-order crystal field strength, S^k (in cm^{-1}), from various energy level fits for Er^{3+} in crystals (from [35])

System	Ref.	Site symmetry	N^a	S^4	S^6
YAG	285	D_2	9	337	207
YVO_4	286	D_{2d}	Not stated	184	92
$LaCl_3$	287	C_{3h}	4	38	76
LaF_3	288	C_{2v}	9	123	153
$CsCdBr_3$	289	C_{3v}	6	238	31
$Cs_3Lu_2Br_9$	290	C_{3v}	6	251	44
$Cs_3Lu_2Cl_9$	291	C_{3v}	6	257	48
$Cs_2NaErCl_6$	277	O_h	2	272	61
$Cs_2NaErCl_6$	35	O_h	2	287	60

[a] Number of crystal field parameters fitted

er systems which are quoted here, change significantly the values of the CF strength parameters which describe a first-order CF effect. For instance, the changes in the magnitude of the k=4 CF strength amount to 1, 8 and 0% for garnets [285], $CsCdBr_3$ [289] and $Cs_3Lu_2Cl_9$ [291], respectively. For the compounds with Cs^+ cations in Table 10, the k=4 and 6 CF strengths show an increasing trend from Br to Cl nearest neighbours of Er^{3+}. The expected trend from Cl to F is observed in LaX_3. The CF strengths for the dimeric system $Cs_3Lu_2Cl_9$ (where three Cl atoms are shared by two Er^{3+}, each of which are 6-coordinate) and the system $Cs_2NaErCl_6$ are fairly similar, proving that their environments are not very different, as considered in more detail in [35].

12.3 Refinements to the Energy Level Parametrization

In the conventional CF analyses of lanthanide ion systems, the CF splittings of certain multiplet terms (e.g. Ho^{3+} $^3K_8$; Pr^{3+} $^1D_2$; Nd^{3+} $^2H(2)_{11/2}$) were poorly modelled. The *SLJ*-dependence of the CF parameters, and their irregular behaviour on crossing the lanthanide series, prompted the introduction of further phenomenological parameters into the CF Hamiltonian. CF parameters which accurately model low-lying multiplets give poor fits for higher-energy multiplet terms. The one-electron CF model assumes that the CF potential experienced is independent of the properties of the remaining electrons, despite their strong electrostatic correlation [223]. Correlation CF corrections to the Hamiltonian have been proposed by Newman and Judd, which take into account the different interactions with the ligand field of multiplet terms with different orbital angular momenta (orbitally-correlated CF) as well as the different interactions of multiplet terms with different spin (spin-correlated CF). The two-electron correlation terms introduce up to 637 parameters for systems with C_1 site symmetry, which reduce down to 41 parameters for O_h symmetry [284]. The spin-correlated CF has received most attention. It is argued that because spin-parallel electrons are subject to an attractive exchange force they are expected to occupy orbitals with a more compact radial distribution than spin-antiparallel electrons. Thus, spin-anti-parallel (minority spin) electrons should be subject to stronger CF interactions [292]. Most of the earlier CF analyses for M_2ALnX_6 systems were carried out on limited datasets pertaining to maximum multiplicity states, so that the importance of this hypothesis could not be evaluated fairly.

The practice in modifying the CF Hamiltonian to include spin-correlation has been to replace the one-electron CF $\sum_i B_q^k C_q^k(i)$ by

$$\sum_i [B_q^k C_q^k(i) + b_q^k \mathrm{S} \cdot \mathrm{s}_i C_q^k(i)] \tag{58}$$

where the sum runs over the 4f electrons. Although the simplicity of the additional term suggests the inclusion of a pseudo-one-body operator, it actually involves a two-body operator since $\mathrm{S} = \sum_j \mathrm{s}_j$. Usually, the ratio $c_k = b_q^k/B_q^k$ is taken to indicate the importance of the spin-correlated CF. For terms of maximum multiplicity, the spin-correlated CF is proportional to the one-electron CF, so that it is important to include non-maximum multiplicity terms to determine the b_q^k parameters. It has been argued [269] that the 'sudden drop' in sixth-rank CF parameters in the second-half of the lanthanide series is due to the fact that the matrix elements of the one-electron operators in Eq. (10) change sign, whereas the matrix elements of the two-electron operators do not. Thus the one- and two- electron contributions add in the first half of the series and cancel in the second half. However, whether there is actually a 'sudden drop' is not clear from Fig. 22.

The earlier attempts to improve the CF analyses of M_2ALnX_6 systems by incorporating terms of the type in Eq. (58) were not very successful in greatly reducing the mean deviation (for example, [272, 273]) although the term dependence of the ratio B_0^4/B_0^6 was removed. Subsequently, a simplified 'δ-function' model, which assumes that the dominant contributions to the correlation CF interactions come from paired electrons within the same angular orbital (with opposite spin), was used to fit the Pr^{3+} energy level scheme in $Cs_2NaPrCl_6$ [293]. Two problematic terms in this case, using a one-electron CF Hamiltonian, are $^1D_2$ and $^1G_4$ (Table 8). In fact, the calculated energies [293], using the δ-function model, were 9810 cm^{-1} for level 24 (Γ_1) and 10522 cm^{-1} for level 27 (Γ_5), both of $^1G_4$, which are far from the experimental values (Table 8).

With the advent of more extensive datasets, further impetus was placed in the application of the spin-correlated CF model, with rank 4 and 6 operators [223, 267, 279, 281, 294]. The improvement in the standard deviation of the CF analysis for 91 levels of $Cs_2NaTbBr_6$ with the inclusion of these two additional parameters is 27%, but rather less for Cs_2NaYCl_6:Sm (1.4%), $Cs_2NaEuCl_6$ (14.1%), Cs_2NaYF_6:Eu (15.4%) and $Cs_2NaTbCl_6$ (8.4%). The improvement for the Cs_2NaTbX_6 systems is more marked for X=Br than X=F, since the ^5D, ^5G and ^5H CF levels are poorly fitted in the former case [267]. It was suggested that these results, and the signs of c_k parameters for several systems, show the importance of the orbitally correlated CF [223], and of ligand polarization and covalency in determining the correlation CF [212, 223, 267, 279, 281]. However, to conclude from the most recent CCF fits, there is no 'magic fix' CCF parameter which significantly improves the standard deviation of energy level fits and 'rehabilitates the rogue multiplets' [280].

The calculated splitting of the $^2H(2)_{11/2}$ levels in Er^{3+} [295] (and Nd^{3+} [296]) compounds is always smaller than experimental splitting. An empirical correction has been proposed which includes a multiplying factor for the fourth-order diagonal reduced CF matrix element $\langle ^2H(2)||C^4||^2H(2)\rangle$. The correction is efficient for $^2H(2)_{11/2}$ and $^2H(2)_{9/2}$ and for those levels which are coupled to them by spin-orbit interaction, such as $^4I_{9/2}$, $^4F_{9/2}$ and $^4G_{11/2}$. With the multiplying factor 1.717, the mean deviation in fitting 58 levels of $Cs_2NaErCl_6$ was decreased by 18% [35]. This correction has approximately the same effect as the $g^4_{10,A}$ operator of the correlation CF.

It is, however, more pleasing to have a physically intuitive model which improves the fitting process. Denning [267] has pointed out that the correlation CF effective operator arises from terms of the type

$$H_{CCF} = -(1/\Delta E)\left[\sum_m \langle\psi_i|G|\psi_m\rangle\langle\psi_m|H_{CF}|\psi_f\rangle + \sum_m \langle\psi_i|H_{CF}|\psi_m\rangle\langle\psi_m|G|\psi_f\rangle\right] \tag{59}$$

where G is the Coulomb operator, and the sum is over the states ψ_m of the same parity configuration that differs from f^N by two electrons. An alternative fitting process employs first-order CF matrix elements between the states of the f^N configuration and interacting states of other configurations. This is a more natural way of correcting the energies of f^N CF states because no new hypotheses need to be included, but the CF model is extended to include relevant states whose symmetries permit interaction with f^N states. Faucher and Garcia have successfully employed this model to the refinement of the energy level structure of $PrCl_3$ and other systems, by including interactions with the $4f^{N-1}5d$ configuration via odd-rank CF parameters [297, 298]. In other cases, however, the configuration interaction of $4f^N$ with $4f^{N-1}6p$ via even-rank CF parameters was found to be most effective in reducing the fitting errors [299–301]. Indeed, this type of configuration interaction has been found to be the case in centrosymmetric systems [302] where the CF interaction of f^N states with $f^{N-1}d$ is forbidden by symmetry. In Table 8 the energy level fits for Pr^{3+} in $Cs_2NaPrCl_6$, with and without the inclusion of 4f6p configuration interaction, are compared. The mean deviation of the energy level fit is reduced by a factor of 2.9 (from 32.7 cm^{-1} to 11.6 cm^{-1}), and the CF splittings of $^1D_2$ and $^1G_4$ are well-modelled [207]. The additional parameters introduced into the fit are required to describe the excited configuration 4f6p and its interaction with $4f^2$. These were the interconfiguration parameters, R^k; the spin-orbit coupling parameter, ζ_p; and the CF parameter $B^4_0(f,p)$, so that 13 (instead of 10) parameters were varied freely. In the case of Pr^{3+}, and especially for the $^1D_2$ and $^1G_4$ states, it is observed that the configuration interaction is primarily due to certain large CF matrix elements between the two configurations, and the expression for

their calculation has been given in [207]. The extent of interaction is reflected in the eigenvectors of the CF states, for example, for the f^2 level at 10327 cm^{-1}, the wavefunction is

$$\begin{aligned}\left(f^2\right)^1G_4(a\Gamma_5) = 64.09\%{}^1G_4\left(f^2\right) + 32.09\%{}^3F_4\left(f^2\right) + 1.60\%{}^3H_4\left(f^2\right) \\ + 0.36\%{}^1G_4(fp) + 0.25\%{}^1F_3(fp)\end{aligned} \tag{60}$$

The quality of the CF fit for Pr^{3+} in $Cs_2NaPrCl_6$, including configuration interaction, is not sensitive to the variation of the energy gap between the $4f^2$ and 4f6p configurations. This is not the case for Tm^{3+} systems, and in addition the perturbing configuration is found to be of the type $f^{13}p^5$ [303] rather than $f^{11}p$. For example, the mean deviation in fitting 38 (out of a possible 40) energy levels of Tm^{3+} in $Cs_2NaTmCl_6$ is reduced from 55.4 cm^{-1} to 10.9 cm^{-1} by including the $f^{12}p^6/f^{13}p^5$ configuration interaction. The nature of the $f^{13}p^5$ configuration is of interest. Since the gap between $4f^{12}$ and this configuration is fitted to be at 38,500 cm^{-1} (rather than the expected ca. 200,000 cm^{-1} for $4f^{13}5p^5$), and Ionova et al. [246] have assigned charge transfer bands at ca. 48,000 cm^{-1} in the spectra of $TmCl_6^{3-}$, it is assumed that the p-orbital hole is not in the Tm^{3+} 5p orbital but within the chloride ligand 3p orbital [213]. Further evidence for the interaction of the f^N configuration with a charge transfer configuration comes from the fit of 75 levels of Er^{3+} in $Cs_2NaErCl_6$ with a mean deviation of 10.5 cm^{-1}, compared to that of 19.8 cm^{-1} in the standard one-electron model [282]. The p electrons involved originate from the $3p^6$ chloride orbitals, which are in part projected onto the central Er^{3+} coordinate system as a unique orbital with p-character [282]. The preferred interaction of $4f^N$ configurations with $4f^{N-1}4p^1$ at the beginning of the lanthanide series, and with $4f^{N+1}3p^5$ at the end of the $Cs_2NaLnCl_6$ series, follows the respective tendencies of Ln^{3+} ions to oxidation and reduction. Furthermore, these trends in the mixing of ligand p-orbital character into f^N configurations can explain the variation of electron-phonon coupling strengths across the lanthanide series, since these are strongest at the beginning and at the end of the series. The appreciable ligand orbital admixture is also expected to be important in energy transfer processes.

In studies of low-symmetry systems, the inclusion of a second-order correlation CF effect does not change significantly the values of the CF parameters which describe the first-order CF effect [35]. More sensitive changes might be anticipated with the use of only two first-order CF parameters for M_2ALnX_6 systems. It is found that the inclusion of two correlation CF parameters increases the value of $B_0^4(B_0^6)$ by 2.2% (10.4%) in $Cs_2NaPrCl_6$ [272], but decreases the respective values by 23.8% (16.1%) in Cs_2NaYCl_6:Tm^{3+} [212]. These changes in parameter values are outside the fitting errors of the first-order CF parameters. However, the outcome is even more dramatic when the values from fits with and without the inclusion of configuration in-

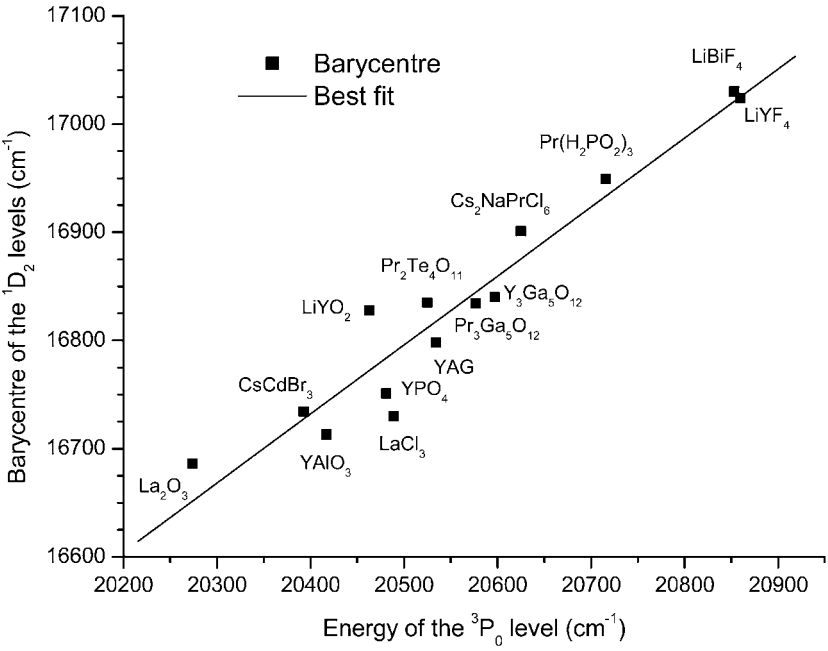

Fig. 23 Plot of $^1D_2$ barycentre energy against $^3P_0$ nondegenerate level energy for Pr^{3+} in various systems. (Data from [207]). The *best fit line* is drawn through the points

teraction are compared. For $Cs_2NaPrCl_6$, the value of $B_0^4(B_0^6)$ without the inclusion of configuration interaction increases by 72% (172%) [207], whereas the corresponding values show a decrease of 59% and an increase of 210% for $Cs_2NaTmCl_6$ [213]. Clearly, the values of CF parameters for different Ln^{3+} should be compared with caution.

A criterion for evaluating incorrect energy level assignments has recently been proposed [304]. The barycentre energies of $^{2S+1}L_J$ terms are plotted against one another for a series of systems containing the relevant Ln^{3+} ion, and the deviation from linearity is taken to indicate an incorrect assignment in a particular system. When the barycentre data for $^3P_0$ and $^3P_1$ are plotted against one another, the data point from $Cs_2NaPrCl_6$ sits upon the straight line fit. However, Fig. 23 shows that considerable scatter occurs in the plot of the $^1D_2$ barycentre energy against $^3P_0$. This may not only represent the possibility of incorrect assignments, but alternatively, of cases where the $^1D_2$ levels are perturbed by configuration interaction. Thus the $Cs_2NaPrCl_6$ data point in Fig. 23 lies about 50 cm^{-1} away from the best-fit line.

13
Energy Transfer in M_2ALnX_6 Systems

Much of the motivation for the study of the electronic, vibrational and vibronic properties of M_2ALnX_6 systems is towards the understanding of ET phenomena. ET can involve the radiationless transfer of energy from the site of its absorption in a crystal by a donor (sensitizer), over distances greater than interatomic separations, to an acceptor (activator) without collision or conversion to thermal energy. The transfer is resonant if the energy transferred matches the difference in electronic energy between levels of both the donor and acceptor systems. More often, nonresonant ET involves the creation or annihilation of phonons at the donor and/or acceptor sites. Radiative ET from a donor to an acceptor involves a photon, and the donor lifetime is unchanged unless it is the same species as the acceptor.

The f^N excited states of Cs_2NaLnX_6 systems are long-lived (Table 11). Lifetimes of $f^{N-1}d$ states are listed in Table 12. Although ET can be very efficient in these crystals their softness and hygroscopic properties make them unsuitable for optical applications. However, due to the high site symmetry of Ln^{3+}, these materials serve as model systems for understanding ET processes of lanthanide ions.

Neglecting effects due to stimulated emission and reabsorption of emitted light, for one type of emitting centre in a M_2ALnX_6 system, the (natural) lifetime τ of a particular state is related to the population or emission intensity of a transition from that state, I, at time t, following pulsed excitation at t=0, by

$$I(t) = I(0)\exp(-kt), \quad \text{where} \quad k = 1/\tau \tag{61}$$

where k is the sum of the radiative (k_r) and nonradiative (k_{nr}) decay processes. Some of the tabulated lifetimes (Table 11) are approximate due to deviations from exponential behaviour. However, it is clear that the lifetimes are longer than for Ln^{3+} at lower symmetry sites. For example, compare the $^4F_{9/2}$, $^4I_{9/2}$ lifetimes of Er^{3+} in LaF_3:Er^{3+} (0.1 mol%): 0.75, 0.15 ms [349], CaF_2:Er^{3+} (0.2 mol%): <0.98, 0.02 ms [350], YVO_4:Er^{3+} (1 mol%): 10, 10 μs [286] (where the Er^{3+} site symmetries are C_2, tetragonal and D_{2d}, respectively) with those listed in Table 11. The variation in measured lifetimes from sample to sample (Table 11) is due to the crystal quality, since M_2ALnCl_6 systems in particular are moisture sensitive. Excited states are then quenched by the ET to trap sites such as those with oxychloride or hydroxide species coordinated to Ln^{3+}.

Studies in the 1970s by Weber [351], Watts [352] and others have shown that three regimes occur for ET when the donor (i.e. sensitizer, D) concentration is increased: (i) when the concentration of donors is small, direct (one-step) relaxation from an excited donor (D*) to an acceptor (i.e. activator, A) without diffusion occurs (giving nonexponential donor decay, followed by exponential decay); (ii) at higher donor concentrations, fast migra-

Table 11 Natural lifetimes of $4f^N$ CF levels in M_2ALnX_6 systems[a]

Ln^{3+}	Host (dopant conc. mol%)	Luminescent *SLJ* term	Temp. (K)	Lifetime[b]	Reference
Pr	$Cs_2NaPrCl_6$	$^3P_0$	80 [10]	53±9* [140±4*]	[147]
	$Cs_2NaPrCl_6$	$^3P_0$	80 [20]	43* [108*]	[305, 306]
	Cs_2NaYCl_6 (10)	$^3P_0$	300	118*	[260]
	Cs_2NaYCl_6 (~1)	$^3P_0$	300 [80] 10	141±20* [273±15*] 413±2*	[147]
	Cs_2NaYCl_6 (0.1)	$^3P_0$	80 [20]	277* [473*]	[305, 306]
	Cs_2NaYBr_6	$^3P_0$	300 [80] 10	87±7* [266±30*] 575±50*	[147]
	Cs_2NaYBr_6	$^3P_1$	300 [80]	87±7* [49±2*]	[147]
Nd	$Cs_2NaNdCl_6$	$^4D_{3/2}$	300	75**	[247]
	$Cs_2NaNdCl_6$	$^4F_{3/2}$	300 [77]	1.2 [5]	[307, 308]
	$Cs_2NaLnCl_6$ (1) (Ln=Y, La)	$^4F_{3/2}$	300 [77]	4.1 [11]	[307, 308]
	Cs_2NaYCl_6 (0.5,1,5)	$^4D_{3/2}$	300	100*, 90*, 70*	[247]
	$Cs_2NaGdCl_6$ (1)	$^4F_{3/2}$; $^4G_{7/2}$	300 [80]	4.3 [6.4]; 30±4* [74±6*]	[274]
	$Cs_2NaYbCl_6$ (99)	$^4F_{3/2}$	300	700*	[274]
	Rb_2KNdF_6	$^4F_{3/2}$	300	318*	[309]
	Cs_2KNdF_6	$^4F_{3/2}$	300	717*	[309]
	Cs_2KLaF_6 (10, 40)	$^4F_{3/2}$	300	3.2, 1.4	[309]
	Rb_2NaYF_6 (1)	$^4F_{3/2}$	4, 77, 300, 568	6, 10.7, 4.4, 2.85	[259]
Sm	$Cs_2NaSmCl_6$	$^4G_{5/2}$	10 [300]	86* [3.2*]	[310–312]
	Cs_2NaYCl_6 (0.5)	$^4G_{5/2}$	10	17	[310, 313, 314]
	$Cs_2NaGdCl_6$ (0.1)	$^4G_{5/2}$	10 [300]	17 [9.3]	[311, 315–318]
Eu	$Cs_2NaEuCl_6$	$^5D_0$	295 [80]	0.65 [68*]	[319]
	$Cs_2NaEuCl_6$	$^5D_0$	12	5.6±0.7	[320, 321]
	$Cs_2NaEuCl_6$	$^5D_1$	293 [80]	(66±3)* [0.53±0.03]	[320, 322]
	$Cs_2NaEuCl_6$	$^5D_2$;$^5D_1$;$^5D_0$	300 [80]	80* [520*]; 0.16 [0.71]; 2.0 [2.7]	[323]
	Cs_2NaYCl_6 (1)	$^5D_1$; $^5D_0$	12	7.4±0.5;11.1	[320, 322]
	$Cs_2NaTbCl_6$ (1–15)	$^5D_1$	293 [80]	24±1* [1.3±0.1]	[324–326]
	$Cs_2NaGdCl_6$	$^5D_1$	80	8.3	[317]
	Cs_2NaYF_6 (0.1, 20)	$^5D_1$; $^5D_0$	295	1.24±0.05, 0.22±0.01; 15±1, 13±1	[25]
	Cs_2NaYF_6 (0.1, 20)	$^5D_2$; $^5D_1$; $^5D_0$	4	84±4*, 49±3*; 2.7±0.1, 2.5±0.1; 15±1, 15±1	[25]
Gd	$Cs_2NaGdCl_6$	$^6P_{7/2}$	4.2	13±2	[327]
	$Cs_2NaGdCl_6$	$^6I_{7/2}$	4.2	3.1±0.2	[327]

tion between donors before ET from D* to A gives an exponential decay of donor emission; and (iii) at low A concentrations, diffusion-limited decay occurs (with a time-dependent change from non-exponential to exponential donor decay). Case (ii) may be analysed by a hopping mechanism, which

Table 11 (continued)

Ln^{3+}	Host (dopant conc. mol%)	Luminescent *SLJ* term	Temp. (K)	Lifetime[b]	Reference
Tb	$Cs_2NaTbCl_6$	$^5D_3$; $^5D_4$	8	45*; 9.5	[242]
	$Cs_2NaTbCl_6$	$^5D_4$	293 [80]	6.6±0.2 [9.4±0.2]	[324]
	Cs_2NaYCl_6 (1)	$^5D_4$	293 [80]	6.9±0.2 [9.9±0.4]	[324]
	Cs_2NaTbF_6	$^5D_3$;$^5D_4$	77 [10]	4* [14*]; 16.9 [17.3]	[328]
	Cs_2KInF_6 (0.1–10)	$^5D_3$;$^5D_4$	16	8; 18	[329]
	$Cs_2NaTbBr_6$	$^5D_3$;$^5D_4$	77 [10]	32* [110*]; 5.9 [4.0]	[230, 330]
Ho	$Cs_2NaHoCl_6$	$^5I_7$	85	50	[122]
	$Cs_2NaHoCl_6$	$^5I_5$	300 [85]	48 [108]	[331]
	$Cs_2NaHoCl_6$	$^5F_3$; $^5F_5$	20	1.2±0.5; 15	[148, 332]
	$Cs_2NaHoCl_6$	$^5F_5$	300 [80] 10	4.5 [5.5] 6.9	[323, 333]
	$Cs_2NaHoCl_6$	$^5F_5$	300 [85]	7 [10]	[186]
	$Cs_2NaHoCl_6$	$^5I_7$; $^5I_5$; $^5F_5$	300	27±9; 48; 7	[185]
	$Cs_2NaHoCl_6$	$^5I_7$; $^5I_5$; $^5F_5$	85	35±15; 107; 10	[185]
	$Cs_2NaHoCl_6$	$^5I_4$; $^5F_5$; $^5F_3$	15	75; 12±3; 1.2±0.5	[185]
	Cs_2NaYCl_6 (0.01)	$^5F_5$	295 [80]	5.5 [14.7]	[334]
	Cs_2NaYCl_6 (1, 20)	$^5F_5$	300 [80]	5.9 [6.5], 6.1 [6.6]	[323, 333]
	Cs_2NaYCl_6 (0.7)	$^5F_3$; $^5S_2$	15–20	9.3±2; 40±2	[148, 185]
	$Cs_2NaSmCl_6$ (98)	$^5F_5$	300 [80]	70* [50*]	[333]
	$Cs_2NaYbCl_6$ (99)	$^5F_5$	300 [80]	35* [20*]	[333]
	$Cs_2NaYbCl_6$ (99)	$^5F_5$	300 [85]	300* [140*]	[149]
	$Cs_2NaYbCl_6$ (1)	$^5F_3$; $^5S_2$	20	9±2; 44±15	[185]
	$Cs_2NaGdCl_6$ (1)	$^5F_3$; $^5S_2$; $^5F_5$	300	2.8±0.1; 6±2; 7	[185]
	$Cs_2NaGdCl_6$ (1)	$^5F_3$; $^5S_2$; $^5F_5$	85	5.7±0.1; 19.9±0.6; 22.5±1.5	[185]
	$Cs_2NaGdCl_6$ (1)	$^5F_3$; $^5S_2$; $^5F_5$	20	8.5±1.5; 38±3; 28±5	[185, 148]
	$Cs_2NaTmCl_6$ (99)	$^5F_3$; $^5F_5$	20	270*; 2	[332]
	$Cs_2NaErCl_6$ (99)	$^5F_5$	300 [85]	0.2–1 [0.1–0.6]	[186]
	$Cs_2NaHoBr_6$	$^5F_5$	300–30	0.6–1.1	[187]
	$Cs_2NaHoBr_6$	$^5F_3$	20	80*	[187]
	$Cs_2NaHoBr_6$	$^5I_5$	300 [85]	11 [16]	[187]
	Cs_2NaYBr_6 (dilute)	$^5F_3$; $^5F_5$; $^5I_5$	300 [85]	1 [3.3]; 4.4 [14]; 66 [102]	[187]
Er	$Cs_2NaErCl_6$	$^4I_{9/2}$; $^4F_{9/2}$; $^4S_{3/2}$; $^2G_{9/2}$	85	18.9±1.3; 7.5; 4.6±0.5; 4.4±1.0	[335]
	$Cs_2NaErCl_6$	$^4I_{13/2}$; $^4I_{11/2}$; $^4I_{9/2}$; $^4F_{9/2}$; $^4S_{3/2}$	300 [77]	22 [-]; - [4.7]; 6.5 [21]; 3.8 [8.5]; 0.5 [0.5]	[336, 337]
	$Cs_2NaErCl_6$	$^4F_{9/2}$	1.2	9.1	[338]
	$Cs_2NaErCl_6$	$^4S_{3/2}$; $^4I_{9/2}$	50–300	Graphical form	[339]
	Cs_2NaYCl_6 (0.1–100)	$^4S_{3/2}$; $^4F_{9/2}$; $^4I_{9/2}$	10–300	Graphical form	[340, 341]
	Cs_2NaYCl_6 (0.1, 100)	$^4S_{3/2}$	80	8.2, 4.0	[342]
	Cs_2NaYCl_6 (2, 10)	$^4S_{3/2}$; $^4I_{11/2}$	15	11.2, 11.0; 83.6, 45	[343]
	$Cs_2NaEr_{0.2}Yb_{0.4}Y_{0.4}Cl_6$	$^4I_{11/2}$; $^4I_{9/2}$; $^4F_{9/2}$; $^4S_{3/2}$	300	4.1; 32.5; 8.6; 0.37	[337, 339]

Table 11 (continued)

Ln^{3+}	Host (dopant conc. mol%)	Luminescent *SLJ* term	Temp. (K)	Lifetime[b]	Reference
Tm	$Cs_2NaTmCl_6$	$^3H_4$	300 [20]	1 [1.6]	[332]
	$Cs_2NaTmCl_6$	$^3P_2$	300	59*	[344]
	$Cs_2NaTmCl_6$	$^3H_4$	300	4*	[345]
	Cs_2NaYCl_6 (1, 5, 25)	$^1D_2$; $^1G_4$; $^3H_4$	300	71*, 60*, 54*; 380*, 300*, 130*; 990*, 930*, 580*	[345]
	$Cs_2NaGdCl_6$ (1)	$^1G_4$; $^3H_4$	20	6; 20–50	[332]
	$Cs_2NaGdCl_6$ (0.1)	$^1G_4$	10	4.5	[346]
	$Cs_2NaGdCl_6$ (0.1, 1, 10)	$^1D_2$; $^1G_4$; $^3F_3$; $^3H_4$	300	101*, 95*, 51*; 1.92, 1.30, 145*; 243*, 194*, 75*; 3.9, 4.1, 3.3	[344, 347]
	$Cs_2NaHoCl_6$ (1)	$^3F_3$	20	2	[332]
Yb	$Cs_2NaHoCl_6$ (1)	$^2F_{5/2}$	300 [30]	6 [13]	[149]
	$Cs_2NaHoCl_6$ (50)	$^2F_{5/2}$	300	1	[149]
	$Cs_2NaNdCl_6$ (60)	$^2F_{5/2}$	300–13 [13–12]	150? [5.3]	[348]

[a] The variations are due to changes in crystal quality, absorption of moisture and the presence of concentration gradients in crystals

[b] Values are in ms except starred values: * in μs; ** in ns

also predicts an exponential donor decay, but which leads to a different dependence upon donor concentration and interaction parameters.

Generally, CF levels within a given multiplet term are in thermal equilibrium (i.e. they have the same lifetime). A slow relaxation rate (k') from an upper to a lower multiplet term (shown in Fig. 24a) produces a noticeable rise-time in the decay of emission from the lower state, following pulsed excitation:

$$I(t) = I(0)\exp(-kt) + I'(0)[k'/(k-k')][\exp(-k't) - \exp(-kt)] \qquad (62)$$

where $I'(0)$ is the population of the upper state at t=0.

Table 12 Lifetimes of $4f^{N-1}5d$ CF levels in M_2ALnX_6 systems

Ln^{3+}	Host (dopant conc. mol%)	Luminescent *SLJ* term	Temp. (K)	Lifetime (ns)	Reference
Ce	Cs_2NaYCl_6 (10)	$d^1\ T_{2g}$	300	~30	[260]
	$Cs_2LiLaCl_6$ (1)	$d^1\ T_{2g}$	300	36.4±0.3	[256]
	Rb_2NaYF_6 (1)	$d^1\ T_{2g}$	300	70–90	[258]
	Cs_2NaYF_6 (1)	$d^1\ T_{2g}$	300	42	[258]
Pr	$Cs_2NaPrCl_6$	$f^1d^1\ ^3F_2$	8	13	[206]
	Cs_2NaYCl_6 (1)	$f^1d^1\ ^3F_2$	8	18	[206]
	Cs_2NaYCl_6 (10)	$f^1d^1\ ^3F_2$	300	~20	[260]

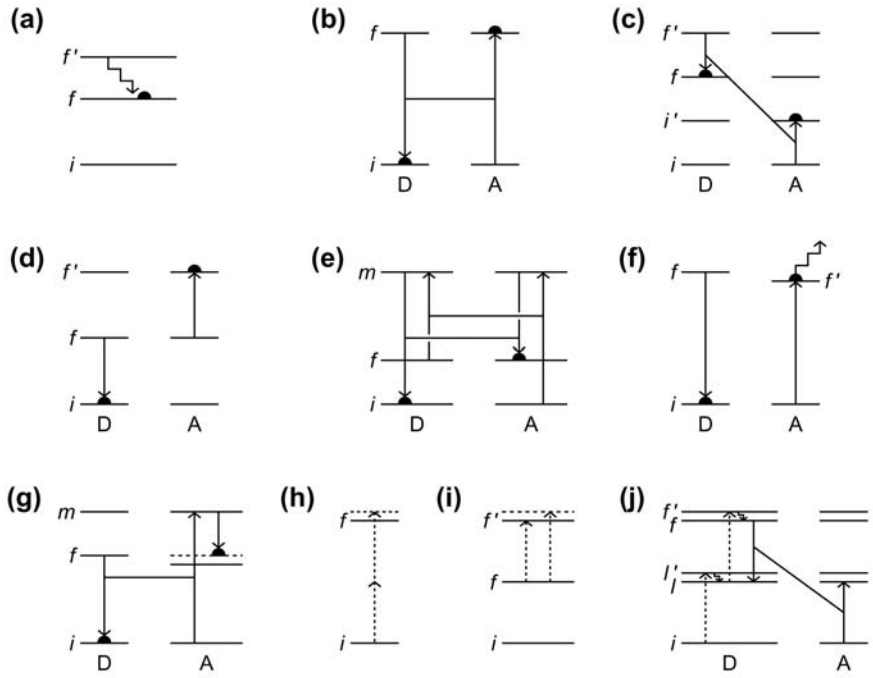

Fig. 24a–j Energy transfer mechanisms in M_2ALnX_6 systems: **a** multiphonon relaxation; **b** migration; **c** cross-relaxation; **d** ET upconversion; **e** second-order two-body ED, ED-ED, ED ET; **f** diagonal one-phonon-assisted ET; **g** nondiagonal one-phonon-assisted ET; **h** TP absorption; **i** excited state absorption terminating upon electronic and vibronic levels; **j** photon avalanche upconversion. D,A represent Donor and Acceptor, respectively. *Horizontal or slanted links* represent various coupling mechanisms. *Wavy arrows* represent phonon emission or absorption. *Dashed arrows* represent the laser pump. *Dashed energy levels* are vibronic states. In most cases, only one illustration of the several possible diagrams is given. *i*, *l*, *f* represent f^N states, and *m* is an opposite-parity state. Where applicable, *semicircles* represent the final D and A states. Refer to Sect. 13 for explanations

Single-ion nonradiative decay for Ln^{3+} diluted into transparent host elpasolite crystals, where the energy gap is greater than the Debye cutoff, is primarily due to multiphonon relaxation (with rate k_{mp}). In some cases, first order selection rules restrict phonon relaxation between states, such as between Γ_{1g} and Γ_{4g}, or between Γ_{2g} and Γ_{5g}, CF states for MX_6^{3-} systems. The dependence of the multiphonon relaxation rate, k_{mp}, upon the energy gap to the next-lowest state (ΔE) has been investigated for other systems and is given by a relation such as [353, 354]

$$k_{mp} = \beta[\exp(-\alpha\Delta E)] \tag{63}$$

where α and β are constant for a particular host lattice. From a survey of the luminescent and non-luminescent states of M_2ALnCl_6 systems it has been observed that as long as a state is populated, then in the absence of concentration quenching effects or restrictive selection rules, the state should be luminescent provided that ΔE is spanned by five or more phonons [355]. For M_2ALnCl_6 systems, since the highest energy phonon is 279–296 cm^{-1} for Ce-Yb (Table 1), this means that ΔE>ca. 1120–1180 cm^{-1}. Thus, for example in the $Cs_2NaLnCl_6$ series, weak luminescence occurs from the $(^6F_{5/2})\Gamma_7$ level of Dy^{3+} (ΔE=1270 cm^{-1}), and from the $(^4G_{7/2})\Gamma_8$ level of Nd^{3+} (ΔE=1374 cm^{-1}) [355]. M^{c}Caw has pointed out that the lifetimes of states of Cs_2NaTbX_6 systems decrease for the heavier halides, which he accounted for by the increase in k_r (due to more intense vibronic sidebands associated with higher ligand polarizability) [330]. Although this seems to be the case for the $^5D_4$ state (Table 11), the lifetime of the $^5D_3$ state shows the reverse trend. A simple trend is not evident from other systems (e.g. Table 11: Cs_2NaYX_6:Ln^{3+}, X=Cl, F). Slower multiphonon relaxation rates due to lower vibrational frequencies would lead to longer lifetimes for systems with the heavier halides. However, additional factors, such as the crystal quality and ease of hydrolysis of M_2ALnX_6, also play roles in determining the experimental lifetimes of neat systems.

13.1 Resonant Energy Transfer

In this section, the transfer of excitation energy from the donor to the acceptor, with no energy mismatch involved, by the ET mechanism, is discussed. Other possible transfer mechanisms, such as radiative transfer [356] and photoconductivity, are not considered here. Nonradiative ET between adjacent Ln^{3+} ions involves only a one-step process which requires the direct coupling of the ions by various electric (ED-ED, ED-EQ, EQ-EQ), and/or magnetic (MD-MD) interactions; by exchange interactions if their wavefunctions overlap [357] (not considered to be important since the Ln^{3+} separation in Cs_2NaLnX_6 is large, $a/\sqrt{2}$~0.75 nm, Fig. 1a); or by superexchange interactions involving intervening ions. The donor-acceptor separations for the elpasolite system $Cs_2NaTmCl_6$ are listed in Table 13 for the nth (n=1...6) nearest neighbour shells.

Examples of two-body ET are shown in Figs. 24b,c. Migration, Fig. 24b, represents the case when the donor and acceptor are the same species. However, it can also occur nonresonantly since there may be a slight energy mismatch from the donor to the acceptor site, which can be compensated by acoustic phonons. In the second cross-relaxation mechanism, Fig. 24c, the emission from level f' is quenched, and level i' is populated. If the acceptor level is an excited state (often the same as the donor state, as in Fig. 24d), the process is called ET upconversion. The term cooperative ET upconver-

Table 13 Structural data, MD-MD and EQ-EQ $^1G_4 \rightarrow {}^3H_4$ resonant energy transfer rates between Tm^{3+} ions in $Cs_2NaTmCl_6$ at 300 K[a]

n-th nearest neighbour acceptor	Distance (pm) from Tm^{3+} donor	Number of like neighbours	MD-MD transfer rate (s^{-1})	EQ-EQ transfer rate (s^{-1})
1	755.6	12	1.92×10^4	1.91×10^5
2	1068.6	6	1200	4882
3	1308.8	24	1420	671
4	1511.2	12	230	187
5	1689.6	24	310	108
6	1805.9	8	60	11

[a] Effective field effects have not been included. Data from [360, 364]

sion (or cooperative sensitization) is generally reserved for the 3-body process (not shown) where two donor ions, D*, such as Yb^{3+} simultaneously excite an acceptor ion, A, such as Tb^{3+} [356].

Generally, the ET processes are studied by following the quenching of the donor emission D*, and its replacement by acceptor emission, A*. For elpasolite systems, resonant ET is uncommon in comparison with nonresonant transfer. One example is the quenching of $^1G_4$ emission in $Cs_2NaTmCl_6$, subsequently discussed. The cross-relaxation in $Cs_2NaSm_xEu_yGd_{1-x-y}Cl_6$: Sm^{3+} $(^4G_{5/2})\Gamma_7$ [18086]$\rightarrow(^6H_{7/2})\Gamma_8$ [1208] and Eu^{3+} $(^7F_1)\Gamma_4$ [360]$\rightarrow(^5D_0)\Gamma_1$ [17208] shows some mismatch although it has been treated as resonant [315].

The theory of resonant nonradiative ED-ED ET was formulated by Förster, and extended by Dexter to include other interaction mechanisms. From the Fermi Golden Rule, the ET rate, W_{DA}, between an excited donor (D*) and an acceptor (A) in nondegenerate states is proportional to the square of the interaction matrix element, *J*, [358]:

$$W_{DA} = \frac{4\pi^2}{h} J^2 G_{overlap} \tag{64}$$

where the overlap integral $G_{overlap}$ is defined as

$$G_{overlap} = \int g_D(E) g_A(E) dE \tag{65}$$

and $g_D(E)$ and $g_A(E)$ are the normalized lineshape functions of the radiative emission of D* and the radiative absorption of A. For electrostatic multipolar interactions, the interaction matrix element is given by

$$J = \langle \mathrm{D}, \mathrm{A}^* | \mathrm{H}_{ET} | \mathrm{D}^*, \mathrm{A} \rangle \tag{66}$$

in which H_{ET} is the ET interaction Hamiltonian between the k_1-pole of D^* and the k_2-pole of A [358]:

$$\mathrm{H}_{ET} = e^2 \sum_{\substack{k_1 k_2 \\ q_1 q_2}} \mathrm{C}^{k_1 k_2}_{q_1 q_2} \mathrm{D}^{(k_1)}_{q_1} \mathrm{D}^{(k_2)}_{q_2} \tag{67}$$

and the angular factor is expressed as

$$\mathrm{C}^{k_1 k_2}_{q_1 q_2}(\theta,\phi) = \frac{(-1)^{k_1}}{R^{k_1+k_2-1}} \left[\frac{(2k_1+2k_2+1)!}{(2k_1)!(2k_2)!}\right]^{1/2} \times \begin{pmatrix} k_1 & k_2 & k_1+k_2 \\ q_1 & q_2 & -(q_1+q_2) \end{pmatrix} \mathrm{C}^{(k_1+k_2)}_{q_1+q_2}(\theta,\phi)^* \tag{68}$$

which is another expression of the T factor in Eq. (34).

The overlap integral reflects the requirement of energy conservation in the ET process. Its value is uncertain because the homogeneous linewidth of solid-state spectra can be up to three orders of magnitude smaller than the inhomogeneous linewidth [359]. A value of 8×10^{21} J^{-1} has been adopted for the calculation of MD-MD ET in $Cs_2NaTmCl_6$ [360].

Due to such uncertainties, and the lack of knowledge about the electronic matrix element, *J*, many previous analyses of ET phenomena have attempted to ascertain the mechanism from the inter-ion distance dependence of the transfer rate, which is R^{-10}, R^{-8} and R^{-6} for EQ-EQ, EQ-ED and ED-ED (or MD-MD) ET, respectively. In the Inokuti-Hirayama approach, the donor luminescence intensity as a function of time is given by [361]

$$[I(t)/I(0)] = \exp\left[-t/\tau_0 - \Gamma(1-3/s)(c/c_0)(t/\tau_0)^{3/s}\right] \tag{69}$$

where c_0 is the critical transfer concentration and c is the acceptor concentration; τ_0 is the lifetime in the absence of quenching by the acceptor; and Γ represents the gamma function. Here, s is the fitting parameter to identify the type of multipole interaction, being equal to 6, 8 and 10 for ED-ED, ED-EQ and EQ-EQ ET, respectively. The model neglects the migration between donor ions, and does not take into account the angular dependence of donor-acceptor transfer. It has been employed to analyse the quenching of the $^1G_4$ blue emission in neat $Cs_2NaTmCl_6$ [346]. Several of the cross-relaxation pathways are resonant to within experimental error, and one of these, Fig. 24c, is

$$\mathrm{D}^* f'\left(^1\mathrm{G}_4\right)\Gamma_{5g}[20,851] + \mathrm{A}i\left(^3\mathrm{H}_6\right)\Gamma_{1g}[0] \rightarrow \mathrm{D}f\left(^3\mathrm{H}_5\right)\mathrm{a}\Gamma_{4g}[8241] + \mathrm{A}^* i'\left(^3\mathrm{H}_4\right)\Gamma_{3g}[12,607] \tag{70}$$

The efficiency of luminescence quenching, η:

$$\eta = W_{DA}/(W_{RAD} + W_{DA}) = 1 - \tau/\tau_0 \tag{71}$$

where τ and τ_0 are the lifetimes with, and in the absence of ET, is >90% in a $Cs_2NaGdCl_6$:Tm^{3+} sample with 10 mol% doping. The results indicate that

s=6, although the curve fitting is rather insensitive to the value of s. The refinements to the theory which include migration [362] and the presence of acceptor sites as discrete shells [363] would require further parameters.

An alternative approach without any fitting is to assume a certain type of interaction, and then calculate J in Eq. (66), and hence W_{DA} in Eq. (64). This has been done for the MD-MD interaction in Eq. (70), since the donor and acceptor transitions are ED forbidden but MD allowed. The interaction energy is calculated between the magnetic dipoles μ_{D^*} and μ_A, for the appropriate orientations and numbers of ions in each acceptor shell [360]. The results are listed in Table 13, column 4. It is evident that the dominant D*-A ET interaction occurs for the 12 Tm^{3+} nearest neighbours, with a nonradiative ET rate of the order 10^4–10^5 s^{-1}, so that the efficiency of quenching the $^1G_4$ emission is almost 100% for neat $Cs_2NaTmCl_6$, as observed experimentally.

Other resonant (as well as nonresonant) quenching mechanisms are however, possible, for this system. For example, considering the fact that both nonradiative transitions are EQ allowed, the site-site coupling strength is given by

$$J = \langle {}^3H_4, {}^3H_5 | H_{DA} | {}^3H_6, {}^1G_4 \rangle \tag{72}$$

where H_{DA} is the EQ-EQ interaction operator, and the values of W_{DA} thus calculated [364] for EQ-EQ interaction are listed in Table 13, column 5. The ET rate now exceeds that due to MD-MD interaction, for the nearest acceptor shells, and the first nearest-neighbour EQ-EQ ET dominates. It has been pointed out that the EQ-EQ ET rate differs from the MD-MD ET rate not only in its stronger dependence (by a factor R^{-4}) upon donor-acceptor distance, but also regarding its geometrical anisotropy [364, 365].

EQ-EQ energy migration is calculated to be fast (~10^7 s^{-1}) for the $^1G_4$ state of Tm^{3+} in $Cs_2NaTmCl_6$ [364], and of the order 10^9 $s^{-1}$for the $^2F_{5/2}$ state of Yb^{3+} in $Cs_2NaYbCl_6$ [366]. For other cases, such as the $^5D_0$ state of Eu^{3+} in $Cs_2NaEuCl_6$, migration is not possible by ED-ED, MD-MD or EQ-EQ mechanisms. Besides exchange interactions, one further mechanism can be formulated by taking Förster-Dexter theory to higher order, where donor and acceptor ions undergo virtual transitions to opposite-parity intermediate states, as in Fig. 24e, where D and A are the same species [367]. Following this ED,ED-ED,ED mechanism, the migration rate to first shell neighbours for the $^5D_0$ state of the above Eu^{3+} system is calculated to be ~500 s^{-1}. Experimental measurements of the luminescence decay from $^5D_0$ in neat $Cs_2NaEuCl_6$ have been made at long decay times [321]. In this regime, migration becomes important and the decay is exponential with a decay constant $k+k_M$, where k_M is the migration rate. The derived value of k_M was in the region 10^2 s^{-1}, in reasonable agreement with calculation.

13.2 Phonon-assisted Energy Transfer: Diagonal Process

The CF of Ln^{3+} varies from site to site due to the presence of defects, dislocations or lattice strains which inhomogeneously broaden and shift the energy levels. In this case, and also in other cases where there is an energy mismatch between the donor and acceptor excitations, energy conserving mechanisms are required. These can involve many-body processes [356] or the absorption or emission of phonons (crystal lattice vibrations). The conventional theory of phonon-assisted ET has been proposed [368] (and following the authors Holstein, Lyo and Orbach, it is hereafter abbreviated to HLO theory), and incorporates electron-phonon coupling as well as multipole interactions between the donor and acceptor ions. This *diagonal* process involves electronic matrix elements between only the donor and acceptor f-electron energy levels, such as in Fig. 24f. The matrix element for the site-site coupling Hamiltonian is given by Eq. (66). Since the multipole interaction in a centrosymmetric system is limited to EQ (and higher terms), the process may be represented by (EQ↔EQ,V), where this includes (EQ-EQ,V) and (V,EQ-EQ) [369], so that theory is of second-order, but it refers to a parity allowed electronic process. As pointed out in [368], the "Förster" ET rate for a one-phonon process would be given by the square of the site-site coupling matrix element, multiplied by the convolution of the emission profile at one site with the absorption profile of the other (with both profiles including the vibronic sidebands). However the 'spectral overlap' treatment approaches the HLO treatment only when the ion-phonon interaction takes place at one site only. If phonon interactions take place at both sites in the ET process, the ET rate cannot be obtained from spectral overlap considerations [368].

We only consider the one-phonon-assisted process in the weak-coupling limit, where D and A are taken to be the same species. For an isotropic crystal, the donor-acceptor ET rate is given, for a large energy mismatch (~100 cm^{-1}) between the donor and acceptor excitations, ΔE (also equal to the phonon energy), under the Debye phonon model, by the expression [368]

$$W_{DA} = \frac{J^2(f-g)^2|\Delta E|}{\pi\hbar^4\rho}\left(\sum_s \frac{\alpha_s}{u_s^5}\right)\left\{\begin{matrix} n(|\Delta E|)+1 \\ n(|\Delta E|)\end{matrix}\right\} \tag{73}$$

where f and g denote the (diagonal) electron-phonon coupling strengths for ground and excited states, respectively; ρ is the mass density; u_s is the velocity of sound (spread velocity) for the particular polarization index s; α_s is about 1, and concerns the average value of the strain tensor of solid angle Ω:

$$\alpha_s k^2 = \frac{1}{4}\langle \left(e_{s,\alpha}k_\beta + e_{s,\beta}k_\alpha\right)^2 \rangle_\Omega \tag{74}$$

where $e_{s,\alpha}$ is the αth component of the polarization vector for the s polarization (i.e. longitudinal or transverse); and k is the magnitude of the phonon wavevector. The quantities at the top ($n(|\Delta E|)+1$, referring to phonon emission) and bottom ($n(|\Delta E|)$, referring to phonon absorption) of Eq. (73) are Bose factors, where

$$n(|\Delta E|) = \left[\exp\left(|\Delta E|/k_B T\right) - 1\right]^{-1} \tag{75}$$

When $|\Delta E| < k_B T$, the expression at Eq. (73) simplifies to

$$W_{DA} = \frac{J^2 (f-g)^2}{\pi \hbar^4 \rho}\left(\sum_s \frac{\alpha_s}{u_s^5}\right) k_B T \tag{76}$$

By contrast, when there is a small energy mismatch between the donor and acceptor excitations, the donor-acceptor ET rate is given by

$$W_{DA} = \frac{J^2 (f-g)^2 |\Delta E|^2 R^2}{6\pi \hbar^6 \rho}\left(\sum_s \frac{\alpha_s}{u_s^7}\right) k_B T \tag{77}$$

where R is the donor-acceptor intersite distance.

Several conclusions may be drawn from the results from Eqs. (76) and (77). First, Eq. (77) is considerably smaller than Eq. (76), so that for small energy mismatch, ET between similar ions is unlikely to occur by this mechanism. Second, the phonon modulation of the lattice serves to make the site energies equal, only when the electron-phonon coupling strengths (at each site) differ in the ground and excited electronic states, and when the phonon wavelength is less than the distance between the two sites. Thus the transfer rate of the one-phonon-assisted process (Eq. 76) is independent of the energy mismatch, and linearly dependent upon temperature. These considerations led HLO to formulate higher-order mechanisms for phonon-assisted ET involving two phonons [368]. However, in general the ET rates between lanthanide ions in elpasolite lattices appear to be far too small, when estimated from the diagonal mechanism, since the electronic matrix elements J_{QQ} are small, and the difference $(f–g)$ between f^N excited-state and ground state electron-phonon coupling constants is small.

13.3 Phonon-assisted Energy Transfer: Nondiagonal Process

A second type of mechanism, (EQ↔EDV) for phonon-assisted ET involves nondiagonal electronic matrix elements, since one phonon is involved in an EDV transition at one site to compensate the energy mismatch, whilst also introducing odd-parity electronic operators making a transition from a $4f^N$

state to a $4f^{N-1}5d^1$ state. An EQ transition occurs at the other site. One case is illustrated in Fig. 24g, where the EQ transition at the donor is coupled by multipolar interactions with the EDV transition at the acceptor ion. The Debye phonon model approximation was used as in HLO theory, although it is a good approximation only when the phonon involved is an (odd-parity) acoustic mode with small wavevector **k**. Then, when the intersite energy mismatch is large, and $|\Delta E| < k_B T$, the ET rate is given by [369]

$$W_{DA} \cong \frac{J^2(\Delta E)^2}{\pi \hbar^4 \rho} \sum_s \frac{\alpha_s}{u_s^5} (k_B T) \tag{78}$$

where from Eq. (66):

$$J = \langle [\mathrm{D}], \mathrm{A}^* | \mathrm{H}_{DQ} | [\mathrm{D}^*], \mathrm{A} \rangle \tag{79}$$

and H_{DQ} is the dipole-quadrupole interaction operator. The square brackets represent the first-order approximative perturbation wavefunctions of the donor by taking the localized electron-phonon coupling Hamiltonian as the perturbation operator. Under the same conditions, $|\Delta E| < k_B T$, the ET rate for the case when the intersite energy mismatch is small, is found to be twice that in Eq. (78). It is important that the interference factor $\left|e^{\pm i\mathbf{k}\cdot\mathbf{R}} - 1\right|^2 \approx |1-1|^2 = 0$ present in the diagonal HLO treatment is changed to be $\left|e^{\pm i\mathbf{k}\cdot\mathbf{R}} + 1\right|^2 \approx |1+1|^2 = 4$ now, so that a small energy mismatch in nonresonant ET (including energy migration) can be made up by one nondiagonal phonon-assisted ET process, provided that the phonon density of states is sufficient. The ET rate for this process increases quadratically with increasing intersite energy mismatch, and linearly with temperature.

The phonon involved has recently been described by a running lattice wave model and the same significant difference between the coherence effects of the diagonal and nondiagonal ET cases was found to occur [369]. However, some further insights are gained. In particular, optical phonons with **k**=0 and appreciable energy (250 cm^{-1}, for example) can make important contributions to one-phonon-assisted nondiagonal ET processes. The site selection rule (Eq. 29) for the EDV process operates, as well as certain 3j symbol triangle selection rules for angular momentum. For example, under the Judd-closure approximation, for an EDV donor transition, the triangle relation (J_f, λ, J_i) with λ=2,4,6 must be satisfied; and for an EQ acceptor transition, (J_f, 2, J_i). The extension of the nondiagonal phonon-assisted ET model to two-phonon-assisted processes (EDV↔EDV) is straightforward and although the formulae are more complex, simple vibronic selection rules operate. Contrary to HLO theory, according to the running lattice wave model of the phonon involved [369], an optical phonon with nonzero **k** and high symmetry (therefore, high density of states), can make an important contribution to *both* the nondiagonal and diagonal ET processes.

The HLO model has generally been tested by observing the temperature-dependence of the transfer rate, but no detailed calculations of ET rates, by including the evaluation of electronic factors, have been made for Ln^{3+} systems. In principle, such calculations are tractable for the nondiagonal case but have not yet been forthcoming. The general approach of the data analysis for nonresonant ET processes in lanthanide elpasolite systems has been to utilize a R^{-6} dependence of the transfer rate (i.e. for EDV↔EDV processes) and to allow for transfer to successive shells of acceptor neighbours (without detailed consideration of the electronic matrix elements or the phonons involved, Sect. 13.4.1), or to employ a spectral overlap model (Sect. 13.4.2). Some of these studies are now reviewed.

13.4 Experimental Studies of Energy Transfer

13.4.1 Concentration Quenching in Neat Elpasolite Systems

The emission from certain multiplets of diluted lanthanide elpasolite systems is quenched by ion-ion cross relaxations in the neat materials (Fig. 24c, where D and A are the same species). Some examples of these concentration quenchings are the $^4F_{3/2} \rightarrow {}^4I_{9/2}$ emission of Nd^{3+} in $Cs_2NaNdCl_6$ [308] and M_2KNdF_6 (M=Rb, Cs) [309]; the $^5D_1 \rightarrow {}^7F_0$ emission of Eu^{3+} in $Cs_2NaEuCl_6$ [322] and Cs_2NaYF_6:Eu^{3+} [25]; the $^4G_{5/2} \rightarrow {}^6H_{5/2}$ emission of Sm^{3+} in $Cs_2NaSmCl_6$ [314]; the $^4S_{3/2} \rightarrow {}^4I_{15/2}$ emission of Er^{3+} in $Cs_2NaErCl_6$ [335, 341, 342]; and the $^3P_0 \rightarrow {}^3H_4$ emission of Pr^{3+} in $Cs_2NaPrCl_6$ [305]. All of the cross-relaxation processes responsible for these quenchings are nonresonant and presumably correspond to (EDV↔EDV) processes, since the ET rate is inversely proportional to the sixth power of the interion separation, R. The nearest neighbour dependence of the transfer rate has been systematically calculated using a shell model [305, 306] and a crystal model [370, 371], and the application to Pr^{3+} is summarized here.

In the absence of migration between donors or acceptors, and of acceptor-donor back-transfer, the decay of the emission of the Ln^{3+} donor ion participating in a two-ion cross-relaxation process with identical acceptors, Fig. 24c is described by [305]

$$\frac{I(t)}{I(0)} = \exp\left(-k - \sum_{n}^{shells} r_n k_n\right) t \qquad (80)$$

at weak excitation intensities, where k_n is the transfer rate to the nth-shell acceptor, with occupancy factor r_n; k is the (radiative plus nonradiative) decay constant for an isolated donor ion. Considering only ED-ED interactions in a face-centred cubic lattice, this equation may be formulated as

$$\frac{I(t)}{I(0)} = \exp(-kt) \prod_{n}^{allshells} \exp\left(-r_n \left(\frac{R_1}{R_n}\right)^6 k_{ET} t\right) \tag{81}$$

where k_{ET} is the ET rate to a single ion at the position of nearest neighbour acceptor at distance R_1. This equation applies to a single donor ion, which thus has an exponential decay. However, for diluted crystals, randomly-distributed donors will have different shell occupancy factors for acceptor ions, so that the sum of the exponential decay processes will become non-exponential. This is taken into account by including the statistical probability, $O_{r_n}^{N_n}(x)$, of a specific shell n in which surrounding r_n sites are occupied by a lanthanide ion from N_n possible positions (and the remaining sites occupied by the ion Y^{3+} in $M_2ALn_xY_{1-x}Cl_6$, which is not involved in ET processes). The probability of a particular distribution with r_1 Ln^{3+} ions in shell 1, r_2 in shell 2, etc., is then the product of these statistical probabilities over the n shells, so that Eq. (81) may be written as

$$\frac{I(t)}{I(0)} = \exp(-kt) \prod_{n}^{allshells} \sum_{r_n}^{N_n} O_{r_n}^{N_n}(x) \times \exp\left(-r_n \left(\frac{R_1}{R_n}\right)^6 k_{ET} t\right) \tag{82}$$

As pointed out in Section 13.1, even at x=1, some 98% of the ET to the acceptors is included up to the 3rd shell. At x<0.02, only the singly-occupied shell is probable, whereas at x=0.15 there is an equal probability of single and double occupancy of the shell. The model assumes a uniform dielectric, even though some nearby ions block the ET pathway to more distant ones. Deviations from exponential decay are apparent when $k_{ET} \sim k$, but at large values of k_{ET} the n=1 factor dominates to give a double-exponential decay, with the fast process giving k_{ET} directly. For x=1, the decay is exponential with a decay constant equal to $k(1)=k+14.4k_{ET}$. Figure 25a shows the computed decay curves for various ratios of k_{ET} and k.

In the case of $Cs_2NaPr_xY_{1-x}Cl_6$, the cross-relaxation for quenching $^3P_0$ emission, Fig. 24c, is nonresonant and is a EDV-EDV process, of which there are several pathways, such as

$$\left(^3P_0\right)\Gamma_1[20,602](D^*) \rightarrow \left(^1G_4\right)\Gamma_5[10,325] + \nu_4[99](D) \tag{83a}$$

$$\left(^3H_4\right)\Gamma_1[0](A) \rightarrow \left(^1G_4\right)\Gamma_4[9894] + \nu_3 ZB[285](A^*) \tag{83}$$

where the square brackets denote energies (cm^{-1}), referring to Cs_2NaYCl_6:Pr^{3+}. Note that both processes are spin-forbidden so that the ET process does not completely quench the $^3P_0$ emission even for x=1. The emission decay curves, Fig. 25a, show the effect of the shortening of the lifetime and the non-exponential behaviour as x increases. The two fitted curves (x=0.25 and 0.5) in Fig. 25b utilise k=3610 s^{-1} (from the pure expo-

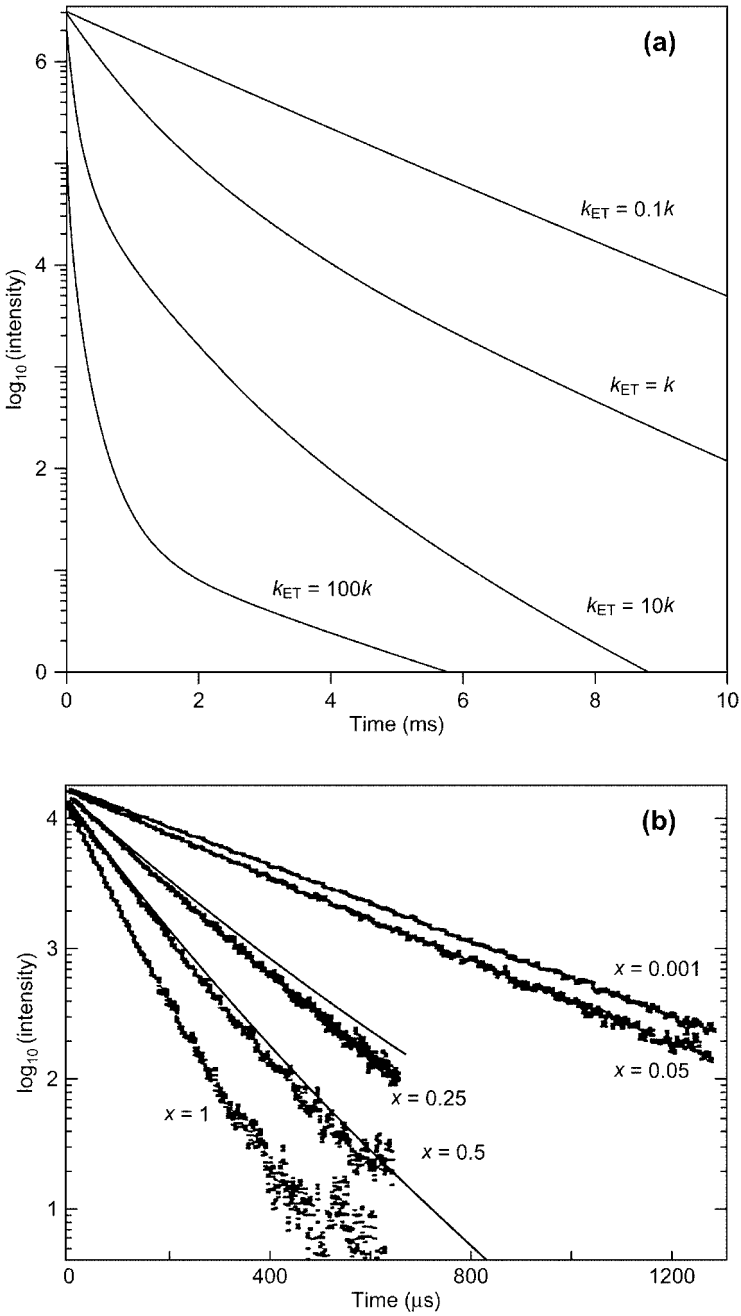

Fig. 25a, b Luminescence decay curves **a** computed for different ratios of k_{ET} and k (Eq. 82 with x=0.25 and k=500 s^{-1}) [314]; **b** 468 nm excited 80 K luminescence decay curves for $Cs_2NaY_{1-x}Pr_xCl_6$ for different x, with the computed curves for x=0.25, 0.5 employing k=3610 s^{-1} and k_{ET}~1350 s^{-1} (Adapted from [305, 314])

nential decay of a very dilute crystal) and k_{ET}=1350 s^{-1} (from the exponential decay of a crystal with x=1, with constant k_{ET}) [305].

The shell model has been applied to the quenching of the $^4G_{5/2}$ emission of Sm^{3+} in $Cs_2NaY_{1-x}Sm_xCl_6$, with less satisfactory results. Again, the cross-relaxation processes are certainly nonresonant, but the EQ↔EDV process cannot be excluded. Some factors which might account for the deviation of fitted decay profiles from experiment have been discussed [310, 314], including the presence of migration and the size inequality of Ln^{3+} and Y^{3+}, which would affect the shell occupancies. Better agreement of simulated decay curves with experimental decay curves was found when the donor-acceptor ET was truncated to occur just over the first few shells [311], so that the nature of the multipole-multipole interaction then becomes unclear. One factor which is not taken into account is the fact that the quenching can occur by many different EDV-EDV and/or EQ↔EDV pathways, each with a different cross-relaxation rate, and that the relative importance will change with temperature if the initial states are thermally populated.

A more general microscopic model, the crystal model [370], has been formulated for dipole-dipole ET in which an 'angular class' of ions (made up, from the translational symmetry properties of the lattice, of the set of acceptor ions having the same angular orientation with respect to the donor ion) is employed instead of a shell. The model does not include migration between donor ions, or back transfer. The phonon part is not considered, since the model is based upon the distance-dependence of the transfer rate to the angular classes of acceptor ions. The master equation for (EDV↔EDV) processes is [370]

$$\frac{I(t)}{I(0)} = \exp\left[(-k - x\zeta(6)L(l)k_{ET})t\right] \tag{84}$$

where $\zeta(6)$ is the Reimann zeta function for the order 6 of dipole-dipole interaction, and $L(l)$ is a lattice parameter for the l-th angular class. Note that $\ln[(I(t)/I(0)]$ shows a linear dependence with acceptor concentration, x. The crystal model was further extended [371] to take into account the deviations of fitted curves, using the behaviour (Eq. 84), from experimental data at intermediate values of x. These deviations were not attributed to migration effects, but to the statistical fluctuations of the populations of angular classes. Thus a correction term, $\Delta_{stat}(x,t)$, was introduced which depends upon the average of the statistical fluctuations in the population of acceptors and which leads to closer agreement with experiment at early time stages.

Finally, it is noted that the absence of emission from a particular energy level, in a crystal with a high concentration of optical centres, may arise from several other reasons. First, level bypassing may occur in the more concentrated crystals when the excitation is into an upper level which can undergo a cross-relaxation process to a rather lower level. This is the case for the quenching of $^5F_4 \rightarrow {}^5I_8$ green emission of Ho^{3+} in neat $Cs_2NaHoCl_6$,

when excitation is into the next-highest multiplet term, $^5F_3$. The (nonresonant) cross-relaxation process $^5F_3 \rightarrow {}^5F_5$ at the donor, and $^5I_8 \rightarrow {}^5I_7$ at the acceptor produces intense red $^5F_5 \rightarrow {}^5I_8$ emission [333]. Second, the elpasolite systems Cs_2NaLnX_6 (X=Cl, Br) are particularly hygroscopic so that defect-sites readily occur with the Ln^{3+} ion adjacent to oxychloride or hydroxide ions. Thus, the $^5D_0$ state of Eu^{3+} in $Cs_2NaEuCl_6$ exhibits a non-exponential, faster decay for samples where such defects are present [319]. It is interesting, however, that the decay characteristics are more sensitive to the presence of these defects than are the emission spectra themselves.

13.4.2
Cross-relaxation Involving Different Donor and Acceptor Species

The shell model has been utilized in the interpretation of the ET cross-relaxation processes in systems of the type $Cs_2NaLn_xLn'_{1-x}Cl_6$ and $Cs_2NaLn_xLn'_yB_{1-x-y}Cl_6$, where Ln=Sm, Ln′=Eu, B=Gd or Y [312, 313, 316–318], with varying degrees of success. A two-centre crystal model has been developed for these types of system and the predicted emission decay behaviour resembles the double exponential type [372].

Other $M_2ALnLn'Cl_6$ systems where f^N-f^N ET processes have been observed between Ln and Ln′ are Ho and Er [186]; and Yb and Ho or Nd [149, 333, 348]. The f^1d^1 Pr^{3+}-d^1 Ce^{3+} ET is evident when exciting into Pr^{3+} absorption bands and observing the Ce^{3+} $d^1 \rightarrow f^1$ emission [206, 260]. By fitting the decay of the 295 K Ce^{3+} emission to an expression of the form

$$I = A[\exp(-t/\tau_{Ce}) - \exp(-t/\tau_{Pr})] \tag{85}$$

where $I(0)=0$ and A is a constant, the d→f emission lifetimes were found to be 30 ns and 20 ns for Ce^{3+} and Pr^{3+}, respectively [260]. The decay of the Pr^{3+} $f^1d^1 \rightarrow f^2$ emission has also been measured in neat $Cs_2NaPrCl_6$ (13 ns) and dilute $Cs_2NaY_{0.99}Pr_{0.01}Cl_6$ (18 ns) at 8 K, where the concentration quenching was attributed to a nonresonant cross-relaxation from the lowest f^1d^1 level [206].

The major interest in this section focuses upon the Tb^{3+} to Eu^{3+} ET in the systems $Cs_2NaTb_{1-x}Eu_xCl_6$, $Cs_2NaEu_xTb_{0.005}Y_{0.995-x}$ and $Cs_2NaEu_{0.05}Tb_yY_{0.95-y}$ because the explanation for this ET process is elusive up to the present. This $Tb^{3+} \rightarrow Eu^{3+}$ ET has been investigated in the system $Tb_{0.66}Eu_{0.33}P_5O_{14}$ [373], and a summary of previous work is given therein. It was found that the $^5D_1 \rightarrow {}^7F_1$ emission lines of Eu^{3+} were observed on excitation of the $^5D_4$ manifold of Tb^{3+}, and the $^5D_1$ lifetime was found to be equal to the $^5D_4$ lifetime under these conditions [373]. Two possible transfer processes were considered at low temperature:

$$Tb^{3+}(^5D_4) + Eu^{3+}(^7F_0) + \text{phonon(s)} \rightarrow Tb^{3+}(^7F_4) + Eu^{3+}(^5D_0) \tag{86a}$$

$$Tb^{3+}\left({}^5D_4\right) + Eu^{3+}\left({}^7F_0\right) \rightarrow Tb^{3+}\left({}^7F_6\right) + Eu^{3+}\left({}^5D_1\right) + \text{phonon(s)} \qquad (86b)$$

where the phonon energies are ~20–300 cm^{-1} in Eq. (86a), and~1000 cm^{-1} in Eq. (86b), and Eq. (86b) was concluded to be the most important process.

The energy level diagrams for the Tb^{3+} and Eu^{3+} systems in elpasolite lattices are shown in Fig. 26a. In the first experimental study of Tb^{3+}-Eu^{3+} transfer in elpasolite hosts, the quenching of the $^5D_4$ emission produced luminescence from the $^5D_0$ level of Eu^{3+}. No emission was detected from $^5D_1$, although this luminescence could be observed upon direct excitation of $^5D_1$ in $Cs_2NaTb_{1-x}Eu_xCl_6$, so that Eq. (86b) was excluded from the ET, and the most likely processes were formulated as Eqs. (86a) and (86c):

$$Tb^{3+}\left({}^5D_4\right) + Eu^{3+}\left({}^7F_1\right) \rightarrow Tb^{3+}\left({}^7F_4\right) + Eu^{3+}\left({}^5D_0\right) + \text{phonon(s)} \qquad (86c)$$

Equation (86c) would infer a strong temperature dependence, by a factor >100, between the 77 K and 295 K ET rates.

The emission intensity from $^5D_4$ in the system $Cs_2NaTb_{1-x}Eu_xCl_6$ was fitted to an equation of the type of Eq. (80), where the summation was just represented by k_{ET} [324–326]. The graph of the resulting parameter, k_{ET}, with concentration of Eu^{3+}, x, at 293 K is shown in Fig. 26b, and its linearity was taken to indicate that (i) the same process operates over the entire concentration range at 293 K, and (ii) the ET involves only one Eu^{3+} ion. The behaviour was found to be different at 80 K (Fig. 26b), where k_{ET} varies linearly with x only for x=0.01–0.15, but is smaller, and independent of x when x=0.85–0.99 [325]. The luminescence decay curves for $Cs_2NaEu_xTb_{0.005}Y_{0.995-x}$ at 77 K and 295 K showed slight deviation from exponential behaviour [374], and the ET rate is again greater at room temperature, and varies roughly linearly with Eu^{3+} concentration (Fig. 26b). In this system the migration between donors is negligible, so that the transfer occurs from the excited Tb^{3+} ion to nearest neighbour Eu^{3+} ion. For the system $Cs_2NaEu_{0.05}Tb_yY_{0.95-y}Cl_6$, where the Tb^{3+} concentration was varied [374], only the decay curves for $y \geq 0.5$ were single exponential at 295 K. The plot of the $Tb^{3+} \rightarrow Eu^{3+}$ ET rate against Tb^{3+} concentration, y, for this system is shown in Fig. 26c. The regions where k_{ET} is independent of y (e.g. up to y~0.05 at 77 K) correspond to negligible donor migration. The transfer rate decreases above y~0.5.

The intensity of the Eu^{3+} $^5D_0$ emission in Cs_2NaTb_{1-x} Eu_xCl_6, following pulsed excitation into Tb^{3+} $^5D_4$, was well-fitted to an expression analogous to Eq. (85), where the first lifetime corresponds to that of $^5D_0$ for the corresponding concentration of Eu^{3+} diluted into Cs_2NaYCl_6, and the second lifetime to the Tb^{3+} $^5D_4$ lifetime. This shows the direct feeding of $^5D_0$ from $^7F_4$, in the presence of fast migration between Tb^{3+} donors.

Attempts have been made to calculate the cross-relaxation rate from Tb^{3+} to Eu^{3+} by using the spectral overlap model, which employs the donor emission spectrum and its overlap with the acceptor absorption spectrum. It is

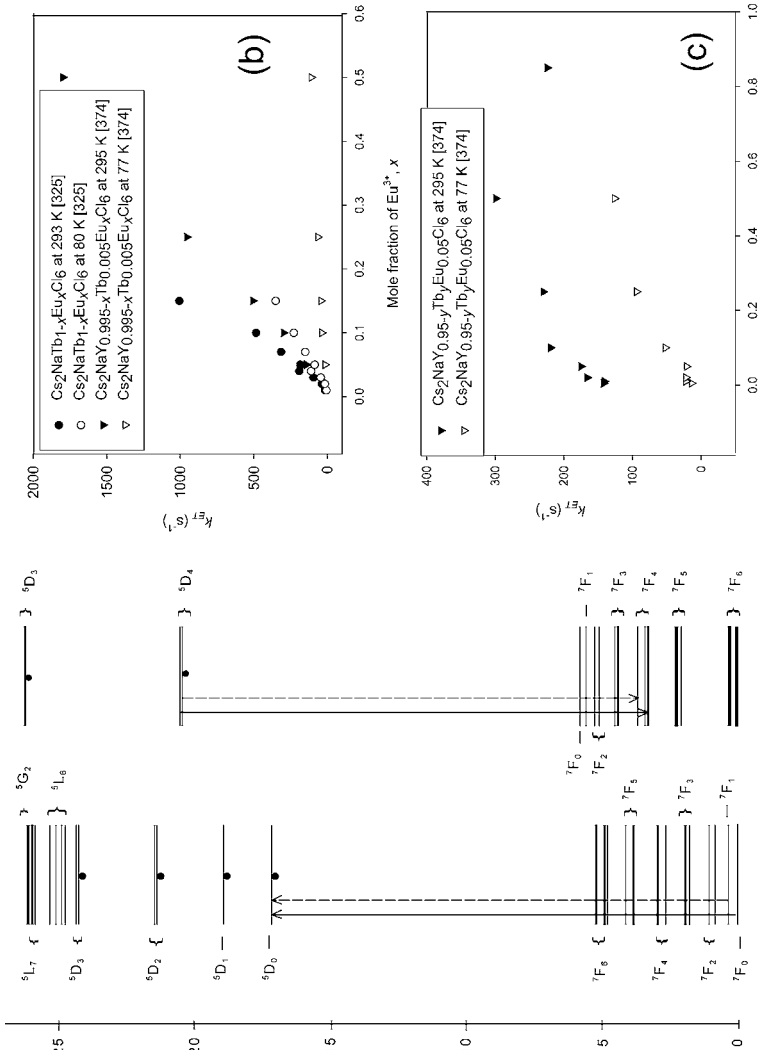

Fig. 26 **a** Partial energy level diagrams for Tb^{3+} and Eu^{3+} in the $Cs_2NaLnCl_6$ elpasolite lattice, showing the luminescent states and the possible cross-relaxation pathways for ET in this system—*full line* (Eq. 86a), *dotted line* (Eq. 86c). The process is EDV-EDV but the nature of the phonons involved is not indicated in the diagram; **b**,**c** Plot of ET rates from the $^5D_4$ state, k_{ET}, at room and liquid nitrogen temperatures against concentration of Eu^{3+} or Tb^{3+} in the crystal (Data from [216, 228]. Figures adapted from [325, 374])

noted that this model treats these EDV transitions as if they are electronic transitions. Both of the Tb^{3+} emission and the Eu^{3+} absorption spectra are EDV in character, with the exception of a few MD lines. The electronic transition element, *J*, in the Fermi Golden rule (Eq. 64) was calculated from the components of the transition moments, M_{if} and M_{fi}, which in turn were related with the transition oscillator strengths (Eq. 15). Explicitly, the interaction energy, *J*, between the dipole at the donor site, M_D, and that at the acceptor site, M_A, is given by the expression

$$J = \frac{1}{4\pi\varepsilon_0 R^3} M_D \cdot C \cdot M_A \tag{87}$$

where M_B comprises the Cartesian vector components of the transition moment of B=A or D; and C is the dipolar coupling tensor [375]. The interaction energies were summed over the nearest neighbour shells. The lineshape function (Eq. 65) was calculated from the widths and energies of the spectral features, assuming Lorentzian shapes. From the spectral profiles, the Tb^{3+}-Eu^{3+} spectral overlap must occur between hot bands in the $(^7F_0)\Gamma_{1g} \rightarrow (^5D_0)\Gamma_{1g}$ absorption spectrum (with oscillator strengths 10^{-11} to 10^{-12}), and vibronic structure in the $^5D_4 \rightarrow {}^7F_4$ emission spectrum (with oscillator strengths $\leq 10^{-9}$). By an examination of the individual spectral overlaps, the $Tb^{3+} \rightarrow Eu^{3+}$ ET rate was calculated to be of the order 10^{-4} s^{-1} [376], which is far from the measured value at 80 K in $Cs_2NaTb_{0.1}Eu_{0.1}Cl_6$ of 228 s^{-1}. A more detailed calculation along similar lines has also been made of the transfer rate in $Cs_2NaY_{0.995-x}Tb_{0.005}Eu_xCl_6$, and the discrepancy with experiment was also found to be of the order 10^{-4} to 10^{-5} [374]. Near agreement between experimental and calculated (by the spectral overlap approach) ET rates could only be achieved by treating the Tb^{3+} $^5D_4 \rightarrow {}^7F_4$ and Eu^{3+} $^7F_0$, $^7F_1 \rightarrow {}^5D_0$ multiplet to multiplet transition manifolds as continuous and perfectly overlapping spectral distributions [374]. This pseudo-agreement is then a similar result just as for $Tb^{3+} \rightarrow Eu^{3+}$ ET in low-symmetry systems, where spectral features are broad (e.g. in mixed tris-(acetylacetonato) Tb^{3+}-Eu^{3+} dimers, where in solution at 295 K, k_{ET} (calc)~(3–8)×10^4 s^{-1} and k^{ET} (obs)~5×10^4 s^{-1}) [377]. However, as pointed out by Moran et al., there is little justification to ignore the detailed, well-characterized structural and spectral information available from the elpasolite systems when making this type of calculation.

A more recent *spectral* study of $Tb^{3+} \rightarrow Eu^{3+}$ ET in the system $Cs_2KTb_{0.9}Eu_{0.1}Cl_6$ showed that ET occurs from Tb^{3+} $^7F_4$ to Eu^{3+} $^5D_0$ (and not to $^5D_1$) at 300 K, but that this was totally quenched at 11 K [378], so that the initial Eu^{3+} acceptor state is not $^7F_0$. Finally, it is noted that the spectral overlap model has been used successfully to account for the $Tb^{3+} \rightarrow Eu^{3+}$ ET in $Na_3[Tb_{0.01}Eu_{0.99}(ODA)_3]\cdot 2NaClO_4 \cdot 6H_20$ (ODA=oxydiacetate), where k_{ET} 100 s^{-1} at 295 K [379].

13.4.3 Upconversion

Various processes can lead to upconversion (i.e. emission of photons of higher energy than the pump energy) for M_2ALnX_6 systems, but with the exclusion of second harmonic generation. Considering one-colour excitation only in the following, (simultaneous) TP absorption, Fig. 24h, is a single-ion process which can populate an electronic state (or a vibronic state involving an even parity vibration, subject to the relevant selection rules) which occurs only during the laser pulse. Second, (sequential) ESA is another single ion process occurring during the laser pulse, which may populate a terminal electronic state (f', Fig. 24i) or vibronic state (dotted line above f', Fig. 24i) from an initially populated excited state f (Fig. 24i). This process frequently competes with ET upconversion, Fig. 24d, which is at least a two-ion process.

Some of the upconversions reported for neat lanthanide elpasolite systems are: from red ($^5F_5$) to ultraviolet/blue ($^5G_5$, $^5F_3$) in $Cs_2NaHoCl_6$ [334]; red to blue [338] and green to ultraviolet [35, 277, 336, 380] in $Cs_2NaErCl_6$; from blue ($^1D_2$) to ultraviolet ($^3P_2$) in $Cs_2NaTmCl_6$ [344]; and for doped systems, from infrared to green ($^4S_{3/2}$) in $Cs_2NaEr_{0.2}Yb_{0.4}Y_{0.4}Cl_6$ [337, 381]; blue ($^5D_4$) to ultraviolet in Rb_2KInF_6:Tb^{3+} [329]; and blue to ultraviolet in $Cs_2NaY_{1-x}Pr_xCl_6$ [260]. Generally, the upconversion mechanism has not been conclusively identified, but some ways of attempting this are now reviewed.

Ignoring ESA, and the population of f from higher levels in Fig. 24d, then in the case of continuous excitation, assuming the steady state [382], the time dependent populations of levels f and f' in Fig. 24d are given by

$$\frac{dn_f}{dt} = Pn_i - \frac{n_f}{\tau_f} - 2Un_f^2 \tag{88a}$$

$$\frac{dn_{f'}}{dt} = Un_f^2 - \frac{n_{f'}}{\tau_{f'}} \tag{88b}$$

where P is the ground state absorption rate constant; U is the ion pair upconversion rate coefficient; n_j the population of level j; and τ_j are the single-ion lifetimes, so that

$$2Un_f^2 + \frac{n_f}{\tau_f} = Pn_i \tag{89}$$

which infers that for a given pump power, an increase in τ_f will lead to an increase in n_f, and to stronger emission from level f'. By contrast, the emission from f' following ESA (Fig. 24i), from a short pulse is independent of τ_f, and decays exponentially with lifetime $\tau_{f'}$.

Other distinguishing features between ESA and ET upconversion have been discussed in detail elsewhere [382], and in summary are (i) the presence of a risetime under pulsed excitation (which may disappear under

square wave excitation) in the emission from f' for the latter, but not the former; (ii) under certain experimental conditions, the intensity of an n-photon excitation process will scale as the n-th power of the excitation power [383]; (iii) the ET upconversion excitation spectrum closely resembles the (ground state) absorption spectrum, with the line profile of the former being approximately the square of that of the latter. In the case of ESA, additional features may be present, corresponding to the multiple absorption peaks in the upconversion process; (iv) the luminescence following ET upconversion will show a quadratic concentration dependence, whereas no such marked variation will result following ESA.

The most numerous, and most studied upconversions are those of Er^{3+} in $Cs_2NaLnCl_6$ (Ln=Y, Er, Yb). Referring to the energy levels of this system in Fig. 9d, the following upconversions have been observed. First, red to blue upconversion was reported at 15 K, with excitation into $^4F_{9/2}$ [277]. The blue emission exhibited a quadratic intensity dependence upon the laser power. The intensity was Er^{3+}-concentration dependent, with samples of Cs_2NaYCl_6 doped with <1 mol% Er^{3+} not giving detectable emission. Using a 10-ns pulse with frequency 1 Hz (to eliminate a possible population build-up in long-lived excited states), the upconverted emission from $^2G_{9/2}$ exhibited a rise-time >10 ms, so that it derives from a cross-relaxation process [277]. Several schemes can be formulated, whether phonon-assisted, or as follows for resonant EQ-EQ ET:

$$^4I_{9/2}a\Gamma_8[12,358](D^*) + {}^4I_{9/2}a\Gamma_8[12,358](A^*) \rightarrow {}^2G_{9/2}a\Gamma_8[24,425](A^{**}) + {}^4I_{15/2}c\Gamma_8[287](D) \quad (90a)$$

$$\text{or} \rightarrow {}^2G_{9/2}\Gamma_6[24,459](A^{**}) + {}^4I_{15/2}\Gamma_6[259](D) \quad (90b)$$

Equation (90) can be modelled by a 4-level system, involving $^2G_{9/2}$ (f'), $^4F_{9/2}$, $^4I_{9/2}$ (f) and $^4I_{15/2}$ [380], similar to Eqs. (88)a,b, except that level f is fed by branching from $^4F_{9/2}$, instead of being pumped directly from the ground state. Whereas the solution Eq. (89) refers to the steady state, the solution for the decay of $^2G_{9/2}$ luminescence following pulsed excitation is rather more complex. Although the experimental decay curve can be well-modelled, the upconversion rate constant U is not well-determined [380].

Upconversion to $^4G_{11/2}$ has been reported under red excitation, and attributed to the ET process involving $^4F_{9/2}$ and $^4I_{9/2}$ initial excited states [384]. Upconversion to $^2G_{9/2}$ has also been reported at 10 K under continuous wave green (514.5 nm) or blue (488 nm) excitation [335]. Again the presence of a risetime in the $^2G_{9/2}$ emission suggests that an ET process occurs, but in this case the $^4S_{3/2}$ term is involved, for example:

$$^4S_{3/2}a\Gamma_8[18,265](D^*) + {}^4I_{13/2}\Gamma_6[6492](A^*)$$

$$\rightarrow {}^4I_{15/2}a\Gamma_8[0](D) + {}^2G_{9/2}b\Gamma_8[24,519] + \nu_3[238](A^{**}) \quad (91)$$

although the contribution of ESA from $^4I_{13/2}$ has not been investigated.

Concerning the green to ultraviolet upconversion of Er^{3+} in elpasolites, a TP excitation process has been proposed for the population of the Er^{3+} $^2H(2)_{9/2}$ $a\Gamma_8$ state at 36,224±12 cm^{-1} in $Cs_2NaErCl_6$ at 15 K under pulsed laser excitation at 18,270 cm^{-1} [277], because the emission did not exhibit a rise-time and it could not be observed under continuous excitation. There is no pure electronic state at 2×18,270=36,540 cm^{-1}, but a vibronic state could be populated, corresponding to the excitation of one quantum of ν_1 in the $a\Gamma_8$ state. More recently, this upconversion to $^2H(2)_{9/2}$ has been achieved at 10 K using pulsed laser excitation at approximately 19,130 cm^{-1} (or several higher energies) so that in this case the upconversion mechanism is either ESA or cross-relaxation involving $^4S_{3/2}$ [35].

Finally, the infrared or red to green upconversion of Er^{3+} has also received attention. Luminescence from $^4S_{3/2}$ showed a risetime of ~6 ms, and exhibited a quadratic dependence upon incident laser power, upon excitation into the $^4F_{9/2}$ term of $Cs_2NaErCl_6$ [277]. Continuous wave infrared (~1 μm) excitation into $^4I_{11/2}$ is upconverted to green emission for $Cs_2NaErCl_6$ [385] and $Cs_2NaEr_{0.2}Yb_{0.4}Y_{0.4}Cl_6$ [337, 381]. The power-emission intensity dependence in the case of $Cs_2NaErCl_6$ is quadratic, and the emission intensity does not vary much between 100–300 K. The process has been assigned to a mechanism involving two ions initially in the $^4I_{11/2}$ state [385].

The reverse of upconversion is downconversion, where each quantum of (vacuum) ultraviolet radiation is converted to several quanta of infrared or visible radiation (quantum cutting) [386]. For example, the highest energy emission for the excitation of $Cs_2LiTmCl_6$:Nd^{3+} by 476.9 nm radiation is below ca. 11,300 cm^{-1}, since the cross-relaxation of $^1G_4$ Tm^{3+} level leads to the excitation of Tm^{3+} $^3H_5$ and Nd^{3+} $^4F_{3/2}$ [344].

13.4.4 Energy Transfer in Transition Metal-Lanthanide Systems

Some studies have been undertaken to investigate upconversion phenomena in elpasolite lattices doped with both rare earth and d-block ions. These have generally employed the d-block element as a sensitizer, having (i) a large (often spin-allowed) absorption cross-section in the near infrared-visible region, which overlaps the f^N emission; (ii) a wide gap to the next lower energy level, to minimize nonradiative losses and the probability of back-transfer from the lanthanide ion; and (iii) the capability of chemical tuning of the energy levels, to match the activator requirements, by ligand replacement. Cresswell et al. [345] chose Re^{4+} ($5d^3$) as sensitizer because it has electronic states at 13,850 and 15,300 cm^{-1} (but no others up to 29,000 cm^{-1}) which have intraconfigurational d-d transitions with lifetimes ~60 μs at 295 K. Thus when Cs_2NaYCl_6 was co-doped with Tm^{3+} and Re^{4+}, ET from

the latter to the former occurred under 647 nm excitation, since the Re^{4+} emission at 727 nm was quenched and the Re^{4+} $^2T_{2g}$ absorption bands appeared in the excitation spectrum of the Tm^{3+} infrared emission. A similar behaviour was found for the Cs_2ZrCl_6 host [387]. The ET was envisaged to occur to the $^3H_4$ or $^3H_5$ Tm^{3+} states, which then led to upconversion to the $^1D_2$ and $^1G_4$ states. $Yb^{3+}\rightarrow Re^{4+}$ ET is very efficient in $Cs_2NaYbCl_6$:Re^{4+}, leading to upconverted emission from the Re^{4+} $^2T_{2g}$ state [388]. Upconverted luminescence was also observed from both Tm^{3+} and Mo^{3+} in $Cs_2NaY_{0.9}Tm_{0.05}Mo_{0.05}Cl_6$ upon excitation in the $^3H_4$ Tm^{3+} state [387]. ET from Yb^{3+} to Mo^{3+} in $Cs_2NaYbCl_6$:Mo^{3+} is very efficient [369]. Taking advantage of the long lifetimes of Er^{3+} intermediate states, and of the near-transparency of Os^{4+} ($5d^4$) between 12,000 and 20,000 cm^{-1}, Cs_2NaYCl_6 was co-doped with Os^{4+} and Er^{3+} to give green Er^{3+} emission upon excitation into Os^{4+} levels near 11,000 cm^{-1} [343]. IR to visible upconversion was found to be inefficient in $Cs_2NaScCl_6$:Pr^{3+}:V^{3+} [389].

13.4.5 Photon Avalanche

Photon avalanche is a phenomenon where strong emission is obtained at shorter wavelengths than the excitation wavelength, even with very weak ground-state absorption at the pump wavelength [390–394]. The term refers to the orders-of-magnitude jump in emission intensity when the pump laser intensity crosses just above the critical threshold. A general energy level scheme for the avalanche process is shown in Fig. 24j. Very weak pump absorption from the ground state populates the f^N (vibronic) level l', which relaxes nonradiatively to the metastable level l. The strong ESA $l\rightarrow f'$ is followed by nonradiative decay to the emitting level f. Avalanche can then occur if the cross-relaxation probability $f\rightarrow l$ at the donor, and $i\rightarrow l$ at the acceptor, is higher than the relaxation rate from f to levels below l. Thus the ESA from level l is enhanced because one cross-relaxation decay of level f produces two ions, each in level l, which can then undergo ESA to level f. The mechanisms for the initial population of level l, besides thermal population, include absorption into a weak phonon sideband with subsequent nonradiative relaxation, and absorption of Raman scattered radiation. By analogy to Eq. (88), assuming that the phonon relaxations $f'\rightarrow f$ and $l'\rightarrow l$ are fast compared with other processes, then the following equations describe the excitation process in Fig. 24j [392]:

$$\frac{dn_i}{dt} = -P(l')n_i + W_l n_l + bW_f n_f - Un_i n_f \tag{92a}$$

$$\frac{dn_l}{dt} = P(l')n_i - P(f')n_l - W_l n_l + (1-b)W_f n_f + 2Un_i n_f \tag{92b}$$

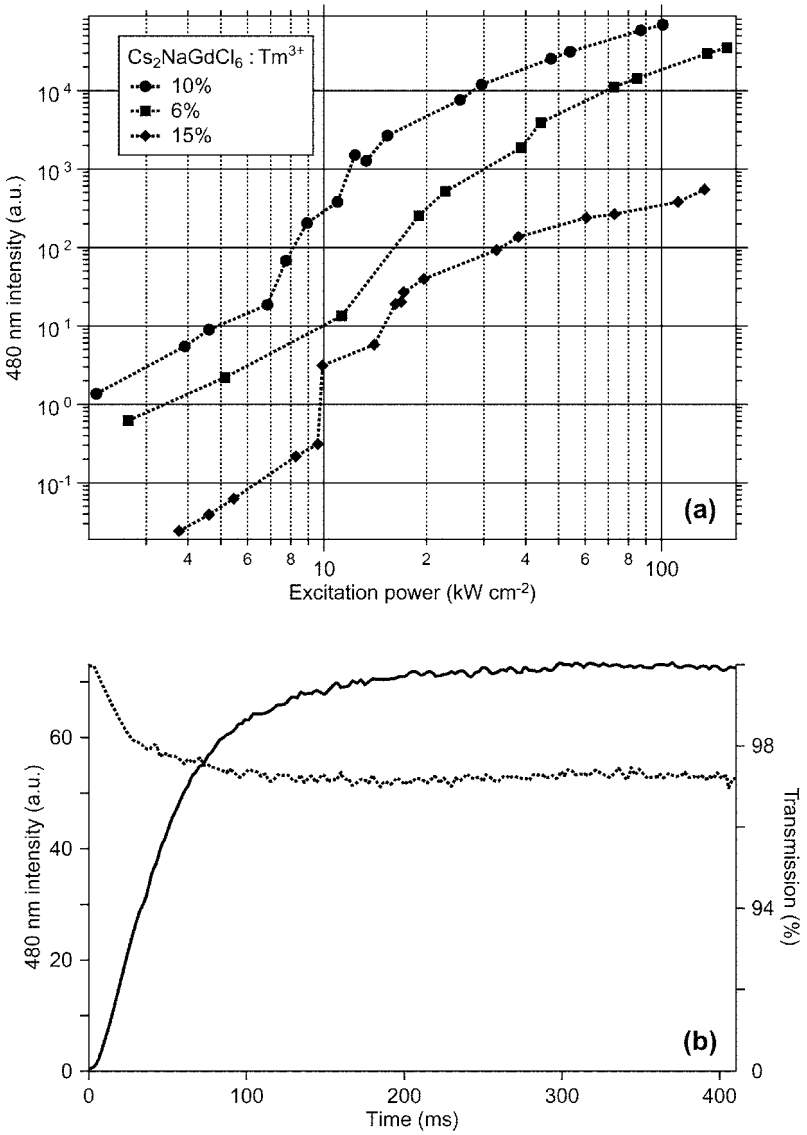

Fig. 27 **a** Power dependence of the 480 nm blue upconverted emission intensity of $Cs_2NaGdCl_6$:Tm^{3+} (6, 10 and 15 mol%). **b** Temporal dependence of this emission (*continuous line, left-hand ordinate) and of the transmitted laser beam (dotted line, right-hand ordinate)* for the 10 mol% sample under high excitation power, 14.5 P_{thres}. (Adapted from [347])

$$\frac{dn_f}{dt} = P(f')n_l - W_f n_f - U n_i n_f \tag{92c}$$

with $n_i+n_f+n_l=1$, and where W_x is the single ion relaxation rate of level x; and b is the branching ratio of the decay of level f. $P(l')$ is the pump rate to feed l', $P(f')$ feeds f'; and U is the cross-relaxation rate constant. Although these beam energies are equal, the pump rate also depends upon the absorption cross section, which is very small for $P(l')$, but large for $P(f')$. Then, if $U>bW_f$, photon avalanche appears above the following threshold value of $P(f')$ [392]:

$$P_{thres} = \frac{W_l(U + W_f)}{U - bW_f} \tag{93}$$

Whereas many examples of the photon avalanche phenomenon exist in the literature, only one study has been made for elpasolite systems [347], for $Cs_2NaGdCl_6$:Tm^{3+}, where the blue upconverted emission is due to the $^1G_4 \rightarrow {}^3H_6$ transition. However, the situation is rather more complex than in Fig. 24j because several other processes can occur, which also lead to emission from $^1D_2$. Three features related to the $^1G_4$ emission are highlighted here. First, Fig. 27a shows that a quadratic emission intensity-excitation power dependence is obtained at low excitation intensities for samples of $Cs_2NaGdCl_6$:Tm^{3+} doped with between 6–15 mol% Tm^{3+}. However, a dramatic increase of the emission intensity appears above the excitation threshold value, ca. 9 kW cm^{-2}. In Fig. 27a, the slope increases to 6 for the 10 mol% Tm^{3+}-doped sample. Second, the time-dependence of the upconverted emission exhibits different behaviour at different excitation powers. A notable difference from other systems is that, at the threshold excitation power, P_{thres}, the blue emission has an almost linear rise-time which is followed by a further slower rise over several seconds. Third, at high excitation powers, the establishment of the stationary state is quicker, and the $^3F_4 \rightarrow {}^1G_4$ ESA decreases the transmitted laser light by several percent, Fig. 27b.

14 Conclusions

This review has summarised and commented upon the literature up to the end of 2002. The electronic spectra of elpasolite systems are complex and mainly vibronic in character. Whereas the major features can be interpreted in terms of localized moiety-mode vibrations, our understanding of the fine structure requires a more detailed investigation of the lattice dynamics of these systems in the future. One- and two-photon studies of certain lanthanide elpasolite systems have recently enabled extensive energy level datasets to be obtained, and the parametrization of these has revealed the need for the incorporation of other interacting configurations into the calculation.

The study of f-d transitions of Ln^{3+} in M_2ALnX_6 systems is in its infancy, but promises to yield more clearly-resolved spectra than for the lower-symmetry hosts studied thus far. This is partly because of the higher degeneracy of CF levels in the elpasolite hosts, leading to fewer possible transitions, as well as to the more restrictive selection rules pertaining to these transitions. Resonant energy transfer in elpasolite systems is well-understood, but the understanding and calculation of nonresonant processes is far from satisfactory.

Acknowledgements This work was supported by the City University of Hong Kong Strategic Research Grant 7001199. I am indebted to Prof. Xia Shangda and Dr. Michèle Faucher for long and fruitful collaborations. I also thank my two PhD students Drs. Michael Chua and Chris Mak, and other collaborators, especially Profs. Mike Reid, Norman Edelstein and Roberto Acevedo. In addition, I thank both Prof. Xia and Dr. Faucher for carefully reading and correcting the manuscript, especially for Prof. Xia's detailed suggestions about formulae and statements in Sects. 6–8 and 13.3.

1 Appendix

The O_h point group character table and the O (and O^* double group) multiplication table are given in Tables A1 and A2.

Table A1 Character table for O_h molecular point group

O_h ($m3m$)		E	$8C_3$	$6C_2$	$6C_4$	$3C_2$	i	$6S_4$	$8S_6$	$3\sigma_h$	$6\sigma_d$		
Γ_{1g}	A_{1g}	1	1	1	1	1	1	1	1	1	1		$x^2+y^2+z^2$
Γ_{2g}	A_{2g}	1	1	−1	−1	1	1	−1	1	1	−1		
Γ_{3g}	E_g	2	−1	0	0	2	2	0	−1	2	0		$(2z^2\text{-}x^2\text{-}y^2, x^2\text{-}y^2)$
Γ_{4g}	T_{1g}	3	0	−1	1	−1	3	1	0	−1	−1	(R_x,R_y, R_z)	
Γ_{3g}	T_{2g}	3	0	1	−1	−1	3	−1	0	−1	1		xz, yz, xy
Γ_{1u}	A_{1u}	1	1	1	1	1	−1	−1	−1	−1	−1		
Γ_{2u}	A_{2u}	1	1	−1	−1	1	−1	1	−1	−1	1		
Γ_{3u}	E_u	2	−1	0	0	2	−2	0	1	−2	0		
Γ_{4u}	T_{1u}	3	0	−1	1	−1	−3	−1	0	1	1	(x, y, z)	
Γ_{5u}	T_{2u}	3	0	1	−1	−1	−3	1	0	1	−1		

Table A2 Multiplication table for O and O^* molecular point group (O_h=$O\times C_i$)

O	A_1	A_2	E	T_1	T_2	E′ (Γ_6)	E″ (Γ_7)	U′ (Γ_8)
$A_1(\Gamma_1)$	A_1	A_2	E	T_1	T_2	E′	E″	U′
$A_2(\Gamma_2)$	A_2	A_1	E	T_2	T_1	E″	E′	U′
$E(\Gamma_3)$	E	E	A_1+A_2+E	T_1+T_2	T_1+T_2	U′	U′	E′+E″+U′
$T_1(\Gamma_4)$	T_1	T_2	T_1+T_2	$A_1+E+T_1+T_2$	$A_2+E+T_1+T_2$	E′+U′	E″+U′	E′+E″+2U′
$T_2(\Gamma_5)$	T_2	T_1	T_1+T_2	$A_2+E+T_1+T_2$	$A_1+E+T_1+T_2$	E″+U′	E′+U′	E′+E″+2U′
$E'(\Gamma_6)$	E′	E″	U′	E′+ U′	E″+U′	A_1+T_1	A_2+T_2	$E+T_1+T_2$
E″ (Γ_7)	E″	E′	U′	E″+ U′	E′+ U′	A_2+T_2	A_1+T_1	$E+T_1+T_2$
U′ (Γ_8)	U′	U′	E′+E″+U′	E′+E″+2U′	E′+E+2U′	$E+T_1+T_2$	$E+T_1+T_2$	$A_1+A_2+E+2T_1+2T_2$

References

1. Barnes JC, Peacock RD (1971) J Chem Soc A 558
2. Jamison SP, Reeves RJ, Pavlichuk PP, Jones GD (1999) J Lumin 83/84:429
3. Jones GD, Reeves RJ (2000) J Lumin 87/89:1108
4. Zhang HY, Brundage RT, Yen WM (1984) J Lumin 31/32:257
5. Salley GM, Valiente R, Güdel HU (2002) J Phys Condens Matter 14:5461
6. Aarstrand V, Fotteler T, Beck W, Ricard D, Gâcon J-C (2001) J Phys Condens Matter 13:735
7. Mazurak Z, Ratuszna A, Daniel P (1999) J Lumin 82:163
8. Meyer G (1982) Progr Solid State Chem 14:141
9. Taylor MD (1962) Chem Rev 62:503
10. Taylor MD, Carter CP (1962) J Inorg Nucl Chem 24:387
11. Corbett JD (1983) Inorg Syn 22:31
12. Corbett JD (1983) Inorg Syn 22:39
13. Meyer G, Axe P (1982) Mater Res Bull 17:1447
14. Meyer G, Staffel T, Dötsch S, Schleid T (1985) Inorg Chem 24:3504
15. Friedich G, Seifert HJ (1994) J Therm Anal 41:725
16. Morss LR, Siegel M, Stinger L, Edelstein N (1970) Inorg Chem 9:1771
17. Baud M, Baraduc L, Gaille P, Cousseins J-C (1971) CR Acad Sci Paris 272:1328
18. Meyer G, Gaebell H-C (1978) Z Anorg Allg Chem 445:147
19. Meyer G, Dietzel E (1979) Rev Chim Minérale 16:189
20. Meyer G, Linzmeier P (1977) Rev Chim Minérale 14:52
21. Meyer G Hwu S-J Corbett JD (1986) Z Anorg Allg Chem 585:208
22. Mermant G, Primot J (1979) Mater Res Bull 14:45
23. Aléonard S, Pouzet C (1968) J Appl Cryst 1:113
24. Védrine A, Besse J-P, Baud G, Capestan M (1970) Rev Chim Minérale 7:593
25. Tanner PA, Yulong L, Edelstein NM, Murdoch KM, Khaidukov NM (1997) J Phys Condens Matter 9:7817
26. Feldner K, Hoppe R (1980) Z Anorg Allg Chem 471:131
27. Siddiqi I, Hoppe R (1970) Z Anorg Allg Chem 374:225
28. Bucher E, Guggenheim HJ, Andres K, Hull GW, Cooper AS (1974) Phys Rev B10:2945
29. Hemon A, Le Bail A, Courbion G (1990) Eur J Solid St Inorg Chem 27:905
30. Garton G, Wanklyn BM (1967) J Cryst Growth 1:49
31. Knox K, Mitchell DW (1961) J Inorg Nucl Chem 21:253
32. Meyer G (1980) Z Naturforsch 35b:394
33. Morss LR (1974) J Inorg Nucl Chem 36:3876
34. Güdel HU, Furrer A, Blank H (1990) Inorg Chem 29:4081
35. Tanner PA, Mak CSK, Kwok W-M, Phillips DL, Faucher MD (2002) Phys Rev B66:165203
36. Zinenko VI, Zamkova NG (2000) J Exp Theor Phys 91:314
37. Gorev MV, Misyul SV, Bovina AF, Iskornev IM, Kokov IT, Flerov IN (1986) J Phys C Solid St Phys 19:2441
38. Aleksandrov KS, Bovina AF, Voronov VN, Gorev MV, Iskornev IM, Melnikova SV, Misjul SV, Prokert F, Flerov IN (1985) Japan J Appl Physics 24:699
39. Friedrich G, Fink H, Seifert HJ (1994) Thermochim Acta 234:287
40. Knudsen GP (1984) Solid State Commun 49:1045

41. Knudsen GP, Voss FW, Nevald R, Amberger H-D (1982) In: McCarthy GJ, Silber HB, Rhyne JJ (eds) Rare earths in modern science and technology. Plenum, New York, vol 3:335
42. Schwartz RW, Watkins SF, O'Connor CJ, Carlin RL (1976) J Chem Soc Faraday Trans 2 72:565
43. Krupski M, Morawski P, Usachev AE (1997) J Phys Condens Matter 9:6427
44. Bleaney B, Stephen AG, Walker PJ, Wells MR (1982) Proc R Soc London A381:1
45. Makarova IP, Misyul SV, Muradyan LA, Bovina AF, Simonov VI, Aleksandrov KS (1984) Phys Status Solidi B 121:481
46. Veenendaal EJ, Brom HB (1982) Physica 113B:118
47. Veenendaal EJ, Brom HB, Ihringer J (1982) Physica 114B:31
48. Selgert P, Lingner C, Lüthi B (1984) Z Phys B55:219
49. Aleksandrov KS, Melnikova SV, Misyul SV (1987) Phys Status Sol A 104:545
50. Ihringer J (1982) Solid State Commun 41:525
51. Flerov IN, Gorev MV, Voronov VN (1996) Soviet Phys Solid State 38:396
52. Dance JM, Grannec J, Tressaud A, Moreno M (1992) Phys Status Solidi B 173:579
53. Khaïroun S, Tressaud A, Grannec J, Dance JM, Yacoubi A (1988) Phase Transitions 13:157
54. Couzi M, Khaïroun S, Tressaud A (1986) Phys Status Solidi A 98:423
55. Vtyurin AN, Bulou A, Krylov AS, Voronov VN (2001) Phys Solid State 43:2154
56. Gorev MV, Flerov IN, Tressaud A, Grannec J, Faget H, Sonntag R, Linhart J (1997) Ferroelectric Lett 22:127
57. Tressaud A, Khaïroun S, Couzi M (1986) Phys Status Solidi A 98:417
58. Meyer G, Gaebell H-C (1978) Z Naturforsch 33b:1476
59. Roser MR, Xu J, White SJ, Corruccini LR (1992) Phys Rev B45:12337
60. Furrer A, Güdel HU (1997) Phys Rev B56:15062
61. Nakajima T, Suzuki H (1994) J Low Temp Phys 96:47
62. Nakamoto K (1997) Infrared and Raman spectra of coordination compounds, 5th edn. Wiley, New York
63. Dines T, Clark RJH (1982) Advances in infrared and Raman spectroscopy. In: Clark RJH, Hester RE (eds). Heyden, London, vol 9, p 282
64. Wybourne B (1965) Spectroscopic properties of rare earths. Wiley, New York
65. Görller-Walrand C, Binnemans K (1998) Handbook on the physics and chemistry of rare earths, vol 25, p 101
66. Xia S, Tanner PA (in preparation)
67. Faulkner TR, Richardson FS (1978) Mol Phys 35:1141
68. Griffith JS (1980) The theory of transition metal ions. Cambridge University Press, Cambridge, UK
69. Axe JD (1964) Phys Rev 116:A42
70. Ning L, Wang D, Xia S, Thorne JRG, Tanner PA (2002) J Phys Condens Matter 14:3833
71. Ceulemans A, Vandenberghe GM (1993) J Chem Phys 98:9372
72. Tanner PA, Kumar RKK, Jayasankar CK, Reid MF (1994) J Alloys Compds 215:349
73. Tsukerblat BS (1994) Group theory in chemistry and spectroscopy. Academic Press
74. Tanner PA, Shen M-Y (1994) Spectrochim Acta 50A:997
75. Lentz A (1974) J Phys Chem Solids 35:827
76. Ning L, Tanner PA, Xia S (2003) Vibrational Spectr 31:51
77. Barbanel A, Dushin RB, Mikhailova NK, Chudnovskaya GP (1979) Radiokhimiya 21:706

78. Barbanel A, Dushin RB, Kolin VP, Mikhailova NK, Chudnovskaya GP (1975) Koord Khim 1:411
79. Stręk W, Mazurak Z, Szafranski C, Hanuza J, Hermanowicz K, Jezowska-Trzebiatowska B (1984) Chem Phys 84:269
80. Jezowska-Trzebiatowska B, Ryba-Romanowski W, Mazurak Z, Hanuza J (1980) Chem Phys 50:209
81. Amberger H-D (1978) Spectrochim Acta 34A:627
82. Amberger H-D (1982) (private communication)
83. Becker R, Lentz A, Sawodny W (1976) Z Anorg Allg Chem 420:210
84. Nissen-Sobocińska B, Stręk W, Hanuza J, Hermanowicz K, Denisenko G, Aleksandrov KS, Voronov VN (1995) J Appl Spectr 62:877
85. Amberger H-D (1980) Z Anorg Allg Chem 467:231
86. Amberger H-D, Fischer RD, Rosenbauer GG (1976) Trans Met Chem 1:242
87. Haley LV, Koningstein JA (1976) J Raman Spectr 5:305
88. Amberger H-D, Rosenbauer GG, Fischer RD (1977) J Phys Chem Solids 38:379
89. Papatheodorou GN (1977) J Chem Phys 66:2893
90. Papatheodorou GN (1975) Inorg Nucl Chem Lett 11:483
91. Tanner PA, Xia S, Liu YL, Ma Y (1997) Phys Rev B55:12182
92. Amberger H-D, Rosenbauer GG, Fischer RD (1976) Molec Phys 32:1291
93. Kanellakopulos B, Amberger H-D, Rosenbauer GG, Fischer RD (1977) J Inorg Nucl Chem 39:607
94. Amberger H-D (1978) Z Anorg Allg Chem 489:48
95. Photiadis GM, Børresen B, Papatheodorou GN (1998) J Chem Soc Faraday Trans 94:2605
96. Dracopoulos V, Gilbert B, Børresen B, Photiadis GM, Papatheodorou GN (1997) J Chem Soc Faraday Trans 93:3081
97. Acevedo R, Tanner PA, Meruane T, Poblete V (1996) Phys Rev B54:3976
98. Amberger H-D (1978) Inorg Nucl Chem Lett 14:491
99. Fish GE, Rhyne JJ, Lynn JW, Patterson HH (1979) Bull Am Phys Soc 24:429
100. Sinkovits RS, Bartram RH (1991) J Phys Chem Solids 52:1137
101. Gutowski M, Boldyrev AI, Simons J, Rak J, Blazejowski J (1996) J Am Chem Soc 118:1173
102. Tinkham M (1964) Group theory and quantum mechanics. McGraw-Hill, New York
103. Chodos S (1971) PhD Dissertation, University of California, Los Angeles
104. O'Leary GP, Wheeler RG (1970) Phys Rev B1:4409
105. Zinenko V (1998) J Exp Theor Phys 87:944
106. Bührer W, Güdel HU (1987) J Phys C Solid State Phys 20:3809
107. Furrer A, Güdel HU, Darriet J (1985) J Less Common Metals 111:223
108. Prokert F, Aleksandrov KS (1984) Phys Status Solidi B 124:503
109. Huber MCE, Sandeman RJ (1986) Rep Prog Phys 49:397
110. Flint CD (1976) Adv Infrared Raman Spectrosc 2:53
111. Ballhausen CJ, Hansen AE (1972) Ann Rev Phys Chem 23:15
112. Faulkner TR, Richardson FS (1978) Mol Phys 36:193
113. Tanner PA, Siu GG (1992) Mol Phys 75:233
114. Sztucki J (1993) Chem Phys Lett 203:383
115. Schatz PN (1965) Spectrochim Acta 21:617
116. Henderson B, Imbusch GF (1989) Optical spectroscopy of inorganic solids. Clarendon Press, Oxford, UK
117. Judd BR (1962) Phys Rev 127:750
118. Orera VM, Trinkler LE, Merino RI, Larrea A (1995) J Phys Condens Matter 7:9657

119. Malta OL, Gouveia EA, de Sa GF (1984) J Lumin 31/32:225
120. Hubert S, Meichenin D, Zhou BW, Auzel F (1991) J Lumin 50:7
121. Nielson CW, Koster JF (1963) Spectroscopic coefficients for p^n, d^n and f^n configurations. MIT Press, Cambridge MA
122. Tanner PA (1985) Chem Phys Lett 119:213
123. Tanner PA, Jayasankar CK, Richardson FS (1988) Molec Phys 65:49
124. Schwartz RW, Brittain HG, Riehl JP, Yeakel W, Richardson FS (1977) Molec Phys 34:361
125. Piepho SB, Schatz PN (1983) Group theory in spectroscopy. Wiley, New York
126. Tanner PA (1997) J Mol Struct 405:103
127. Görller-Walrand C, Fluyt L, Ceulemans A, Carnall WT (1991) J Chem Phys 95:3099
128. Crooks SM, Reid MF, Tanner PA, Zhao YY (1997) J Alloys Compd 250:297
129. Karraker DG (1968) Inorg Chem 7:473
130. Gruen DM, DeKock CW (1966) J Chem Phys 45:455
131. Boghosian S, Papatheodorou GN (1996) Handbook on the physics and chemistry of rare earths, vol 23, p 435
132. Huskowska E, Riehl JP (2000) J Lumin 86:137
133. Judd BR (1979) J Chem Phys 70:4830
134. Malta OM (1981) Molec Phys 42:65
135. Judd BR (1988) Handbook on the physics and chemistry of rare earths, vol 11, p 137
136. Reid MF, Richardson FS (1983) Chem Phys Lett 95:501
137. Burdick GW, Downer MC (1991) Eur J Solid State Inorg Chem 28:217
138. Peacock RD (1975) Struct Bonding 22:83
139. Henrie DE, Fellows RL, Choppin GR (1976) Coord Chem Rev 18:199
140. Judd BR (1980) In: Edelstein N (ed) Lanthanide and actinide chemistry and spectroscopy. American Chemical Society, Washington DC, p 267
141. Judd BR (1980) Phys Scripta 21:543
142. Schwartz RW, Banerjee AK (1981) Chem Phys Lett 79:19
143. Sztucki J (1993) Chem Phys Lett 203:383
144. Hellwege KH (1951) Z Phys 129:626
145. Mason SF, Peacock RD, Stewart B (1975) Molec Phys 30:1829
146. Yersin H, Otto H, Zink JI, Gliemann G (1980) J Am Chem Soc 102:951
147. Tanner PA (1986) Mol Phys 57:697
148. Tanner PA (1986) Chem Phys Lett 126:137
149. Tanner PA (1986) Mol Phys 58:317
150. Axe JD, Sorokin PP (1963) Phys Rev 130:945
151. Faulkner TR, Richardson FS (1979) Mol Phys 38:1165
152. Tanner PA, DePiante A, Richardson FS, Reid MF (1987) Mol Phys 60:1037
153. Luxbacher T, Fritzer HP, Flint CD (1995) Chem Phys Lett 232:571
154. Galczynski M, Stręk W (1992) In: Stręk W et al. (eds) Proceedings of the 2nd International School on Excited States of Transition Elements, Karpacz 1991. World Scientific, Singapore, p 355
155. Lohr L (1970) J Am Chem Soc 92:2210
156. Yamada N, Shionoya S (1971) J Phys Soc Japan 31:841
157. Morley JP, Faulkner TR, Richardson FS, Schwartz RW (1982) J Chem Phys 1734
158. Foster DR, Richardson FS, Schwartz RW (1985) J Chem Phys 82:601
159. Foster DR, Richardson FS, Schwartz RW (1985) J Chem Phys 82:618
160. Morley JP, Faulkner TR, Richardson FS (1982) J Chem Phys 77:1710
161. Foster DR, Richardson FS (1985) J Chem Phys 82:1085
162. Morley JP, Faulkner TR, Richardson FS, Schwartz RW (1981) J Chem Phys 75:539

163. Hasan Z-U, Richardson (1982) Mol Phys 45:1299
164. Schwartz RW, Faulkner TR, Richardson FS (1979) Mol Phys 38:1767
165. Xia S, Reid MF (1993) J Phys Chem Solids 54:777
166. Stewart B (1993) Chem Phys Lett 206:106
167. Malta OL (1995) J Phys Chem Solids 56:1053
168. Reid MF, Richardson FS (1984) Mol Phys 51:1077
169. Burdick GW, Duan CK, Reid MF, Mak CSK, Tanner PA (2002) 23rd Rare Earth Research Conference, Davis, California, July 13–18, 2002, PES-08, p 85
170. Acevedo R, Cortes E, Meruane T, Vasquez SO, Flint CD (1994) An Quim 90:334
171. Acevedo R, Meruane T, Cortes E, Vasquez SO, Flint CD (1994) Theor Chim Acta 88:99
172. Acevedo R, Flint CD, Meruane T, Munoz G, Passman M, Poblete V (1997) Theochem J Mol Struct 390:109
173. Tanner PA, Hurtado O, Meruane T, Acevedo R (2001) J Alloys Compds 323/324:718
174. Griffith JS (1962) The irreducible tensor method for molecular symmetry groups. Prentice-Hall, Englewood Cliffs, NJ
175. Stavola M, Dexter DL (1979) Phys Rev B20:1867
176. Stavola M, Isganitis L, Sceats MG (1981) J Chem Phys 74:4228
177. Dexpert-Ghys J, Auzel F (1984) J Chem Phys 80:4003
178. Satten RA (1964) J Chem Phys 40:1200
179. Cohen E, Moos HW (1967) J Chem Phys 161:268
180. Loudon R (1964) Proc Phys Soc 84:379
181. Chen LC, Berenson R, Birman JL (1968) Phys Rev 170:639
182. Bron WE (1969) Phys Rev 185:1163
183. Richman I, Satten RA, Wong EY (1963) J Chem Phys 39:1833
184. Chodos S, Satten RA (1975) J Chem Phys 62:2411
185. Tanner PA (1987) J Chem Soc Faraday Trans 2 83:1367
186. Tanner PA (1987) J Chem Soc Faraday Trans 2 83:553
187. Tanner PA (1986) Chem Phys Lett 132:116
188. Torres DI, Freire JD, Katiyar RS (1997) Phys Rev B56:7763
189. Bron WE (1965) Phys Rev 140:A2005
190. Kühner DH, Lauer HV, Bron WE (1972) Phys Rev B5:4112
191. Ning L (2002) (private communication)
192. Satten RA, Johnston DR, Wong EY (1968) Phys Rev 171:370
193. Urland W (1979) Z Naturforsch 34a:1507
194. Urland W, Feldner K, Hoppe R (1980) Z Anorg Allg Chem 465:7
195. O'Connor CJ, Carlin RL, Schwarz RW (1977) J Chem Soc Faraday Trans 2 73:361
196. Schwarz RW, Hill NJ (1974) J Chem Soc Faraday Trans 2 70:124
197. Bleaney B, Stephen AG, Walker PJ, Wells MR (1981) Proc Roy Soc Lond A376:235
198. Fish GE, North MH, Stapleton HJ (1980) J Chem Phys 73:4807
199. Amberger H-D, Fischer RD, Rosenbauer GG (1975) Ber Bunsenges Phys Chem 79:1226
200. Amberger H-D, Fischer RD, Rosenbauer GG (1976) Z Phys Chem 102:279
201. Tanner PA, Liu YL (1994) J Alloys Compds 204:207
202. Nguyen A-D (1997) Phys Rev B55:5786
203. Chua M, Tanner PA (1997) Chem Phys 218:83
204. Xia S, Williams GM, Edelstein N (1989) Chem Phys 138:255
205. Chua M, Tanner PA, Xia S (1997) Chem Phys Lett 274:554
206. Tanner PA, Mak CSK, Faucher MD, Kwok DL, Phillips DL, Mikhailik V (2003) Phys Rev B67:115102

207. Tanner PA, Mak CSK, Faucher MD (2001) J Chem Phys 114:10860
208. Wang D, Xia S, Faucher MD, Tanner PA (2004) J Phys Condens Matter 16:6243
209. Tanner PA (1985) Mol Phys 54:883
210. Tanner PA (1986) J Chem Phys 85:2344
211. Richardson FS (1986) J Chem Phys 85:2345
212. Thorne JRG, Zeng Q, Denning RG (2001) J Phys Condens Matter 13:7403
213. Tanner PA, Mak CSK, Faucher MD (2004) J Phys Chem A 108:5278
214. Mak CSK, Tanner PA, Tröster T, Xia S (2002) J Phys Chem Solids 63:1623
215. Lupei A, Lupei V, Enaki VN, Presura C, Petraru A (1999) Spectrochim Acta A55:773
216. Morrison ID, Berry AY, Denning RG (1999) Mol Phys 96:43
217. Axe JD (1964) Phys Rev A 136:42
218. Judd BR, Pooler DR (1982) J Phys C 15:591
219. Downer MC, Bivas A, Bloembergen N (1982) Opt Commun 41:335
220. Downer MC, Bivas A (1983) Phys Rev B 28:3677
221. Grassano U (1992) In: Di Bartolo BD (ed) Optical properties of excited states in solids. Plenum, New York, p 643
222. Doni E, Girlanda R, Parravicini GP (1974) Phys Status Solidi B 65:203
223. Berry AJ, McCaw CS, Morrison ID, Denning RG (1996) J Lumin 66/67:272
224. Berry AJ, Denning RG, Morrison ID (1997) J Chem Phys 106:8967
225. Sztucki J (1993) J Phys Condens Matter 5:6773
226. Sztucki J (1994) J Lumin 60/61:681
227. Berry AJ, Morrison ID, Denning RG (1998) Mol Phys 93:1
228. Thorne JRG, Jones M, McCaw CS, Murdoch KM, Denning RG, Khaidukov NM (1999) J Phys Condens Matter 11:7851
229. Thorne JRG, Karunathilake A, Choi H, Denning RG, Luxbacher T (1999) J Phys Condens Matter 11:7867
230. McCaw CS, Murdoch KM, Denning RG (2003) Mol Phys 101:427
231. Deren PJ, Stręk W (1996) J Lumin 69:295
232. Bouazaoui M, Jacquier B, Linarès C, Stręk W (1991) J Phys C Solid State Phys 3:921
233. Bouazaoui M, Jacquier B, Linarès C, Stręk W, Cone RL (1991) J Lumin 48/49:318
234. Kundu L, Banerjee AK, Chowdhury M (1991) Chem Phys Lett 181:569
235. Ceulemans A, Vandenberghe GM (1996) Phys Rev B 53:8310
236. Ceulemans A, Vandenberghe GM (1994) J Alloys Compds 207/208:102
237. Chua M, Tanner PA (1996) Phys Rev B54:R11014
238. Reid MF, Burdick GW, Kooy HJ (1994) J Alloys Compds 207/208:78
239. Sztucki J, Stręk W (1986) Phys Rev B34:3120
240. Reid MF, Richardson FS (1984) Phys Rev B29:2830
241. Wang D, Ning L, Xia S, Tanner PA (2003) J Phys Condens Matter 15:2681
242. Morrison ID (1992) PhD Thesis, University College, Oxford
243. Ning L, Xia S, Tanner PA (2002) J Phys Condens Matter 14:8677
244. Ryan JL, Jørgensen CK (1966) J Phys Chem 70:2845
245. Nugent LJ, Baybarz RD, Burnett JL, Ryan JL (1973) J Phys Chem 77:1528
246. Ionova G, Krupa JC, Gerard I, Guillaumont R (1995) New J Chem 19:677
247. Collombet A, Guyot Y, Mak CSK, Tanner PA, Joubert M-F (2001) J Lumin 94/95:39
248. Tanner PA, Mak CSK, Edelstein NM, Murdoch K, Liu G, Huang J, Seijo L, Barandiarán Z (2003) J Am Chem Soc 125:13225
249. Mak CSK (2002) PhD Thesis, City University of Hong Kong
250. van Pieterson L, Reid MF, Wegh RT, Meijerink A (2001) J Lumin 94:79
251. Jüstel T, Krupa JC, Wiechert DU (2001) J Lumin 93:179
252. Schwartz RW, Schatz PN (1973) Phys Rev B8:3229

253. van't Spijker JC, Dorenbos P, van Eijk CWE, Wickleder MS, Güdel H-U, Rodnyi PA (1997) J Lumin 72/74:786
254. Dorenbos P (2000) Phys Rev B62:15650
255. Combes CM, Dorenbos P, van Eijk CWE, Krämer KW, Güdel H-U (1999) J Lumin 82:299
256. Rodnyi PA, Mikhailik VB, Stryganyuk GB, Voloshinovskii AS, van Eijk CWE, Zimmerer GF (2000) J Lumin 86:161
257. van Loef EVD, Dorenbos P, van Eijk CWE, Krämer KW, Güdel H-U (2002) J Phys Condens Matter 14:8481
258. Pawlik T, Spaeth J-M (1997) J Appl Phys 82:4236
259. Aull BF, Jenssen HP (1986) Phys Rev B34:6647
260. Laroche M, Bettinelli M, Girard S, Moncorgé R (1999) Chem Phys Lett 311:167
261. Tanner PA, Mak CSK, Faucher MD (2001) Chem Phys Lett 343:309
262. Makhov VN, Kirikova NY, Kirm M, Krupa JC, Liblik P, Lushchik A, Luschik C, Negodin E, Zimmerer (2002) Nucl Instrum Methods Phys Res A486:437
263. van Pieterson L, Reid MF, Wegh RT, Soverna S, Meijerink A (2002) Phys Rev B65:45113
264. Ning L, Duan CK, Xia S, Reid MF, Tanner PA (2004) J Alloys Compds 366:34–40
265. Guyot Y, Collombet A, Somatri T, Tkachuk A, Joubert M-F (2002) J Alloys Compds 341:174
266. van Pieterson L, Wegh RT, Meijerink A, Reid MF (2001) J Chem Phys 115:9382
267. Denning RG (1999) Spectrochim Acta A55:1757
268. Morrison CA, Leavitt RP, Wortman DE (1980) J Chem Phys 73:2580
269. Reid MF, Richardson FS (1985) J Chem Phys 83:3831
270. Tanner PA, Mak CSK, Zhou X, Faucher MD (in preparation)
271. Richardson FS, Reid MF, Dallara JJ, Smith RD (1985) J Chem Phys 83:3813
272. Reid MF, Richardson FS, Tanner PA (1987) Mol Phys 60:881
273. Jayasankar CK, Richardson FS, Reid MF, Tanner PA (1987) Mol Phys 61:635
274. Tanner PA, Richardson FS, Quagliano J (1991) J Chem Soc Faraday Trans 87:1707
275. Dushin RB, Nekhoroshkov SN (1996) Radiochem 38:198
276. Ankudinov AL, Dushin RB (1995) Phys Solid State 37:885
277. Hasan Z, Biyikli L, Sellars MJ, Khodaparast GA, Richardson FS, Quagliano J (1997) Phys Rev B56:4518
278. Reid MF, Richardson FS, Tanner PA (1987) Mol Phys 60:881
279. Thorne JRG, McCaw CS, Denning RG (2000) Chem Phys Lett 319:185
280. McCaw CS, Denning RG (2003) Mol Phys 101:439
281. Denning RG, Berry AJ, McCaw CS (1998) Phys Rev B57:R2021
282. Faucher MD, Tanner PA (2003) Mol Phys 101:983
283. Görller-Walrand C, Binnemans K (1996) Handbook on the physics and chemistry of rare earths, vol 23, p 121
284. Garcia D, Faucher M (1995) Handbook on the physics and chemistry of rare earths, vol 21, p 263
285. Gruber B, Quagliano JR, Reid MF, Richardson FS, Hills ME, Seltzer MD, Stevens SB, Morrison CA, Allik TH (1993) Phys Rev B48:15561
286. Capobianco JA, Kabro P, Ermeneux FS, Moncorgé R, Bettinelli M, Cavalli E (1997) Chem Phys 214:329
287. Krämer KW, Güdel H-U, Schwartz RW (1997) Phys Rev B56:13830
288. Carnall WT, Goodman GL, Rajnak K, Rana RS (1988) Report ANL-88-8, Argonne Nat Lab, Illinois, USA, February 1988
289. Quagliano JR, Cockroft NJ, Gunde KE, Richardson FS (1996) J Chem Phys 105:9812

290. Hehlen MP, Güdel H-U, Quagliano JR (1994) J Chem Phys 101:10303
291. Lüthi SR, Güdel H-U, Hehlen MP, Quagliano JR (1998) Phys Rev B57:15229
292. Newman DJ, Siu GG, Fung WYP (1982) J Phys C Solid State Phys 15:3113
293. Burdick GW, Richardson FS (1997) J Alloys Compds 250:293
294. Berry AJ, Denning RG, Morrison ID (1997) Chem Phys Lett 266:195
295. Moune OK, Garcia D, Faucher M (1991) J Phys Chem Solids 52:513
296. Faucher M, Garcia D, Porcher P (1989) C R Acad Sci Paris 308:603
297. Garcia D, Faucher M (1989) J Chem Phys 91:7461
298. Garcia D, Faucher M (1989) J Chem Phys 90:5280
299. Faucher MD, Moune OK (1997) Phys Rev A55:4150
300. Moune OK, Jayasankar CK, Faucher MD, Lejus AM (1999) Mater Sci Forum 315/317:415
301. Moune OK, Faucher MD, Jayasankar CK, Lejus AM (1999) J Lumin 85:59
302. Faucher MD, Moune OK, Garcia D, Tanner P (1996) Phys Rev B53:9501
303. Faucher MD (1998) Eur Phys J D3:9
304. Antic-Fidancev E (2000) J Alloys Compds 300/301:2
305. Vasquez SO, Flint CD (1995) Chem Phys Lett 238:378
306. Vasquez SO, Flint C (1999) Bol Soc Chil Quim 44:487
307. Tofield BC, Weber HP (1974) Phys Rev B10:4560
308. Stręk W, Mazurak Z, Szafranski C, Hanuza J, Hermanowicz K, Jezowska-Trzebiatowska B (1984) Chem Phys 84:269
309. Merchandt P, Grannec J, Chaminade J-P, Fouassier C (1980) Mater Res Bull 15:1113
310. Luxbacher T, Fritzer HP, Gatterer K, Flint CD (1995) J Appl Spectrosc 62:26
311. Luxbacher T, Fritzer HP, Flint CD (1995) J Phys Condens Matter 7:9683
312. Luxbacher T, Fritzer HP, Flint CD (1997) J Lumin 71:313
313. Luxbacher T, Fritzer HP, Flint CD (1997) J Lumin 71:177
314. Luxbacher T, Fritzer HP, Sabry-Grant R, Flint CD (1995) Chem Phys Lett 241:103
315. Luxbacher T, Fritzer HP, Flint CD (1998) J Alloys Compds 275/277:250
316. Luxbacher T, Fritzer HP, Flint CD (1998) Spectrochim Acta A54:2099
317. Luxbacher T, Fritzer HP, Flint CD (1997) Spectrochim Acta A54:2027
318. Luxbacher T, Fritzer HP, Flint CD (1997) SPIE 3176:124
319. Duckett MR, Flint CD (1997) SPIE 3176:108
320. Bettinelli M, Flint CD, Duckett M (1991) In: Stręk W (ed) Second International School on Excited States of Transition Elements, Sept 2–6. World Sci Publ, Karpacz, Poland, p 21
321. Bettinelli M, Flint CD (1991) J Phys Condens Matter 3:7053
322. Bettinelli M, Flint CD (1991) J Phys Condens Matter 3:4433
323. Stewart-Darling FL (1982) PhD Thesis University of London
324. Bettinelli M, Flint CD (1990) J Phys Condens Matter 2:8417
325. Bettinelli M, Flint CD (1991) In: Stręk W (ed) Second International School on Excited States of Transition Elements, Sept 2–6. World Sci Publ, Karpacz, Poland, p 304
326. Bettinelli M (1989) In: Flint CD (ed) Vibronic processes in inorganic chemistry. Kluwer, North-Holland, p 347
327. de Vries AJ, Blasse G (1988) J Chem Phys 88:7315
328. Berry AJ (1995) D Phil Thesis University of Oxford
329. Buñuel MA, Lozano L, Chaminade JP, Moine B, Jacquier B (1999) Opt Mater 13:211
330. McCaw CS (1998) D Phil Thesis University of Oxford
331. Tanner PA (1986) J Phys Chem 90:5605
332. Tanner PA (1984) Mol Phys 53:813
333. Banerjee A, Stewart-Darling F, Flint CD, Schwartz RW (1981) J Phys Chem 85:146

334. Humbs W, Strasser J, Braun D, Sabry-Grant R, Drndarski S, Flint CD, Yersin H (1997) SPIE 3176:114
335. Tanner PA (1988) Mol Phys 63:365
336. Ryba-Romanowski W, Mazurak Z, Jezowska-Trzebiatowska B (1982) J Lumin 27:177
337. Mazurak Z, Lukowiak E, Jezowska-Trzebiatowska B, Ryba-Romanowski W (1984) J Lumin 29:47
338. Campbell M, Humbs W, Strasser J, Yersin H, Flint CD (1997) SPIE 3176:103
339. Ryba-Romanowski W, Dominiak-Dzik G, Golab S (1994) J Phys Condens Matter 6:1593
340. Campbell M, Flint CD (1996) Acta Phys Polonica 90:151
341. Campbell M, Flint CD (1998) Spectrochim Acta 54A:1583
342. Campbell M, Flint CD (1997) SPIE 3176:98
343. Wermuth M, Schmitz A, Güdel HU (2001) Phys Rev B63:245118
344. Tanner PA, Mak CSK, Kwok WM, Phillips DL, Joubert M-F (2002) J Phys Chem B106:3606
345. Cresswell PJ, Robbins DJ, Thomson AJ (1978) J Lumin 17:311
346. Tanner PA, Choi TK, Hoffman K (1993) Appl Spectrosc 47:1084
347. Joubert MF, Guy S, Cuerq S, Tanner PA (1997) J Lumin 75:287
348. Ryba-Romanowski W, Golab S (1998) J Mol Struct 450:223
349. Weber MJ (1967) Phys Rev 156:231
350. Tallant DR, Miller MP, Wright JC (1976) J Chem Phys 65:510
351. Weber MJ (1971) Phys Rev B4:2932
352. Watts RK, Richter HJ (1972) Phys Rev B6:1584
353. van Dijk JMF, Schuurmans MFH (1983) J Chem Phys 78:5317
354. Schuurmans MFH, van Dijk JMF (1984) Physica 123B:131
355. Tanner PA (1988) Chem Phys Lett 145:134
356. Chua M, Tanner PA (1996) J Lumin 66/67:203
357. Hadad CZ, Vasquez SO (1999) Phys Rev B 60:8586
358. Kushida T (1973) J Phys Soc Jpn 34:1318
359. Szabo A (1970) Phys Rev Lett 25:924
360. Tanner PA, Chua M, Reid MF (1993) Chem Phys Lett 209:539
361. Inokuti M, Hirayama F (1965) J Chem Phys 43:1978
362. Yakota M, Tanimoto O (1967) J Phys Soc Jpn 22:779
363. Dornauf H, Heber J (1980) J Lumin 22:1
364. Chua M, Tanner PA, Reid MF (1994) J Lumin 58:356
365. Vasquez SO (1999) Phys Rev B60:8575
366. Tanner PA, Chua M, Reid MF (1995) J Alloys Compds 225:20
367. Chua M, Tanner PA (1999) Chem Phys 250:267
368. Holstein T, Lyo SK, Orbach R (1981) In: Yen WM, Selzer PM (eds) Laser spectroscopy of solids. Springer, Berlin Heidelberg New York, p 39
369. Xia S, Tanner PA (2003) Phys Rev B66:214305
370. Vasquez SO (1996) J Chem Phys 104:7652
371. Vasquez SO (1997) J Chem Phys 106:8664
372. Vasquez SO (1998) J Chem Phys 108:723
373. Laulicht I, Meirman S (1986) J Lumin 34:287
374. Moran DM, May PS, Richardson FS (1994) Chem Phys 186:77
375. Chua M, Tanner PA, Reid MF (1994) J Lumin 60/61:838
376. Tanner PA, Liu Y-L, Chua M, Reid MF (1994) J Alloys Compds 207/208:83
377. Tanaka F, Ishibashi T (1996) J Chem Soc Faraday Trans 92:1105
378. Villafuerte-Castrejon ME, Alvarez ME, Caldino U (2001) Ferroelectrics Lett 28:103

379. Berry ME, May PS, Hu Q (1997) J Lumin 71:269
380. Tanner PA, Chua M, Kwok W-M, Phillips DL (1999) Phys Rev B60:13902
381. Mazurak Z, Lukowiak E, Jezowska-Trzebiatowska B (1985) J Lumin 33:159
382. Gamelin DR, Güdel HU (2001) Top Curr Chem 214:1
383. Pollnau M, Gamelin DR, Lüthi SR, Güdel HU, Hehlen MP (2000) Phys Rev B61:3337
384. Campbell M, Flint CD (1996) Acta Phys Polonica 90A:151
385. Ryba-Romanowski W, Golab S, Pisarski WA (1995) J Phys Condens Matter 7:7397
386. Wegh RT, Donker H, van Loef EVD, Oskam KD, Meijerink A (2000) J Lumin 87/89:1017
387. Kirk AD, Furer N, Güdel HU (1996) J Lumin 68:77
388. Gamelin DR, Güdel HU (2000) Acc Chem Res 33:235
389. Reinhard C, Güdel HU (2003) J Lumin 102/103:373
390. Joubert MF, Guy S, Jacquier B (1993) Phys Rev B48:10031
391. Joubert MF (1999) Opt Mater 11:181
392. Joubert MF, Guy S, Jacquier B, Linarès C (1994) Opt Mater 4:43
393. Joubert MF, Guy S, Jacquier B, Linarès C (1995) J Appl Spectrosc 62:126
394. Case WE, Koch ME, Kueny AW (1990) J Lumin 45:351

Author Index Volumes 201–241

Author Index Vols. 26–50 see Vol. 50
Author Index Vols. 51–100 see Vol. 100
Author Index Vols. 101–150 see Vol. 150
Author Index Vols. 151–200 see Vol. 200

The volume numbers are printed in italics

Subject Index